ALFVÉN WAVES IN LOW-MASS STAR-FORMING REGIONS

Clare E. Martin

A Thesis Submitted for the Degree of PhD
at the
University of St Andrews

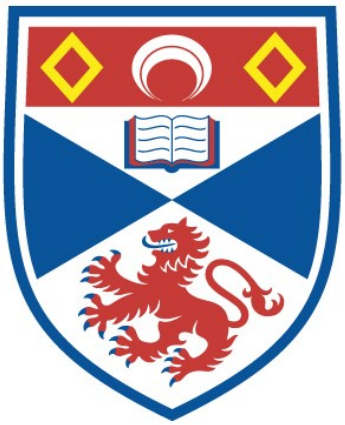

1999

ALFVÉN WAVES IN LOW-MASS STAR-FORMING REGIONS

CLARE E. MARTIN

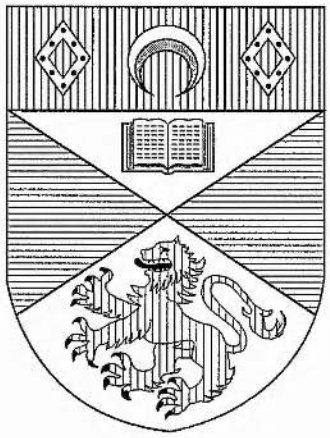

THESIS SUBMITTED FOR THE DEGREE OF DOCTOR OF PHILOSOPHY
OF THE UNIVERSITY OF ST ANDREWS
FEBRUARY 1999

TL D308

And as for those who felt that humanity needed the spur of suffering to make it great, well they could go out and find anew the tragedies that ... would never go away, things like lost love, betrayal by friends, death, bad results in the lab.

Kim Stanley Robinson

1. I, Clare Ellen Martin, hereby certify that this thesis, which is approximately 54,000 words in length, has been written by me, that it is the record of work carried out by me and that it has not been submitted in any previous application for a higher degree.

   Date: ..25.2.99.. Signature of Candidate: ....

2. I was admitted as a research student in October 1995 and as a candidate for the degree of Ph.D. in October 1996; the higher study for which this is a record was carried out in the University of St Andrews between October 1995 and February 1999.

   Date: ...25.2.99.. Signature of Candidate: ....

3. I hereby certify that the candidate has fulfilled the conditions of the Resolution and Regulations appropriate for the degree of Ph.D. in the University of St Andrews and that the candidate is qualified to submit this thesis in application for that degree.

   Date: ....25.2.99. Signature of Supervisor: ...

4. In submitting this thesis to the University of St Andrews I understand that I am giving permission for it to be made available for use in accordance with the regulations of the University Library for the time being in force, subject to any copyright vested in the work not being affected thereby. I also understand that the title and abstract will be published, and that a copy of the work may be made and supplied to any bona fide library or research worker.

   Date: ..25.2.99.. Signature of Candidate: ....

Abstract

Low-mass star-forming regions have a lifetime which is greater than their dynamical time and must therefore be, in an average sense, in mechanical equilibrium. The work presented here proposes that an equilibrium exists between the self-gravity, gas pressure, and the magnetic field and the waves it supports. Specifically the equilibrium in the direction perpendicular to the ordered magnetic field is given by the Lorentz force, while that parallel to the field is given by an Alfvén wave pressure force.

The work detailed in this thesis models a low-mass star-forming region as a one-dimensional gas slab with a magnetic field lying perpendicular to the layer. Analytical, self-consistent models are formulated to study the equilibrium parallel to the background magnetic field. It is found that both short-wavelength (modelled using the WKB approximation) and large-amplitude, long-wavelength Alfvén waves can provide the necessary support parallel to the magnetic field, generating model cloud thicknesses that are consistent with the observations. The effect of damping by the linear process of ion-neutral friction is considered. It is found that the damping of the waves is not a necessary condition for the support of the cloud although it is an advantage. The possible sources of these waves are discussed.

The Alfvén waves are also found to make an important contribution to the heating of a low-mass star-forming region. By modelling the dominant heating and cooling mechanisms in a molecular cloud, it is discovered that a cloud supported against its self-gravity by short-wavelength Alfvén waves will be hotter at its outer edge than in the central regions.

These models successfully describe a low-mass star-forming region in equilibrium between its self-gravity, the gas pressure and an Alfvén wave pressure force. The question of the stability of such an equilibrium is considered, specifically that of an isothermal gas slab supported by short-wavelength Alfvén waves. The initial results suggest that the presence of a magnetic field and its associated Alfvén waves have a stabilising effect on the layer, and encourage further consideration of the role of Alfvén waves in low-mass star-forming regions.

Acknowledgements

I would like to offer my thanks to:

My supervisor Eric Priest, Jean Heyvaerts for invaluable advice and Thomas Neukirch for helpful discussions.

My parents, Anna and Simon for their support during an excessive number of years at university!

Jennifer Hodge and my Dad for being brave enough to prove read my thesis.

Clodagh, Jenny, Jim, Marvyn and my Mum for keeping me sane!

Clare Parnell for a great working environment and my friends in the Solar Group, especially for the five-a-side football!

jms for a great story.

The Particle Physics and Astronomy Research Council (PPARC) for funding.

Contents

Chapter 1

Introduction

The story so far:
In the beginning the Universe was created.
This has made a lot of people very angry and been widely regarded as a bad move.

Douglas Adams

Molecular clouds are the birth places of stars within our Galaxy. They form stars with masses which range from just a tenth of a solar mass up to fifty solar masses, from the cold, dense molecular gas that lies between the stars in the interstellar medium. A molecular cloud is defined as an astrophysical object which can be observed in its brightest line, the rotational transition ($J = 1 - 0$) of carbon monoxide at a wavelength of 2.6 mm (Myers 1999), and its name refers to the fact that the main constituent of the cloud is molecular hydrogen.

1.1 Properties of molecular clouds

Molecular clouds are observed to be very diverse objects with masses and spatial scales over a range of values. Generally it is possible to separate them into two different classes[1]: giant molecular clouds (GMCs) and smaller complexes sometimes known as dwarf or dark molecular clouds (DMCs). Giant molecular cloud complexes are vast objects, containing $\sim 10^5 - 10^6\,M_\odot$ or more within tens of parsecs (see Table 1.1),

[1] A third class of molecular clouds is known as the high-latitude clouds (HLCs). These relatively small objects are not gravitationally bound, although they may be bound by the external pressure of the medium (Myers 1987).

	DMC	GMC
Mass ($M_\odot$)	$\leq 10^3$	$\sim 10^5 - 10^6$
Size (pc)	a few to ten	several tens
Molecular hydrogen number density (m^{-3})	$\sim 10^9$	$\sim 10^8$
Temperature (K)	~ 10	$\sim 10 - 20$
Lifetime (yr)	$\geq 10^8$	$\sim 10^7$

Table 1.1: The physical properties of typical giant molecular cloud complexes (GMCs) and low-mass star-forming regions (DMCs) (Myers 1987, 1999; Shu et al. 1987).

which form massive stars and star clusters. An example of such a complex can be found in Orion, namely the Orion A and B giant molecular cloud complexes, which are the closest such objects to us at a distance of ~ 500 pc. These dynamic objects, probably assembled and dispersed as they cross the spiral arms (Shu et al. 1987; Young & Scoville 1991; Scoville 1992), are observed to be composed of smaller clumps which have physical properties akin to those of the dwarf or dark molecular clouds (Shu et al. 1987). The smaller cloud complexes contain up to $\sim 10^3\,M_\odot$ and have radii of a few parsecs (Table 1.1). They form isolated, single stars (rather than clusters of stars as in GMCs) which are low-mass, solar-type objects; hence, throughout this thesis these complexes will generally be referred to as low-mass star-forming regions. These regions are not observed solely within the spiral arms of the Galaxy. They are likely to exist for a period of time greater than that taken to bridge the gap between the arms and thus have lifetimes $\geq 10^8$ yr (Shu et al. 1987; see also Table 1.1). The most well known low-mass star-forming regions are in Taurus which is at a distance of ~ 140 pc.

A map of the Taurus molecular cloud complex is shown in Figure 1.1, reproduced from Mizuno et al. (1995) (their Figure 2). It shows clearly that the structure of a molecular cloud is very complicated, containing elements of both a filamentary and clumpy nature. The determination of the non-uniform density structure from observations of molecular clouds is dependent on the molecular line which is used to map the region. This is because each line which is used to probe the cloud is sensitive only to certain densities (e.g. see Myers 1999). The $J = 1 - 0$ line of ^{12}CO, which is used to define a molecular cloud, is sensitive to densities of $\sim 10^8\ m^{-3}$ ($\sim 10^2\ cm^{-3}$); the $J = 1 - 0$ line of ^{13}CO, used to produce the intensity map in Figure 1.1, can trace densities of $\sim 10^9\,m^{-3}$ ($\sim 10^3\,cm^{-3}$); while densities of $\sim 10^{10}\,m^{-3}$ ($\sim 10^4\,cm^{-3}$) can be probed using for example ammonia (NH_3) (Shu et al. 1987; Myers 1999). Thus it is not possible to map all of the elements in a molecular cloud complex — the whole complex,

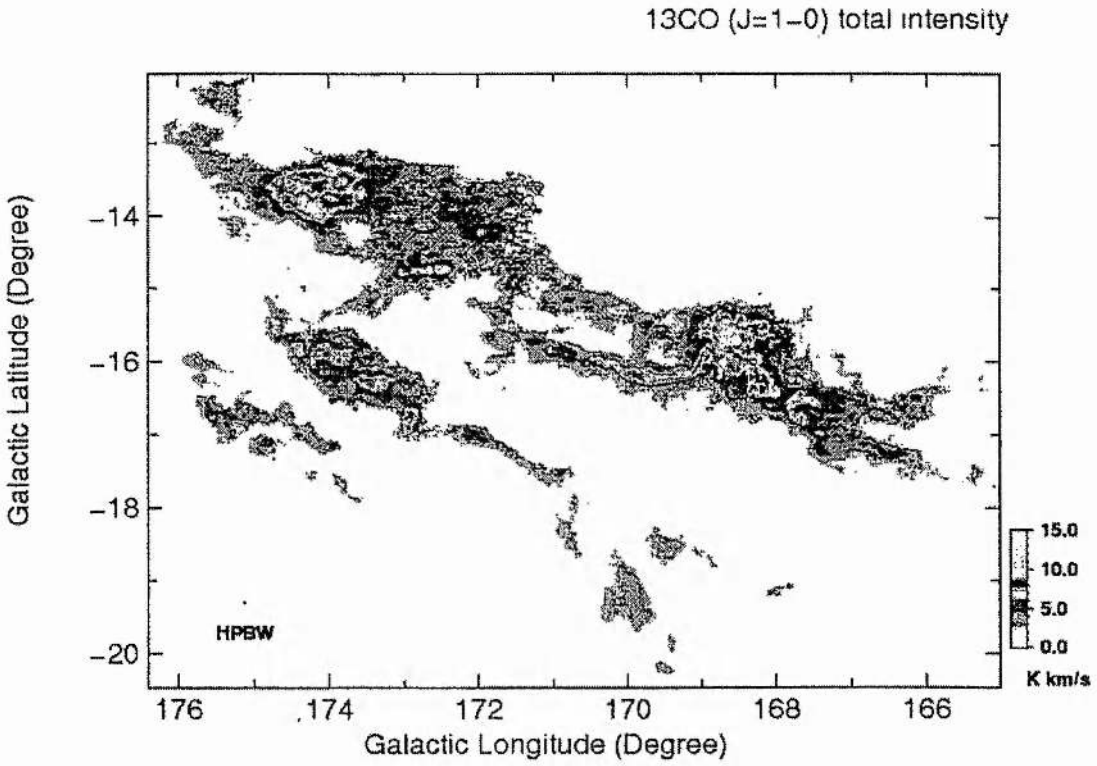

Figure 1.1: The Taurus molecular cloud complex mapped in the J = 1 − 0 line of ^{13}CO at a wavelength of 2.7 mm, reproduced from Mizuno et al. 1995. Note that the longest dimension is $\sim$ 25 pc (Myers 1999).

the clumps and the cores (as detailed in Figure 1.2) — using just one molecular line, rather ^{12}CO can be used to reveal the basic structure of the whole complex, while NH_3 can probe the dense cores.

Each molecular cloud complex contains molecules, atomic species, ions, dust grains and possibly embedded stars. Over one hundred different types of molecule have been observed in the interstellar medium and they are found to be mostly organic compounds (Myers 1999). The most abundant molecule is hydrogen (H_2). Carbon monoxide (^{12}CO) has a fractional abundance, relative to hydrogen, of just $\sim 10^{-4}$, but it is its permanent dipole moment that makes it such a useful observational tool. The fractional ionization in molecular clouds, away from the HII regions surrounding embedded stars, is very low ($\sim 10^{-6}$) but very important. The ions play a crucial role in the chemistry of the cloud, and allow the magnetic field (Section 1.1.1) and neutrals to be coupled together by ion-neutral collisions (which is particularly pertinent to the work reported in this thesis). Another constituent of molecular clouds is the dust grains (sometimes

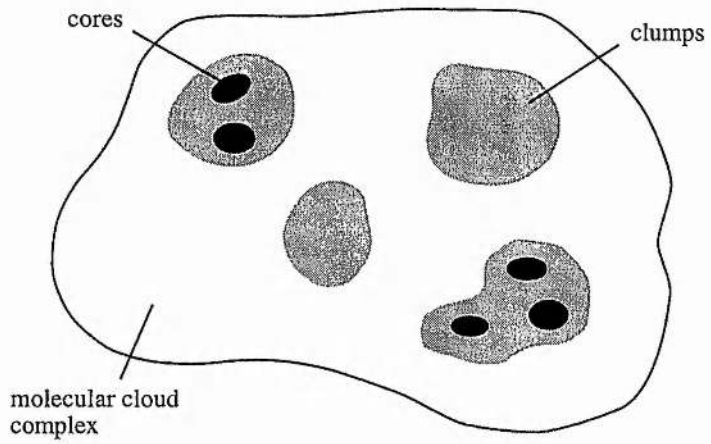

Figure 1.2: A schematic of the structures found in a molecular cloud complex. The region is defined as a complex because carbon monoxide maps reveal that more than one component within the map has closed contours (see Figure 1.1). These components are called 'clumps', while the 'cores' (or 'dense cores') are the star-forming condensations (Hartquist et al. 1993; Myers 1999).

simply referred to as grains). Some of these solid particles (e.g. silicates) are formed in the winds of cool supergiant stars while others, which contain ice, may be condensed in the cooler, dense regions of the clouds. It is the dust grains, which are typically $\sim 0.1\mu$m in size, that give rise to the extinction or obscuration of starlight. In low-mass star-forming regions the visual extinction into the clouds is typically a few magnitudes, increasing to ten magnitudes in the cores; the giant complexes can have extinctions far greater than this (Shu et al. 1987; Myers 1999). It is the extinction of background starlight by the dust which lead to the notation 'dark' molecular clouds.

The typical temperature of a low-mass star-forming region is observed to be $\sim 10\,\mathrm{K}$ throughout these clouds (Myers & Benson 1983; Shu et al. 1987) and hence the sound speed is given by

$$c = \sqrt{\frac{k_B T}{\bar{m}}} = 0.19\,\mathrm{km\,s^{-1}} \left(\frac{T}{10\,\mathrm{K}}\right)^{\frac{1}{2}}, \tag{1.1}$$

where k_B is Boltzmann's constant, T is the temperature and $\bar{m} = 2.3 m_H$ is the mean molecular weight (Shu et al. 1987). The fluid velocities (or turbulent velocities) are observed from the carbon monoxide line widths to be $\sim 1 - 3\,\mathrm{km\,s^{-1}}$ (Myers 1987; Myers & Goodman 1988) and are thus supersonic. These velocities (Δv) actually correlate with the size (R) of the region being observed via a power law, $\Delta v \propto R^{\alpha}$ where $\alpha \sim 0.5 - 0.6$ (Larson 1981; Shu et al. 1987 and references therein).

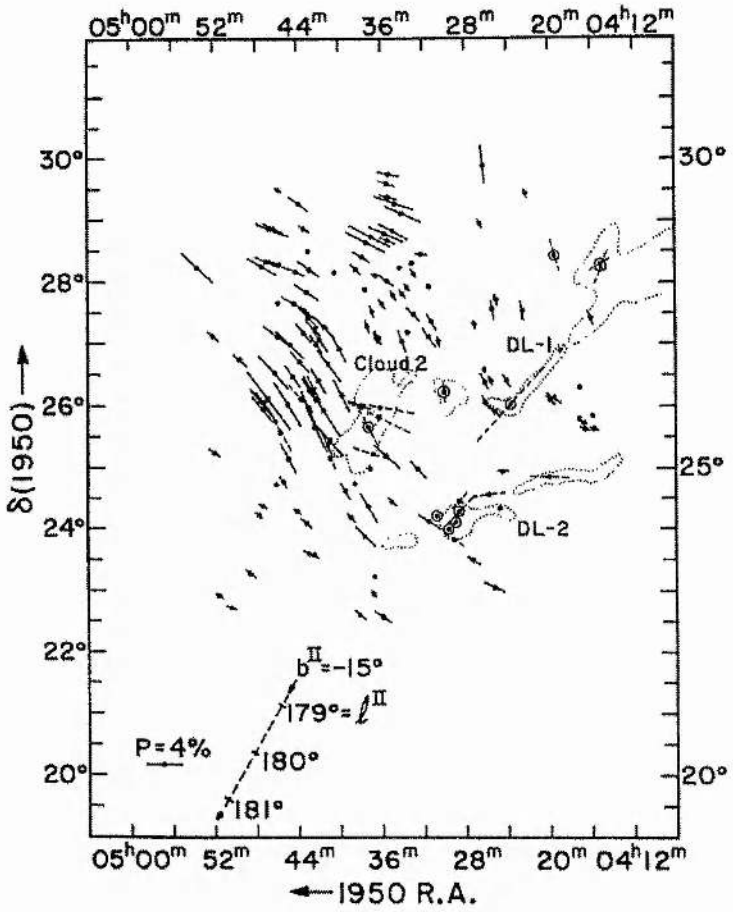

Figure 1.3: The linear polarisation across the Taurus molecular cloud complex, reproduced from Moneti et al. (1984). The dotted lines outline the major condensations in the complex. The direction of polarisation is parallel to the magnetic field.

1.1.1 Magnetic fields

It is possible to observe the line-of-sight magnetic field strength in molecular clouds using the Zeeman effect in the lines of hydroxide (OH) (e.g. Crutcher et al. 1993) and neutral hydrogen (HI) (e.g. Goodman & Heiles 1994), and more recently cyanide (CN) (Crutcher et al. 1996). The advantage of using OH lines over HI lines is simply that OH is a molecular species whereas HI is atomic. Thus observations using HI probably measure the field in the lower density edges of molecular clouds where there may be a greater atomic component; whereas observations of OH, which requires number densities $> 10^9\,\mathrm{m}^{-3}$ ($10^3\,\mathrm{cm}^{-3}$) to become excited, perhaps offer a better probe of the whole cloud. The molecular lines of CN allow the magnetic field within the dense cores to be

studied. See also Crutcher et al. (1993). These observations reveal a typical magnetic field strength in molecular clouds of $\sim 1 - 10$ nT ($\sim 10 - 100\,\mu$G) (Shu et al. 1987; Myers & Goodman 1988). For example, Crutcher et al. (1993) determined an average field strength of 1.6 nT (16 μG) in their survey of dark clouds. This compares with the average interstellar magnetic field which is found to be ~ 0.5 nT ($\sim 5\,\mu$G).

Significantly, these observations together with polarimetry studies of magnetic field structure (e.g. Moneti et al. 1984; Rao et al. 1998), show that the magnetic field is ordered on the scale of molecular clouds (Moneti et al. 1984; Goodman & Heiles 1994). An example is given in Figure 1.3 which is reproduced from Moneti et al. (1984) (their Figure 1). It shows the linear polarisation of background starlight in the Taurus molecular cloud complex; the direction of polarisation is assumed to be parallel to the magnetic field.

Magnetic field strengths of the order observed within molecular clouds imply an Alfvén velocity of

$$v_A = \frac{B}{\sqrt{\mu\rho}} = 4.55\,\mathrm{km\,s^{-1}} \left(\frac{B}{10\,\mathrm{nT}}\right) \left(\frac{n_{H_2}}{10^9\,\mathrm{m^{-3}}}\right)^{-\frac{1}{2}}, \tag{1.2}$$

where B is the magnetic field strength, μ is the magnetic permeability of free space, $\rho = 2.3 m_H n_{H_2}$ is the mass density (Shu et al. 1987) and n_{H_2} is the molecular hydrogen number density. This shows that the observed fluid velocities are supersonic but subalfvénic, and that the Alfvén mach number is $M_A = \Delta v / v_A \sim 0.2 - 0.7$.

1.2 The basic equations

The equations of magnetohydrodynamics (MHD) offer a clear description of the interaction between a plasma, which is an electrically conducting fluid, and a magnetic field; and as such have proved invaluable in the study of magnetic fields in star formation. The MHD equations are built up from the combined influences of electromagnetism (Maxwell's equations and Ohm's law) and fluid mechanics, and they treat the medium under consideration as a continuous plasma, i.e. there are no individual particles. For a description of the formulation of the basic equations of magnetohydrodynamics refer to, for example, Priest (1982).

To be able to use a magnetohydrodynamical approach for the study of molecular clouds there are two main criteria that need to be satisfied. Firstly, the Debye length[2]

[2]Locally within a plasma there will be a slight charge imbalance which will result in an electric field. This field has a length-scale which is given by the Debye length (λ_D).

(λ_D) must be much less than other length-scales of interest within the cloud (λ_L), i.e. $\lambda_D \ll \lambda_L$ — it is this criteria that defines a plasma. The Debye length is given by

$$\lambda_D = \sqrt{\frac{\epsilon_0 \, k_B \, T}{n \, e^2}} \tag{1.3}$$

(e.g. Priest 1982), where $\epsilon_0 = 8.85 \times 10^{-12}\,\mathrm{F\,m^{-1}}$ is the permittivity of free space, $k_B = 1.38 \times 10^{-23}\,\mathrm{J\,K^{-1}}$ is Boltzmann's constant, T is the temperature, n is the charge density and $e = 1.60 \times 10^{-19}\,\mathrm{C}$ is the elementary charge. For values typical of low-mass star-forming regions, $T \sim 10\,\mathrm{K}$ and $n \sim 10^3\,\mathrm{m^{-3}}$, this takes a value of $\lambda_D \approx 7\,\mathrm{m}$. The typical length-scale in a molecular cloud is $\lambda_L \sim 0.1\,\mathrm{pc} \sim 10^{15}\,\mathrm{m}$ and thus the condition that $\lambda_D \ll \lambda_L$ is easily satisfied. The second criterion is that the speeds (V) in the cloud are non-relativistic, that is $V \ll c$, where the speed of light is $c = 3 \times 10^8\,\mathrm{m\,s^{-1}}$. From the discussions of typical cloud properties given in the previous section, the velocities can be estimated as $V < 5 \times 10^3\,\mathrm{m\,s^{-1}} \ll c$, as required.

Molecular clouds are known to contain neutral species (which make up the bulk of the mass), ions, electrons and charged and neutral grains. The electromagnetic forces act directly on the charged components of the gas — the ions, electrons and charged grains — and it is the drag between the neutral and charged constituents that transmits these forces to the neutral species. For simplicity the grains are neglected[3] which leaves a three-fluid system for the neutrals (n), electrons (e) and ions (i). This system can be further reduced to a two-fluid set of MHD equations by treating the ions and electrons as a single fluid, the plasma. This is an excellent approximation given that the relative speed of the electrons and ions that is required to maintain the observed magnetic field is just $(v_i - v_e) \sim 10^{-7} - 10^{-2}\,\mathrm{m\,s^{-1}}$, much less than the typical velocities observed in low-mass star-forming regions (Mouschovias 1991).

By a simple length-scale argument it can be shown that the magnetic field is 'frozen' to the charged species; the electrons and ions are free to travel along the field lines, but otherwise (perpendicular motions) the magnetic field and charged species move as one. The dimensionless parameter known as the magnetic Reynolds number,

$$R_m = \frac{\lambda_L \, V}{\eta}\,, \tag{1.4}$$

where $\eta = 1/(\mu\sigma)$ is the magnetic diffusivity, $\mu = 4\pi \times 10^{-7}\,\mathrm{H\,m^{-1}}$ is the magnetic permeability and σ is the electric conductivity, indicates whether this frozen-flux theorem is indeed valid. If $R_m \gg 1$ then the molecular gas is a perfectly conducting fluid,

[3]The grains can nevertheless play an important role in the interiors of molecular clouds, particularly in the chemistry of these regions and as possible agents for heating or cooling the gas (Dyson & Williams 1997).

any diffusion being negligible, and the magnetic field is frozen to the charged species. In a low-mass star-forming region $\lambda_L \sim 10^{15}$ m, $V \sim 10^3\,\mathrm{m\,s^{-1}}$ say, and the electric conductivity is given by

$$\sigma_{ei} = \frac{n_e\, e^2}{m_e\, \nu_{ei}} \sim 10^7\, T^{\frac{3}{2}}\,\mathrm{s^{-1}} \tag{1.5}$$

(Mouschovias 1991 and references therein), where n_e is the number density of the electrons, m_e is the electron mass and ν_{ei} is the collision frequency of the electrons with the ions. For a typical temperature of $T \sim 10$ K, the magnetic Reynolds number is determined to be $R_m \sim 10^{20} \gg 1$ as required (see also Mouschovias 1991).

A broad picture of the physics in a molecular cloud, within the two-fluid description, suggests that the neutral species would affect the plasma through the gravitational field (which is generated by the far more numerous neutral species) and collisions, while the plasma affects the neutrals solely through collisions (ion-neutral drag). In more detail this picture is altered by the microscopic processes of ionization and recombination which allow there to be a mass and momentum exchange between the plasma and neutrals. This more accurate picture gives the two-fluid magnetohydrodynamic equations (Mouschovias 1991) as: the equation of mass continuity for the plasma

$$\frac{\partial \rho_i}{\partial t} + \nabla \cdot (\rho_i \mathbf{v}_i) = S_i \tag{1.6}$$

and for the neutrals

$$\frac{\partial \rho_n}{\partial t} + \nabla \cdot (\rho_n \mathbf{v}_n) = -S_i\,; \tag{1.7}$$

the equation of motion for the plasma

$$\frac{\partial}{\partial t}(\rho_i \mathbf{v}_i) + \nabla \cdot (\rho_i \mathbf{v}_i \mathbf{v}_i) = -2\nabla P_i + (\mathbf{B} \cdot \nabla)\frac{\mathbf{B}}{\mu} - \nabla\left(\frac{B^2}{2\mu}\right) - \rho_i \nabla\phi + F_{in} + F_{inel} \tag{1.8}$$

and for the neutrals

$$\frac{\partial}{\partial t}(\rho_n \mathbf{v}_n) + \nabla \cdot (\rho_n \mathbf{v}_n \mathbf{v}_n) = -\nabla P_n - \rho_n \nabla\phi - F_{in} - F_{inel}\,; \tag{1.9}$$

the induction equation for a perfectly conducting fluid

$$\frac{\partial \mathbf{B}}{\partial t} = \nabla \times (\mathbf{v}_i \times \mathbf{B})\,; \tag{1.10}$$

Poisson's equation

$$\nabla^2 \phi = 4\pi G \rho_n\,; \tag{1.11}$$

and the isothermal gas pressures

$$P_i = \rho_i c_i^2 \tag{1.12}$$

and

$$P_n = \rho_n c_n^2 \,. \tag{1.13}$$

Note that the plasma quantities have been denoted by a subscript i and the neutral quantities by a subscript n. Within these equations ρ is the mass density, $\mathbf{v}$ is the velocity, S_i is the net rate at which the plasma density is increased by microscopic processes, P is the pressure, $\mathbf{B}$ is the magnetic field, ϕ is the gravitational potential, F_{in} and F_{inel} are the frictional forces on the ions due to the neutrals and the microscopic processes respectively, G is the gravitational constant and c is the isothermal sound speed. For expressions for S_i, F_{in} and F_{inel} refer to Mouschovias (1991). The equations of state (Eqs 1.12 and 1.13) reflect the assumption that the molecular gas is isothermal, a good approximation which is justified by the observations of low-mass star-forming regions (Section 1.1). (Note that this assumption replaces the MHD energy equation (Priest 1982).) Given the predominance of the neutrals over the plasma ($\rho_n \gg \rho_i$) it is possible to neglect some of the terms in the above equations. Firstly, given that the plasma and neutrals are assumed to be at the same temperature, the pressure of the plasma (P_i) may be discarded in Eq. (1.8); and secondly, the microscopic processes have very little influence of the mass of the neutrals, allowing $S_i = 0$ in Equation (1.7).

To be able to reduce these equations to a one-fluid system the ambipolar diffusion — the diffusion (motion) of the plasma relative to the neutrals — needs to be considered. Put simply, if the ambipolar diffusion is negligible so that $v_i \simeq v_n$ then the molecular gas can be treated as a single compressible fluid. This can be considered to be the case if the ambipolar diffusion time-scale is greater than other time-scales of interest. The one-fluid equations are particularly useful for the study of large-scale (long-wavelength) processes which allow the relatively high-frequency (short-wavelength) plasma phenomena to be ignored, i.e. assuming charge neutrality (Mouschovias 1991). Under these assumptions a low-mass star-forming region is described by the magnetohydrodynamic equations, for a fluid with a frozen-in magnetic field, viz: the equation of mass continuity

$$\frac{\partial \rho}{\partial t} + \nabla \cdot (\rho \mathbf{v}) = 0 \,, \tag{1.14}$$

the equation of motion

$$\rho \frac{\partial \mathbf{v}}{\partial t} + \rho \, (\mathbf{v} \cdot \nabla) \, \mathbf{v} = -\nabla P + \mathbf{j} \times \mathbf{B} \, - \rho \nabla \phi \,, \tag{1.15}$$

the induction equation (frozen-in magnetic field)

$$\frac{\partial \mathbf{B}}{\partial t} = \nabla \times (\mathbf{v} \times \mathbf{B}) \,, \tag{1.16}$$

Poisson's equation

$$\nabla^2\phi = 4\pi G\rho \tag{1.17}$$

and an isothermal equation of state

$$P = \rho c^2 , \tag{1.18}$$

where the gravity is defined as $\mathbf{g} = -\nabla\phi$. In the equation of motion (Eq. 1.15) the current density ($\mathbf{j}$) is described by Ampère's law

$$\mathbf{j} = \nabla \times \frac{\mathbf{B}}{\mu} , \tag{1.19}$$

which allows the Lorentz force ($\mathbf{j} \times \mathbf{B}$) to be written as

$$\mathbf{j} \times \mathbf{B} = (\mathbf{B} \cdot \nabla)\frac{\mathbf{B}}{\mu} - \nabla\left(\frac{B^2}{2\mu}\right) . \tag{1.20}$$

Note that the first term on the right-hand side of the above equation is the magnetic tension force, while the second term is the magnetic pressure force.

This is the set of equations which will be used throughout the subsequent chapters to describe the role of Alfvén waves in low-mass star-forming regions. The justification for adopting these single-fluid MHD equations, by neglecting the ambipolar diffusion, will be given a posteriori (see Section 1.4).

1.3 The need for cloud support

Giant molecular clouds, such as the Orion nebula, are far from equilibrium. In contrast, isolated low-mass star-forming regions, for example Taurus, and the clumps in giant cloud complexes must be near mechanical equilibrium as they have a lifetime which is greater than their dynamical time. They are also observed to have a mass greater than their Jeans mass but are not found to be collapsing.

Consider firstly the time-scales in a self-gravitating molecular cloud. The free-fall collapse (dynamic) time-scale is given by

$$t_F = \sqrt{\frac{3\pi}{32G\rho}} , \tag{1.21}$$

where ρ is the mass density and G is the gravitational constant; for a typical number density of $n_{H_2} \sim 10^9\ \mathrm{m}^{-3}$ ($\sim 10^3\ \mathrm{cm}^{-3}$) this yields $t_F \sim 10^6$ yr, much less than the expected lifetime of a low-mass star-forming region. However, as the cloud is threaded by a magnetic field the ambipolar diffusion time-scale also needs to be considered. This

is the time-scale at which the neutral particles would fall through the magnetic field and charged particles, and is given by

$$t_{AD} = \frac{L^2}{\mathcal{D}}, \tag{1.22}$$

where L is the characteristic length-scale of the magnetic field and $\mathcal{D}$ is a diffusion coefficient. The ratio of this diffusion time-scale to the dynamical time-scale may be approximated by the expression

$$\frac{t_{AD}}{t_F} \sim \frac{\gamma C}{2\sqrt{2\pi G}} \sim 8, \tag{1.23}$$

where γ is a drag coefficient and C is a weak function of the gas temperature (see also Section 1.4) (Shu 1983; Shu et al. 1987). Hence, it can be seen that the diffusion time-scale, being in order of magnitude $t_{AD} \sim 10^7$ yr, is slower than that for free-fall collapse but still less than the lifetime of a low-mass star-forming region which is $\sim 10^8$ yr or more.

Secondly, consider the Jeans mass M_J — the critical mass at which the internal gas pressure is no longer sufficient for hydrostatic support and the cloud will gravitationally collapse — which is given approximately by the expression

$$M_J \sim \left(\frac{k_B T}{\bar{m} G}\right)^{\frac{3}{2}} \frac{1}{\sqrt{\rho}}, \tag{1.24}$$

where k_B is Boltzmann's constant, T is the temperature and $\bar{m}$ is the mean molecular weight. For a typical temperature and number density of 10 K and $\sim 10^9$ m^{-3} ($\sim 10^3$ cm^{-3}) respectively, this gives $M_J \sim 3$ M$_\odot$, clearly implying that in typical low-mass star-forming regions $M_J \ll M_{cloud}$ and the cloud should, in the absence of other influences such as turbulence or magnetic fields, be undergoing free-fall collapse. However, if all such clouds within the Galaxy were in a state of free-fall collapse then the predicted star formation rate (SFR) would be larger than the actual rate, of $\sim 3 - 5$ M$_\odot$ yr^{-1}, by a factor of $\sim 10 - 100$ depending on the amount of mass assumed to be contained within these clouds (see also Zuckerman & Palmer 1974; Field 1978; Shu et al. 1987).

Having shown explicitly that low-mass star-forming regions have both a lifetime greater than their dynamical time and a mass which is greater than their Jeans mass, attention needs to be given to the mechanism by which these clouds are supported against their own gravity.

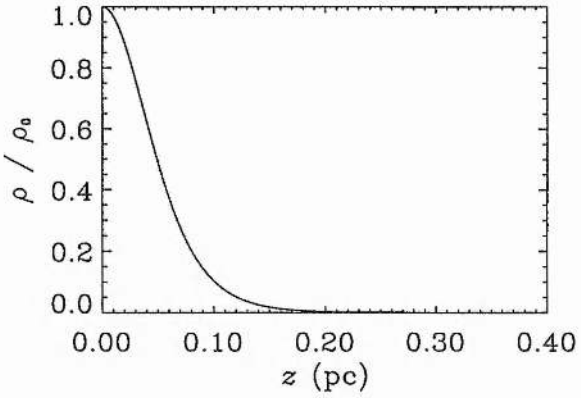

Figure 1.4: The mass density profile of an isothermal gas slab in equilibrium between its gas pressure and self-gravity, plotted for a column density $\mathcal{M} = 10^{-1}\,\mathrm{kg\,m^{-2}}$ and a temperature $T = 10\,\mathrm{K}$.

Gravity versus gas pressure

If the mechanical equilibrium of a self-gravitating cloud is determined solely by the internal gas pressure and gravity then the equilibrium equation would be

$$\nabla P = \rho \mathbf{g}\,, \tag{1.25}$$

where P is the gas pressure, ρ is the mass density and $\mathbf{g}$ is the gravitational acceleration. For an isothermal layer with $P(z) = \rho(z)c^2$, where c is the sound speed, and $\mathbf{g} = -g(z)\hat{\mathbf{z}}$ this equation becomes

$$c^2 \frac{d\rho}{dz} = -\rho g\,, \tag{1.26}$$

which together with the self-gravitation equation (Eq. 1.17)

$$\frac{dg}{dz} = 4\pi G\rho\,, \tag{1.27}$$

where z is the height above the central plane and G is the gravitational constant, can be used to determine the density profile of the layer. By eliminating the gravity (g) between Equations (1.26) and (1.27) and then integrating, the density profile is shown to be

$$\frac{\rho}{\rho_0} = \mathrm{sech}^2\left(\frac{z}{H}\right) \tag{1.28}$$

(Spitzer 1968), where ρ_0 is the density at the central plane ($z = 0$), $H = c^2/(\pi G\mathcal{M})$ is a scale-height and $\mathcal{M}$ is the column density; such a density profile is plotted in Figure 1.4.

For a typical low-mass star-forming region the column density is given by

$$\mathcal{M} = 3.8 \times 10^{-2}\,\mathrm{kg\,m^{-2}} \left(\frac{n_{H_2}}{10^9\,\mathrm{m^{-3}}}\right)^{\frac{1}{2}} \left(\frac{c}{0.2\,\mathrm{km\,s^{-1}}}\right), \tag{1.29}$$

where n_{H_2} is the number density of hydrogen molecules, and thus the scale-height becomes

$$H = 0.16\,\mathrm{pc} \left(\frac{n_{H_2}}{10^9\,\mathrm{m^{-3}}}\right)^{-\frac{1}{2}} \left(\frac{c}{0.2\,\mathrm{km\,s^{-1}}}\right). \tag{1.30}$$

The thickness of the gas layer can be defined as twice the height at which the mass density has fallen by a factor of e from its central value, i.e. $2 \times z(\rho/\rho_0 = 1/\mathrm{e})$. From this definition, Equation (1.28) reveals that the isothermal gas layer would have a thickness of $\simeq 2H$ ($\simeq 0.35$ pc). This calculation suggests that the isothermal layer would be akin to a 'flattened pancake'[4], which is inconsistent with observations of low-mass star-forming regions (Myers 1987; Shu et al. 1987).

In conclusion, all of the evidence presented here — the lifetime being greater than the dynamical time, the mass being greater than the Jeans mass and the solution for an isothermal layer (Spitzer 1968) — clearly indicates the need for some additional support against the self-gravity of a low-mass star-forming region. This support would act to hinder gravitational collapse and hence a flattened pancake morphology.

1.3.1 Candidates for the support

There have been many candidates for the additional support discussed by various authors over the years. These include rotation (Field 1978), internal cloud hydrodynamic turbulence (Bonazzola et al. 1987, 1992), turbulence via stellar outflows (Norman & Silk 1980; McKee 1989), and magnetic fields and the waves which they support (Arons & Max 1975; Shu et al. 1987; Fatuzzo & Adams 1993; McKee & Zweibel 1995; Gammie & Ostriker 1996). Of these, magnetic fields offer a great deal of promise. Observations show them to be ordered on the scale of molecular clouds (see Section 1.1.1), suggesting that they are indeed dynamically significant. In addition, typical observed velocities show that a low-mass star-forming region is a low-β environment — where the plasma beta (β) is defined as the ratio of the gas pressure to the magnetic pressure — with fluid velocities that are supersonic but subalfvénic (Section 1.1).

[4]It is important to note that this description of a low-mass star-forming region would also apply to more realistic geometries since the magnetic field threading the cloud would provide support perpendicular to its direction via the Lorentz force (see also Section 1.3.1).

It is difficult for supersonic turbulence to explain these line widths or indeed to provide support for the cloud in the form of a turbulent pressure as it is highly dissipative; the fluctuations would need to be replenished on very short time-scales (e.g. see Field 1978; Shu et al. 1987). In contrast, magnetic fields and the hydromagnetic waves they support are not easily dissipated. Any disturbance within the cloud would generate magnetohydrodynamic (MHD) waves, but Zweibel & Josafatsson (1983) showed that the longest lived mode is an Alfvén wave propagating parallel to the magnetic field; while the short-wavelength compressional waves, which propagate perpendicular to the field, are damped closest to the source. Further evidence as to the importance of the magnetic field and MHD waves in molecular clouds comes from the line-width-size relation. Observations of carbon monoxide (CO) line widths, which correspond to supersonic turbulence, have shown that they correlate with the size of the region being observed. This correlation has been empirically determined to be a power law, i.e. $\Delta v \propto R^{\alpha}$ (Larson 1981), where R is the radius of the observed region and $\alpha \sim 0.5 - 0.6$ (Shu et al. 1987 and references therein). This relation has been explained by the presence of hydromagnetic waves in the clouds (Arons & Max 1975; Mouschovias & Psaltis 1995). Indeed, Mouschovias & Psaltis (1995) show that a large-amplitude, long-wavelength Alfvén wave gives a line-width-size relation

$$\Delta v \simeq 1.4\,\mathrm{km\,s^{-1}} \left(\frac{B}{30\,\mu\mathrm{G}}\right)^{\frac{1}{2}} \left(\frac{R}{1\,\mathrm{pc}}\right)^{\frac{1}{2}} \tag{1.31}$$

which is in excellent agreement with the observational result.

The structure of molecular clouds has been observed to be very clumpy, with condensations forming over a wide range of spatial scales (e.g. Falgarone & Puget 1986). This structure has been considered with respect to the magnetic waves propagating within these clouds (Elmegreen 1990, 1997), particularly those compressive modes which dissipate rapidly by steepening into shocks (Zweibel & Josafatsson 1983). Elmegreen (1990, 1997) finds that some of the cloud substructure may be explicable by the non-linear damping of hydromagnetic waves.

The work in this thesis follows the proposal that a low-mass star-forming region is supported against its self-gravity by the gas pressure, the magnetic field and the waves it supports. In particular, the molecular gas is supported perpendicular to the ordered magnetic field by the Lorentz force (see Section 1.3.1) and parallel to the field by Alfvén waves which would act on the background gas like a pressure force (Dewar 1970).

Shu, Adams & Lizano (1987) concluded in their review article that Alfvén waves were able to provide support along the magnetic field, particularly if the fluctuating component of the field (giving the Alfvén wave) was of a similar magnitude to the

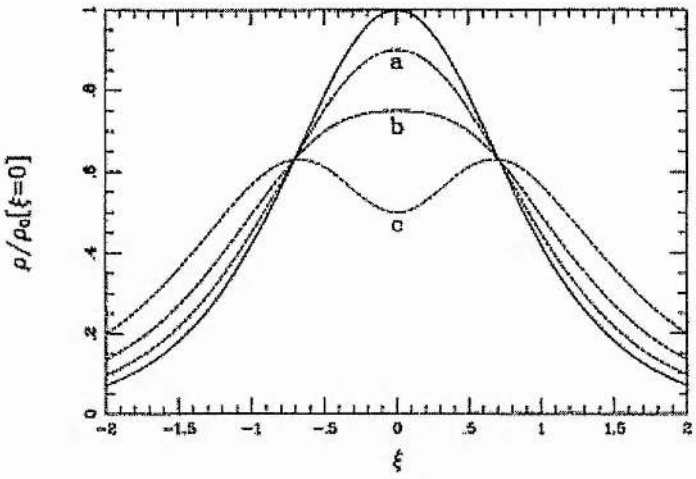

Figure 1.5: The time-averaged profiles of mass density generated by Alfvén wave propagation in a thermally supported slab, reproduced from Fatuzzo & Adams (1993). The solid line is the profile of the unperturbed state, while the dashed lines represent an increase in the amplitude of the Alfvén wave from a – c.

background field, i.e. $\delta B \simeq B_0$; this corresponds to the fluid velocities being of a similar magnitude to the Alfvén velocity ($\Delta v \simeq v_A$). Following on from this Fatuzzo & Adams (1993) considered Alfvén wave propagation in a thermally supported slab (see Section 1.3). They found that these waves are a viable candidate for supporting a cloud even in the absence of damping, which they took to be by the linear process of ion-neutral friction (see Section 1.4 for further discussion of this process). Figure 1.5, reproduced from Fatuzzo & Adams (1993) (their Figure 7), shows that as the amplitude of the Alfvén waves increases they are able to displace and support larger masses away from the equilibrium state. In addition, Fatuzzo & Adams (1993) considered the effect of magnetoacoustic waves in a magnetically supported gas slab; a slab supported in the direction perpendicular to the field lines by the Lorentz force. Here they found that the waves actually compressed the equilibrium state, although the overall effect was minimal compared to the magnetic support. McKee & Zweibel (1995) generalised the Fatuzzo & Adams (1993) result for the Alfvén waves. They considered waves which had a short-wavelength when compared to the length-scale of the background medium, i.e. the WKB approximation (see Appendix A), and found that in a steady state the wave energy density is proportional to the square root of the mass density. Thus the Alfvén wave pressure supporting the cloud could be written as the polytropic equation

of state

$$P_w(\mathbf{r}) \propto \sqrt{\rho(\mathbf{r})}\,, \tag{1.32}$$

where P_w is the wave pressure and ρ is the mass density. However, this result was determined by neglecting the self-gravity in the equations. The papers discussed so far (Shu et al. 1987; Fatuzzo & Adams 1993; McKee & Zweibel 1995) all approached the question of wave support from an analytical point of view. In contrast, Gammie & Ostriker (1996) performed self-consistent numerical simulations of magnetohydrodynamic waves in molecular clouds. They adopted a slab symmetry with an isothermal equation of state and self-gravity but neglected the damping of the waves by ion-neutral friction. The simulations concluded that large-amplitude ($\Delta v \simeq v_A$) waves could support the model clouds against self-gravity.

Support perpendicular to the magnetic field

It has been understood for many years that the static magnetic field can support clouds in the direction perpendicular to itself via the Lorentz force (Eq. 1.20). The extent of the support perpendicular to the field can be described in terms of a critical mass (M_{crit}) above which the magnetic support would fail and the cloud would undergo gravitational collapse. This mass,

$$M_{crit} = 5 \times 10^5\,\mathrm{M}_\odot \left(\frac{B}{3\,\mu\mathrm{G}}\right)^3 \left(\frac{n_p}{1\,\mathrm{cm}^{-3}}\right)^{-2}\,, \tag{1.33}$$

where B is the magnetic field and n_p is the number density of protons, is determined from calculations of the equilibria of isothermal, self-gravitating clouds with a frozen-in magnetic flux (Mouschovias & Spitzer 1976; Mouschovias 1995).

1.4 Alfvén waves in weakly ionized media

Zweibel & Josafatsson (1983) concluded that the longest lived wave mode in a molecular cloud is a (shear) Alfvén wave propagating parallel to the magnetic field. Such waves are transverse in nature, meaning that the velocity perturbation associated with the wave (v) is perpendicular to the direction of propagation (k), i.e. $\mathbf{k} \cdot \mathbf{v} = 0$. They are incompressible ($\nabla \cdot \mathbf{v}$) and are driven by the magnetic tension force (see Eq. 1.20). Generally, the (shear) Alfvén wave has a phase speed

$$\frac{\omega}{k} = v_A \cos\theta_B\,, \tag{1.34}$$

where ω is the frequency, k is the wavenumber, v_A is the Alfvén speed and θ_B is the angle of propagation with respect to the magnetic field, which for parallel propagation

($\theta_B = 0$) is simply equal to the Alfvén speed. Differentiating this expression (Eq. 1.34) with respect to the wavenumber gives the group velocity, which is the velocity at which information (energy) is transmitted; this too is equal to the Alfvén velocity (v_A). Finally it can be noted that the ratio of the magnetic energy ($b^2/2\mu$, where b is the magnetic field perturbation) to the kinetic energy ($\rho v^2/2$) in an Alfvén wave is equal to unity. For a more detailed look at the Alfvén wave see, for example, Priest (1982).

A low-mass star-forming region is a weakly ionized environment, the mass of the ionized part being $\sim 10^{-6}$ that of the neutral mass. However, the Alfvén waves acting to support the cloud will only act directly on the charged component. Thus in order for the cloud to be supported as a whole there needs to be very good coupling between the ions and neutrals within the cloud. If this were not the case the electric component of the cloud would still be supported but the neutral mass (by far the greater part of the cloud) would not, hence giving the cloud a flattened pancake morphology (as in Section 1.3). This coupling is provided by the friction exerted on the ions by the neutrals, which is given by the expression

$$\mathbf{f}_{n\rightarrow i} = -\rho_i \rho_n \gamma \left(\mathbf{v}_i - \mathbf{v}_n\right) , \tag{1.35}$$

where ρ_i, ρ_n and $\mathbf{v}_i$, $\mathbf{v}_n$ are the mass densities and velocities of the ions and neutrals respectively, and $\gamma = 3.5 \times 10^{13}\,\mathrm{cm^3\,g^{-1}\,s^{-1}}$ is a drag coefficient (Draine et al. 1983; Shu et al. 1987).

Consider the two-fluid magnetohydrodynamic equations (Eqs 1.6 – 1.13), neglecting the effects of the microscopic processes but retaining the friction on the ions due to the neutrals. In a slab geometry (all of the gradients being in the z-direction) with the magnetic field described by

$$\mathbf{B} = B_0\,\hat{\mathbf{z}} + b(z,t)\,\hat{\mathbf{x}},$$

where B_0 is the static field and $b(z,t)$ is an Alfvénic perturbation (perpendicular to B_0), the equations reduce to the equation of motion for the plasma (Eq. 1.8)

$$\rho_i \frac{\partial \mathbf{v}_i}{\partial t} = \frac{B_0}{\mu}\frac{\partial \mathbf{b}}{\partial z} - \nabla\left(\frac{b^2}{2\mu}\right) + \rho_i \mathbf{g} + \mathbf{f}_{n\rightarrow i} , \tag{1.36}$$

the equation of motion for the neutrals (Eq. 1.9)

$$\rho_n \frac{\partial \mathbf{v}_n}{\partial t} = -\nabla P_n + \rho_n \mathbf{g} - \mathbf{f}_{n\rightarrow i} , \tag{1.37}$$

the induction equation (Eq. 1.10)

$$\frac{\partial \mathbf{b}}{\partial t} = B_0 \frac{\partial \mathbf{v}_i}{\partial z} , \tag{1.38}$$

the self-gravitation equation (Eq. 1.11)

$$\frac{dg}{dz} = 4\pi G\rho_n \tag{1.39}$$

and the equation of state $P_n = \rho_n c^2$, where c is the isothermal sound speed. Once again the plasma quantities have been denoted by a subscript i and the neutral quantities by a subscript n. In the above equations the mass density is $\rho(z)$, the Alfvénic velocity perturbation is $v(z,t)\hat{\mathbf{x}}$ and the gravitational acceleration is $\mathbf{g} = -g(z)\hat{\mathbf{z}}$. The equations of motion (Eqs 1.36 and 1.37) can be averaged over time, for waves which have periods less than the free-fall time (Eq. 1.21), to give

$$0 = -\nabla \left\langle \frac{b^2}{2\mu} \right\rangle + \rho_i \mathbf{g} \tag{1.40}$$

and

$$0 = -\nabla P_n + \rho_n \mathbf{g}\,. \tag{1.41}$$

These expressions are subtracted from Equations (1.36) and (1.37) respectively, to leave the equations of motion for the Alfvén waves,

$$\rho_i \frac{\partial \mathbf{v}_i}{\partial t} = \frac{B_0}{\mu}\frac{\partial \mathbf{b}}{\partial z} - \rho_i\rho_n\gamma\left(\mathbf{v}_i - \mathbf{v}_n\right) \tag{1.42}$$

and

$$\rho_n \frac{\partial \mathbf{v}_n}{\partial t} = \rho_i\rho_n\gamma\left(\mathbf{v}_i - \mathbf{v}_n\right)\,. \tag{1.43}$$

If the wave motions are assumed to be of the form $\exp\left(i\left(kz - \omega t\right)\right)$, where k is the wavenumber and ω the angular frequency, then Equations (1.42) and (1.43), together with the induction equation (Eq. 1.38) become

$$-i\omega\rho_i v_i = \frac{B_0}{\mu}\, ikb - \rho_i\rho_n\gamma\left(v_i - v_n\right)\,, \tag{1.44}$$

$$-i\omega\rho_n v_n = \rho_i\rho_n\gamma\left(v_i - v_n\right) \tag{1.45}$$

and

$$-i\omega b = B_0 ikv_i \tag{1.46}$$

and can be used to determine the dispersion relation, viz:

$$k^2 v_{Ai}^2 = \omega^2\left(1 + \frac{\rho_n\gamma}{\rho_i\gamma - i\omega}\right)\,, \tag{1.47}$$

where $v_{Ai} = B_0/\sqrt{\mu\rho_i}$ is the ion Alfvén speed.

The extent of the coupling between the ions and neutrals within the cloud is dependent upon the wave frequency ω, for which there are two limiting cases:

(a) $\omega \gg \rho_i\gamma$; $\omega \gg \rho_n\gamma$

From Equation (1.45) it can be seen that

$$v_n = v_i \left(\frac{\rho_i\gamma}{\rho_i\gamma - i\omega} \right) , \tag{1.48}$$

which in this limiting case shows that $v_n \ll v_i$ and hence the neutrals are not well coupled to the ions.

(b) $\omega \ll \rho_i\gamma$

In contrast this limit implies, by Equation (1.48), that $v_n \simeq v_i$ and hence the coupling between the neutrals and ions is very good, allowing the MHD waves to support the cloud as a whole. In this limit, where there is no difference between the mean velocity of the ions and that of the neutrals, the assumption that the ambipolar diffusion is negligible and hence that the one-fluid MHD equations are valid, is justified (Section 1.2).

Comparing these two limits the maximum value the wave frequency can take, while still allowing some coupling between the electric and neutral components of the molecular cloud, is

$$\omega_{max} = \rho_i\gamma = \rho_n\xi\gamma , \tag{1.49}$$

where ξ is the ionized mass fraction. For a cosmic-ray ionization rate of $\zeta = 10^{-17}\,\mathrm{s}^{-1}$ this takes a value of

$$\xi = \frac{\rho_i}{\rho_n} = 4.84 \times 10^{-6} \left(\frac{n_{H_2}}{10^9\,\mathrm{m}^{-3}} \right)^{-\frac{1}{2}} \tag{1.50}$$

using $\rho_n = 2.3 m_H n_{H_2}$ (Shu et al. 1987; Mouschovias 1995) and $\rho_i = C\sqrt{\rho_n}$, where for average metal depletions and low temperatures $C = 3 \times 10^{-16}\,\mathrm{cm}^{-\frac{3}{2}}\,\mathrm{g}^{\frac{1}{2}}$ (Elmegreen 1979; Shu et al. 1987). The maximum wave frequency gives a minimum wave period of

$$\tau_{min} = \frac{2\pi}{\omega_{max}} = 3.06 \times 10^5\,\mathrm{yr} \left(\frac{n_{H_2}}{10^9\,\mathrm{m}^{-3}} \right)^{-\frac{1}{2}} \tag{1.51}$$

and so waves which have a period much less than 10^5 yr do not contribute to the Alfvén wave support of the whole cloud, regardless of the degree to which they are damped.

It is important to note explicitly the dependence of this wave period on the ionization fraction of the cloud: $\tau_{min} \propto \xi^{-1} \propto \zeta^{-1/2}$ (Elmegreen 1979). The value adopted for the ionization rate in Equation (1.50) gives a very low ionized mass fraction which is thought to be typical in these clouds (Shu et al. 1987; Hartquist & Williams 1995). However, the value of τ_{min} can be affected by a variation in the cosmic-ray ionization rate (Farquhar et al. 1994) as well as embedded or external

sources of ultraviolet or x-ray radiation (Gredel et al. 1989; Le Bourlot et al. 1993; Tiné et al. 1997; Yan & Dalgarno 1997) depending upon the location and point of evolution of the cloud (Hartquist et al. 1993). Such sources yield x-ray dominated regions (XDRs) (e.g. Tiné et al. 1997) and photodissociation regions, or photon dominated regions (PDRs) (e.g. Le Bourlot et al. 1993) in which the ionization rate may be substantially increased. For example, an ionization rate of $\zeta = 10^{-12}\,\mathrm{s}^{-1}$ (Tiné et al. 1997), for typical number densities of $\sim 10^9\,\mathrm{m}^{-3}$, reduces the minimum wave period (τ_{min}) to $\sim 10^3\,\mathrm{yr}$.

Considering these waves still further leads to the introduction of a maximum wave period τ_{max}; the wavelength of the MHD wave must be less than the size of the cloud given that the fundamental mode must have a wavelength of that order, and also because such a long wavelength would offer only very little support to the gas. Thus, $\tau_{max} = R_c/v_A$ is given by

$$\tau_{max} = 1.07 \times 10^6\,\mathrm{yr} \left(\frac{R_c}{5\,\mathrm{pc}}\right) \left(\frac{10\,\mathrm{nT}}{B}\right) \left(\frac{n_{H_2}}{10^9\,\mathrm{m}^{-3}}\right)^{\frac{1}{2}}, \tag{1.52}$$

where R_c is the radius of the cloud and v_A is the Alfvén speed of the neutrals and ions together which is given by (Eq. 1.2)

$$v_A = 4.55\,\mathrm{km\,s}^{-1} \left(\frac{B}{10\,\mathrm{nT}}\right) \left(\frac{n_{H_2}}{10^9\,\mathrm{m}^{-3}}\right)^{-\frac{1}{2}}.$$

Alfvén waves with periods in the range τ_{min} (Eq. 1.51) to τ_{max} (Eq. 1.52) and speeds v_A (Eq. 1.2) will have wavelengths of the order $\sim 0.1 - 1\,\mathrm{pc}$. Such waves are the longest lived modes in a molecular cloud (Zweibel & Josafatsson 1983).

In the limit where there is good coupling between the ions and neutrals (case (b)) the dispersion relation (Eq. 1.47), using a Taylor series expansion, becomes

$$kv_A \simeq \pm\,\omega \left(1 + \frac{i}{2}\,\frac{\omega\rho_n}{(\rho_i + \rho_n)\,\rho_i\gamma}\right), \tag{1.53}$$

where $v_A = B_0/\sqrt{\mu(\rho_i + \rho_n)}$. Thus it is possible to define a damping rate, for a wave to damp by a factor e, as

$$\Gamma = k_i v_A = \frac{1}{2}\,\frac{\omega^2\rho_n}{(\rho_i + \rho_n)\,\rho_i\gamma}, \tag{1.54}$$

where k_i is the imaginary term in the dispersion relation. Given that the ionized mass fraction is so small (Eq. 1.50) the damping rate can be written as

$$\Gamma = \frac{1}{2}\,\frac{\omega^2}{\xi\rho_n\gamma} \tag{1.55}$$

to a very good approximation. In terms of the wave period (τ) and the molecular hydrogen number density (n_{H_2}) this parameter has a value of

$$\Gamma = 9.61 \times 10^{-5}\,\mathrm{yr}^{-1} \left(\frac{n_{H_2}}{10^9\,\mathrm{m}^{-3}}\right)^{-\frac{1}{2}} \left(\frac{\tau}{10^5\,\mathrm{yr}}\right)^{-2}, \tag{1.56}$$

corresponding to a damping time of

$$t_d = \frac{1}{\Gamma} = 1.04 \times 10^4\,\mathrm{yr} \left(\frac{n_{H_2}}{10^9\,\mathrm{m}^{-3}}\right)^{\frac{1}{2}} \left(\frac{\tau}{10^5\,\mathrm{yr}}\right)^{2} \tag{1.57}$$

and a damping length of

$$l = v_A t_d = 4.84 \times 10^{-2}\,\mathrm{pc} \left(\frac{B}{10\,\mathrm{nT}}\right) \left(\frac{\tau}{10^5\,\mathrm{yr}}\right)^{2}. \tag{1.58}$$

It can be observed from Equations (1.52) and (1.57) that the time-scales of interest in a low-mass star-forming region supported by an Alfvén wave pressure are shorter than the ambipolar diffusion time $\tau_{AD} \sim 10^7$yr (Section 1.3). This means that the ambipolar diffusion can be neglected and that the single-fluid magnetohydrodynamic equations are valid when considering the wave support of a low-mass star-forming region.

The ion-neutral friction relied upon to couple the two components of the cloud is also a linear process acting to dampen the magnetohydrodynamic waves propagating through the cloud. Other processes which can dampen the Alfvén waves include two basic non-linear mechanisms: the steepening of the waves into shocks and the coupling of the waves to acoustic modes, which dissipate rapidly (Zweibel & Josafatsson 1983). However, Zweibel & Josafatsson (1983) suggest that the most effective damping mechanism is non-linear steepening of the waves into shocks, caused by the wave magnetic pressure gradient, followed by linear ion-neutral friction. For waves which propagate parallel to the unperturbed magnetic field the damping rate for this non-linear effect is found to be

$$\Gamma_{NL} = \frac{\omega\,\Delta v^2}{v_A^2} \tag{1.59}$$

(Zweibel & Josafatsson 1983), where Δv is the turbulent fluid velocity. This corresponds to a damping length of

$$l_{NL} = 1.53\,\mathrm{pc} \left(\frac{n_{H_2}}{10^9\,\mathrm{m}^{-3}}\right)^{-\frac{3}{2}} \left(\frac{B}{10\,\mathrm{nT}}\right)^{3} \left(\frac{\tau}{10^5\,\mathrm{yr}}\right) \left(\frac{\Delta v}{1\,\mathrm{km\,s}^{-1}}\right)^{-2} \tag{1.60}$$

for typical parameters within this study. Now the non-linear damping process will completely dominate the linear process if $l_{NL} \ll l$. This is generally not the case for realistic fluid velocities (e.g. see Myers & Goodman 1988 and references therein) and so the damping within this model is taken to be solely by the linear process of ion-neutral friction.

1.4.1 The source of the waves

The required efficiency of the ion-neutral coupling results in a minimum period for waves supporting the cloud of $\sim 10^5$ yr for a typical ionization fraction. Which source within a low-mass star-forming region could generate waves of this period? Of course, any motion not parallel to the direction of the unperturbed magnetic field will generate waves, but consider in turn: an expanding HII region (Arons & Max 1975); and the orbital motions within the gas as a whole, namely, large-scale (Falgarone & Puget 1986) or protostellar condensations (Arons & Max 1975).

The first of these possible sources, the Strömgren sphere, is unlikely to prove viable within the environment under consideration here as these molecular clouds produce low-mass stars which are not strongly ionizing. In addition, this source would only be available in clouds with embedded stars and thus could not provide support for a quiescent cloud which had not yet formed any stars.

Secondly, consider the orbital motions of the clumps and cores (Hartquist et al. 1993) within the cloud. Kepler's third law states that

$$\tau_K^2 = \frac{4\pi^2}{GM} R^3 , \tag{1.61}$$

where τ_K is the period, G is the gravitational constant, M is the mass and R is the orbital radius. Larson (1981) first showed there to be a correlation between the observed mass densities and sizes of molecular clumps, which states approximately that

$$\frac{M_{clump}}{100\,\mathrm{M}_\odot} = \left(\frac{R_{clump}}{1\,\mathrm{pc}}\right)^2 \tag{1.62}$$

(e.g. see Falgarone & Puget 1986) and allows Equation (1.61) to be written

$$\tau_K = 9.37 \times 10^6\,\mathrm{yr} \left(\frac{R_{clump}}{1\,\mathrm{pc}}\right)^{\frac{1}{2}} . \tag{1.63}$$

Hence for large-scale condensations within a molecular cloud $R_{clump} \sim 0.1$ pc say, the period is $\tau_K \sim 3 \times 10^6$ yr, which is greater than the calculated minimum period of $\sim 10^5$ yr and thus represents a viable source for the waves providing the support. Decreasing the size of the clump down to the typical size of a protostellar core, 1 $\mathrm{M}_\odot$ in 100 AU say, reduces the period to just $\sim 10^3$ yr. This would appear to suggest that the orbital motions of cores do not represent a useful source if the ionization fraction is given by Equation (1.50). However, if the ionization rate is increased, say by an embedded star within the core (as discussed above), then these cores could act as an additional source for the Alfvén waves.

1.4.2 The detection of Alfvén waves

In a recent paper Charnley (1998) considers the possibility of detecting Alfvén waves in molecular clouds by using molecular spectroscopy. Alfvén waves with frequencies higher than those used to support the cloud do not result in very good coupling between the ions and neutrals (case (a) above) and hence there will be some degree of ambipolar diffusion (ion-neutral drift). This drift may play a significant role in the chemistry of the cloud, producing spatial variations in some molecular abundances (Charnley 1998). Charnley (1998) considers the affect of these Alfvén waves on the deuterium chemistry of the molecular cloud and discovers effects that may be observable via spectroscopy. Indeed Charnley & Butner (private communication) have detected the predicted variations of the N_2D^+/N_2H^+ molecular abundance ratio in one dark cloud.

1.5 Aims

This introduction has demonstrated the need for some additional support against the self-gravity of low-mass star-forming regions and presented a strong case for that support to be provided by magnetic fields and the waves they support. In summary, the fields are observed to be ordered on the scale of molecular clouds with field strengths of $\sim 1 - 10\,\mathrm{nT}$ ($\sim 10 - 100\,\mu\mathrm{G}$). It is well known that the Lorentz force associated with this field is able to support the cloud in the direction perpendicular to the magnetic field (Mouschovias & Spitzer 1976). The Alfvén wave which propagates parallel to the field is the longest lived mode in a molecular cloud (Zweibel & Josafatsson 1983); other, compressional modes dissipate rapidly, as do waves which have velocities greater than the Alfvén velocity (McKee & Zweibel 1995). The properties of the observed turbulence correspond to magnetic support (Shu et al. 1987), indeed large-amplitude, long-wavelength Alfvén waves give a line-width-size relation which is in good agreement with observational values (Arons & Max 1975; Mouschovias & Psaltis 1995).

The aim of this thesis is to study, in a self-consistent manner, the role that Alfvén waves play in supporting a low-mass star-forming region against its self-gravity parallel to the ordered magnetic field. To facilitate an analytical approach to this work a low-mass star-forming region is modelled as a one-dimensional gas slab. In Chapter 2 an equilibrium model is developed to ascertain the ability of short-wavelength (WKB approximation) Alfvén waves to support an isothermal gas slab. Initially, the waves are assumed to originate in a central source plane and subsequently, according to a density-dependent source function. Having established the viability of wave support, Chapter 3 considers what effect this may have on the thermal equilibrium of a low-mass

star-forming region: do the Alfvén waves which support the cloud play a significant role in heating the gas? In Chapter 4 the WKB approximation is neglected, allowing an equilibrium model to be developed which considers the part played by long-wavelength Alfvén waves in supporting an isothermal gas layer. Finally, Chapter 5 undertakes a preliminary analysis of the stability of a wave-supported molecular cloud. The work is summarised and conclusions drawn in Chapter 6, which also briefly notes possible avenues for future investigations of Alfvén waves in low-mass star-forming regions.

Chapter 2

A WKB model of Alfvén wave support

Sometimes I think the surest sign that intelligent life exists elsewhere in the Universe is that none of it has tried to contact us.

Bill Watterson

The observational and theoretical evidence presented in Chapter 1 clearly indicates the importance of magnetic fields in the dynamics of low-mass star-forming regions and the role these fields need to play in determining the mechanical equilibrium of a cloud. Perpendicular to the ordered magnetic field a low-mass star-forming region is supported against its self-gravity by the Lorentz force (see Chapter 1, Section 1.3.1 for further discussion) and it is proposed that parallel to the field the support is provided by the gas pressure together with an Alfvén wave pressure force. This chapter presents an analytical self-consistent model describing such support. In particular the following analysis considers the role of short-wavelength Alfvén waves in determining the mechanical equilibrium of a cloud by utilising a WKB approximation.

2.1 The model

Within this study a low-mass star-forming region is modelled as a one-dimensional slab where the gravity, which acts to collapse the cloud, is opposed by the internal gas pressure and the Alfvén wave pressure force (see Figure 2.1). In this first approach it is assumed that the Alfvén waves are emitted from the innermost part of the cloud, the wave sources being located in the central plane.

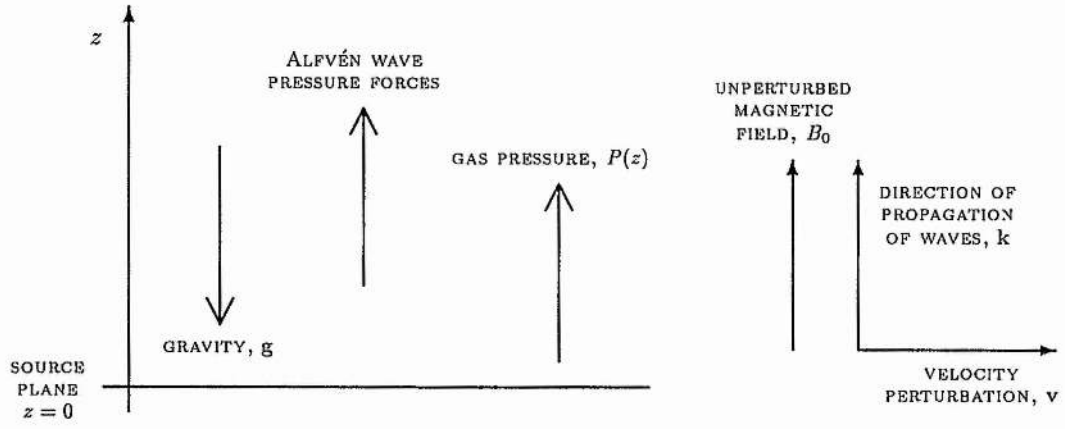

Figure 2.1: A representation of the model showing the Alfvén wave pressure force and the gas pressure counteracting the gravity.

All of the gradients are in the z-direction, the central source plane being at $z = 0$, such that

mass density:	$\rho = \rho(z)$
gravity:	$\mathbf{g} = -g(z)\,\hat{\mathbf{z}}$
velocity:	$\mathbf{v} = v(z,t)\,\hat{\mathbf{x}}$
magnetic field:	$\mathbf{B} = B_0\,\hat{\mathbf{z}} + b(z,t)\,\hat{\mathbf{x}}$
pressure:	$P = \rho(z)\,c^2$

where the gas is assumed to be isothermal with a sound speed c. The velocity perturbation $v(z,t)$ is linearly polarised and taken to be Alfvénic in nature, and is therefore perpendicular to the direction of the applied uniform magnetic field (B_0). The associated magnetic perturbation is $b(z,t)$. Such wave motions do not induce any compression in the gas, which is treated as a single fluid (the neutrals and ions being taken together; see Chapter 1, Section 1.2).

2.2 The equations

The magnetohydrodynamic equation of motion including gravity (Eq. 1.15) is

$$\rho\,\frac{\partial \mathbf{v}}{\partial t} + \rho\,(\mathbf{v}\cdot\nabla)\mathbf{v} = -\nabla P + (\mathbf{B}\cdot\nabla)\,\frac{\mathbf{B}}{\mu} - \nabla\left(\frac{B^2}{2\mu}\right) + \rho\mathbf{g}\,, \tag{2.1}$$

where ρ is the mass density, $\mathbf{v}$ is the velocity, P is the pressure, $\mathbf{B}$ is the magnetic field, $\mathbf{g}$ is the gravity and μ is the magnetic permeability of free space.

For wave periods shorter than the characteristic free-fall time (Chapter 1, Section 1.4), which is normally longer than the fundamental Alfvén wave period in a low-β plasma, this equation can be averaged over time to allow the effect of the waves on the gas layer to be observed. The result is an equilibrium equation (or force-balance equation) between the gravity, the gas pressure and the pressure exerted by the Alfvén waves,

$$0 = -\nabla P - \nabla \left\langle \frac{b^2(z,t)}{2\mu} \right\rangle + \rho \mathrm{g}\,, \tag{2.2}$$

where $b(z,t)$ is the magnetic field perturbation. Since all of the components of this equation are functions of z only, the equilibrium equation can be written

$$\frac{dP}{dz} + \frac{d}{dz}\frac{\langle b^2 \rangle}{2\mu} = -\rho g\,. \tag{2.3}$$

Subtracting this equilibrium equation from the equation of motion (Eq. 2.1) leaves an equation describing the motion of the MHD wave, viz:

$$\rho \frac{\partial v}{\partial t} - \frac{B_0}{\mu}\frac{\partial b}{\partial z} = 0\,. \tag{2.4}$$

Note that there is no explicit linearisation involved in determining Equations (2.3) and (2.4); the form of the velocity (v) and the associated magnetic field perturbation (b) leave the Alfvén wave pressure as the single non-linear term. The wave acts directly on the ions and electrons in the cloud with the neutrals (n) supported, in turn, by the friction force that they exert on the ions (i)

$$\mathbf{f}_{n\to i} = -\rho_i \rho_n \gamma (\mathbf{v}_i - \mathbf{v}_n)\,, \tag{2.5}$$

where γ is a drag coefficient (Draine et al. 1983; Shu et al. 1987). Thus a term appears on the right-hand side of the equation of motion to represent the friction between the neutrals and ions, such that

$$\rho \frac{\partial v}{\partial t} = \frac{B_0}{\mu}\frac{\partial b}{\partial z} - \Gamma \rho v\,, \tag{2.6}$$

where Γ is the damping rate (see also Chapter 1, Section 1.4). In the perfectly conducting limit the induction equation (Eq. 1.16) is described by

$$\frac{\partial \mathbf{B}}{\partial t} = \nabla \times (\mathbf{v} \times \mathbf{B})\,, \tag{2.7}$$

which, through the definitions of the magnetic field ($\mathbf{B}$) and velocity ($\mathbf{v}$), reduces to

$$\frac{\partial b}{\partial t} = B_0 \frac{\partial v}{\partial z}\,. \tag{2.8}$$

The magnetic field perturbation (b) can be eliminated from Equation (2.6) by differentiating it with respect to time (t) and using Equation (2.8) to give the wave propagation equation

$$\frac{\partial^2 v}{\partial t^2} = v_A^2 \frac{\partial^2 v}{\partial z^2} - \Gamma \frac{\partial v}{\partial t}, \tag{2.9}$$

where $v_A = B_0/\sqrt{\mu\rho}$ is the Alfvén speed.

Assuming harmonic wave motion allows both the velocity and magnetic perturbations to be written as

$$v(z,t) = \Re\left(\tilde{v}(z)\,\mathrm{e}^{-i\omega t}\right) \qquad \text{and} \qquad b(z,t) = \Re\left(\tilde{b}(z)\,\mathrm{e}^{-i\omega t}\right),$$

where ω is the frequency and $\tilde{v}$, $\tilde{b}$ are the complex wave amplitudes

$$\tilde{v}(z) = v_1(z) + iv_2(z) \qquad \text{and} \qquad \tilde{b}(z) = b_1(z) + ib_2(z).$$

Substituting these expressions into the wave propagation equation (Eq. 2.9) gives

$$v_A^2 \frac{d^2\tilde{v}}{dz^2} + \omega^2\tilde{v} + i\Gamma\omega\tilde{v} = 0, \tag{2.10}$$

and similarly the induction equation (Eq. 2.8) becomes

$$-i\omega\tilde{b} = B_0 \frac{d\tilde{v}}{dz}. \tag{2.11}$$

The corresponding time-averaged wave pressure is given by

$$\langle b^2(z,t)\rangle = \frac{1}{2}\left(b_1^2 + b_2^2\right), \tag{2.12}$$

which allows the equilibrium equation to be written as

$$\frac{d}{dz}\left(\rho c^2 + \frac{b_1^2 + b_2^2}{4\mu}\right) = -\rho g, \tag{2.13}$$

where the gas pressure $P = \rho c^2$. The model is described by this equation together with the wave propagation equations (Eqs 2.10 and 2.11) and the self-gravitation equation

$$\frac{dg}{dz} = 4\pi G\rho, \tag{2.14}$$

where G is the gravitational constant.

2.2.1 WKB waves

The WKB approximation is a method for solving wave equations in a non-uniform medium which is varying over a scale much larger than the wavelength of the waves propagating within the medium. In the case where the wavelengths of the Alfvén waves are short compared with the size of the cloud, this approximation can be applied to the wave equations calculated above (see Appendix A).

Consider the wave propagation equations (Eqs 2.10 and 2.11) and let the wave amplitude of the velocity perturbation be written as $\tilde{v}(z) = \mathcal{V}(z)\,\mathrm{e}^{i\phi(z)}$, where $\phi(z)$ is varying at a faster rate than $\mathcal{V}(z)$. (Specifically $\phi(z)$ is varying on the scale of a local wavelength while $\mathcal{V}(z)$ is varying on the scale-length of the non-uniform medium.) In this case Equation (2.10) can be written as

$$v_A^2\left(-\mathcal{V}\left(\frac{d\phi}{dz}\right)^2 + i\mathcal{V}\,\frac{d^2\phi}{dz^2} + 2i\,\frac{d\mathcal{V}}{dz}\,\frac{d\phi}{dz}\right) + \omega^2\mathcal{V} + i\Gamma\omega\mathcal{V} = 0\,, \tag{2.15}$$

which upon equating the real and imaginary terms gives

$$\frac{d\phi}{dz} = \frac{\omega}{v_A}\,, \tag{2.16}$$

and

$$\frac{d}{dz}\left[\ln\left(\mathcal{V}^2\,\frac{d\phi}{dz}\right)\right] = -\frac{\Gamma}{v_A}\,. \tag{2.17}$$

Similarly let the wave amplitude of the magnetic field perturbation be written as $\tilde{b}(z) = \mathcal{B}(z)\,\mathrm{e}^{i\phi(z)}$ so that Equation (2.11) becomes

$$\mathcal{B} = -\frac{B_0\mathcal{V}}{\omega}\,\frac{d\phi}{dz}\,. \tag{2.18}$$

This equation can be written as

$$\frac{d}{dz}\left[\ln(\mathcal{V}^2)\right] = \frac{d}{dz}\left[\ln\left(\frac{\mathcal{B}^2}{(d\phi/dz)^2}\right)\right] \tag{2.19}$$

given that ω and B_0 are constants. Substituting this expression into Equation (2.17) and using $d\phi/dz = \omega/v_A$ (Eq. 2.16), reduces the wave propagation equations to just one, namely

$$\frac{d}{dz}\left[\ln\left(\frac{\mathcal{B}^2}{\sqrt{\rho}}\right)\right] = -\frac{\Gamma}{v_A}\,. \tag{2.20}$$

In the particular case of WKB waves the wave pressure term becomes

$$\langle b^2(z,t)\rangle = \frac{\mathcal{B}^2}{2}\,, \tag{2.21}$$

and thus the equilibrium equation (Eq. 2.3) is

$$\frac{d}{dz}\left(\rho c^2 + \frac{\mathcal{B}^2}{4\mu}\right) = -\rho g\,. \tag{2.22}$$

The wave energy density

Within a WKB approximation and a steady state the wave energy density obeys an equation similar to a standard radiative transfer equation which, in regions where no waves are emitted, can be simply written in the form

$$\nabla \cdot (\epsilon \, \mathbf{v}_g) = -\kappa_v \, \epsilon \,, \tag{2.23}$$

where ϵ is the energy density, κ_v is the volume absorption coefficient and $\mathbf{v}_g$ is the group velocity. In comparison, letting $U = \mathcal{B}^2/4\mu$ simply reduces the wave propagation equation (Eq. 2.20) to the Alfvén wave energy transport equation,

$$\frac{d}{dz}\left(\frac{U}{\sqrt{\rho}}\right) = -\Gamma \, \frac{\sqrt{\mu}}{B_0} \, U \,, \tag{2.24}$$

given that the group velocity is simply the Alfvén velocity. This shows that U can be described as a wave energy density, noting that in an Alfvén wave energy is transmitted partly as magnetic energy ($B^2/2\mu$) and partly as kinetic energy ($\rho v^2/2$), the electrical energy being insignificant.

Thus the equations describing the model have been reduced to just three within this WKB approximation: the wave equation

$$\frac{d}{dz}\left(\frac{U}{\sqrt{\rho/\rho_0}}\right) = -\frac{\Gamma}{v_{A_0}} \, U \,, \tag{2.25}$$

where ρ_0 is the mass density and v_{A_0} is the Alfvén velocity, at the central plane ($z = 0$); the equilibrium equation

$$\frac{d}{dz}\left(\rho c^2 + U\right) = -\rho g \,; \tag{2.26}$$

and the self-gravitation equation (Eq. 2.14)

$$\frac{dg}{dz} = 4\pi G \rho \,.$$

These are the equations which will be solved in the following section, together with the boundary conditions $U = U_0$, $\rho = \rho_0$ and $g = 0$ at the central plane ($z = 0$). The first of these conditions reflects the assumption that the Alfvén waves are emitted from the central plane. The value of the central mass density together with that of the central wave energy density are determined from the column density of the gas layer. The relation between these parameters will be calculated a posteriori.

2.3 Results

The set of equations describing the model (Eqs 2.25, 2.26 and 2.14) will now be solved to give the density profile and hence the 'thickness' of the isothermal gas layer, in two cases: without any wave damping; and including wave damping in accordance with ion-neutral friction.

2.3.1 Without damping

In the absence of damping, i.e. when $\Gamma = 0$, the WKB wave equation (Eq. 2.25) integrates to give

$$U = U_0 \sqrt{\frac{\rho}{\rho_0}}, \tag{2.27}$$

where ρ_0 and U_0 are the mass and energy densities at the central plane. Substituting this expression for the wave energy density into the equilibrium equation (Eq. 2.26) leaves

$$c^2 \frac{d\rho}{dz} + U_0 \frac{d}{dz}\left(\sqrt{\frac{\rho}{\rho_0}}\right) = -\rho g, \tag{2.28}$$

which together with the self-gravitation equation (Eq. 2.14) can be used to find the relationship between the gravity (g) and the mass density (ρ). Eliminating the height (z) between these equations (Eqs 2.14 and 2.28) and integrating gives

$$(1 - \sqrt{\tilde{\rho}})(1 + \lambda + \sqrt{\tilde{\rho}}) = \frac{g^2}{8\pi G \rho_0 c^2}, \tag{2.29}$$

where $\tilde{\rho} = \rho/\rho_0$ and

$$\lambda = \frac{U_0}{\rho_0 c^2} \tag{2.30}$$

is defined as the magnetisation parameter (see Section 2.3.3 for a discussion of the values of this parameter). This expression for the gravity (g) can then be inserted back into the self-gravitation equation (Eq. 2.14) to give the density stratification. By defining

$$u = \sqrt{(1 - \sqrt{\tilde{\rho}})(1 + \lambda + \sqrt{\tilde{\rho}})},$$

Equation (2.14) can be written as

$$z = \frac{2c}{\sqrt{8\pi G \rho_0}} \int_0^u \frac{du}{\left[\sqrt{(1 + \lambda/2)^2 - u^2} - \lambda/2\right]^2}. \tag{2.31}$$

Applying the substitution $u = (1 + \lambda/2)(2t/1 + t^2)$, expanding and integrating, gives finally

λ	ρ_0 (kg m^{-3})	U_0 (J m^{-3})	Thickness (pc)
0	1.75×10^{-17}	0	0.20
10	1.59×10^{-18}	9.52×10^{-13}	1.84
20	8.33×10^{-19}	9.98×10^{-13}	3.49
30	5.64×10^{-19}	1.01×10^{-12}	5.13
40	4.27×10^{-19}	1.02×10^{-12}	6.77

Table 2.1: The central mass density (ρ_0), central energy density (U_0) and thickness of an isothermal gas slab supported by waves without damping, with column density $\mathcal{M} = 10^{-1}$ kg m^{-2} and temperature $T = 10$ K, for increasing values of the parameter λ; where $\lambda = U_0/\rho_0 c^2$ is the ratio between the wave pressure and the isothermal gas pressure at the central plane ($z = 0$).

$$z = \frac{2c\,(1+\lambda/2)}{\sqrt{8\pi G\rho_0}} \left[\frac{\lambda/2}{1+\lambda} \frac{\sqrt{(1-\sqrt{\tilde{\rho}})(1+\lambda+\sqrt{\tilde{\rho}})}}{(1+\lambda/2)\sqrt{\tilde{\rho}}} \right.$$
$$\left. + \frac{1+\lambda/2}{(1+\lambda)^{3/2}} \ln \left\{ \frac{\sqrt{1+\lambda+\sqrt{\tilde{\rho}}} + \sqrt{(1+\lambda)(1-\sqrt{\tilde{\rho}})}}{\sqrt{1+\lambda+\sqrt{\tilde{\rho}}} - \sqrt{(1+\lambda)(1-\sqrt{\tilde{\rho}})}} \right\} \right]. \tag{2.32}$$

This expression fully describes the relationship between the mass density ratio ($\tilde{\rho}$) and the height above the central plane (z) where $\tilde{\rho} = 1$ at $z = 0$ and $\tilde{\rho} \to 0$ as $z \to \infty$. Note that the magnetisation parameter (λ) is inversely proportional to the plasma beta (β) and therefore larger values of λ correspond to the magnetic field becoming increasingly dominant within the cloud dynamics.

Shown in Table 2.1 is the thickness of an isothermal gas slab with column density $\mathcal{M} = 10^{-1}$ kg m^{-2} and temperature $T = 10$ K, for increasing values of λ. The case $\lambda = 0$ represents a cloud in which there is no wave support and hence the gravity is balanced by the internal gas pressure alone (see also Chapter 1, Section 1.3). The column density ($\mathcal{M}$) is given by the expression

$$\mathcal{M} = \frac{2}{\sqrt{2\pi G}} \sqrt{\rho_0 c^2\,(1+\lambda)} \tag{2.33}$$

and the thickness of the slab is defined as twice the height above the central plane at which the central mass density has decreased by a factor of e, i.e. $2 \times z(\tilde{\rho} = 1/\mathrm{e})$.

Figure 2.2 shows simply that increasing the value of the parameter λ, i.e. increasing the wave support, increases the thickness of the isothermal gas slab. Maintaining the same column density requires the mass density at the central plane to decrease as wave

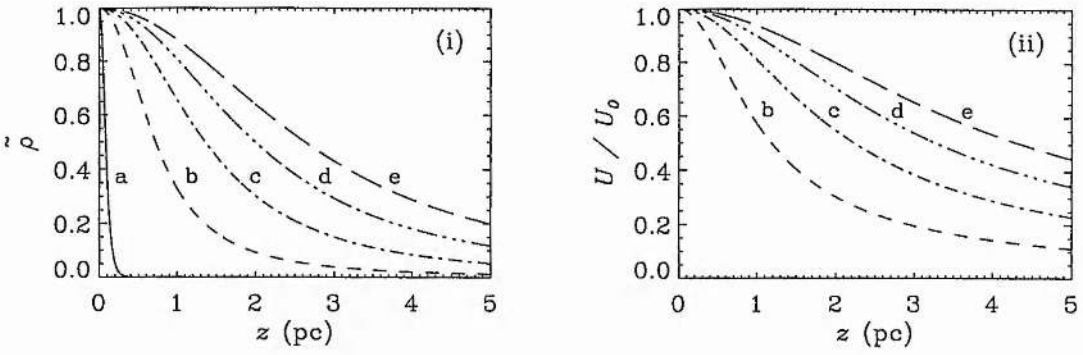

Figure 2.2: The (i) mass density ratio and (ii) energy density ratio profiles of an isothermal gas slab supported by waves without damping, with column density $\mathcal{M} = 10^{-1}\,\mathrm{kg\,m^{-2}}$ and temperature $T = 10\,\mathrm{K}$, for (a) $\lambda = 0$, (b) $\lambda = 10$, (c) $\lambda = 20$, (d) $\lambda = 30$ and (e) $\lambda = 40$; where $\lambda = U_0/\rho_0 c^2$ is the ratio between the wave pressure and the isothermal gas pressure at the central plane ($z = 0$).

support increases (see Figure 2.3) so that the material in the layer becomes more evenly distributed. Altering the column density and temperature naturally brings about a change in the thickness of the slab. For example, increasing the column density will favour gravity and hence reduce the size of the slab, whereas increasing the temperature will favour the gas pressure and so increase the thickness. As can be seen from Equation (2.32) and Figure 2.4 there is a linear relationship between the height above the central plane (z) and the parameter λ, showing that a higher temperature together with a lower column density would increase the thickness of the layer more markedly as the value of λ is increased.

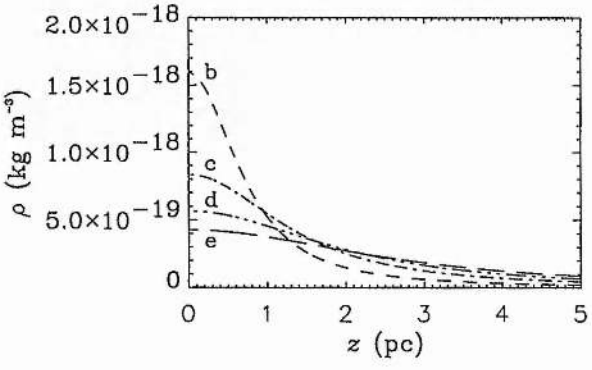

Figure 2.3: The mass density profiles as for Figure 2.2.

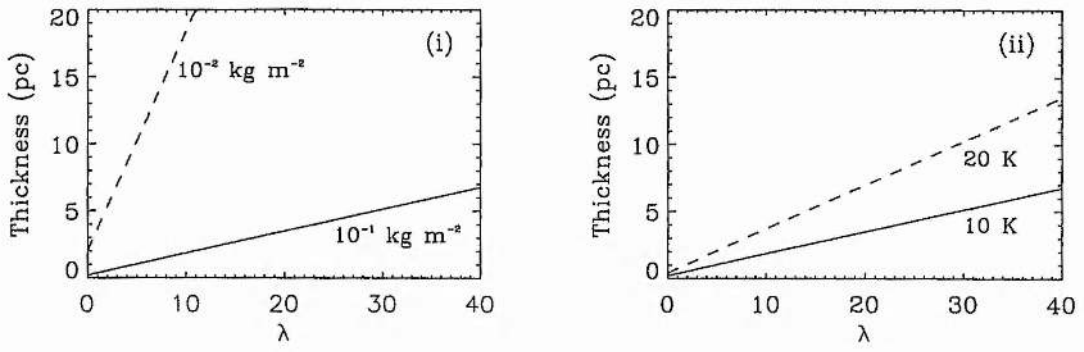

Figure 2.4: The thickness of an isothermal gas slab supported by waves without damping plotted against the parameter λ for (i) different values of the column density ($\mathcal{M}$) with temperature $T = 10\mathrm{K}$ and (ii) different values of the temperature (T) with column density $\mathcal{M} = 10^{-1}\,\mathrm{kg\,m^{-2}}$.

Hence it can be seen from these results that damping is not a prerequisite for the Alfvén waves to support a molecular cloud out to typical observed radii, providing the value of λ and hence the magnitude of the magnetic field perturbation is large enough. The wave flux ($\sim U v_A$) is conserved along the direction of propagation but the Alfvén speed (v_A) is not and so it is the resulting gradient in the wave energy density (U) (see Figure 2.2) that provides the support.

2.3.2 With damping

Friction between the ions and neutrals is the mechanism by which a low-mass star-forming region is supported as a whole (given that the magnetic field will act directly on the electric component of the cloud and not the neutrals). This ion-neutral friction is a linear process which will act to damp the Alfvén waves propagating through the layer (see also Chapter 1, Section 1.4; Zweibel & Josafatsson 1983).

In the limit when there is good coupling between the ions and the neutrals the damping rate is given by

$$\Gamma = \frac{1}{2}\frac{\omega^2}{\xi\rho_n\gamma}$$

(Eq. 1.55), where ω is the wave frequency, ξ is the ionization fraction, ρ_n is the mass density of the neutrals and γ is a drag coefficient (Draine et al. 1983; Shu et al. 1987). The total mass density is $\rho \simeq \rho_n$, and this allows the above equation to be written as

$$\Gamma = \frac{\kappa}{\sqrt{\rho/\rho_0}}, \tag{2.34}$$

where $\kappa = \omega^2/2C\gamma\sqrt{\rho_0}$ (see Chapter 1, Section 1.4). Using this expression for the damping rate, the WKB wave equation (Eq. 2.25) integrates to give

$$U = U_0\sqrt{\tilde{\rho}}\,\mathrm{e}^{-kz}\,, \tag{2.35}$$

where

$$k = \frac{\kappa\sqrt{\mu\rho_0}}{B_0} = 2.12\times10^{-16}\ \mathrm{m}^{-1}\left(\frac{\tau}{10^5\ \mathrm{yr}}\right)^{-2}\left(\frac{B_0}{10\ \mathrm{nT}}\right)^{-1}$$

is a damping parameter and τ is the period of the Alfvén waves.

As in the previous section, using the self-gravitation equation (Eq. 2.14) to eliminate the gravity (g) from the equilibrium equation (Eq. 2.26) gives an expression describing the density stratification

$$\frac{d}{dz}\left(\tilde{\rho}+\lambda\sqrt{\tilde{\rho}}\,\mathrm{e}^{-kz}\right) = -\sqrt{\frac{8\pi G\rho_0}{c^2}}\ \tilde{\rho}\,\sqrt{1+\lambda-\tilde{\rho}-\lambda\sqrt{\tilde{\rho}}\,\mathrm{e}^{-kz}}\,. \tag{2.36}$$

No analytical solution of this equation has been found but using the substitution

$$u = \sqrt{1+\lambda-\tilde{\rho}-\lambda\sqrt{\tilde{\rho}}\,\mathrm{e}^{-kz}}\,,$$

where $u = 0$ at $z = 0$, reduces it to the form

$$\frac{du}{dz} = \sqrt{\frac{2\pi G\rho_0}{c^2}}\left(\sqrt{\frac{\lambda^2}{4}\,\mathrm{e}^{-2kz}+1+\lambda-u^2}-\frac{\lambda}{2}\,\mathrm{e}^{-kz}\right)^2, \tag{2.37}$$

in which it is solved numerically.

The mass and energy density ratio profiles given by an intermediate value of the damping parameter k ($10^{-17}\mathrm{m}^{-1}$) are shown in Figure 2.5, with the actual density profiles shown in Figure 2.6. As in the case without damping, increasing the value of λ increases the thickness of the cloud but in addition it also accentuates the rise in density occurring either side of the central plane. The increase in density can be seen in the expression

$$\frac{d\tilde{\rho}}{dz} = \frac{kU-\rho_0\tilde{\rho}g}{\rho_0c^2+U/2\tilde{\rho}}\,, \tag{2.38}$$

which is obtained from the equilibrium equation (Eq. 2.26) and the wave propagation equation (Eq. 2.25): a positive density gradient is given when $kU > \rho_0\tilde{\rho}g$. This criterion is satisfied in a region near the central plane where the value of the wave energy density is at its maximum (as in Figure 2.5(ii)). Clearly increasing the initial value of the wave energy density, i.e. increasing λ, will increase the extent of this region. Such a mass distribution is supported against gravity by an Alfvénic pressure which is essentially a zero-mass 'material'.

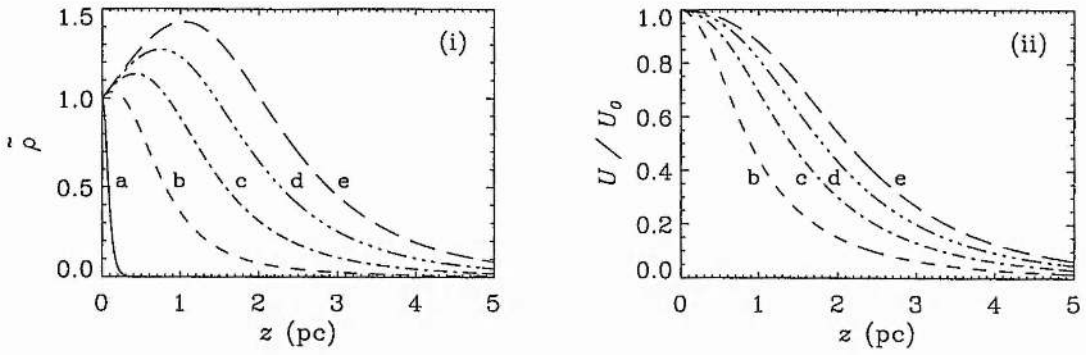

Figure 2.5: The (i) mass density ratio and (ii) energy density ratio profiles of an isothermal gas slab supported by waves including damping, with column density $\mathcal{M} = 10^{-1}\,\mathrm{kg\,m^{-2}}$, temperature $T = 10\,\mathrm{K}$ and damping parameter $k = 10^{-17}\,\mathrm{m^{-1}}$, for (a) $\lambda = 0$, (b) $\lambda = 10$, (c) $\lambda = 20$, (d) $\lambda = 30$ and (e) $\lambda = 40$; where $\lambda = U_0/\rho_0 c^2$ is the ratio between the wave pressure and the isothermal gas pressure at the central plane ($z = 0$).

The actual thicknesses of the gas slabs represented by these profiles are shown in Table 2.2, the last column of which contains for comparison the results for a cloud supported by waves without any damping. The isothermal layers have column density $\mathcal{M} = 10^{-1}\,\mathrm{kg\,m^{-2}}$ and temperature $T = 10\,\mathrm{K}$, and thus from Equation (2.33) the same central mass and energy densities as shown in Table 2.1. Notice that increasing the value of the parameter k does not necessarily increase the size of the gas slab (see Figure 2.7). If the damping is too strong then the wave is stopped well within the density distribution and the ability for these waves to provide any overall support for the gas is lost. And so for each value of k increasing the value of the parameter λ

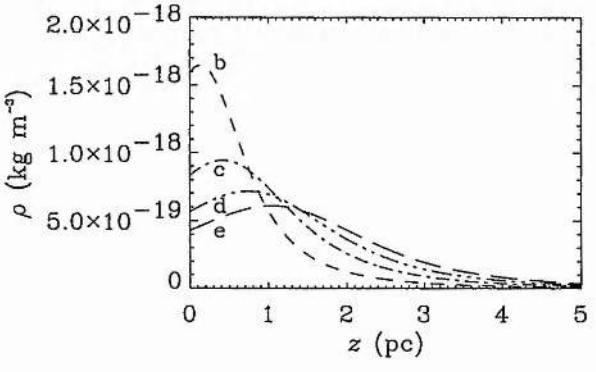

Figure 2.6: The mass density profiles as for Figure 2.5.

λ	Thickness (pc): k (m^{-1})			Thickness without damping (pc)
	10^{-16}	10^{-17}	10^{-18}	
0	0.20	0.20	0.20	0.20
10	1.32	1.97	1.87	1.84
20	1.74	3.70	3.56	3.49
30	1.99	5.19	5.29	5.13
40	2.17	6.47	7.04	6.77

Table 2.2: The thickness of an isothermal gas slab with a column density of $\mathcal{M} = 10^{-1}\,\mathrm{kg\,m^{-2}}$ and a temperature of $T = 10\,\mathrm{K}$ for increasing values of the parameters λ and k; where $\lambda = U_0/\rho_0 c^2$ is the ratio between the wave pressure and the isothermal gas pressure at the central plane ($z = 0$) and k is a damping parameter.

will continue to increase the thickness of the layer but only up to a certain value, at which point the waves have been completely damped. Thus introducing the damping has complicated the linear relationship between the thickness of the slab and λ (see Figure 2.8) although the benefits of a low column density and high temperature are still prevalent.

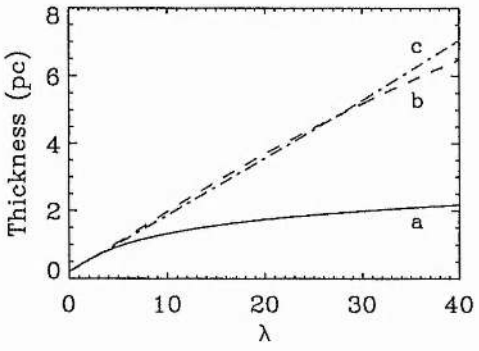

Figure 2.7: The thickness of an isothermal gas slab supported by waves including damping, with column density $\mathcal{M} = 10^{-1}\,\mathrm{kg\,m^{-2}}$ and temperature $T = 10\,\mathrm{K}$, plotted against the parameter λ for (a) $k = 10^{-16}\,\mathrm{m^{-1}}$, (b) $k = 10^{-17}\,\mathrm{m^{-1}}$ and (c) $k = 10^{-18}\,\mathrm{m^{-1}}$.

2.3.3 Discussion

The values displayed in Table 2.2 show how the thickness of the slab varies with decreasing damping and then with no damping at all. A direct comparison between the support with damping and that without is illustrated in Figure 2.9 for different values

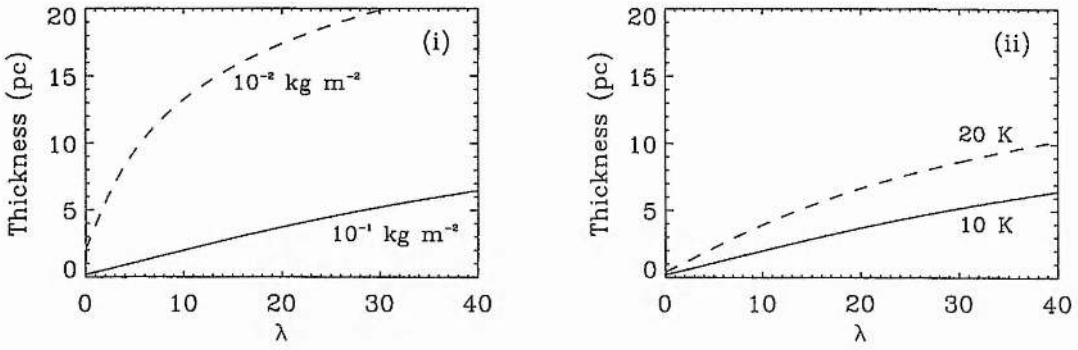

Figure 2.8: The thickness of an isothermal gas slab supported by waves including damping, with $k = 10^{-17}\,\mathrm{m}^{-1}$, plotted against the parameter λ for (i) different values of the column density ($\mathcal{M}$) with temperature $T = 10\,\mathrm{K}$ and (ii) different values of the temperature (T) with column density $\mathcal{M} = 10^{-1}\,\mathrm{kg\,m}^{-2}$.

of the parameter k, from $10^{-16}\,\mathrm{m}^{-1}$ for strong damping through to $10^{-18}\,\mathrm{m}^{-1}$ for weak damping. It can be seen that when the waves are only weakly damped, the gradient in the wave energy density increases slightly, resulting in a small increase in cloud support and thus a marginally larger value for the thickness. However, if the damping is too strong then the thickness of the gas slab actually decreases relative to that without any damping. The upper limit of the parameter k ($\sim 10^{-16}\,\mathrm{m}^{-1}$), which gives the strongest damping, arises from considering the maximum wave frequency ω_{max} (see Chapter 1, Section 1.4) as $k \propto \omega^2$. This is the limit at which there can be some coupling by friction between the ions and the neutrals. However, to achieve good coupling and hence support of the cloud as a whole the wave frequency $\omega \ll \omega_{max}$ and thus $k \ll k_{max}$, i.e. $k \ll 10^{-16}\,\mathrm{m}^{-1}$, which is advantageous for cloud support.

The second key parameter in determining the extent of cloud support and hence the thickness of the layer is

$$\lambda = \frac{U_0}{\rho_0 c^2} = \frac{b^2}{2\beta B_0^2}, \tag{2.39}$$

where the plasma beta $\beta = 2\mu P/B_0^2$ and $U_0 = b^2/4\mu$ (see Section 2.2.1). For a typical plasma beta of

$$\beta = 5.79 \times 10^{-3} \left(\frac{T}{10\,\mathrm{K}}\right) \left(\frac{n_{H_2}}{10^9\,\mathrm{m}^{-3}}\right) \left(\frac{B}{10\,\mathrm{nT}}\right)^{-2} \tag{2.40}$$

this parameter takes the value $\lambda \sim 85\ (b^2/B_0^2)$. However $b/B_0 \simeq v/v_A$, where v is the velocity associated with the magnetic field perturbation (b). Now the fluid velocity is supersonic but subalfvénic ($v \leq v_A$) and typical values (see Chapter 1, Section 1.1) of

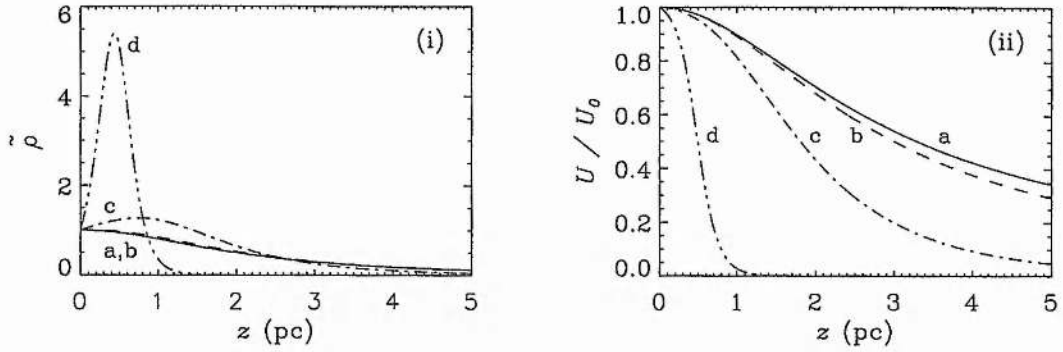

Figure 2.9: The (i) mass density ratio and (ii) energy density ratio profiles of an isothermal gas slab with column density $\mathcal{M} = 10^{-1}\,\mathrm{kg\,m^{-2}}$, temperature $T = 10\,\mathrm{K}$ and $\lambda = 30$ for (a) support by waves in the absence of damping, and support by waves including damping with (b) $k = 10^{-18}\,\mathrm{m^{-1}}$, (c) $k = 10^{-17}\,\mathrm{m^{-1}}$ and (d) $k = 10^{-16}\,\mathrm{m^{-1}}$.

$v \sim 1 - 3\,\mathrm{km\,s^{-1}}$ (Myers 1987) and $v_A \sim 4.5\,\mathrm{km\,s^{-1}}$ give $\lambda \sim 5 - 35$, which corresponds to cloud thicknesses of up to a few parsecs (see Table 2.2) akin to observations. For turbulent velocities approaching the Alfvén value (Myers & Goodman 1988; Goodman & Heiles 1994; Mouschovias & Psaltis 1995) the parameter $\lambda \sim 80$; in the case where there is no damping this would result in a continuous increase in the thickness as $z \propto \lambda$ (see Figure 2.4). However, with damping included the resultant thickness of the layer would depend on the value chosen for the parameter k (see Figure 2.7): the strongest value gives a thickness of only ~ 2 pc, while an order of magnitude less gives ~ 10 pc (equivalent to a radius of ~ 5 pc), which is in good agreement with observations of low-mass star-forming regions (e.g. see Shu et al. 1987).

In summary, it has been shown that Alfvén waves can provide the required support for a low-mass star-forming region along the magnetic field lines, while support perpendicular to the field lines is provided by the Lorentz force. The damping of these waves is not a necessary condition for this support, but weak damping is both likely and favourable.

2.4 Introducing a source function

The results described in the previous section demonstrate how short-wavelength Alfvén waves can support an isothermal gas layer against its self-gravity, assuming that these waves are generated by a δ-function source located at the central plane ($z = 0$). The presence of a general increase in mass density away from the central plane (Figure 2.5),

which is enhanced by higher values of the magnetisation (λ) and damping (k) parameters, encourages the inclusion of a source function within the model. This would imply that all of the waves are no longer emitted from $z = 0$, but that all points within a 'source region' would emit waves in both the positive and negative z-directions.

The source function is chosen to depend on the mass density ratio ($\tilde{\rho}$) through a power law

$$\sigma(\tilde{\rho}) = \tilde{\rho}^{\gamma}\,, \tag{2.41}$$

where γ is the power-law index; positive values of γ ensure that the number of sources is reduced as the mass density decreases and hence that there is a negative gradient of wave sources as the height above the central plane (z) is increased. This guarantees that there will be a greater number of waves propagating away from the central plane which act to support, rather than compress, the cloud (Shu et al. 1987). The density dependence is included in the wave equation (Eq. 2.25) through a source function

$$\mathrm{S}(\tilde{\rho}) = \Phi\,\frac{\rho_0 c^2}{H}\,\sigma(\tilde{\rho})\,, \tag{2.42}$$

where Φ is a dimensionless source parameter, ρ_0 is the mass density at the central plane, c is the sound speed and $H = \sqrt{c^2/2\pi G\rho_0}$ is a scale-height, to give

$$\frac{d}{dz}\left(\frac{U_+}{\sqrt{\tilde{\rho}}}\right) = -k\,\frac{U_+}{\sqrt{\tilde{\rho}}} + \frac{\mathrm{S}}{2} \tag{2.43}$$

and

$$-\frac{d}{dz}\left(\frac{U_-}{\sqrt{\tilde{\rho}}}\right) = -k\,\frac{U_-}{\sqrt{\tilde{\rho}}} + \frac{\mathrm{S}}{2}\,. \tag{2.44}$$

Here the quantities denoted by a $+$ represent the waves propagating away from the source in the positive z-direction, while those with a subscript $-$ correspond to waves propagating in the negative z-direction. Completing the system of equations describing this model are the equilibrium equation (Eq. 2.26), which becomes

$$\frac{d}{dz}\left(\rho_0\tilde{\rho}c^2 + U_+ + U_-\right) = -\rho_0\tilde{\rho}g\,, \tag{2.45}$$

and the self-gravitation equation (Eq. 2.14)

$$\frac{dg}{dz} = 4\pi G\rho_0\tilde{\rho}\,.$$

Adding and subtracting the two wave equations (Eqs 2.43 and 2.44) gives

$$\frac{dF}{dz} = -k\,\frac{U}{\sqrt{\tilde{\rho}}} + \mathrm{S} \tag{2.46}$$

and

$$\frac{d}{dz}\left(\frac{U}{\sqrt{\bar{\rho}}}\right) = -kF \tag{2.47}$$

respectively, where $F = (U_+ - U_-)/\sqrt{\bar{\rho}}$ and $U = U_+ + U_-$, which upon eliminating F leaves a single wave equation, viz:

$$\frac{d^2}{dz^2}\left(\frac{U}{\sqrt{\bar{\rho}}}\right) = k^2\frac{U}{\sqrt{\bar{\rho}}} - k\mathrm{S}\,. \tag{2.48}$$

Equations (2.48), (2.45) and (2.14) are now made dimensionless according to

$$\tilde{U} = \frac{U}{\rho_0 c^2} \qquad \text{and} \qquad \zeta = \frac{z}{H}$$

to leave, having eliminated the gravity (g) between the equilibrium and self-gravitation equations,

$$\frac{d^2}{d\zeta^2}\left(\frac{\tilde{U}}{\sqrt{\tilde{\rho}}}\right) = \tau^2\frac{\tilde{U}}{\sqrt{\tilde{\rho}}} - \tau\Phi\tilde{\rho}^{\gamma} \tag{2.49}$$

$$\frac{d}{d\zeta}\left(\sqrt{1+\tilde{U}_0-\tilde{\rho}-\tilde{U}}\right) = \tilde{\rho}\,, \tag{2.50}$$

where $\tau = kH$ and $\tilde{U}_0$ is the dimensionless total wave energy density at the central plane ($\zeta = 0$). As in Section 2.3.2 no analytical solution of these equations could be found and so they are solved numerically to give the mass density profiles and thicknesses of model clouds, given the appropriate boundary conditions.

2.4.1 Boundary conditions

The equations describing the model are written as three coupled first-order equations,

$$\frac{du}{d\zeta} = w \tag{2.51}$$

$$\frac{dw}{d\zeta} = \tau\left(\tau u - \Phi\tilde{\rho}^{\gamma}\right) \tag{2.52}$$

$$\frac{ds}{d\zeta} = \tilde{\rho} \tag{2.53}$$

by defining $u = \tilde{U}/\sqrt{\tilde{\rho}}$ and $s = \sqrt{1+\tilde{U}_0-\tilde{\rho}-\tilde{U}}$, and noting that the mass density ratio can be expressed as

$$\tilde{\rho} = \left[\frac{\sqrt{4\,(1+u_0-s^2)+u^2}-u}{2}\right]^2, \tag{2.54}$$

where u_0 is the value of the dependent variable u at $\zeta = 0$.

At the central plane ($\zeta = 0$) the mass density ratio is $\tilde{\rho} = 1$ and the wave energy density is $\tilde{U} = \tilde{U}_0$, which implies that $s_0 = 0$ and $u_0 = \tilde{U}_0$. In accordance with the previous results let there be a magnetisation parameter λ (Eq. 2.30) such that

$$\lambda = \frac{U_0}{\rho_0 c^2} = \tilde{U}_0 \,, \tag{2.55}$$

implying simply that at the central plane $u_0 = \lambda$.

The symmetry of the model about the central plane suggests that there will be an equal number of positively and negatively propagating waves, the total wave energy density, and hence the mass density, being symmetrical and continuous through the centre of the sheet. This implies that the variable u (described by Eq. 2.51) is also symmetrical and continuous through $\zeta = 0$, i.e. $w_0 = 0$.

At the outer boundary, as $\zeta \to \infty$, $\tilde{\rho} \to 0$ and consequently $\tilde{U} \to 0$ meaning that the dependent variable $s \to \sqrt{1 + \tilde{U}_0}$. Strictly the three independent boundary conditions required to solve Equations (2.51) – (2.53) are $s = 0$ and $w = 0$ at $\zeta = 0$, plus $s \to \sqrt{1 + \tilde{U}_0}$ as $\zeta \to \infty$. However to allow the results of this model to be easily compared with those for the δ-function source distribution the magnetisation parameter λ (Eq. 2.55) has been introduced, effectively over-specifying the problem. Thus, to satisfy the boundary conditions at infinity (namely that $\tilde{\rho} \to 0$ and $\tilde{U} \to 0$, i.e. that the dependent variable u is exponentially decaying as $\zeta \to \infty$)[1], the source parameter Φ is not independently specified, rather it is determined by the solution.

In the following section the equations describing the model (Eqs 2.51 – 2.53) are solved for an isothermal gas layer with a temperature T and column density $\mathcal{M}$ and a given value of the magnetisation parameter (λ), the damping parameter (k) and the index of the power law (γ).

[1]This can be illustrated by considering the wave equation (Eq. 2.49) as $\zeta \to \infty$. Given that there are no more wave sources as $\tilde{\rho} \to 0$ this equation becomes simply

$$\left.\frac{d^2u}{d\zeta^2}\right|_{\zeta\to\infty} = \tau^2 u(\zeta \to \infty) \,,$$

which has the solution

$$u(\zeta \to \infty) = Ae^{\tau\zeta} + Be^{-\tau\zeta} \,,$$

where A and B are the integration constants. However there are no wave sources at infinity and thus the exponentially decaying solution is chosen. Note that numerically infinity is defined to be the point at which the mass density ratio has fallen below the accuracy of the program.

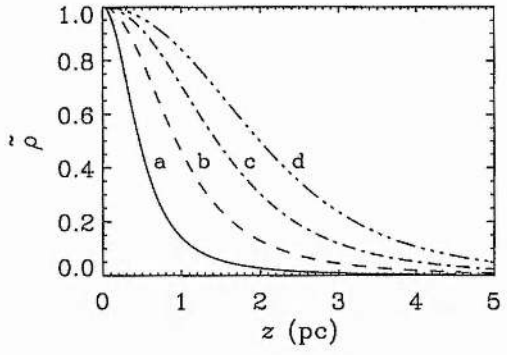

Figure 2.10: The mass density ratio profiles of an isothermal gas slab supported by waves including damping and a density-dependent source function, with column density $\mathcal{M} = 10^{-1}\,\mathrm{kg\,m^{-2}}$, temperature $T = 10\,\mathrm{K}$, damping parameter $k = 10^{-17}\,\mathrm{m^{-1}}$ and power-law index $\gamma = 3$, for (a) $\lambda = 10$, (b) $\lambda = 20$, (c) $\lambda = 30$ and (d) $\lambda = 40$; where $\lambda = U_0/\rho_0 c^2$ is the ratio between the wave pressure and the isothermal gas pressure at the central plane ($z = 0$).

2.4.2 Results

The mass density profiles in Figure 2.10 are plotted for typical values of the temperature, column density and damping for increasing values of the magnetisation parameter (λ). The index of the power law is chosen to give a cubic ($\gamma = 3$) density-dependent source function (Eq. 2.42). These profiles show no increase in mass density away from the central plane, a result which is in contrast with that of a δ-function wave source (see Figure 2.5). The thicknesses of the isothermal gas layers shown in Figure 2.10 are given in Table 2.3. When compared to those values generated using a δ-function source it can be seen that the inclusion of a source function has reduced the thickness of the layer by over a parsec, particularly for stronger values of the magnetisation parameter (λ). With a δ-function source the increase in mass density away from the central plane strengthens the gas pressure and thus increases the thickness of the cloud; removing this enhancement in density reduces the extent of the isothermal gas slab, as reflected in Table 2.3. In addition, the density-dependent source function implies that there will be waves propagating inwards towards the central plane ($\zeta = 0$), as well as out towards infinity ($\zeta \to \infty$). These inwardly propagating waves act with the self-gravity to compress the cloud, thus causing a further reduction in the thickness of the gas layer as compared to that given by just outwardly propagating waves.

The benefit of including a source function in the model is further illustrated when the damping is increased to its strongest value ($k = 10^{-16}\,\mathrm{m^{-1}}$). Figure 2.11, together

λ	Thickness (pc)	
	Density-dependent source	δ-function source
10	1.18	1.97
20	2.35	3.70
30	3.57	5.19
40	4.85	6.47

Table 2.3: The thickness of an isothermal gas slab with a column density of $\mathcal{M} = 10^{-1}\,\mathrm{kg\,m^{-2}}$, a temperature of $T = 10\,\mathrm{K}$, a damping parameter of $k = 10^{-17}\,\mathrm{m^{-1}}$ and increasing values of the parameter λ for a density-dependent source function (with power-law index $\gamma = 3$) and a δ-function source.

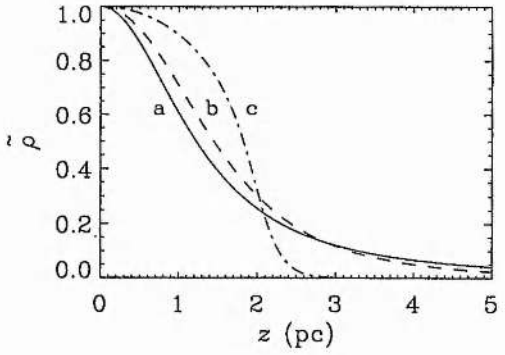

Figure 2.11: The mass density ratio profiles of an isothermal gas slab supported by waves including damping and a density-dependent source function, with column density $\mathcal{M} = 10^{-1}\,\mathrm{kg\,m^{-2}}$, temperature $T = 10\,\mathrm{K}$, magnetisation parameter $\lambda = 30$ and power-law index $\gamma = 3$, for (a) $k = 10^{-18}\,\mathrm{m^{-1}}$, (b) $k = 10^{-17}\,\mathrm{m^{-1}}$ and (c) $k = 10^{-16}\,\mathrm{m^{-1}}$.

k ($\mathrm{m^{-1}}$)	Thickness (pc)	
	Density-dependent source	δ-function source
10^{-18}	3.13	5.29
10^{-17}	3.57	5.19
10^{-16}	3.92	1.99

Table 2.4: The thickness of an isothermal gas slab with a column density of $\mathcal{M} = 10^{-1}\,\mathrm{kg\,m^{-2}}$, a temperature of $T = 10\,\mathrm{K}$, a magnetisation parameter of $\lambda = 30$ and increasing values of the damping parameter k for a density-dependent source function (with power-law index $\gamma = 3$) and a δ-function source.

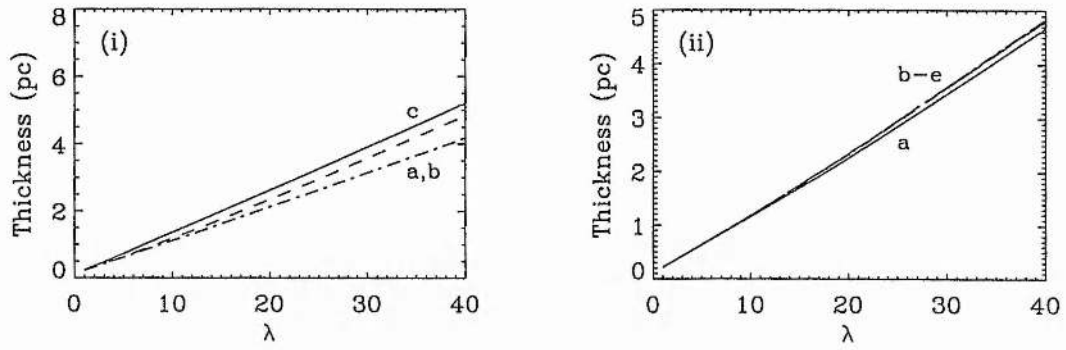

Figure 2.12: The thickness of an isothermal gas slab supported by waves including damping and a density-dependent source function, with column density $\mathcal{M} = 10^{-1}\,\mathrm{kg\,m^{-2}}$ and temperature $T = 10$ K, plotted against the parameter λ for (i) increasing values of the damping parameter k, (a) $10^{-18}\,\mathrm{m^{-1}}$, (b) $10^{-17}\,\mathrm{m^{-1}}$ and (c) $10^{-16}\,\mathrm{m^{-1}}$ with $\gamma = 3$; and (ii) increasing values of the power-law index γ, (a) 1, (b) 2, (c) 3, (d) 4 and (e) 5 with $k = 10^{-17}\,\mathrm{m^{-1}}$.

with Table 2.4, show that increasing the strength of the damping continues to enhance the thickness of the gas slab (see also Figure 2.12(i) which shows how the thickness of the layer increases as the magnetisation parameter (λ) is increased). As the damping parameter k is increased the mass density is redistributed so that there is a greater amount of mass in the central regions of the sheet; however, this no longer results in a large increase in mass density away from the central plane (as observed in Figure 2.9).

The importance of the nature of the source function, i.e. the value of the index of the power law (γ), is considered in Figure 2.12(ii). It can be clearly seen that, while there is a slight decrease in support for a linear relation ($\gamma = 1$), the specific structure of the source function has very little influence on the thickness of the isothermal gas layer. In contrast, the advantages of a lower column density ($\mathcal{M}$) and a higher temperature (T) are still clearly present, as can be seen in Figure 2.13.

As in Section 2.3 the key parameters in determining the amount of support given to the gas layer are the damping parameter (k) and the magnetisation parameter (λ). For typical velocities within these clouds (Chapter 1, Section 1.1) the magnetisation parameter takes values of $\lambda \sim 5 - 35$ (Eq. 2.39) which, in the case of a distribution of wave sources, correspond to cloud thicknesses of a few parsecs, the lower limit of the observational values. However, as the fluid velocity approaches the Alfvén value the parameter $\lambda \sim 80$ and the radii of these clouds increases to ~ 5 pc for a typical value of the damping (as can be seen from Figure 2.12(ii) there will only be a small variation in

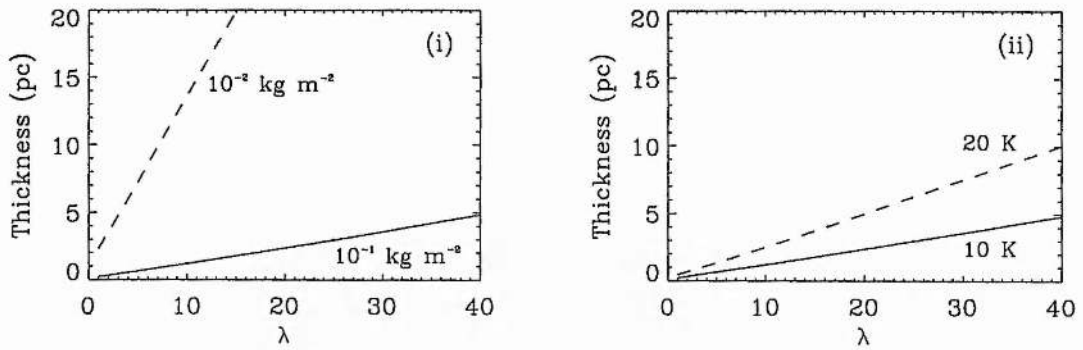

Figure 2.13: The thickness of an isothermal gas slab supported by waves including damping and a density-dependent source function, with $k = 10^{-17}$ m^{-1} and $\gamma = 3$, plotted against the parameter λ for (i) different values of the column density ($\mathcal{M}$) with temperature $T = 10$ K and (ii) different values of the temperature (T) with column density $\mathcal{M} = 10^{-1}$ kg m^{-2}.

the thickness of the layer as the damping is varied), a result which is in good agreement with observations of low-mass star-forming regions (Shu et al. 1987).

In summary, the inclusion of a density-dependent source function within the model has removed any increase in mass density away from the central plane; this is clearly demonstrated in Figure 2.14 where the mass and energy density ratio profiles have been plotted for a density-dependent source function in comparison with a δ-function source. The density profiles generated using a distribution of wave sources have thicknesses of a few parsecs which, although less than those determined by a δ-function source, are in good agreement with the observational values.

2.5 Summary

The work presented in this chapter has described a self-consistent, one-dimensional model which successfully provides the necessary support for a low-mass star-forming region parallel to its ordered magnetic field. The support is provided by short-wavelength Alfvén waves, generated by the orbital motions of condensations of material within the cloud (Chapter 1, Section 1.4.1), which act on the gas through a pressure force. The waves have been shown to be able to provide support against self-gravity even in the absence of damping, given that the wave flux is conserved along the direction of propagation. However, weak damping caused by the friction between the ionic and neutral components of the cloud is both likely and favourable, acting to enhance the thickness

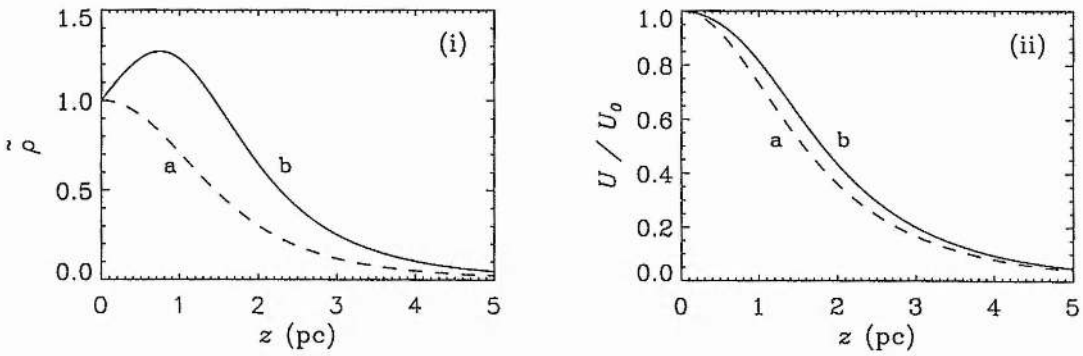

Figure 2.14: The (i) mass density ratio and (ii) energy density ratio profiles of an isothermal gas slab supported by waves including damping, with column density $\mathcal{M} = 10^{-1}\,\mathrm{kg\,m^{-2}}$, temperature $T = 10$ K, magnetisation parameter $\lambda = 30$ and damping parameter $k = 10^{-17}\,\mathrm{m^{-1}}$, for (a) a density-dependent source function (with power-law index $\gamma = 3$) and (b) a δ-function source.

of the gas layer.

Generally the support of the cloud is increased for higher values of the magnetic field perturbation (reflected in the magnetisation parameter λ). However, in the case of a δ-function source, if the damping is too strong the thickness of the cloud reaches a maximum value at which point the waves have been completely damped. In addition, for larger values of the damping parameter (k), particularly when coupled with a strong value for the parameter λ, the presence of a δ-function source can cause the mass density to increase away from the central plane to values that are higher than the central density. Such an effect is eliminated by the introduction of a density-dependent source function, which consequently causes a reduction in the calculated thickness of the gas layer. However there is a continual increase in this thickness, both for strong and weak damping, as the value of the fluid velocity increases towards the Alfvén velocity.

Overall this model describing short-wavelength Alfvén wave support shows that realistic values of the magnetisation parameter result in significant mechanical support, even in the absence of damping, generating model cloud thicknesses which are in good agreement with the observational values. Such a result signifies the importance of Alfvén waves in low-mass star-forming regions and encourages further consideration of this problem in the following chapters.

Chapter 3

A temperature-dependent model

... to search for a radio signal from an extraterrestrial source is probably as culture-bound a presumption as to search the galaxy for a good Italian restaurant.

Terence McKenna

The previous chapter described how short-wavelength Alfvén waves could successfully provide additional support against the self-gravity of a low-mass star-forming region, parallel to the ordered magnetic field. Such support leaves the model gas layer in equilibrium between the *isothermal* gas pressure, an Alfvén wave pressure force and the self-gravity — an equilibrium which results in cloud thicknesses that are in good agreement with observational values (see Chapter 2, Section 3.3 for a fuller discussion). In this chapter a simplified representation of the thermal equilibrium in a low-mass star-forming region will be considered in order to ascertain the effect that this has on the wave support of the cloud and vice versa. Of particular interest is the relative importance of the heating generated by the Alfvén waves as they propagate through the slab.

3.1 Thermal equilibrium

There are many processes which can contribute to the heating and cooling of a molecular cloud, the relative efficiency of these processes being determined by the composition and physical conditions of the cloud and the surrounding medium. For the purposes of this study a thermal equilibrium equation is required which equates the dominant heating and cooling processes in such a region. For a more detailed theoretical analysis

of the thermal equilibrium in molecular clouds see the reviews by Goldsmith & Langer (1978; hereafter GL78); Black (1987) and Neufeld, Lepp & Melnick (1995). In this chapter the thermal equilibrium under consideration is that of a low-mass star-forming region. These regions typically have temperatures of $\sim 10\,\mathrm{K}$ and visual extinctions of a few magnitudes, up to ten magnitudes in the cores (Myers & Benson 1983; Myers 1999; see also Chapter 1, Section 1).

3.1.1 Heating processes

The two main heating agents of molecular gas are cosmic-ray radiation and ultraviolet photons from nearby stellar sources. These sources are more prevalent in the neighbourhoods of giant molecular clouds than of more isolated low-mass star-forming regions. Minor contributions can include, for example, the heating by molecular hydrogen (H_2) (de Jong et al. 1980; Spaans 1996) and heating by water (H_2O) in warm, dusty clouds (Takahashi et al. 1983); gravitational contraction of clouds (GL78); radiation from embedded sources (Takahashi et al. 1983; Takano 1986); and gas-grain heating (Black 1987; Lis & Goldsmith 1990) which requires the dust temperature to be greater than the gas temperature. As this is not always the case this process can actually act to cool the gas (GL78; Black 1987).

Of the two main heating mechanisms there is evidence to suggest that cosmic-ray radiation is dominant in molecular gas throughout the galaxy. This comes in the form of the ratio of carbon monoxide emission to non-thermal radio emission at 20 cm wavelength (I_{co}/T_{20}), which remains almost constant with distance from the galactic centre (Suchov et al. 1993 and references therein). The constant ratio can be explained if the temperature of the molecular clouds, on a galactic scale, is determined by using cosmic-ray radiation as the principle heating mechanism — the carbon monoxide emission (I_{co}) arises from cosmic-ray heated gas, while the cosmic rays themselves are responsible for the radio emission (T_{20}) (Adler et al. 1991). This lead Suchov, Allen & Heckman (1993) to conclude that "... although ultraviolet photons may well contribute to gas heating in the immediate neighbourhood of hot stars, cosmic rays appear to be the prime source of molecular cloud heating in the general interstellar medium ...".

Heating by ultraviolet photons is certainly important for molecular gas in the vicinity of hot stars, particularly in the outer regions of clouds where the visual extinction is lower[1]. If the cloud has a clumpy structure then the photons can penetrate deeper

[1]de Jong, Dalgarno & Boland (1980) found in their model clouds that the cosmic-ray heating dominates for visual extinctions $A_v \geq 2$ when the cosmic-ray ionization rate is $\zeta = 5 \times 10^{-17}\ \mathrm{s}^{-1}$, and for $A_v \geq 3.5$ when the cosmic-ray ionization rate is an order of magnitude less at $\zeta = 5 \times 10^{-18}\ \mathrm{s}^{-1}$.

into the gas than if the density distribution is simply uniform (Lis & Goldsmith 1990). However, heating by cosmic-ray radiation can be considered to be the minimum heating rate in a molecular cloud. Indeed for molecular hydrogen number densities in the range $3\times10^8 \leq n_{H_2} \leq 10^{10}\,\mathrm{m}^{-3}$ the cosmic-ray heating is found to be sufficient to balance the cooling, giving temperatures of $T \sim 10$ K which are in accordance with observational values (GL78).

Thus, the main heating mechanism in an isolated star-forming region (which does not form any massive, highly ionizing stars) is chosen to be cosmic-ray radiation. The cosmic-ray heating rate is given by

$$\Gamma_{cr} = 8.33 \times 10^8\, \zeta\rho \tag{3.1}$$

(GL78) in SI units, where ζ is the cosmic-ray ionization rate and $\rho = 2.3 m_H n_{H_2}$ is the mass density (Shu et al. 1987). This is a primary ionization rate (and therefore excludes the secondary ionizations) which takes values of $\zeta \sim 2 - 4 \times 10^{-17}\,\mathrm{s}^{-1}$ (GL78; Black 1987) when considering cosmic rays with energies of 10 MeV and above (GL78). Such values give good agreement between observations and detailed models of molecular cloud chemistry (e.g. van Dishoek & Black 1986). Cosmic rays are charged particles and can therefore be influenced by the magnetic field pervading a low-mass star-forming region. Cesarsky & Völk (1978) considered the penetration of cosmic rays into molecular clouds and found that the waves generated by the interaction of the cosmic rays with the magnetic field would only screen the interior of the cloud from very low-energy cosmic rays; those particles with energies less than several tens of MeV, which is the lower limit of the energies considered in determining the ionization rate (GL78).

To this cosmic-ray heating will be added the heating due to the Alfvén waves, which are acting to support the low-mass star-forming regions against their self-gravity (Chapter 2). The wave heating is defined as

$$\Gamma_w = -\frac{dF_w}{dz}, \tag{3.2}$$

where $F_w = U v_A$ is the wave flux, U is the wave energy density and $v_A = B_0/\sqrt{\mu\rho}$ is the Alfvén speed. This leaves Γ_w as

$$\Gamma_w = -\frac{B_0}{\sqrt{\mu}}\,\frac{d}{dz}\left(\frac{U}{\sqrt{\rho}}\right). \tag{3.3}$$

Other authors have previously considered the importance of the dissipation of Alfvén waves for heating molecular clouds (Black 1987). For example, Lis & Goldsmith (1990) determined that this heat source resulted in only a minor contribution to the overall

heating of the Sagittarius B2 molecular cloud — a giant molecular cloud at the galactic centre, which is significantly different from typical clouds in the galactic disk. In contrast Champeaux et al. (1997) found that the heating by Alfvén wave filamentation is important in the warm ($T \sim 8000$ K) ionized interstellar medium. At higher temperatures still ($T \geq 3 \times 10^4$ K) Begelman (1995) concludes that cosmic rays can excite Alfvén waves, which then dissipate and heat the surrounding medium, i.e. the Alfvén waves mediate the cosmic-ray heating of the high temperature interstellar gas. In this chapter the relative importance of the heating generated by Alfvén waves supporting cool ($T \sim 10$ K), low-mass star-forming regions will be considered.

3.1.2 Cooling processes

Collisional excitation of the components of molecular gas followed by radiative decay releases photons which, if they are not re-absorbed, escape and so cool the cloud. The efficiency of this process is very dependent on the composition of the cloud, with species which have a fractional abundance greater than one part in 10^9 being significant (GL78; de Jong et al. 1980; Warin et al. 1996). These species include many different molecules (greater than one hundred species of interstellar molecules are known (Myers 1999)), atoms and ions, but the rotational lines of carbon monoxide (CO) and water (H_2O) are the main coolants for the majority of the gas in molecular clouds. Without these, the typical temperature of a cloud would approach $T \sim 100$ K, as opposed to the observational value of $T \sim 10$ K (Myers 1999).

Carbon monoxide, which has been established from both an observational and theoretical standpoint to be a major constituent of molecular clouds, has a large number of transitions which contribute to the cooling. Indeed for molecular hydrogen number densities less than $\sim 10^{10}\,\mathrm{m}^{-3}$ and temperatures between 10 K and 40 K, ^{12}CO is found to be the dominant coolant (GL78). As the density increases from $\sim 10^9\,\mathrm{m}^{-3}$ other species such as water begin to play an important role, as do the dust grains for densities greater than $\sim 10^{11}\,\mathrm{m}^{-3}$ (Myers 1999). For temperatures an order of magnitude greater than this ($T \sim 100$ K) the cooling due to ionized carbon (C^+), which has an excitation energy equivalent to 92 K, provides a major contribution to the thermal equilibrium of these clouds (Dyson & Williams 1997).

3.2 Model I: Carbon monoxide (CO) cooling

In this first approach the thermal equilibrium is assumed to be described by carbon monoxide (CO) cooling and the combined heating of cosmic-ray radiation and Alfvén

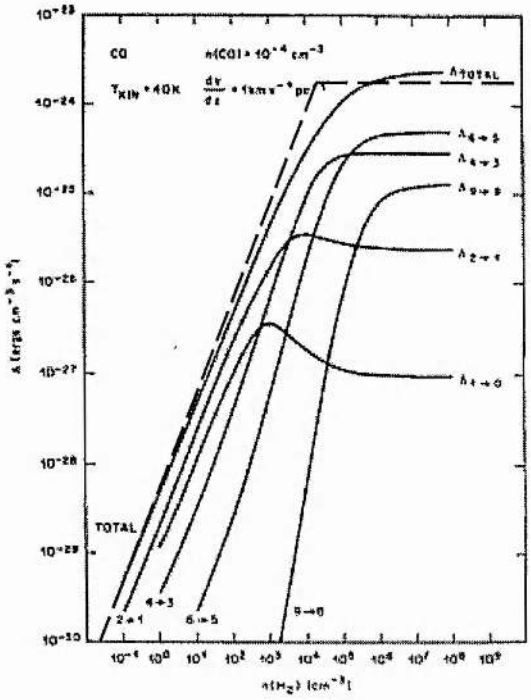

Figure 3.1: The total carbon monoxide (CO) cooling rate ($\Lambda_{\rm TOTAL}$) plotted against the molecular hydrogen number density (n_{H_2}) for a temperature of 40 K; reproduced from GL78. The dashed line represents the fit used within this model and is given by Equation (3.4).

waves. This thermal balance is incorporated into the model for short-wavelength Alfvén wave support which employs a δ-function source of waves, as considered in Chapter 2, Sections 1 – 3.

3.2.1 The cooling

The carbon monoxide cooling is modelled using the results of Goldsmith & Langer (1978). Figure 3.1, which is reproduced from GL78 (their Figure 1), shows the total CO cooling rate ($\Lambda_{\rm TOTAL}$) versus hydrogen number density (n_{H_2}) at a temperature of 40 K. This curve is approximated by the formula

$$\Lambda_{co} = \begin{cases} 5.0 \times 10^{-29}\, n_{H_2} & n_{H_2} < 3 \times 10^4\ {\rm cm}^{-3} \\ 1.5 \times 10^{-24} & n_{H_2} \geq 3 \times 10^4\ {\rm cm}^{-3} \end{cases} \tag{3.4}$$

(where $\Lambda_{co} \equiv \Lambda_{\rm TOTAL}$), which states that the total cooling rate is directly proportional to the hydrogen number density up to a value of $3 \times 10^4\,{\rm cm}^{-3}$, and is a constant value

Molecular hydrogen density (cm^{-3})	Λ ($ergs\,cm^{-3}\,s^{-1}$)
10^2	$1.5 \times 10^{-27} T^{1.4}$
3×10^2	$4.7 \times 10^{-27} T^{1.6}$
10^3	$6.8 \times 10^{-27} T^{2.2}$
4×10^3	$2.3 \times 10^{-26} T^{2.2}$
10^4	$1.5 \times 10^{-26} T^{2.7}$
10^5	$3.8 \times 10^{-26} T^{2.9}$

Table 3.1: The temperature dependence of the total cooling rate at given values of the molecular hydrogen number density (n_{H_2}); reproduced from GL78.

thereafter. This approximation is represented by the dashed line in Figure 3.1. The temperature dependence of this cooling rate (Eq. 3.4) is deduced from the formulae given in Table 3.1, reproduced from GL78 (their Table 4), to be $T^{2.5}$. As such Equation 3.4 can be written

$$\Lambda_{co} = \begin{cases} 4.9 \times 10^{-40}\, n_{H_2}\, T^{2.5} & n_{H_2} < 3 \times 10^{10}\ \mathrm{m}^{-3} \\ 1.5 \times 10^{-29}\, T^{2.5} & n_{H_2} \geq 3 \times 10^{10}\ \mathrm{m}^{-3} \end{cases} \tag{3.5}$$

in SI units. Note that this formula can be expressed in terms of the mass density through the relation $\rho = 2.3 m_H n_{H_2}$ (Shu et al. 1987; Mouschovias 1995), where m_H is the mass density of the hydrogen atom.

3.2.2 The equations

The derivation of the equations which describe a gas layer in equilibrium between its self-gravity, gas pressure and an Alfvén wave pressure force is discussed in detail in Chapter 2 (Section 2). To summarise, this model is described by the equilibrium equation (Eq. 2.26)

$$\frac{d}{dz}(P + U) = -\rho g \tag{3.6}$$

and the self-gravitation equation (Eq. 2.14)

$$\frac{dg}{dz} = 4\pi G \rho\,, \tag{3.7}$$

where z is the height above the central plane, P is the gas pressure (previously assumed to be isothermal), U is the wave energy density, ρ is the mass density, g is the gravity and G is the gravitational constant. Including the effects of damping by ion-neutral

friction, the wave energy density is described by (Eq. 2.35)

$$U = U_0 \sqrt{\frac{\rho}{\rho_0}}\, \mathrm{e}^{-kz}\,, \tag{3.8}$$

where U_0 and ρ_0 are the wave energy density and mass density at the central plane ($z = 0$), and k is the damping parameter. Within this temperature-dependent model the gas pressure is given by the perfect gas law

$$P = \frac{k_B\, \rho\, T}{\bar{m}}\,, \tag{3.9}$$

where k_B is Boltzmann's constant, $\bar{m} = 2.3 m_H$ is the mean molecular weight (Shu et al. 1987) and T is the temperature, which is described by the thermal equilibrium equation

$$\Lambda_{co} = \Gamma_{cr} \tag{3.10}$$

in the absence of wave heating, or

$$\Lambda_{co} = \Gamma_{cr} + \Gamma_w \tag{3.11}$$

in the presence of wave heating.

In the absence of wave heating the expressions for the carbon monoxide cooling (Eq. 3.5) and the cosmic-ray heating (Eq. 3.1) allow the thermal equilibrium equation (Eq. 3.10) to be written as

$$T^{2.5} = \begin{cases} 6.6 \times 10^{21}\, \zeta & \rho < \rho_{crit} \\ 5.6 \times 10^{37}\, \zeta \rho & \rho \geq \rho_{crit} \end{cases} \tag{3.12}$$

in terms of the mass density ρ and the cosmic-ray ionization rate ζ, where the critical mass density is $\rho_{crit} = 1.2 \times 10^{-16}\ \mathrm{kg\,m^{-3}}$ (see Section 2.1). The heating by the Alfvén waves becomes

$$\Gamma_w = \frac{B_0}{\sqrt{\mu}}\, k\, \frac{U}{\sqrt{\rho}}\,, \tag{3.13}$$

through the expression for the wave energy density (Eq. 3.8). By assuming a typical value for the uniform magnetic field of $B_0 \sim 1 - 3\ \mathrm{nT}$ ($\sim 10 - 30\ \mu\mathrm{G}$) say, (Chapter 1, Section 1.1), the above equation is written as

$$\Gamma_w = 10^{-6}\, k\, \frac{U}{\sqrt{\rho}}\,. \tag{3.14}$$

Thus, if the wave heating is included in the thermal equilibrium (Eq. 3.11) the temperature is given by the expression

$$T^{2.5} = \begin{cases} 6.6 \times 10^{21}\, \zeta + 7.9 \times 10^{6}\ k\, U/\rho^{3/2} & \rho < \rho_{crit} \\ 5.6 \times 10^{37}\, \zeta\, \rho + 6.8 \times 10^{22}\ k\, U/\sqrt{\rho} & \rho \geq \rho_{crit}\,. \end{cases} \tag{3.15}$$

The equilibrium equation (Eq. 3.6) can be expanded to give

$$\frac{d\rho}{dz} = -\frac{\bar{m}}{k_B T}\left(\rho g + \frac{dU}{dz}\right) - \frac{\rho}{T}\frac{dT}{dz}, \tag{3.16}$$

where the derivative of the wave energy density is (from Eq. 3.8)

$$\frac{dU}{dz} = \frac{U_0\, \mathrm{e}^{-kz}}{2\sqrt{\rho_0}\sqrt{\rho}}\,\frac{d\rho}{dz} - kU_0\sqrt{\frac{\rho}{\rho_0}}\,\mathrm{e}^{-kz}. \tag{3.17}$$

Excluding the wave heating (Γ_w) the temperature gradient is given by Equation (3.10) as

$$\frac{dT}{dz} = 0 \tag{3.18}$$

for $\rho < \rho_{crit}$, and

$$\frac{dT}{dz} = \frac{2T}{5\rho}\,\frac{d\rho}{dz} \tag{3.19}$$

for $\rho \geq \rho_{crit}$; whereas including Γ_w (Eq. 3.11) leaves

$$\frac{dT}{dz} = -\frac{2c_1}{5}\,\frac{\mathrm{e}^{-kz}}{T^{3/2}\rho}\left(\frac{1}{\rho}\frac{d\rho}{dz} + k\right) \tag{3.20}$$

for $\rho < \rho_{crit}$, and

$$\frac{dT}{dz} = \frac{2}{5T^{3/2}}\left(c_2\,\frac{d\rho}{dz} - c_3\,\mathrm{e}^{-kz}\right) \tag{3.21}$$

for $\rho \geq \rho_{crit}$, where the coefficients are $c_1 = 7.9 \times 10^6\, kU_0/\sqrt{\rho_0}$, $c_2 = 5.6 \times 10^{37}\,\zeta$ and $c_3 = 6.8 \times 10^{22}\, k^2 U_0/\sqrt{\rho_0}$.

In this form the equilibrium and self-gravitation equations (Eqs 3.16 and 3.7) can be solved numerically subject to the two boundary conditions $\rho = \rho_0$ and $g = 0$ at the central plane ($z = 0$), given values for the three parameters: the wave energy density at the central plane (U_0), the damping (k) and the cosmic-ray ionization rate (ζ). These solutions will determine the mass density ratio (ρ/ρ_0) and temperature (T) profiles, together with the thicknesses of model clouds.

3.2.3 Results

In the absence of wave heating ($\Gamma_w = 0$) the equations describing this temperature-dependent model (Eqs 3.16 and 3.7) can be solved to give the mass density ratio and temperature profiles displayed in Figure 3.2 and detailed in Table 3.2. To aid the comparisons with the isothermal model, the central mass and wave energy densities (ρ_0 and U_0) have been chosen to match those given in Table 2.1. As such, the decreasing values of the central mass density (ρ_0), coupled to the increasing values of the central wave energy density (U_0), represent a gradual increase in the amount of Alfvén wave

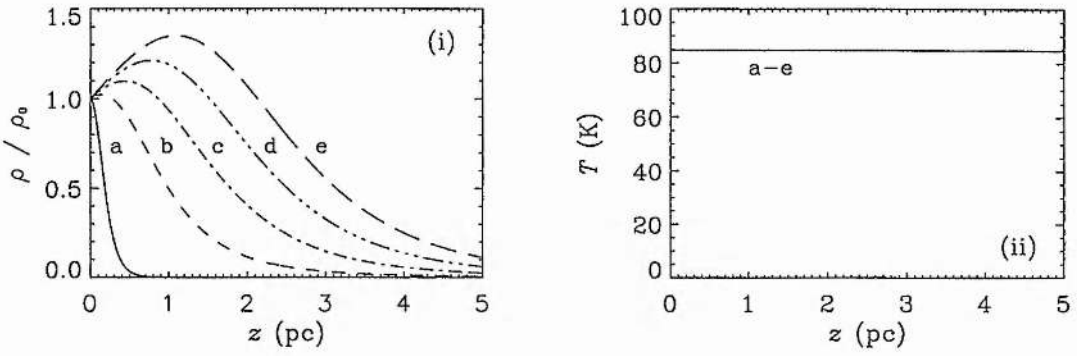

Figure 3.2: The (i) mass density ratio ρ/ρ_0 and (ii) temperature T plotted against the height z for a cosmic-ray ionization rate $\zeta = 10^{-17}\,\mathrm{s}^{-1}$, damping $k = 10^{-17}\,\mathrm{m}^{-1}$ and decreasing values of the central mass density (ρ_0) from a – e. The thermal equilibrium of the layer is determined by the carbon monoxide cooling Λ_{co} and the cosmic-ray heating Γ_{cr} (Eq. 3.10). See Table 3.2 for details.

A

ρ_0 (kg m^{-3})	U_0 (J m^{-3})	Thickness (pc)	$\mathcal{M}$ (kg m^{-2})	T_0 (K)	Figure
1.75×10^{-17}	0	0.46	2.26×10^{-1}	84.74	3.2a
1.59×10^{-18}	9.52×10^{-13}	2.41	1.17×10^{-1}	84.74	3.2b
8.33×10^{-19}	9.98×10^{-13}	4.18	1.09×10^{-1}	84.74	3.2c
5.64×10^{-19}	1.01×10^{-12}	5.72	1.06×10^{-1}	84.74	3.2d
4.27×10^{-19}	1.02×10^{-12}	7.03	1.05×10^{-1}	84.74	3.2e

B

ζ (s^{-1})	k (m^{-1})	Thickness (pc)	$\mathcal{M}$ (kg m^{-2})	T_0 (K)	Figure
5×10^{-17}	10^{-17}	4.66	1.19×10^{-1}	161.3	3.6(i)b, (ii)b
5×10^{-18}	10^{-17}	4.04	1.07×10^{-1}	64.22	3.6(iii)b, (iv)b
10^{-17}	10^{-16}	2.51	1.09×10^{-1}	84.74	–
10^{-17}	10^{-17}	4.18	1.09×10^{-1}	84.74	–
10^{-17}	10^{-18}	4.03	1.09×10^{-1}	84.74	–

Table 3.2: The thickness, column density $\mathcal{M}$ and central temperature T_0 of a gas layer supported by Alfvén waves for (A) decreasing values of the central mass density (ρ_0) with a cosmic-ray ionization rate $\zeta = 10^{-17}\,\mathrm{s}^{-1}$, damping $k = 10^{-17}\,\mathrm{m}^{-1}$ and (B) decreasing values of the cosmic-ray ionization rate (ζ) and damping (k) with a central mass density $\rho_0 = 8.33 \times 10^{-19}\,\mathrm{kg\,m}^{-3}$. The thermal equilibrium of the layer is determined by the carbon monoxide cooling Λ_{co} and the cosmic-ray heating Γ_{cr} (Eq. 3.10). The final column of each table gives the corresponding mass density ratio and temperature profiles.

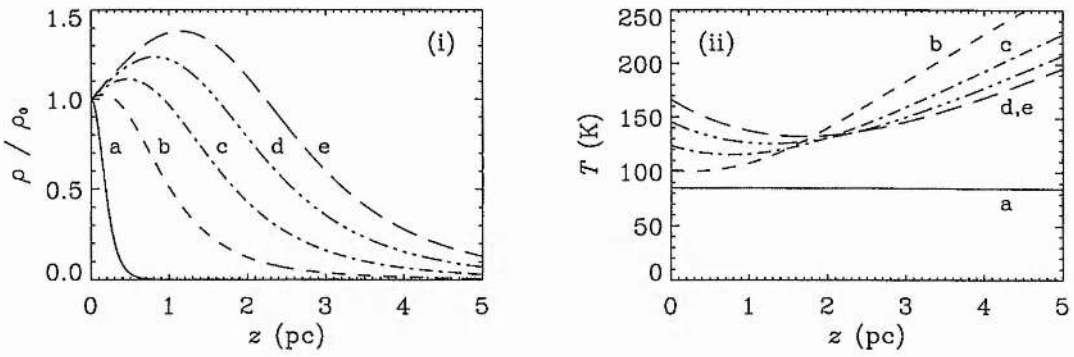

Figure 3.3: The (i) mass density ratio ρ/ρ_0 and (ii) temperature T plotted against the height z for a cosmic-ray ionization rate $\zeta = 10^{-17}\,\mathrm{s}^{-1}$, damping $k = 10^{-17}\,\mathrm{m}^{-1}$ and decreasing values of the central mass density (ρ_0) from a – e. The thermal equilibrium of the layer is determined by the carbon monoxide cooling Λ_{co}, the cosmic-ray heating Γ_{cr} and the wave heating Γ_w (Eq. 3.11). See Table 3.3 for details.

support in the gas layer. This increase in wave support corresponds to an increase in the thickness of the model cloud and hence a decrease in the calculated column density (shown clearly in Table 3.2 and Figure 3.2). Note that, as in the previous chapter, the thickness of the gas layer is defined to be twice the height at which the mass density has fallen by a factor of e from its central value ($2 \times z(\rho/\rho_0 = 1/\mathrm{e})$), and that the column density is given by the expression

$$\mathcal{M} = \sqrt{\frac{2}{\pi G}\left(P_0 + U_0\right)}\,, \tag{3.22}$$

where $P_0 = k_B \rho_0 T_0/\bar{m}$ is the gas pressure at the central plane ($z = 0$).

With no wave heating Equation (3.12) and Figure 3.2(ii) show that, for the mass densities given in Table 3.2, the temperature (T) is independent of the height above the central plane. Consequently the model clouds are at a constant temperature, which is determined by the equilibrium between the cosmic-ray heating and carbon monoxide cooling. This situation is in contrast to that given when the wave heating is introduced into the thermal equilibrium ($\Gamma_w \neq 0$). Figure 3.3 displays the mass density ratio and temperature profiles of the gas slabs described in Table 3.3. These profiles show that increasing the degree of Alfvén wave support in the equilibrium markedly influences the temperature profiles, both in the value of the central temperature (T_0) and the evolution of the profiles with height. Specifically, as the wave support is increased to its maximum value the central temperature of the gas layer is increased to approximately double the value obtained when there is no wave support (U_0) and therefore no wave heating (see

A

ρ_0 (kg m^{-3})	U_0 (J m^{-3})	Thickness (pc)	$\mathcal{M}$ (kg m^{-2})	T_0 (K)	Figure
1.75×10^{-17}	0	0.46	2.26×10^{-1}	84.74	3.3a
1.59×10^{-18}	9.52×10^{-13}	2.45	1.21×10^{-1}	101.5	3.3b
8.33×10^{-19}	9.98×10^{-13}	4.31	1.14×10^{-1}	123.7	3.3c
5.64×10^{-19}	1.01×10^{-12}	5.91	1.12×10^{-1}	145.5	3.3d
4.27×10^{-19}	1.02×10^{-12}	7.27	1.10×10^{-1}	166.2	3.3e

B

ζ (s^{-1})	k (m^{-1})	Thickness (pc)	$\mathcal{M}$ (kg m^{-2})	T_0 (K)	Figure
5×10^{-17}	10^{-17}	4.70	1.21×10^{-1}	180.0	3.6(i)c, (ii)c
5×10^{-18}	10^{-17}	4.22	1.13×10^{-1}	113.5	3.6(iii)c, (iv)c
10^{-17}	10^{-16}	2.60	1.30×10^{-1}	261.7	3.4a
10^{-17}	10^{-17}	4.31	1.14×10^{-1}	123.7	3.4b
10^{-17}	10^{-18}	4.03	1.10×10^{-1}	89.85	3.4c

Table 3.3: The thickness, column density $\mathcal{M}$ and central temperature T_0 of a gas layer supported by Alfvén waves for (A) decreasing values of the central mass density (ρ_0) with a cosmic-ray ionization rate $\zeta = 10^{-17}\mathrm{s}^{-1}$, damping $10^{-17}\mathrm{m}^{-1}$ and (B) decreasing values of the cosmic-ray ionization rate (ζ) and damping (k) with a central mass density $\rho_0 = 8.33 \times 10^{-19}$ kg m^{-3}. The thermal equilibrium of the layer is determined by the carbon monoxide cooling Λ_{co}, the cosmic-ray heating Γ_{cr} and the wave heating Γ_w (Eq. 3.11). The final column of each table gives the corresponding mass density ratio and temperature profiles.

Table 3.3).

The mass density ratio profiles plotted in Figure 3.3(i) show an increase in mass density away from the central plane (see Chapter 2, Equation (2.38) and Figure 2.5). This bump in density is reflected in the temperature profiles, which show an initial decrease in the temperature of the layer. The decrease results from the combined influences of an increase in carbon monoxide cooling and a decrease in the wave heating (as can be seen from Eq. 3.15). A similar effect is observed when the strength of the damping is varied, as shown in Figure 3.4. For the strongest value of the damping ($k = 10^{-16}$ m^{-1}) the three-fold increase in the mass density ratio, and the corresponding rapid decrease in the wave energy density (see Figure 2.9) combine to reduce the temperature of the layer by more than a factor of two (through Eq. 3.15). As a result this model cloud shows a large overall decrease in temperature from the centre of the cloud to the outer edge, as determined by the thickness of the layer. This is in contrast to the other profiles plotted in Figures 3.3 and 3.4, which show that including the wave

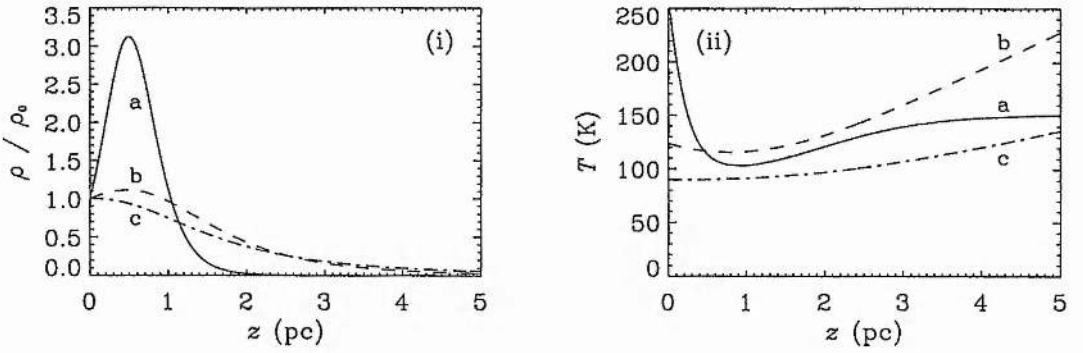

Figure 3.4: The (i) mass density ratio ρ/ρ_0 and (ii) temperature T plotted against the height z for a central mass density $\rho_0 = 8.33 \times 10^{-19}\,\mathrm{kg\,m^{-3}}$, cosmic-ray ionization rate $\zeta = 10^{-17}\,\mathrm{s^{-1}}$ and decreasing values of the damping: (a) $k = 10^{-16}\,\mathrm{m^{-1}}$, (b) $k = 10^{-17}\,\mathrm{m^{-1}}$ and (c) $k = 10^{-18}\,\mathrm{m^{-1}}$. The thermal equilibrium of the layer is determined by the carbon monoxide cooling Λ_{co}, the cosmic-ray heating Γ_{cr} and the wave heating Γ_w (Eq. 3.11). See Table 3.3 for details.

heating in the thermal equilibrium results in a general increase in temperature from the central plane ($z = 0$) to the edge of the cloud.

Figure 3.5 illustrates the relative contributions of the heating processes (Γ_{cr} and Γ_w) for two values of the damping. If the damping is strong, $k = 10^{-16}\,\mathrm{m^{-1}}$, then the wave heating dominates the cosmic-ray heating in the central regions of the cloud and thus the behaviour of the mass and wave energy densities control the initial evolution of the temperature profile (compare Figures 3.5(i) and 3.4(ii), curve a). Conversely, a weak value for the damping, $k = 10^{-18}\,\mathrm{m^{-1}}$, means that the cosmic-ray heating takes the dominant role, the wave heating provides only a slight increase in temperature as the height above the central plane increases (compare Figure 3.5(ii) with Figure 3.4(ii), profile c).

A comparison between the isothermal model of Alfvén wave support (Chapter 2) and the temperature-dependent models including and excluding wave heating is drawn in Figure 3.6 and Table 3.4. Figure 3.6 shows the mass density ratio and temperature profiles of model clouds for two values of the cosmic-ray ionization rate (ζ). As expected the value chosen for ζ effects both the structure and temperature of the cloud as well as the relative importance of the wave heating. If the ionization rate is high, $\zeta = 5 \times 10^{-17}\,\mathrm{s^{-1}}$, then the change induced in the density profile by including the wave heating is minor, the thickness of the slab is increased by only a fraction of a parsec (see Tables 3.2 and 3.3). Likewise, the increase in the central temperature of

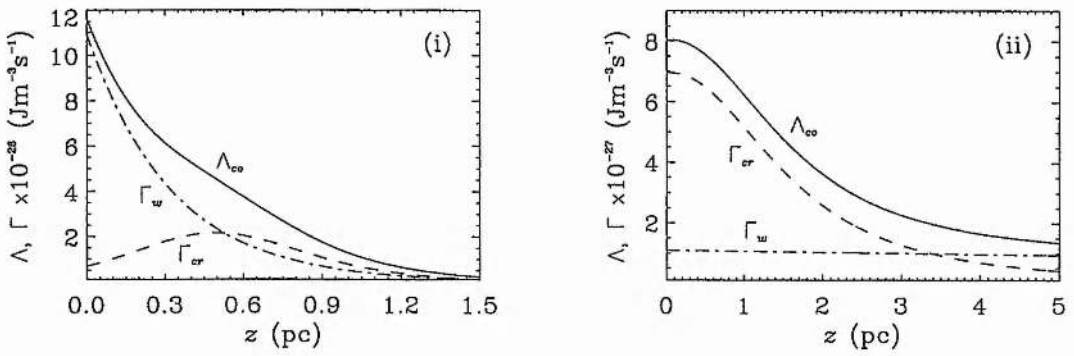

Figure 3.5: The carbon monoxide cooling (Λ_{co}), cosmic-ray heating (Γ_{cr}) and Alfvén wave heating (Γ_w) plotted against the height z for a central mass density $\rho_0 = 8.33 \times 10^{-19}\,\mathrm{kg\,m^{-3}}$, cosmic-ray ionization rate $\zeta = 10^{-17}\,\mathrm{s^{-1}}$ and decreasing values of the damping: (i) $k = 10^{-16}\,\mathrm{m^{-1}}$ and (ii) $k = 10^{-18}\,\mathrm{m^{-1}}$.

the cloud is less significant when compared to the change from the isothermal model; however, including Γ_w does mean that the temperature is no longer at a constant value throughout the cloud. Simply reducing the cosmic-ray ionization rate by an order of magnitude, $\zeta = 5 \times 10^{-18}\,\mathrm{s^{-1}}$, greatly increases the significance of introducing the wave heating into the thermal equilibrium (as shown in Figure 3.6).

ρ_0 (kg m^{-3})	U_0 (J m^{-3})	Thickness (pc)		
		Isothermal	$\Gamma_w = 0$	$\Gamma_w \neq 0$
1.75×10^{-17}	0	0.20	0.46	0.46
1.59×10^{-18}	9.52×10^{-13}	1.97	2.41	2.45
8.33×10^{-19}	9.98×10^{-13}	3.70	4.18	4.31
5.64×10^{-19}	1.01×10^{-12}	5.19	5.72	5.91
4.27×10^{-19}	1.02×10^{-12}	6.47	7.03	7.27

Table 3.4: The thickness of the gas layer for the isothermal model, and the temperature-dependent models excluding ($\Gamma_w = 0$) and including ($\Gamma_w \neq 0$) the wave heating for a cosmic-ray ionization rate $\zeta = 10^{-17}\mathrm{s^{-1}}$, damping $k = 10^{-17}\mathrm{m^{-1}}$ and decreasing values of the central mass density (ρ_0).

Table 3.4 and Figure 3.6 clearly show that the extent of the layer is enhanced by the introduction of temperature dependence into the model, and then again by the inclusion of the wave heating. This correlation is clear given that an increase in the temperature of the layer raises the gas pressure, which in turn provides more support

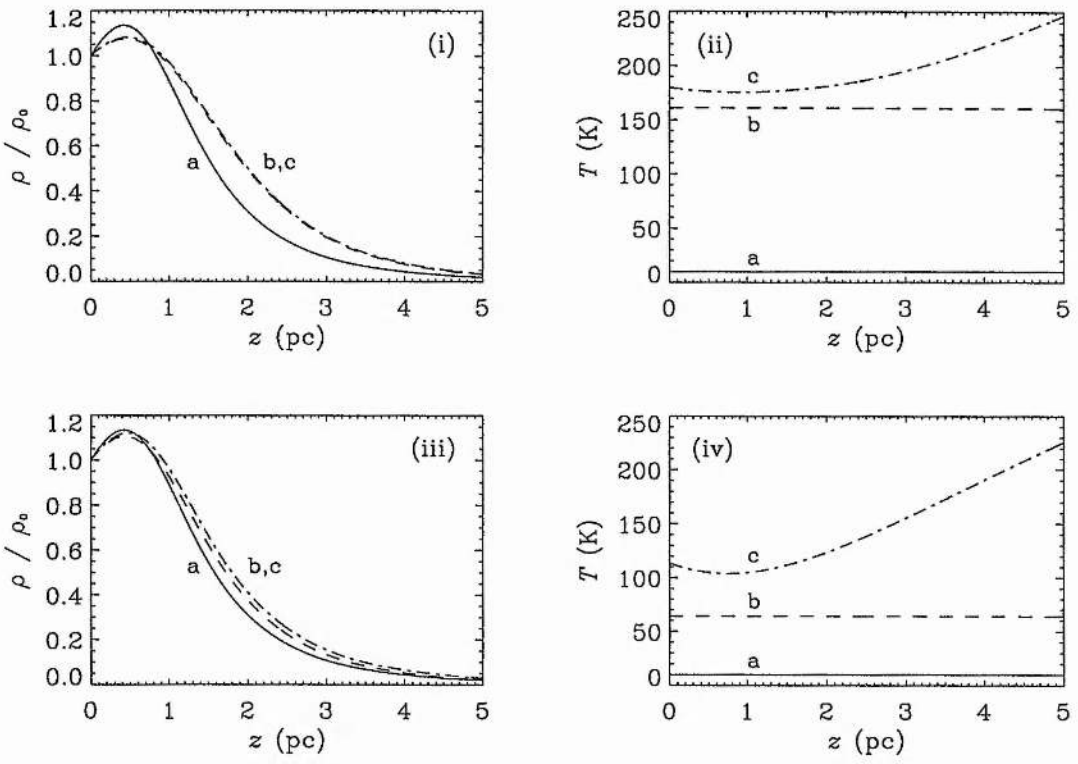

Figure 3.6: The (i), (iii) mass density ratio ρ/ρ_0 and (ii), (iv) temperature T plotted against the height z for (a) the isothermal model, (b) the temperature-dependent model in the absence of wave heating ($\Gamma_w = 0$) and (c) the temperature-dependent model in the presence of wave heating ($\Gamma_w \neq 0$). The curves are plotted for a central mass density $\rho_0 = 8.33 \times 10^{-19}\,\mathrm{kg\,m^{-3}}$, damping $k = 10^{-17}\,\mathrm{m^{-1}}$ and two values of the cosmic-ray ionization rate: $\zeta = 5 \times 10^{-17}\mathrm{s^{-1}}$ in graphs (i) and (ii), and $\zeta = 5 \times 10^{-18}\mathrm{s^{-1}}$ in graphs (iii) and (iv).

against the self-gravity and hence increases the thickness of the gas slab. In summary, this simple model of the thermal equilibrium has shown that the Alfvén waves used to support the cloud can play an important role in heating the cloud and subsequently in determining its thickness.

3.3 Model II: Molecular and ionized carbon (C^+) cooling

The simple model for the thermal equilibrium adopted in the previous section successfully showed that Alfvén wave heating could be important in low-mass star-forming regions. However, the temperatures found in the model clouds (see Figure 3.3 for ex-

ample) are high compared to the observed value of $\sim$ 10K (Shu et al. 1987; Myers 1999). In this section a fuller treatment of the cooling processes found in molecular clouds is adopted — the total molecular cooling as determined by Goldsmith & Langer (1978), together with the cooling contributed by ionized carbon.

3.3.1 The cooling

The formulae given in Table 3.1 express the total cooling rate at a given hydrogen number density, for a number of molecules including carbon monoxide and water (for a comprehensive list refer to GL78). These formulae were determined by GL78 for number densities (n_{H_2}) in the range $10^8\,\mathrm{m}^{-3}$ to $10^{12}\,\mathrm{m}^{-3}$ and temperatures (T) in the range 10 K to 60 K, and they can be written in the form

$$\Lambda_{mol} = aT^b\,, \tag{3.23}$$

where a and b are dependent on the density of the region. Following Lis & Goldsmith (1990), a and b can be fitted using a polynomial in order to obtain an analytical formula for the total cooling rate (Λ_{mol}). These are chosen to be

$$\log_{10} a = 0.44\,x - 31.17 \tag{3.24}$$

and

$$b = \begin{cases} 0.53 & x \leq 6 \\ -0.03\,x^3 + 0.74\,x^2 - 5.68\,x + 14.13 & 6 < x < 11 \\ 2.91 & x \geq 11 \end{cases} \tag{3.25}$$

where $x = \log_{10} n_{H_2}$ (n_{H_2} is given in m^{-3}), as shown in Figure 3.7. The best-fit polynomial chosen to model b is set to a constant upon reaching its maximum (at $n_{H_2} = 10^{11}\,\mathrm{m}^{-3}$), thus avoiding a decrease in the value of this coefficient for densities $n_{H_2} \geq 10^{11}\,\mathrm{m}^{-3}$. In addition, b is also set to a constant value at low number densities ($n_{H_2} \leq 10^6\,\mathrm{m}^{-3}$), at the point where the cubic reaches a minimum. This form of cubic fit is necessary to avoid the coefficient b falling to zero as the density decreases.

The molecular cooling formula (Eq. 3.23) is valid up to temperatures of $\sim$ 60 K, but the results found in the previous model (Section 2.3) suggest that the temperature can become higher than this. Consequently, following the discussion of the cooling processes in Section 1.2, the cooling due to ionized carbon (C^+) is also introduced into the thermal equilibrium. It is given by the expression

$$\Lambda_{C^+} = 8 \times 10^{-33}\,\frac{n_e n_{C^+}}{\sqrt{T}}\,\mathrm{e}^{-\frac{92}{T}} \tag{3.26}$$

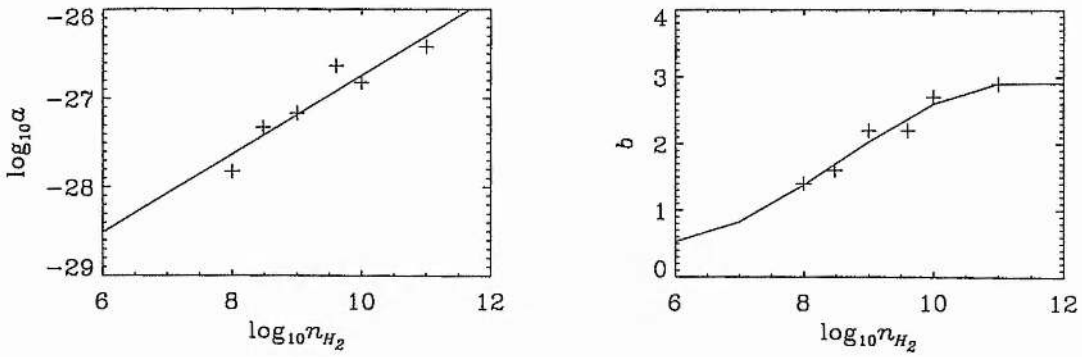

Figure 3.7: The density dependence of the coefficients a and b in Equation (3.23). The plus symbols (+) represent the original values from GL78 and the solid lines (—) show the polynomial fits used within this study (Eqs 3.24 and 3.25).

(Dyson & Williams 1997) in SI units, where n_e is the number density of electrons and n_{C+} is the number density of C^+ ions. These densities are estimated from the paper by de Jong, Dalgarno & Boland (1980), to be

$$\frac{n_e}{n_H} = \frac{n_{C+}}{n_H} = 10^{-6.0-2.5\tanh(A_v-1.0)}, \tag{3.27}$$

where n_H is the number density of hydrogen nuclei and A_v is the visual extinction into the cloud. The gas-to-extinction ratio

$$\frac{N_{H_2}}{A_v} \approx 1.25 \times 10^{25} \tag{3.28}$$

(Dickman 1978) in SI units, relates the visual extinction to the molecular hydrogen column density N_{H_2}. In the context of the models used to describe Alfvén wave support, the mass column density at a height z is given by

$$\mathcal{M} = 2\int_0^z \rho(z)\,dz = \frac{g(z)}{2\pi G}, \tag{3.29}$$

using the equation of self-gravitation (Eq. 3.7). This translates to a number column density of

$$N = \frac{\mathcal{M}}{\bar{m}},$$

where $\bar{m} = 2.3m_H$ (Shu et al. 1987). Thus the visual extinction into the cloud is defined by the expression

$$A_v = \frac{10^{-25}}{2\pi G\bar{m}}\,(g(z_b) - g(z)), \tag{3.30}$$

where $g(z_b)$ is the value of the gravity at the outer boundary of the model cloud.

The molecular cooling (Eq. 3.23) and the cooling by the C^+ ion (Eq. 3.26) will both be used in the following section to model the thermal equilibrium of a gas layer, which is in mechanical equilibrium between its self-gravity, the gas pressure and an Alfvén wave pressure force.

3.3.2 The equations

Within this second description of a temperature-dependent model of Alfvén wave support, the equilibrium and self-gravitation equations (Eqs 3.6 and 3.7),

$$\frac{d}{dz}(P+U) = -\rho g$$

and

$$\frac{dg}{dz} = 4\pi G\rho\,,$$

are joined by the equation of thermal equilibrium

$$\Lambda_{mol} + \Lambda_{C^+} = \Gamma_{cr} + \Gamma_w\,, \tag{3.31}$$

which describes the balance between the molecular (Λ_{mol}) and ionized carbon (Λ_{C^+}) cooling and the cosmic-ray (Γ_{cr}) and wave (Γ_w) heating. The nature of Equation (3.31) precludes the determination of a simple expression for the temperature and so, in this instance, the mass density (ρ), the gravity (g) and the temperature (T) are treated as the three dependent variables. Thus the thermal equilibrium equation is differentiated with respect to the independent variable height (z) to obtain an expression for dT/dz. Considering each contribution to the thermal equilibrium equation in turn, shows that the derivative of the cosmic-ray heating (Eq. 3.1) is

$$\frac{d\Gamma_{cr}}{dz} = 8.33\times10^{8}\,\zeta\,\frac{d\rho}{dz}\,, \tag{3.32}$$

where ζ is the cosmic-ray ionization rate, while that for the Alfvén wave heating (Eq. 3.14) is given by

$$\frac{d\Gamma_w}{dz} = 10^{-6}\,k\,\frac{d}{dz}\left(\frac{U}{\sqrt{\rho}}\right)\,. \tag{3.33}$$

From the description of the wave energy density (U), in Equation (3.8), this expression can simply be written as

$$\frac{d\Gamma_w}{dz} = -10^{-6}\,k^2\,\frac{U_0}{\sqrt{\rho_0}}\,\mathrm{e}^{-kz}\,, \tag{3.34}$$

where k is the damping parameter and U_0, ρ_0 are the wave energy density and mass density at the central plane.

The molecular cooling, which is described by Equation (3.23) differentiates to

$$\frac{d\Lambda_{mol}}{dz} = aT^b \left(\frac{b}{T} \frac{dT}{dz} + \ln T \frac{db}{dz} \right) + T^b \frac{da}{dz}, \tag{3.35}$$

where the derivatives of the coefficients a and b (Eqs 3.24 and 3.25) are

$$\frac{da}{dz} = \frac{da}{d\rho} \frac{d\rho}{dz} = 0.44 \frac{a}{\rho} \frac{d\rho}{dz}, \tag{3.36}$$

plus

$$\frac{db}{dz} = \frac{db}{d\rho} \frac{d\rho}{dz} = \frac{\log_{10} \mathrm{e}}{\rho} \left(-0.09\, x^2 + 1.48\, x - 5.68 \right) \frac{d\rho}{dz} \qquad 6 < x < 11 \tag{3.37}$$

and $db/dz = 0$ for $x \leq 6$ and $x \geq 11$, given that $x = \log_{10} n_{H_2}$, where $n_{H_2} = \rho / 2.3 m_H$ (Shu et al. 1987). The final term in the thermal equilibrium equation (Eq. 3.31) is that describing the cooling by the C^+ ion (Eq. 3.26). By defining

$$f(\rho) = 8 \times 10^{-33} \left(\frac{n_{C+}}{n_H} \right)^2 n_H^2 \tag{3.38}$$

this cooling term may be differentiated with respect to the height (z), to give

$$\frac{d\Lambda_{C+}}{dz} = \frac{\mathrm{e}^{-92/T} f}{T^{3/2}} \left(\frac{92}{T} - \frac{1}{2} \right) + \frac{\mathrm{e}^{-92/T}}{\sqrt{T}} \frac{df}{dz}, \tag{3.39}$$

where

$$\frac{df}{dz} = \frac{8 \times 10^{-33}}{m_H^2} \left(2F\rho \frac{d\rho}{dz} + \frac{10^{-24} F \rho^3}{\bar{m} \log_{10} \mathrm{e}} \operatorname{sech}^2 (A_v - 1.0) \right), \tag{3.40}$$

A_v is the visual extinction (Eq. 3.30) and $F = (n_{C+}/n_H)^2$ is given by Equation (3.27). Combining the derivatives for each of the heating and cooling mechanisms (Eqs 3.32, 3.34, 3.35 and 3.39) results in an expression for the temperature derivative of

$$\frac{dT}{dz} = \frac{Q}{S} \frac{d\rho}{dz} - \frac{R}{S}, \tag{3.41}$$

where Q, R and S are described by the expressions

$$Q = \alpha - T^b \left(ab' \ln T + a' \right) - \frac{2\, \mathrm{e}^{-92/T} f}{\rho \sqrt{T}},$$

$$R = \beta \mathrm{e}^{-kz} + \frac{10^{-24} \mathrm{e}^{-92/T} f \rho}{\bar{m} \sqrt{T} \log_{10} \mathrm{e}} \operatorname{sech}^2 (A_v - 1.0),$$

and

$$S = abT^{b-1} + \frac{\mathrm{e}^{-92/T} f}{T^{3/2}} \left(\frac{92}{T} - \frac{1}{2} \right)$$

given that $\alpha = 8.33 \times 10^8 \zeta$, $\beta = 10^{-6} k^2 U_0 / \sqrt{\rho_0}$, $a' = da/d\rho$ and $b' = db/d\rho$.

The equations describing this temperature-dependent model have now become the equilibrium equation (Eq. 3.6), which can be expanded to

$$\left(\frac{k_B}{\bar{m}}T + \frac{U}{2\rho}\right)\frac{d\rho}{dz} + \frac{k_B}{\bar{m}}\rho\frac{dT}{dz} = kU - \rho g\,, \tag{3.42}$$

given that dU/dz is described by Equation (3.17), where $U = U_0\sqrt{\rho}\mathrm{e}^{-kz}/\sqrt{\rho_0}$ (Eq. 3.8); the self-gravitation equation (Eq. 3.7)

$$\frac{dg}{dz} = 4\pi G\rho$$

and the equation for the temperature (Eq. 3.41)

$$\frac{dT}{dz} - \frac{Q}{S}\frac{d\rho}{dz} = -\frac{R}{S}\,. \tag{3.43}$$

These equations give three first-order differential equations describing the mass density (ρ), the gravity (g) and the temperature (T) in terms of the height (z) above the central plane. In the following section they will be solved, subject to the boundary conditions $\rho = \rho_0$, $g = 0$ and $T = T_0$ at $z = 0$, to give the mass density and temperature profiles of model clouds.

3.3.3 Results

Following the analysis of the previous temperature-dependent model (Section 2.3) the values of the mass density and wave energy density at the central plane (ρ_0 and U_0) are taken to be known quantities. This allows the results generated within this section to be compared to those for an isothermal model of Alfvén wave support (Chapter 2). By choosing ρ_0 and U_0 the central temperature (T_0) can be calculated prior to solving the differential equations (Eqs 3.42, 3.7 and 3.43) by considering the thermal equilibrium equation (Eq. 3.31) at the central plane.

The specifications of this model allow the total pressure of the system, which is given by

$$P_{tot} = P + U\,,$$

where P is the gas pressure (Eq. 3.9) and U is the wave energy density (Eq. 3.8), to be treated as a reasonable physical quantity. As such, the equations describing this model (Eqs 3.42, 3.7 and 3.43) are integrated out to the height at which the total pressure (P_{tot}) equals the interstellar medium (ISM) pressure $n_{H_2}T = 10^4\,\mathrm{cm}^{-3}\,\mathrm{K}$ (e.g. Suchov et al. 1993). This height is defined to be the outer edge of the model cloud and hence the column density of the layer is now calculated from the expression

$$\mathcal{M} = \sqrt{\frac{2}{\pi G}\left(P_0 + U_0 - P_{ism}\right)}\,, \tag{3.44}$$

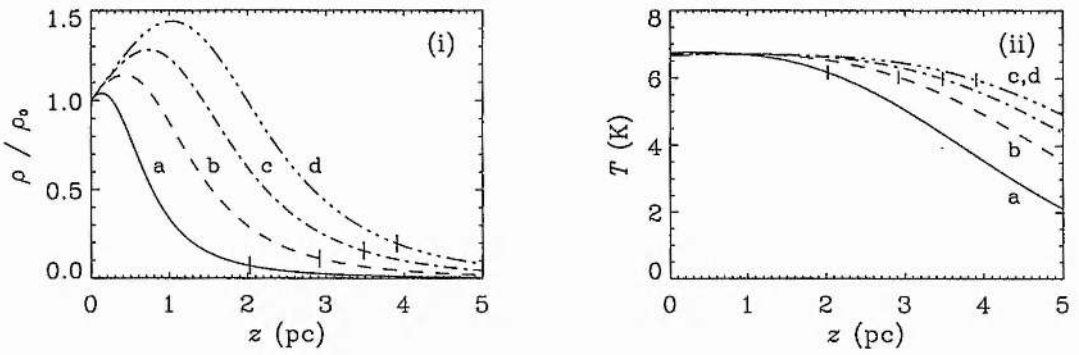

Figure 3.8: The (i) mass density ratio ρ/ρ_0 and (ii) temperature T plotted against the height z for a cosmic-ray ionization rate $\zeta = 10^{-17}\,\mathrm{s}^{-1}$, damping $k = 10^{-17}\,\mathrm{m}^{-1}$ and increasing values of the central wave energy density (U_0) from a – d. The vertical line on each profile marks the edge of the cloud as given by the ISM pressure. The thermal equilibrium of the layer is determined by the molecular cooling Λ_{mol}, the ionized carbon cooling Λ_{C+} and the cosmic-ray heating Γ_{cr}. See Table 3.5 for details.

where P_0 and U_0 are the gas and wave pressures at the central plane ($z = 0$) and P_{ism} is the ISM pressure.

Figure 3.8 shows the mass density ratio (ρ/ρ_0) and temperature (T) profiles of four model clouds in the absence of any heating by the Alfvén waves ($\Gamma_w = 0$). The small vertical lines on each profile indicate the point at which the total pressure of the gas layer has fallen to the ISM value, i.e. the edge of the model cloud. The resulting thickness of the cloud, together with its central temperature is listed in Table 3.5, along with the column density (Eq. 3.44) and the thickness of the cloud as determined by the height at which the mass density has fallen by a factor of e (see also Section 2.3). These values, coupled with Figure 3.8, show that when the wave heating is excluded from the thermal equilibrium equation (Eq. 3.31) the temperature within the model cloud remains almost constant, varying by less than a degree between the centre and edge of the layer. Increasing the amount of Alfvén wave support (increasing the value of the central energy density U_0) and hence enhancing the thickness of the cloud, has very little influence on the temperature of the gas, which is to be anticipated given that $\Gamma_w = 0$.

Figure 3.9 and Table 3.6 detail how this situation is altered when the heating generated by the Alfvén waves is included within the thermal equilibrium. Introducing Γ_w primarily effects the evolution of the temperature as the height above the central plane increases, and as a result influences the extent of the model cloud. Table 3.6 shows

A

ρ_0 (kg m^{-3})	U_0 (J m^{-3})	Thickness (pc)		$\mathcal{M}$ (kg m^{-2})	T_0 (K)	Figure
		1/e	ISM			
1.59×10^{-18}	9.52×10^{-13}	1.91	4.05	9.02×10^{-2}	6.76	3.8a
8.33×10^{-19}	9.98×10^{-13}	3.63	5.83	9.16×10^{-2}	6.72	3.8b
5.64×10^{-19}	1.01×10^{-12}	5.12	6.97	9.19×10^{-2}	6.69	3.8c
4.27×10^{-19}	1.02×10^{-12}	6.38	7.81	9.23×10^{-2}	6.65	3.8d

B

ζ (s^{-1})	k (m^{-1})	Thickness (pc)		$\mathcal{M}$ (kg m^{-2})	T_0 (K)
		1/e	ISM		
5×10^{-17}	10^{-17}	3.70	6.03	9.35×10^{-2}	18.41
5×10^{-18}	10^{-17}	3.60	5.80	9.13×10^{-2}	4.36
10^{-17}	10^{-16}	1.62	1.36	9.16×10^{-2}	6.72
10^{-17}	10^{-17}	3.63	5.83	9.16×10^{-2}	6.72
10^{-17}	10^{-18}	3.50	12.99	9.16×10^{-2}	6.72

Table 3.5: The thickness, column density $\mathcal{M}$ and central temperature T_0 of a gas layer supported by Alfvén waves for (A) increasing values of the central wave energy density (U_0) with a cosmic-ray ionization rate $\zeta = 10^{-17}\,\mathrm{s}^{-1}$, damping $10^{-17}\,\mathrm{m}^{-1}$ and (B) decreasing values of the cosmic-ray ionization rate (ζ) and damping (k) with a central mass density $\rho_0 = 8.33 \times 10^{-19}\,\mathrm{kg\,m}^{-3}$. The thermal equilibrium of the layer is determined by the molecular cooling Λ_{mol}, the ionized carbon cooling Λ_{C^+} and the cosmic-ray heating Γ_{cr}. The final column of table (A) gives the corresponding mass density ratio and temperature profiles.

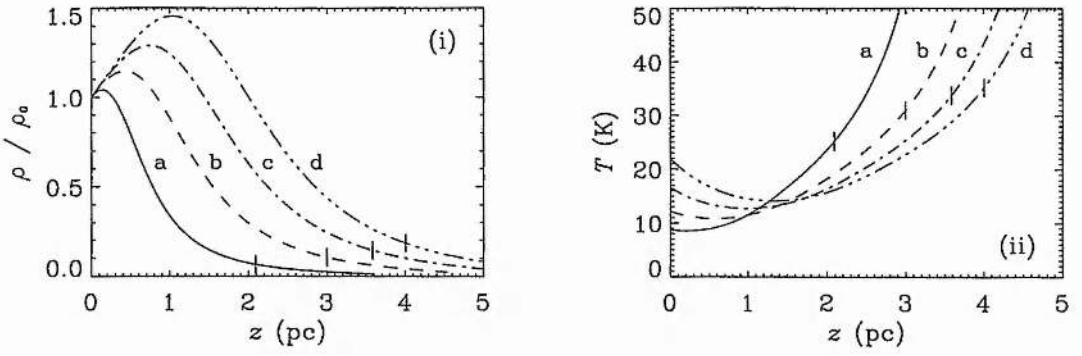

Figure 3.9: The (i) mass density ratio ρ/ρ_0 and (ii) temperature T plotted against the height z for a cosmic-ray ionization rate $\zeta = 10^{-17}\,\mathrm{s}^{-1}$, damping $k = 10^{-17}\,\mathrm{m}^{-1}$ and increasing values of the central wave energy density (U_0) from a – d. The vertical line on each profile marks the edge of the cloud as given by the ISM pressure. The thermal equilibrium of the layer is determined by the molecular cooling Λ_{mol}, the ionized carbon cooling Λ_{C+}, the cosmic-ray heating Γ_{cr} and the wave heating Γ_w (Eq. 3.31). See Table 3.6 for details.

how increasing the value of the central wave energy density heats the central plane of the gas layer up to temperatures of ~ 20 K for the maximum wave support considered here. As in the previous model, the bump in mass density away from the central plane causes a corresponding dip in the gas temperature; however, the wave heating is shown to give rise to a general increase in temperature towards the edge of the cloud. The overall enhancement in T from the centre ($z = 0$) to the edge ($P_{tot} = P_{ism}$) of these model clouds is $\sim 15 - 20$ K (see Figure 3.9(ii)).

The contributions of each of the heating and cooling processes in a typical model cloud ($U_0 = 9.98\times10^{-13}\,\mathrm{J\,m^{-3}}$, $\zeta = 10^{-17}\mathrm{s}^{-1}$, $k = 10^{-17}\mathrm{m}^{-1}$) are shown in Figure 3.10. It can be seen that the Alfvén wave heating (Γ_w) dominates the cosmic-ray heating (Γ_{cr}) throughout the gas layer and thus is clearly a significant heating mechanism. Similarly, the molecular cooling (Λ_{mol}) is by far the more important of the two cooling mechanisms. As the temperature of the cloud begins to rise (see Figure 3.9(ii)) the cooling due to the ionized carbon (Λ_{C+}) becomes more important. However, given that the central regions of the cloud in particular, are at relatively low temperatures the molecular species are the main contributers to the cooling of the gas.

Of particular interest within this model is how the profiles of density and temperature are effected as the damping parameter (k) — which influences the wave heating (Eq. 3.14) — and the cosmic-ray ionization rate (ζ) are varied. Firstly, Fig-

A

ρ_0 (kg m^{-3})	U_0 (J m^{-3})	Thickness (pc)		$\mathcal{M}$ (kg m^{-2})	T_0 (K)	Figure
		1/e	ISM			
1.59×10^{-18}	9.52×10^{-13}	1.91	4.18	9.08×10^{-2}	8.70	3.9a
8.33×10^{-19}	9.98×10^{-13}	3.63	6.00	9.25×10^{-2}	12.15	3.9b
5.64×10^{-19}	1.01×10^{-12}	5.12	7.16	9.30×10^{-2}	16.59	3.9c
4.27×10^{-19}	1.02×10^{-12}	6.38	8.01	9.35×10^{-2}	21.98	3.9d

B

ζ (s^{-1})	k (m^{-1})	Thickness (pc)		$\mathcal{M}$ (kg m^{-2})	T_0 (K)	Figure
		1/e	ISM			
5×10^{-17}	10^{-17}	3.70	6.16	9.40×10^{-2}	21.85	3.12a
5×10^{-18}	10^{-17}	3.60	6.00	9.23×10^{-2}	10.62	3.12c
10^{-17}	10^{-16}	1.62	1.39	9.66×10^{-2}	39.24	3.11a
10^{-17}	10^{-17}	3.63	6.00	9.25×10^{-2}	12.15	3.11b
10^{-17}	10^{-18}	3.50	13.16	9.17×10^{-2}	7.37	3.11c

Table 3.6: The thickness, column density $\mathcal{M}$ and central temperature T_0 of a gas layer supported by Alfvén waves for (A) increasing values of the central wave energy density (U_0) with a cosmic-ray ionization rate $\zeta = 10^{-17}\,\mathrm{s}^{-1}$, damping $10^{-17}\,\mathrm{m}^{-1}$ and (B) decreasing values of the cosmic-ray ionization rate (ζ) and damping (k) with a central mass density $\rho_0 = 8.33 \times 10^{-19}\,\mathrm{kg\,m}^{-3}$. The thermal equilibrium of the layer is determined by the molecular cooling Λ_{mol}, the ionized carbon cooling Λ_{C+}, the cosmic-ray heating Γ_{cr} and the wave heating Γ_w (Eq. 3.31). The final column of each table gives the corresponding mass density ratio and temperature profiles.

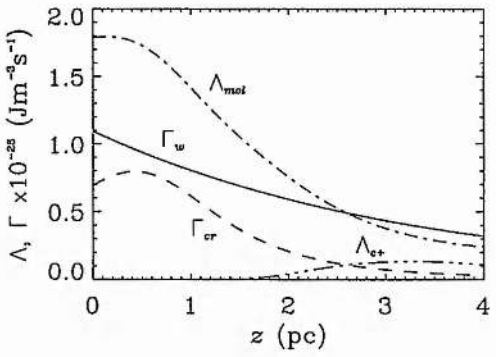

Figure 3.10: The molecular cooling (Λ_{mol}), ionized carbon cooling (Λ_{C^+}), cosmic-ray heating (Γ_{cr}) and Alfvén wave heating (Γ_w) plotted against the height z for a central wave energy density $U_0 = 9.98 \times 10^{-13}\,\mathrm{J\,m^{-3}}$, cosmic-ray ionization rate $\zeta = 10^{-17}\,\mathrm{s^{-1}}$ and damping $k = 10^{-17}\,\mathrm{m^{-1}}$.

ure 3.11 shows three model clouds each with a different value for the damping, from $k = 10^{-16}\,\mathrm{m^{-1}}$ for strong damping to $k = 10^{-18}\,\mathrm{m^{-1}}$ for weak damping. These profiles show that k can play a major role in determining the properties of the model cloud (see also Table 3.6). If the damping is at its strongest then the large increase in mass density away from the central plane causes the temperature to drop rapidly; consequently, the total pressure of the system falls to the interstellar medium value before the density has fallen by a factor of e from its central value. In this case the model cloud is noticeably cooler at its edge than at the central plane. This situation is reversed as the damping is reduced. Indeed, for the weakest value of the damping there is no increase in mass density away from the central plane and the temperature continually increases as the height (z) increases. The changes induced in the density and temperature profiles by varying the cosmic-ray ionization rate (ζ) are less dramatic. The curves of the mass density ratio (ρ/ρ_0) plotted in Figure 3.12(i) show that varying the ionization rate by an order of magnitude (from $\zeta = 5 \times 10^{-17}\,\mathrm{s^{-1}}$ to $\zeta = 5 \times 10^{-18}\,\mathrm{s^{-1}}$) has very little effect on the thickness of the gas layer (see also Table 3.6). However, the higher values of the ionization rate have increased the temperature throughout the cloud by at most ~ 10 K (see Figure 3.12(ii)).

To be able to note the effect these two parameters have in the absence of, as well as in the presence of wave heating (Γ_w), Figure 3.13 shows how the central temperature (T_0) and thickness (as determined by the ISM pressure) of the model clouds vary over a range of values of the damping (k) and the cosmic-ray ionization rate (ζ). Figure 3.13(i) and (ii) reveal that while the central temperature is increased by a factor of four as

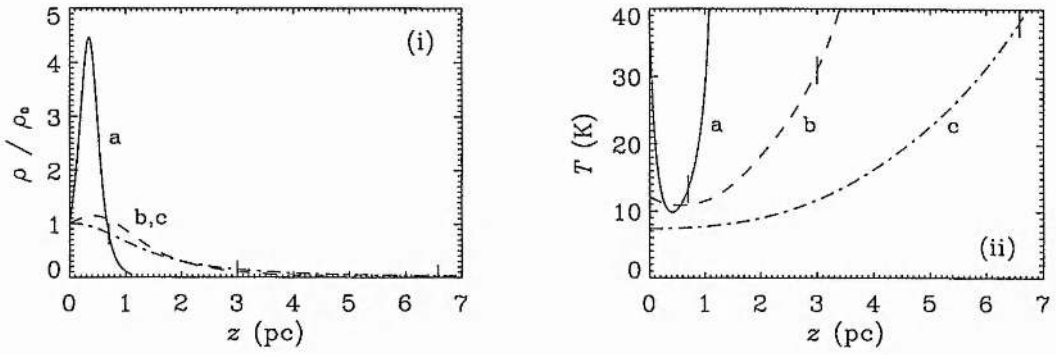

Figure 3.11: The (i) mass density ratio ρ/ρ_0 and (ii) temperature T plotted against the height z for a central wave energy density $U_0 = 9.98 \times 10^{-13}\,\mathrm{J\,m^{-3}}$, cosmic-ray ionization rate $\zeta = 10^{-17}\mathrm{s^{-1}}$ and decreasing values of the damping: (a) $k = 10^{-16}\,\mathrm{m^{-1}}$, (b) $k = 10^{-17}\,\mathrm{m^{-1}}$ and (c) $k = 10^{-18}\,\mathrm{m^{-1}}$. The vertical line on each profile marks the edge of the cloud as given by the ISM pressure. The thermal equilibrium of the layer is determined by the molecular cooling Λ_{mol}, the ionized carbon cooling Λ_{C+}, the cosmic-ray heating Γ_{cr} and the wave heating Γ_w (Eq. 3.31). See Table 3.6 for details.

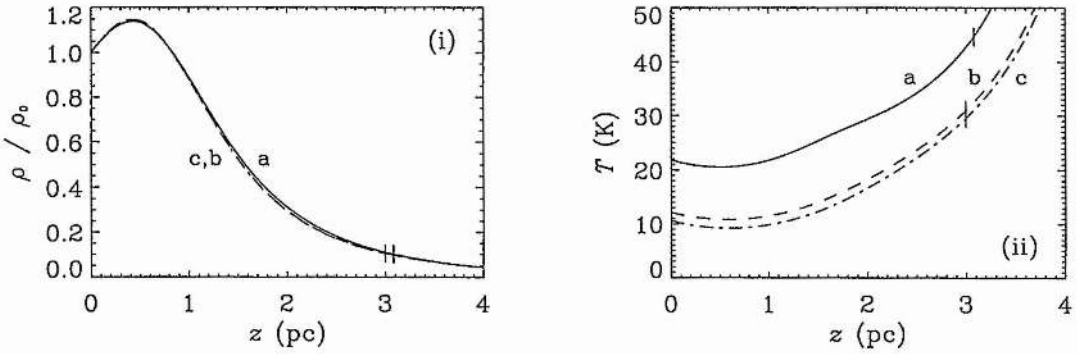

Figure 3.12: The (i) mass density ratio ρ/ρ_0 and (ii) temperature T plotted against the height z for a central wave energy density $U_0 = 9.98 \times 10^{-13}\,\mathrm{J\,m^{-3}}$, damping $k = 10^{-17}\,\mathrm{m^{-1}}$ and decreasing values of the cosmic-ray ionization rate: (a) $\zeta = 5 \times 10^{-17}\mathrm{s^{-1}}$, (b) $\zeta = 1 \times 10^{-17}\,\mathrm{s^{-1}}$ and (c) $\zeta = 5 \times 10^{-18}\,\mathrm{s^{-1}}$. The vertical line on each profile marks the edge of the cloud as given by the ISM pressure. The thermal equilibrium of the layer is determined by the molecular cooling Λ_{mol}, the ionized carbon cooling Λ_{C+}, the cosmic-ray heating Γ_{cr} and the wave heating Γ_w (Eq. 3.31). See Table 3.6 for details.

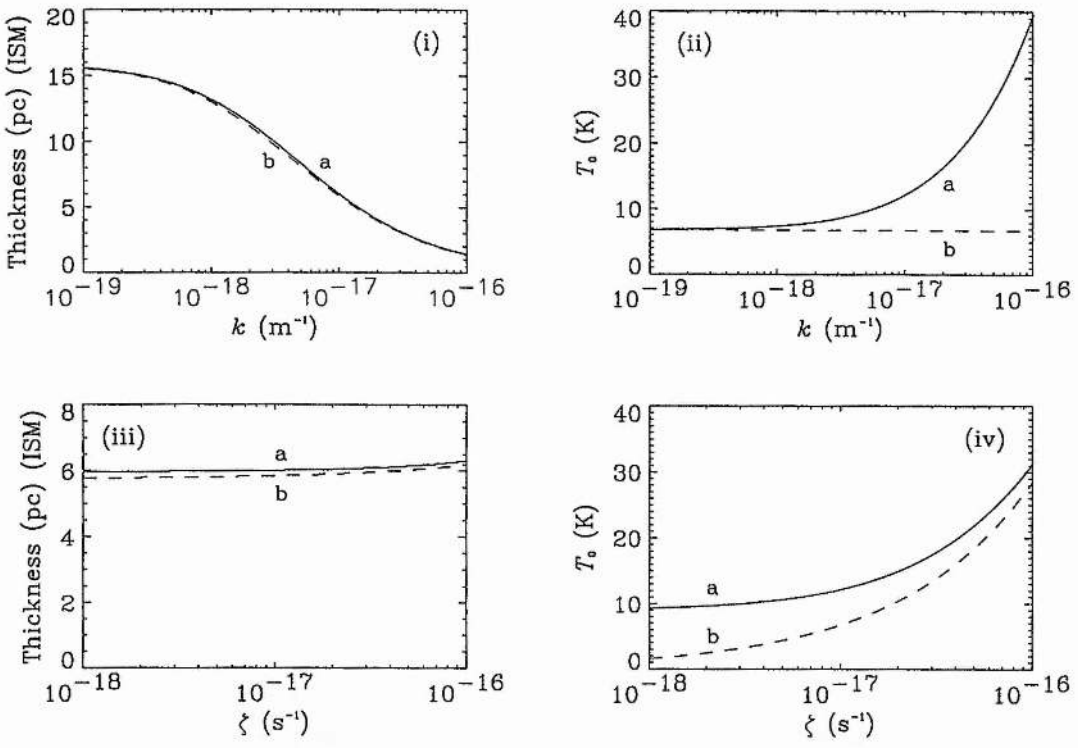

Figure 3.13: The thickness and central temperature T_0 of a gas layer with central wave energy density $U_0 = 9.98 \times 10^{-13}$ J m^{-3} for (i), (ii) varying values of the damping parameter (k) with a cosmic-ray ionization rate $\zeta = 10^{-17}$ s^{-1}, and (iii), (iv) varying values of the cosmic-ray ionization rate (ζ) with a damping $k = 10^{-17}$ m^{-1}. The curves are plotted (a) in the presence of wave heating ($\Gamma_w \neq 0$) and (b) in the absence of wave heating ($\Gamma_w = 0$).

k reaches its strongest value, the actual extent of the cloud is altered very little by the inclusion or exclusion of Γ_w. It can also be observed that very weak values of the damping, $k \approx 10^{-19}$ m^{-1}, minimise the significance of including the wave heating in the thermal equilibrium. A similar effect is apparent when the cosmic-ray ionization rate is increased to higher values, as can be seen in Figure 3.13(ii).

In order to directly compare the results generated by including and excluding the Alfvén wave heating (Γ_w) the central temperatures and thicknesses of the model clouds have been drawn together in Table 3.7. This comparison shows that for a typical damping k and cosmic-ray ionization rate ζ, including Γ_w in the thermal equilibrium has significantly influenced the properties of the model clouds, particularly as the Alfvén wave support is improved (the central wave energy density U_0 is increased).

ρ_0 (kg m^{-3})	U_0 (J m^{-3})	Central Temperature T_0 (K)		Thickness (pc) (ISM)	
		$\Gamma_w = 0$	$\Gamma_w \neq 0$	$\Gamma_w = 0$	$\Gamma_w \neq 0$
1.59×10^{-18}	9.52×10^{-13}	6.76	8.70	4.05	4.18
8.33×10^{-19}	9.98×10^{-13}	6.72	12.15	5.83	6.00
5.64×10^{-19}	1.01×10^{-12}	6.69	16.59	6.97	7.16
4.27×10^{-19}	1.02×10^{-12}	6.65	21.98	7.81	8.01

Table 3.7: The thickness and central temperature (T_0) of the gas layer in the absence of wave heating ($\Gamma_w = 0$), and in the presence of wave heating ($\Gamma_w \neq 0$) for a cosmic-ray ionization rate $\zeta = 10^{-17}$ s^{-1}, damping $k = 10^{-17}$ m^{-1} and increasing values of the central wave energy density (U_0).

The most important effect is on the structure of the temperature profile with height, as can be seen in Figure 3.14. In the absence of wave heating the temperature throughout the layer remains approximately constant (as in the isothermal model) at ~ 7 K; switching on the wave heating results in a greater central temperature and an overall increase in temperature from the central regions to the edge of the cloud. These higher temperatures enhance the gas pressure which is acting to support the layer against its self-gravity and hence slightly increase the thickness of the model cloud.

3.4 Discussion

The work presented in this chapter has discussed aspects of the thermal equilibrium in low-mass star-forming regions, in the presence of an Alfvén wave pressure which is supporting the cloud against its self-gravity. Of particular interest is the role that the Alfvén waves supporting the cloud have in heating the gas. Ultimately, the thermal equilibrium is chosen to be described by the combined cooling of a number of molecular species together with ionized carbon, and the heating generated by cosmic rays and the Alfvén waves. The model shows that neglecting the heating by the waves results in an almost constant temperature throughout the cloud. However, the introduction of wave heating into the thermal equilibrium can have a significant effect on the temperature profile depending upon the relative contributions of each heating mechanism. Within this description the contribution of the cosmic-ray heating is determined by the ionization rate (ζ), while that of the wave heating is given by the central wave energy density (U_0) and, in particular, the damping (k). While the introduction of Alfvén wave heating can cause an initial decrease in the temperature of the model clouds, it is

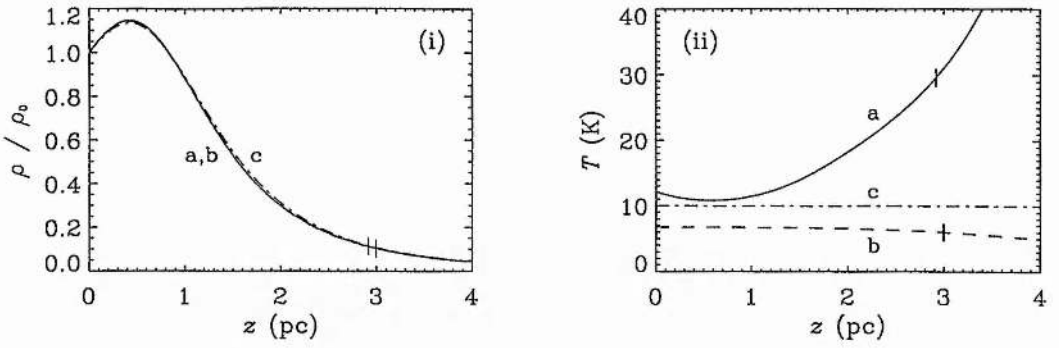

Figure 3.14: The (i) mass density ratio ρ/ρ_0 and (ii) temperature T plotted against the height z for (a) the temperature-dependent model in the presence of wave heating ($\Gamma_w \neq 0$), (b) the temperature-dependent model in the absence of wave heating ($\Gamma_w = 0$) and (c) the isothermal model. The curves are plotted for a central wave energy density $U_0 = 9.98 \times 10^{-13}\,\mathrm{J\,m^{-3}}$, a cosmic-ray ionization rate $\zeta = 10^{-17}\,\mathrm{s^{-1}}$ and damping $k = 10^{-17}\,\mathrm{m^{-1}}$. The vertical line on each profile marks the edge of the cloud as given by the ISM pressure.

shown to generate a substantially higher temperature at the edge of the layer than in the central regions. This overall difference in temperature is deduced, from the results of the temperature-dependent model, to be a factor of ~ 2; the central temperatures are $\sim 10 - 20\,\mathrm{K}$ while the temperatures at the edge of the layer are found to be $\sim 25 - 35\,\mathrm{K}$ for the typical parameters considered here. These temperatures are higher than the observed values although given the approximate nature of the cooling, particularly at low number densities (see Section 3.1), a strict comparison with the observations is not viable.

It is important to note that the initial decrease in temperature is a result of the increase in mass density away from the central plane, which was shown in Chapter 2 to be an artefact of assuming a central source plane. If a distribution of sources is considered then the symmetry of the model about the central plane of the gas layer would in fact preclude any contribution from the wave heating to the central temperature[2], which is therefore determined solely by the cosmic-ray heating and the cooling.

[2]In Section 1.1 the wave heating was shown to be described by the expression (Eq. 3.3)

$$\Gamma_w = -\frac{B_0}{\sqrt{\mu}}\frac{d}{dz}\left(\frac{U}{\sqrt{\rho}}\right).$$

If there is a density-dependent distribution of wave sources then both the wave energy density and mass density are symmetric about the central plane ($z = 0$) and thus $\Gamma_w(z = 0) = 0$.

Thus the introduction of this form of wave support and subsequent wave heating would generate no decrease in temperature away from the central plane but simply a gradual increase with height, upwards from values of ~ 7 K (see Section 3.3). In comparison to the temperature profiles associated with just cosmic-ray heating, which have been shown to be almost constant, there would still be an increase in temperature towards the outer regions of the cloud. In the work of McKee & Zweibel (1995) the wave pressure supporting the cloud was modelled by a polytropic equation of state (Chapter 1, Section 3.1). By assuming hydrostatic equilibrium (a constant total pressure) they concluded that a molecular cloud supported by Alfvén waves should be hotter on the outside than on the inside. This deduction is in agreement with the results of the self-consistent model described in this chapter, which suggest a factor of approximately two increase in temperature through the model clouds.

In the general context of heating the molecular gas by the dissipation of magnetohydrodynamic waves it is important to regard those waves which do not support the cloud but which nevertheless will be generated by the motions of the gas. As discussed in Chapter 1, Zweibel & Josafatsson (1983) showed that compressive waves and waves with shorter wavelengths, particularly those which propagate perpendicular to the magnetic field, will rapidly dissipate into shocks and subsequently heat the gas. This wave damping will provide a local heating mechanism in the vicinity of the wave sources, probably in the central regions of the cloud. As mentioned in Section 1.1, the very low-energy cosmic rays travelling through the cloud can be scattered by magnetic waves and in this manner actually shield some regions of the gas from these charged particles (Cesarsky & Völk 1978; Farquhar et al. 1994). This shielding will be more efficient in regions where there are more waves which are resonantly excited by the cosmic rays (Cesarsky & Völk 1978), perhaps close to the wave sources. Nevertheless, while these regions may have a slight reduction in the cosmic-ray heating they will have the additional local heating attributed to the damping of waves close to the source.

In summary, it has been shown that the Alfvén waves can be an important global heating mechanism. A low-mass star-forming region supported against its self-gravity by these waves will have temperatures at the edge of the cloud which are higher than those found in the central regions.

Chapter 4

A non-WKB model of Alfvén wave support

Only two things are infinite, the universe and human stupidity, and I'm not sure about the former.

Albert Einstein

The WKB approximation is an asymptotic method for solving differential equations which contain a large parameter. For wave equations in a non-uniform medium it can be applied when the medium varies over a scale much larger than the wavelength of the waves propagating within the medium (see also Chapter 2 and Appendix A). In the case of low-mass star-forming regions this assumption may not always hold true and thus it is important to consider the role of Alfvén wave support in the absence of this assumption.

As discussed in Chapter 1 (Section 1.4), in order for the Alfvén waves to be able to provide support to the whole cloud and not just the ionic component, there needs to be very good coupling between the ions and the neutrals through ion-neutral friction. This results in a minimum period for the Alfvén waves of $\sim 10^5$ yr which when combined with a typical Alfvén speed of $\sim 4.5\,\mathrm{km\,s^{-1}}$ gives a wavelength of $\sim 0.5\,\mathrm{pc}$. Given that low-mass star-forming regions have radii of a few parsecs ($\sim 2 - 5$ pc; Shu et al. 1987) the wavelength of these waves is clearly not much smaller than the scale-length over which the clouds vary. Thus, examining the role of long-wavelength Alfvén waves in supporting a low-mass star-forming region against its self-gravity, parallel to its ordered magnetic field, is extremely valuable and will be considered in detail in this chapter.

4.1 The model

In detail, this non-WKB model is described by

mass density:	$\rho = \rho(z)$
gravity:	$\mathbf{g} = -g(z)\,\hat{\mathbf{z}}$
velocity:	$\mathbf{v} = v_x(z,t)\,\hat{\mathbf{x}} + v_y(z,t)\,\hat{\mathbf{y}}$
magnetic field:	$\mathbf{B} = B_0\,\hat{\mathbf{z}} + b_x(z,t)\,\hat{\mathbf{x}} + b_y(z,t)\,\hat{\mathbf{y}}$
pressure:	$P = \rho(z)\,c^2$

where all of the gradients are taken to be in the z-direction. It is assumed to be isothermal, with a sound speed c, and in the perfectly conducting limit. The velocity perturbation together with the subsequent magnetic field perturbation, is taken to be Alfvénic and circularly polarised in nature, viz:

$$\mathbf{v} = v(z)\cos\left(\omega t - \phi_2(z)\right)\hat{\mathbf{x}} + v(z)\sin\left(\omega t - \phi_2(z)\right)\hat{\mathbf{y}}\,,$$

$$\mathbf{b} = b(z)\cos\left(\omega t - \phi_1(z)\right)\hat{\mathbf{x}} + b(z)\sin\left(\omega t - \phi_1(z)\right)\hat{\mathbf{y}}\,, \tag{4.1}$$

where ω is the frequency, v, b are the respective amplitudes and ϕ_2, ϕ_1 are the respective phases. Such perturbations do not induce any compression in the gas. It is assumed that all of the wave sources lie in a central source plane, and that the damping of the waves is by the linear process of ion-neutral friction.

Relation to the WKB model

The model discussed above is directly equivalent to that outlined for the WKB work (see Chapter 2) in all aspects except the description of the velocity and magnetic field perturbations. These perturbations are defined as Alfvénic and linearly polarised within the WKB regime, but as Alfvénic and circularly polarised in this non-WKB model. The linearly polarised waves are described by an equation of the form

$$\mathbf{v} = v(z,t)\,\hat{\mathbf{x}} = \Re\left\{\mathcal{V}(z)\,\mathrm{e}^{-i\phi(z)}\,\mathrm{e}^{i\omega t}\,\hat{\mathbf{x}}\right\}$$

$$\mathbf{b} = b(z,t)\,\hat{\mathbf{x}} = \Re\left\{\mathcal{B}(z)\,\mathrm{e}^{-i\phi(z)}\,\mathrm{e}^{i\omega t}\,\hat{\mathbf{x}}\right\}$$

(Chapter 2, Section 2.2), where $\mathcal{V}$ and $\mathcal{B}$ are the amplitudes, ω is the frequency and ϕ is the phase. In comparison it is possible to write Equation (4.1), describing the circularly polarised waves, as

$$\mathbf{v} = \Re\left\{v(z)\,\mathrm{e}^{i(\omega t - \phi_2(z))}\,\hat{\mathbf{n}}\right\}$$

$$\mathbf{b} = \Re\left\{b(z)\, e^{i(\omega t - \phi_1(z))}\, \hat{\mathbf{n}}\right\}, \tag{4.2}$$

where $\hat{\mathbf{n}} = \hat{\mathbf{x}} - i\hat{\mathbf{y}}$ is a complex unit vector in the xy-plane. These descriptions of the waves illustrate the equivalence between the models used in the WKB and non-WKB regimes.

4.2 The equations

The magnetohydrodynamic equation of motion in this one-fluid model (Eq. 1.15), including gravity and damping, is

$$\rho \frac{\partial \mathbf{v}}{\partial t} + \rho\,(\mathbf{v}\cdot\nabla)\,\mathbf{v} = -\nabla P + \frac{1}{\mu}(\mathbf{B}\cdot\nabla)\,\mathbf{B} - \nabla\left(\frac{B^2}{2\mu}\right) + \rho\mathbf{g} - \Gamma\rho\mathbf{v}, \tag{4.3}$$

where ρ is the mass density, $\mathbf{v}$ is the velocity, P is the gas pressure, $\mathbf{B}$ is the magnetic field, μ is the magnetic permeability of free space, $\mathbf{g}$ is the gravity and Γ is the damping rate which, for this model, is assumed to be a constant. The induction equation in the perfectly conducting limit (Eq. 1.16) is

$$\frac{\partial \mathbf{B}}{\partial t} = \nabla \times (\mathbf{v} \times \mathbf{B})\,. \tag{4.4}$$

Within the context of this model, for wave periods which are shorter than the characteristic free-fall time (Chapter 1, Section 1.4), the time-averaged equation of motion is given by

$$0 = -c^2 \frac{d\rho}{dz} - \frac{\partial}{\partial z}\frac{\left\langle b_x^2 + b_y^2\right\rangle}{2\mu} - \rho g\,. \tag{4.5}$$

It describes the mechanical equilibrium in the isothermal gas sheet between the gas pressure, the Alfvén wave pressure and the gravity. The x- and y-components of the linearised equation of motion and the equation of induction (Eq. 4.4) are

$$\rho \frac{\partial \mathbf{v}}{\partial t} = \frac{B_0}{\mu}\frac{\partial \mathbf{b}}{\partial z} - \Gamma\rho\mathbf{v} \tag{4.6}$$

and

$$\frac{\partial \mathbf{b}}{\partial t} = B_0 \frac{\partial \mathbf{v}}{\partial z}, \tag{4.7}$$

respectively.

Given that it is the magnetic field perturbation which appears in Equation (4.5) it would be ideal to eliminate the velocity perturbation ($\mathbf{v}$) between Equations (4.6) and (4.7). It is possible to do this by writing these perturbations in the form

$$\mathbf{b} = \Re\left\{b(z)\, e^{i(\omega t - \phi_1(z))}\, \hat{\mathbf{n}}\right\}, \tag{4.8}$$

where $\hat{\mathbf{n}}$ is a complex unit vector in the xy-plane (see previous section). Taking 'real' and 'imaginary' components within this description of the circularly polarised waves is equivalent to taking 'sine' and 'cosine' components within the description given by Equation (4.1), given that the amplitude of the waves is real. Thus the velocity and magnetic field perturbations are now written as

$$\mathbf{b} = b_\phi(z)\, \mathrm{e}^{i\omega t}\, \hat{\mathbf{n}} \qquad \text{and} \qquad \mathbf{v} = v_\phi(z)\, \mathrm{e}^{i\omega t}\, \hat{\mathbf{n}}$$

and substituted into Equation (4.6) to give

$$v_\phi = \frac{B_0}{\mu\,(i\omega + \Gamma)\,\rho}\,\frac{db_\phi}{dz}\,. \tag{4.9}$$

In turn, substituting these expressions into Equation (4.7) leaves

$$b_\phi + \left(1 + i\,\frac{\Gamma}{\omega}\right)\frac{d}{dz}\left[\frac{v_A^2}{\Gamma^2+\omega^2}\,\frac{db_\phi}{dz}\right] = 0\,, \tag{4.10}$$

where $v_A^2 = B_0^2/\mu\rho$ is the square of the Alfvén speed. Expanding this equation using

$$b_\phi = b(z)\, \mathrm{e}^{-i\phi(z)} \tag{4.11}$$

(where having eliminated the velocity perturbation $\phi(z) \equiv \phi_1(z)$) gives a real part

$$b + \frac{d}{dz}\left(F\,\frac{db}{dz}\right) + \frac{\Gamma}{\omega}\,\frac{1}{b}\,\frac{d}{dz}\left(Fb^2\phi'\right) - Fb\phi'^2 = 0\,, \tag{4.12}$$

and an imaginary part

$$\frac{\Gamma}{\omega}\,\frac{d}{dz}\left(F\,\frac{db}{dz}\right) - \frac{1}{b}\,\frac{d}{dz}\left(Fb^2\phi'\right) - \frac{\Gamma}{\omega}\,Fb\phi'^2 = 0\,, \tag{4.13}$$

where $F = v_A^2/(\Gamma^2+\omega^2)$. Simply adding and subtracting these two equations, after multiplying each in turn by a factor of Γ/ω, gives

$$\frac{B_0^2}{\mu\omega^2}\,\frac{d}{dz}\left(\frac{1}{\rho}\,\frac{db}{dz}\right) + \left(1 - \frac{B_0^2}{\mu\omega^2}\,\frac{k^2}{\rho}\right) b = 0 \tag{4.14}$$

and

$$\frac{B_0^2}{\mu\omega^2}\,\frac{d}{dz}\left(\frac{b^2 k}{\rho}\right) + \frac{\Gamma}{\omega}\,b^2 = 0\,, \tag{4.15}$$

where $k \equiv d\phi/dz$, which are two equations describing the propagation of the waves through the system. Note that the second term in Equation (4.15) is the only term to contain the constant damping.

Completing the set of equations describing the model are the mechanical equilibrium equation (Eq. 4.5) which, given that

$$\begin{aligned}\left\langle b_x^2 + b_y^2 \right\rangle &= b^2(z) \left\langle \cos^2(\omega t - \phi_1(z)) + \sin^2(\omega t - \phi_1(z)) \right\rangle \\ &= b^2(z)\,, \end{aligned} \tag{4.16}$$

becomes

$$\frac{d}{dz}\left(\rho c^2 + \frac{b^2}{2\mu}\right) = -\rho g\,, \tag{4.17}$$

(note that this equation is identically equal to the z-component of the equation of motion (Eq. 4.3)); and the self-gravitation equation

$$\frac{dg}{dz} = 4\pi G\rho\,, \tag{4.18}$$

where G is the gravitational constant.

Equations (4.14), (4.15), (4.17) and (4.18) are now made dimensionless according to,

$$\begin{aligned} \tilde{\rho} &= \frac{\rho}{\rho_0} \\ \zeta &= \frac{z}{H}\,, \qquad\qquad \text{where} \quad H = \sqrt{\frac{c^2}{2\pi G\rho_0}} \\ \tilde{g} &= \frac{g}{g_b} \\ \tilde{k} &= k\lambda_0 = \frac{k v_{A_0}}{\omega} \\ \tilde{b} &= \frac{b}{B_0}\,, \end{aligned}$$

where ρ_0 is the mass density at the central plane ($z = 0$), H is a scale height, g_b is the gravity at the edge of the cloud ($z \to \infty$), v_{A_0} is the Alfvén speed at the central plane ($z = 0$), ω is the frequency and B_0 is the uniform background magnetic field. This gives the complete set of equations as

$$\frac{d}{d\zeta}\left(\frac{1}{\tilde{\rho}}\frac{d\tilde{b}}{d\zeta}\right) = \delta\left(\frac{\tilde{k}^2}{\tilde{\rho}} - 1\right)\tilde{b} \tag{4.19}$$

$$\frac{d}{d\zeta}\left(\frac{\tilde{b}^2\tilde{k}}{\tilde{\rho}}\right) = -\epsilon\sqrt{\delta}\,\tilde{b}^2 \tag{4.20}$$

$$\frac{d}{d\zeta}\left(\tilde{\rho} + \frac{\tilde{b}^2}{2\beta}\right) = -2\sqrt{\alpha}\,\tilde{\rho}\tilde{g} \tag{4.21}$$

$$\frac{d\tilde{g}}{d\zeta} = \frac{\tilde{\rho}}{\sqrt{\alpha}}\,, \tag{4.22}$$

where the dimensionless parameters are

$$\alpha = \frac{g_b^2}{8\pi G \rho_0 c^2}$$

$$\beta = \frac{c^2}{v_{A_0}^2}$$

$$\delta = \frac{\omega^2 H^2}{v_{A_0}^2}$$

$$\epsilon = \frac{\Gamma}{\omega}.$$

A typical low-mass star-forming region has a column density of $\mathcal{M} \sim 10^{-1}\,\mathrm{kg\,m^{-2}}$, a temperature $T \sim 10\,\mathrm{K}$ (implying a sound speed of $c \sim 0.2\,\mathrm{km\,s^{-1}}$) and a number density $n_{H_2} \sim 10^9\,\mathrm{m^{-3}}$ ($\sim 10^3\,\mathrm{cm^{-3}}$). Such values give the parameter $\alpha \sim 5$, which in effect represents the physical properties of the cloud. A typical Alfvén speed is determined to be $v_A \sim 4.5\,\mathrm{km\,s^{-1}}$ and as such $\beta \sim 10^{-3}$. This parameter represents the importance of the magnetic field compared to the isothermal gas pressure within the cloud dynamics. The third dimensionless parameter is δ and basically represents a *WKB approximation parameter*; increasing the value of δ reduces the significance of the second-order derivative in Equation (4.19), in effect re-introducing the WKB approximation. For a scale height $H \sim 0.2\,\mathrm{pc}$ and a frequency $\omega \sim 5 \times 10^{-13}\,\mathrm{s^{-1}}$, this parameter takes a value of $\delta \sim 10^{-1}$. The final dimensionless parameter ϵ is the *damping parameter*. In Chapter 1, Section 1.4 the damping rate (Γ) is shown to be

$$\Gamma = \frac{1}{2}\frac{\omega^2}{\xi \rho_n \gamma}$$

(Eq. 1.55) where ξ is the ionisation fraction, ρ_n is the mass density of the neutrals and γ is a drag coefficient (Draine et al. 1983; Shu et al. 1987). This expression allows the damping parameter to be written as

$$\epsilon = \frac{\Gamma}{\omega} = \frac{1}{2}\frac{\omega}{\omega_{max}}, \tag{4.23}$$

where $\omega_{max} = \xi \rho_n \gamma$ (Eq. 1.49) is the maximum frequency the Alfvén waves can have whilst still allowing some coupling between the electric and neutral components of the molecular cloud. Thus there is a maximum value for the damping parameter of $\epsilon = 0.5$. The minimum value the wave frequency can take — determined from the condition that the wavelength of the Alfvén wave must be less than the radius of the cloud (see Chapter 1, Section 1.4) — suggests a lower limit on the value of this dimensionless parameter of $\epsilon \sim 0.1$. Note that the higher values of ϵ correspond to stronger damping.

Examining the set of equations (Eqs 4.19 – 4.22) shows that there is no explicit dependence on the independent variable ζ. Thus it is possible to rewrite these equations by taking the gravity ($\tilde{g}$) as the independent variable. Such a description allows the equation of mechanical equilibrium (Eq. 4.21) to be integrated to give

$$\tilde{\rho} + \frac{\tilde{b}^2}{2\beta} = -\alpha\tilde{g}^2 + C\,, \tag{4.24}$$

where the integration constant C is determined from the boundary conditions (see Section 4.2.1); and leaves the remaining equations (Eqs 4.19, 4.20 and 4.22) as

$$\frac{d^2\tilde{b}}{d\tilde{g}^2} = \alpha\delta\left(\frac{\tilde{k}^2}{\tilde{\rho}} - 1\right)\frac{\tilde{b}}{\tilde{\rho}} \tag{4.25}$$

$$\frac{d}{d\tilde{g}}\left(\frac{\tilde{b}^2\tilde{k}}{\tilde{\rho}}\right) = -\sqrt{\alpha\delta}\,\epsilon\,\frac{\tilde{b}^2}{\tilde{\rho}} \tag{4.26}$$

$$\frac{d\zeta}{d\tilde{g}} = \frac{\sqrt{\alpha}}{\tilde{\rho}}\,. \tag{4.27}$$

Relation to the WKB model

It is useful to note how the dimensionless parameters α, β, δ and ϵ incorporated within the equations (Eqs 4.19 – 4.22; or Eqs 4.24 – 4.27) relate back to those used to parameterise the WKB model (Chapter 2). In the WKB regime the two parameters used are the magnetisation parameter

$$\lambda = \frac{U_0}{\rho_0 c^2}$$

(Eq. 2.30), which represents the ratio between the wave pressure (U) and the isothermal gas pressure (ρc^2) at the central plane ($z = 0$), and the damping parameter k (Chapter 2, Section 2.3.2). The parameter λ can be described in terms of α and β by

$$\lambda = 37.97\,\beta\alpha(\alpha - 1)\left(\frac{\mathcal{M}}{10^{-1}\,\mathrm{kg\,m^{-2}}}\right)^{-2}\left(\frac{B}{10\,\mathrm{nT}}\right)^{2}, \tag{4.28}$$

and the damping parameters are related through the expression

$$k = 4.38\times10^{-16}\epsilon\left(\frac{n_{H_2}}{10^{9}\,\mathrm{m^{-3}}}\right)^{\frac{1}{2}}\left(\frac{\tau}{10^{5}\,\mathrm{yr}}\right)^{-1}\left(\frac{B}{10\,\mathrm{nT}}\right)^{-1}, \tag{4.29}$$

where $\mathcal{M}$ is the column density, B is the magnetic field strength, n_{H_2} is the number density and τ is the period of the Alfvén waves. Note that in the WKB model the parameter δ is effectively set equal to infinity.

4.2.1 Boundary conditions

A set of five independent ordinary differential equations describe this model of long-wavelength Alfvén wave support. The first of these is the wave propagation equation (Eq. 4.19) which can be written as the two first-order equations

$$\frac{d\tilde{b}}{d\zeta} = w\tilde{\rho} \tag{4.30}$$

and

$$\frac{dw}{d\zeta} = \delta\left(\frac{\tilde{k}^2}{\tilde{\rho}} - 1\right)\tilde{b}, \tag{4.31}$$

by applying the substitution $w = (1/\tilde{\rho})\, d\tilde{b}/d\zeta$. The remaining equations describe the variation of the wave amplitude with height (Eq. 4.20)

$$\frac{d}{d\zeta}\left(\frac{\tilde{b}^2\tilde{k}}{\tilde{\rho}}\right) = -\epsilon\sqrt{\delta}\,\tilde{b}^2,$$

the mechanical equilibrium of the system (Eq. 4.21)

$$\frac{d}{d\zeta}\left(\tilde{\rho} + \frac{\tilde{b}^2}{2\beta}\right) = -2\sqrt{\alpha}\,\tilde{\rho}\tilde{g}$$

and finally, the self-gravitation (Eq. 4.22)

$$\frac{d\tilde{g}}{d\zeta} = \frac{\tilde{\rho}}{\sqrt{\alpha}}.$$

This fifth-order system of equations, which relates the five dependent variables — the mass density $\tilde{\rho}$, the gravity $\tilde{g}$, the wavenumber $\tilde{k}$, the wave amplitude $\tilde{b}$ and w — to the height ζ, requires five independent boundary conditions.

The amplitude equation (Eq. 4.20) can be expanded and multiplied through by the square of the mass density to give

$$\tilde{\rho}\,\frac{d}{d\zeta}\left(\tilde{b}^2\tilde{k}\right) - \tilde{b}^2\tilde{k}\,\frac{d\tilde{\rho}}{d\zeta} = -\epsilon\sqrt{\delta}\,\tilde{b}^2\tilde{\rho}^2. \tag{4.32}$$

As the height above the central plane increases ($\zeta \to \infty$) the mass density decreases to zero ($\tilde{\rho} \to 0$) and so the amplitude equation (Eq. 4.32) states that

$$\tilde{b}^2\tilde{k} \to 0 \quad \text{as} \quad \zeta \to \infty$$

i.e. either the amplitude $\tilde{b} \to 0$ or the derivative of the phase $\tilde{k} \to 0$ or both variables tend towards zero. In the absence of damping the wave flux, which goes as the wave energy density ($\propto \tilde{b}^2$) multiplied by the Alfvén speed (v_A), is a conserved quantity. For

this condition to be satisfied as $\zeta \to \infty$, and hence $v_A \to \infty$, the wave amplitude $\tilde{b}$ must decrease to zero ($\tilde{b} \to 0$). Introducing the damping into the problem simply adds a sink term to the amplitude equation and as such $\tilde{b} \to 0$ is still valid.

The derivative of the phase ($\tilde{k}$) has no restriction placed on it either by the physics of the model or by the set of equations describing the model and as such may be taken to have an arbitrary value at the central plane. This can be illustrated by considering the case without damping, where Equation (4.20) allows $\tilde{k}$ to be eliminated in favour of an integration constant (see also Section 4.3.1). However there is one special case to note: at the central plane the value $\tilde{k}_0 = 1$ implies that the dimensional variable $k_0 = \omega/v_{A_0}$, and thus at $\zeta = 0$ the equations describing the model (Eqs 4.19 – 4.22; or Eqs 4.24 – 4.27) simply reduce to the WKB equations (see Chapter 2, Section 2.2.1), the second derivative in Equation (4.19) (or Eq. 4.25) equalling zero.

The next variable to be considered is w. Taking Equation (4.19) and integrating over the source (see also Section 4.4),

$$\int_{-\varepsilon}^{+\varepsilon} \frac{d}{d\zeta}\left(\frac{1}{\tilde{\rho}}\frac{d\tilde{b}}{d\zeta}\right) d\zeta - \frac{\omega^2 H^2}{v_{A_0}^2} \int_{-\varepsilon}^{+\varepsilon} \left(\frac{\tilde{k}^2}{\tilde{\rho}} - 1\right) \tilde{b}\, d\zeta = S \int_{-\varepsilon}^{+\varepsilon} \delta(\zeta)\, d\zeta\,, \tag{4.33}$$

where $\delta(\zeta)$ is the delta function of wave sources at the central plane ($\zeta = 0$) and S is the strength of the source, implies that

$$\left[\frac{1}{\tilde{\rho}}\frac{d\tilde{b}}{d\zeta}\right]_{-\varepsilon}^{+\varepsilon} = S\,. \tag{4.34}$$

Note that the integrand in the second term of Equation (4.33) is well behaved and bounded and thus, as can be seen through a Taylor series expansion, the integral is identically equal to zero as $\varepsilon \to 0$. Hence the limit of Equation (4.34) (as $\varepsilon \to 0$), given the symmetry of the model, implies that

$$w_0 = \frac{S}{2}\,, \tag{4.35}$$

i.e. that w_0 is directly related to the strength of the source. It is easy to note the restrictions on the value of this parameter. Firstly, from the mechanical equilibrium equation (Eq. 4.21) it can be seen that

$$\left.\frac{d\tilde{\rho}}{d\zeta}\right|_{\zeta=0} = -\frac{\tilde{b}_0}{\beta}\frac{S}{2}\,. \tag{4.36}$$

Thus, given that the amplitude of the perturbation at the central plane ($\tilde{b}_0$) must be positive, the strength of the source (S) must also take a positive value in order to avoid an increase in density away from the central plane. Secondly, within this model

all of the sources are located at the central plane; this discontinuous source of waves means that the gradient of the wave amplitude is not continuous through the origin, i.e. $w_0 \neq 0$.

Finally, at the central plane ($\zeta = 0$) the mass density has a value of unity ($\tilde{\rho}_0 = 1$) and the gravity is equal to zero ($\tilde{g}_0 = 0$). Thus the five independent boundary conditions required to solve the equations which describe the model (Eqs 4.19 – 4.22) are

$$\tilde{\rho}_0 = 1$$

$$\tilde{g}_0 = 0$$

$$\tilde{b}(\infty) \rightarrow 0$$

w_0 is known

$\tilde{k}_0$ is known.

Note that if the independent variable is chosen to be the gravity ($\tilde{g}$), and hence the model is formulated using Equations (4.24) – (4.27), the second boundary condition listed above is replaced by $\zeta\,(\tilde{g}=0) = 0$.

By considering the equilibrium equation it is possible to use the third boundary condition ($\tilde{b}(\infty) \rightarrow 0$) to obtain an expression for the wave amplitude at the central plane ($\tilde{b}_0$). Given that $\tilde{\rho} = 1$, $\tilde{g} = 0$ and $\tilde{b} = \tilde{b}_0$ at $\zeta = 0$ the integration constant in Equation (4.24) is

$$C = 1 + \frac{\tilde{b}_0^2}{2\beta}\,,$$

and thus the equation becomes

$$\tilde{\rho} = 1 - \alpha\tilde{g}^2 + \frac{1}{2\beta}\left(\tilde{b}_0^2 - \tilde{b}^2\right)\,. \tag{4.37}$$

As the height increases ($\zeta \rightarrow \infty$), and consequently the mass density $\tilde{\rho} \rightarrow 0$ and the gravity $\tilde{g} \rightarrow 1$, the boundary condition $\tilde{b}(\infty) \rightarrow 0$ shows that

$$\tilde{b}_0 = \sqrt{2\beta\,(\alpha - 1)}\,, \tag{4.38}$$

i.e. the initial value of the magnetic field perturbation is uniquely determined by the properties of the gas cloud (the parameter α) and the importance of the magnetic field within that cloud (the parameter β).

These boundary conditions demonstrate that at the central plane the strength of the wave source (w_0), the derivative of the phase of the wave ($\tilde{k}_0$) and the amplitude of the wave ($\tilde{b}_0$, from parameters α and β) all need to be stipulated in order to determine a solution.

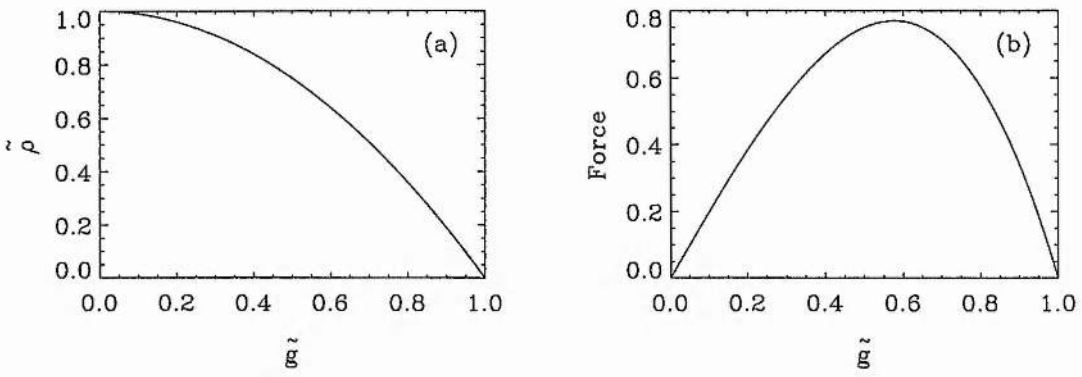

Figure 4.1: (a) Mass density $\tilde{\rho}$ and (b) force acting against gravity $|d/d\zeta(\tilde{\rho} + \tilde{b}^2/2\beta)|$, plotted against gravity $\tilde{g}$ for $\alpha = 1.0001$, $\beta = 10^{-3}$, $\delta = 10^{-1}$, $\tilde{k}_0 = 1.25$ and $w_0 = 10^{-3}$.

The boundary conditions discussed above allow the set of ordinary differential equations describing the model (Eqs 4.19 – 4.22; or Eqs 4.24 – 4.27) to be integrated as an initial-value problem. The following results are presented to the practical limit of numerical accuracy (see Section 4.6.1).

4.3 Results

4.3.1 Without damping

Firstly consider Equations (4.19) – (4.22) with the appropriate boundary conditions, in the absence of damping ($\epsilon = 0$). In this case Equation (4.20) integrates to give

$$\frac{\tilde{b}^2\tilde{k}}{\tilde{\rho}} = f\,, \tag{4.39}$$

where f is a constant representing the wave flux. Substituting this into Equation (4.19) and eliminating the derivative of the phase ($\tilde{k}$), leaves

$$\frac{d}{d\zeta}\left(\frac{1}{\tilde{\rho}}\frac{d\tilde{b}}{d\zeta}\right) = \delta\left(\frac{f^2\tilde{\rho}}{\tilde{b}^4} - 1\right)\tilde{b}\,, \tag{4.40}$$

hence reducing the system of equations by one. Note that the constant $f = \tilde{b}_0^2\tilde{k}_0$ and so the following results will be presented in terms of $\tilde{k}_0$, rather than f, for ease of comparison with the results in the presence of damping ($\epsilon \neq 0$).

Thus the parameter space consists of α, β, δ, $\tilde{k}_0$ and w_0. For a fixed value of the parameter β the amplitude of the magnetic field perturbation ($\tilde{b}_0$), and hence the strength of the Alfvén wave pressure force term in the mechanical equilibrium equation

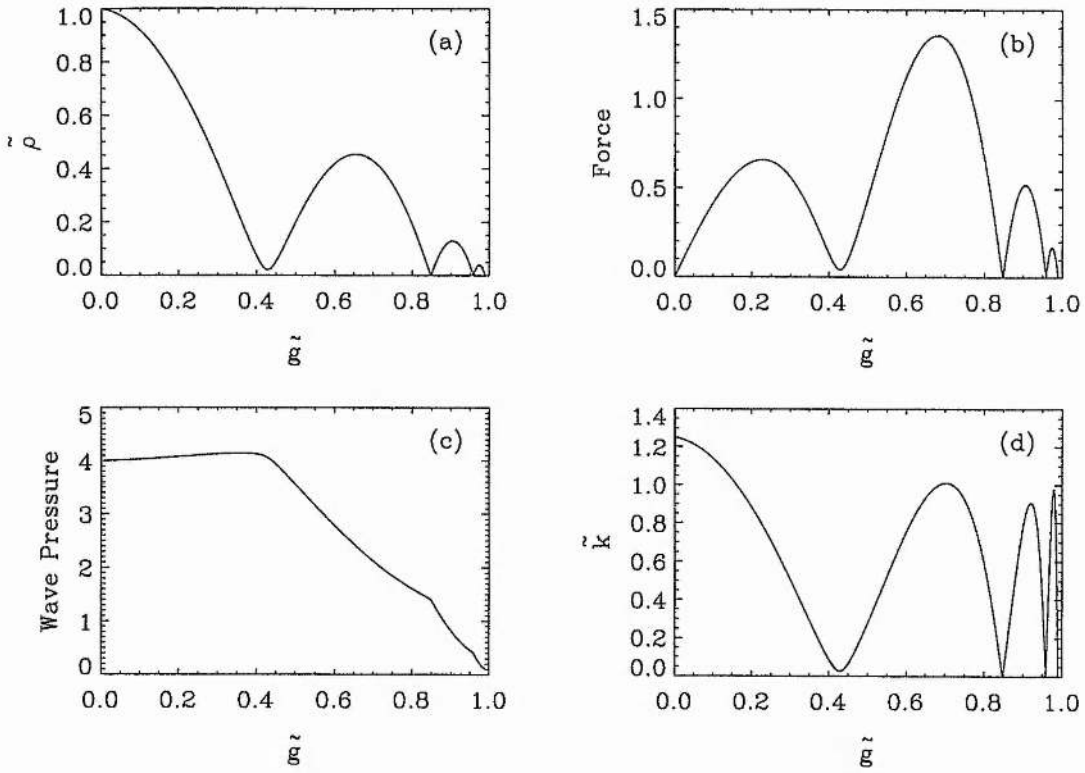

Figure 4.2: (a) Mass density $\tilde{\rho}$, (b) force acting against gravity $|d/d\zeta(\tilde{\rho} + \tilde{b}^2/2\beta)|$, (c) Alfvén wave pressure $\tilde{b}^2/2\beta$ and (d) derivative of the phase $\tilde{k}$, plotted against gravity $\tilde{g}$ for $\alpha = 5$, $\beta = 10^{-3}$, $\delta = 10^{-1}$, $\tilde{k}_0 = 1.25$, and $w_0 = 10^{-3}$.

(Eq. 4.21), is determined by the parameter α. As expected, for low values of this parameter the density profile of the slab is simply that described by the internal gas pressure, the Alfvén waves having no significant effect (see Figure 4.1). In Figure 4.1 the profiles of mass density ($\tilde{\rho}$) and the force acting against gravity ($|d/d\zeta(\tilde{\rho}+\tilde{b}^2/2\beta)|$) have been plotted against the gravity ($\tilde{g}$) rather than the height (ζ). In terms of the height the density profile is simply a sech^2 profile as shown in Figure 1.4 of Chapter 1.

Introducing an Alfvén wave pressure force, by setting the parameter α to a typical value, gives the profiles shown in Figure 4.2. For clarity the corresponding profiles plotted against the dimensionless height (ζ) are shown in Figure 4.3. The sheet has now divided into several subsheets which show a decrease in the maximum mass density the further the subsheet is from the central plane of the cloud ($\zeta = 0; \tilde{g} = 0$), a structure emulated by the profile of the derivative of the phase ($\tilde{k}$) (see Figure 4.2(d)). The force required to support these subsheets against the self-gravity of the layer, shown in

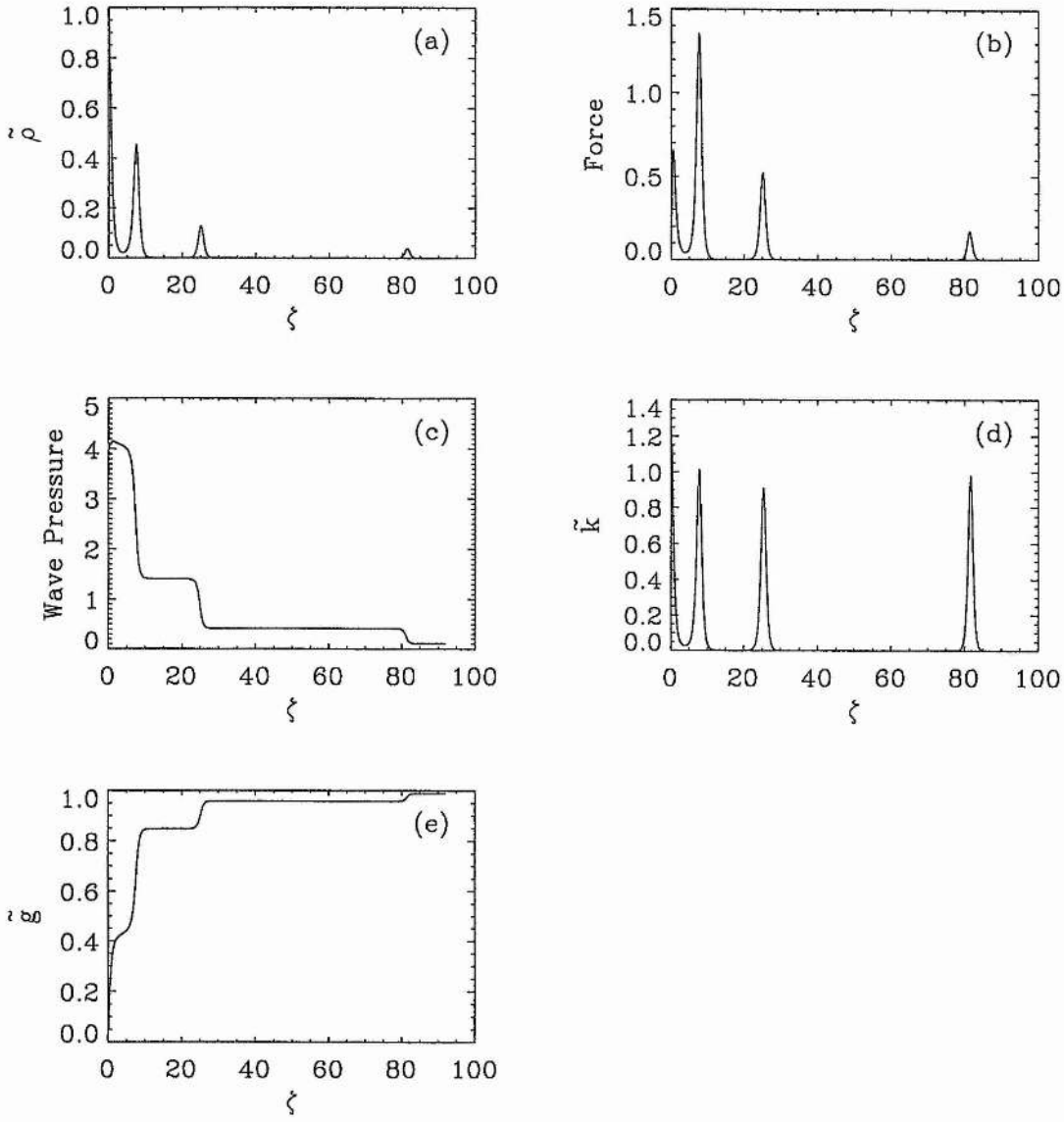

Figure 4.3: (a) Mass density $\tilde{\rho}$, (b) force acting against gravity $|d/d\zeta(\tilde{\rho} + \tilde{b}^2/2\beta)|$, (c) Alfvén wave pressure $\tilde{b}^2/2\beta$, (d) derivative of the phase $\tilde{k}$ and (e) gravity $\tilde{g}$, plotted against height ζ for $\alpha = 5$, $\beta = 10^{-3}$, $\delta = 10^{-1}$, $\tilde{k}_0 = 1.25$, and $w_0 = 10^{-3}$.

Figures 4.2(b) and 4.3(b), increases away from the centre of the layer for those subsheets which represent a substantial fraction of the structure. This correlation is clear given the need to balance the increasing force of gravity. The profiles of the wave pressure ($\tilde{b}^2/2\beta$) and gravity ($\tilde{g}$) with dimensionless height (ζ) are shown in Figures 4.3(c) and 4.3(e) respectively. Both display a step-function-like structure as $\zeta \to 0$ and, correctly, $\tilde{b}^2/2\beta \to 0$ and $\tilde{g} \to 1$ (see Section 4.2.1). The location of the subsheets correlate with the steep changes in gradient observed in these profiles; the change in the wave pressure through such a sheet acts to support it against the self-gravity of the system. Thus the introduction of long-wavelength Alfvén waves into the system has divided the gas layer into distinct subsheets which are held against the gravity of the layer by the Alfvén wave pressure force. It is important to note that such an equilibrium may be subject to a Rayleigh-Taylor type of instability given that the subsheets are essentially being supported by a zero-mass 'material'.

A gas layer in mechanical equilibrium between the isothermal gas pressure and its own self-gravity is described by

$$\frac{\rho}{\rho_0} = \operatorname{sech}^2\left(\frac{z}{H}\right), \tag{4.41}$$

where $H = \sqrt{c^2/2\pi G\rho_0} = c^2/(\pi G\mathcal{M})$ (in the absence of an Alfvén wave pressure) is a scale height and $\mathcal{M}$ is the column density (Spitzer 1968). In terms of the dimensionless variables this expression becomes simply

$$\tilde{\rho} = \operatorname{sech}^2\zeta\,. \tag{4.42}$$

Figure 4.4 shows such pressure supported profiles (solid lines) compared to the density profiles of the first two subsheets seen in Figure 4.3(a) (dashed lines). Note that the dimensionless height (ζ) has been translated to a new variable ζ' defined such that the central peak of the subsheet density profile corresponds to $\zeta' = 0$. These comparisons show that the internal structure of the subsheets, including the central sheet, is simply that given by the internal gas pressure and self-gravity, the Alfvén waves having no significant effect.

It can be observed from Figure 4.4 that the right-hand side of the subsheet density profiles is slightly depressed when compared to the profiles generated by Equation (4.42). This is because the subsheet profiles are not centred around $\tilde{g} = 0$, rather the force of gravity is acting from right to left (positive ζ' to negative ζ') thus moving the profile inward slightly.

In summary, the Alfvén waves do not support the cloud as a whole but provide the global equilibrium of the system, supporting the subsheets against the self-gravity; the

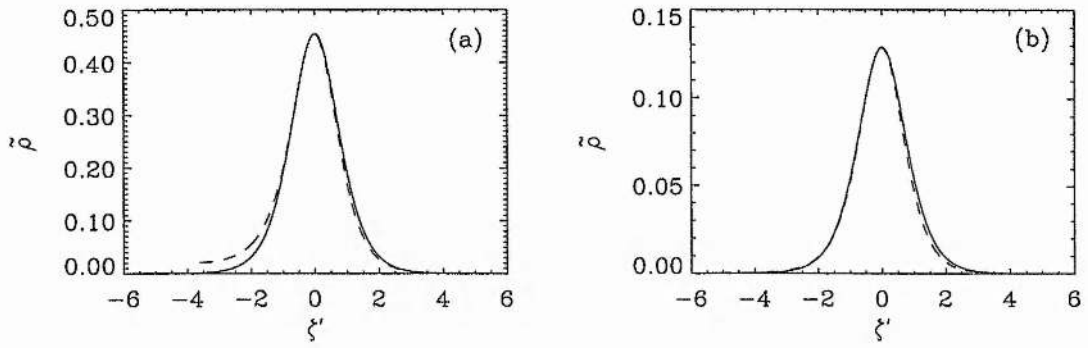

Figure 4.4: The mass density profiles of a gas pressure supported equilibrium (solid lines) compared to the mass density profiles of (a) the first subsheet and (b) the second subsheet seen in Figure 4.3(a) (dashed lines). The horizontal coordinate ζ' is the dimensionless height translated so that the maximum in the mass density of the subsheet is located at $\zeta' = 0$.

equilibrium of the individual subsheets being determined by their internal gas pressure and the gravity.

It is important to see how this situation is affected when the parameters α, β, δ, $\tilde{k}_0$ and w_0 are varied. Firstly consider the parameter α, which can be written as

$$\alpha = 6.82 \left(\frac{\mathcal{M}}{10^{-1}\,\mathrm{kg\,m^{-2}}} \right)^2 \left(\frac{n_{H_2}}{10^9\,\mathrm{m^{-3}}} \right)^{-1} \left(\frac{c}{0.2\,\mathrm{km\,s^{-1}}} \right)^{-2}, \tag{4.43}$$

in terms of the physical properties of the gas layer: the column density ($\mathcal{M}$), the number density at the central plane (n_{H_2}) and the sound speed (c). A slight increase in the column density, say, will increase the parameter α to a significant degree and thus a range of values increasing from $\alpha = 2$ to $\alpha = 50$ have been considered in Figure 4.5. Note that altering the value of α changes the magnetic field perturbation at the central plane ($\tilde{b}_0$) through Equation (4.38); for example $\alpha = 50$ increases the magnitude of the perturbation to approximately a third of the background field (see Table 4.1). Following the evolution of the profiles in Figure 4.5 shows that for higher values of the parameter α the gas layer splits into an increasing number of subsheets. However, for the highest values of α there is also evidence to suggest that the Alfvén wave pressure is able to provide some support to the whole cloud; the mass density is no longer reduced to insignificant values between the subsheets (see Figure 4.5(a)(iv)). Increasing α has increased the value of the magnetic field perturbation and thus enhanced the significance of the gradient in wave pressure, allowing the wave to give some support to the whole gas layer.

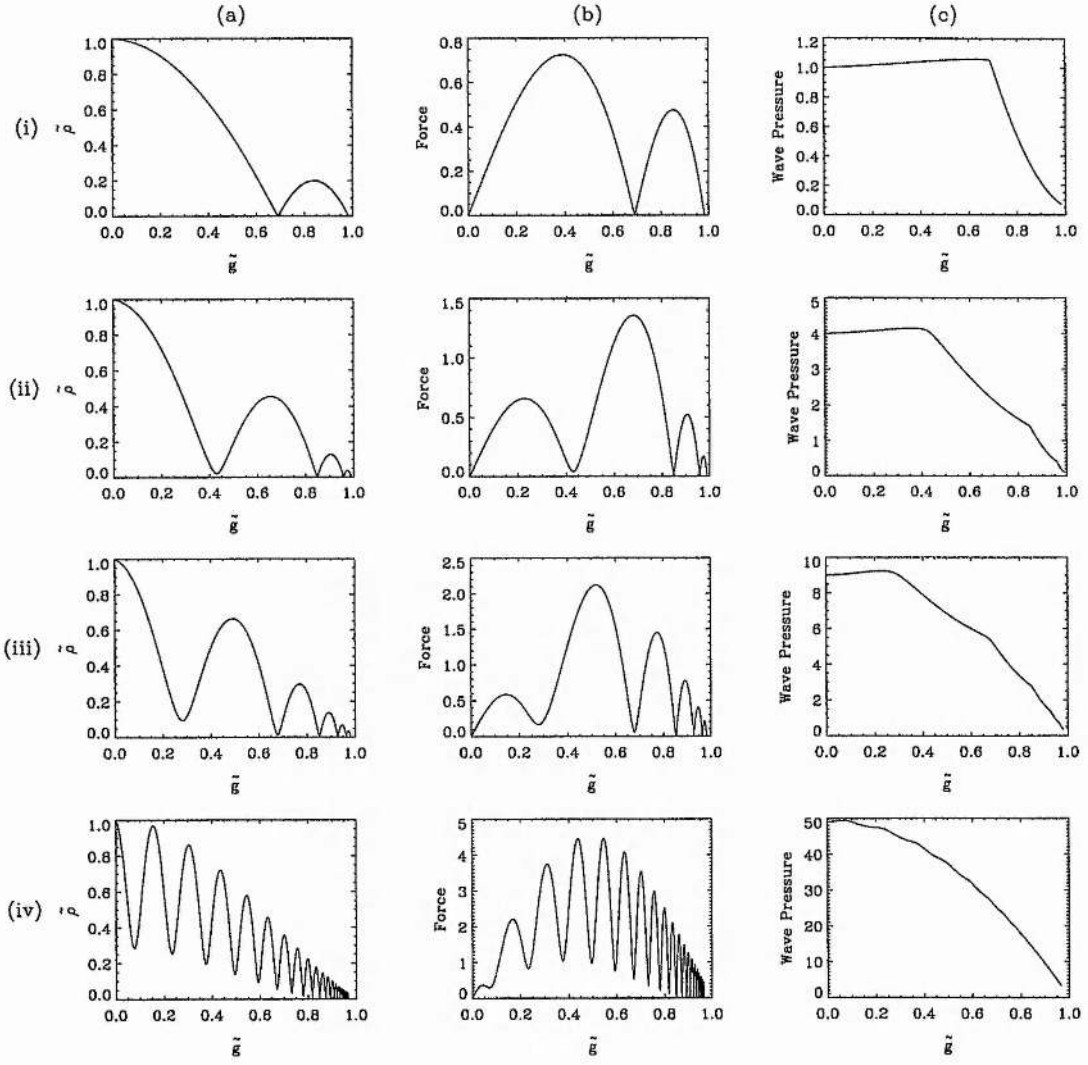

Figure 4.5: (a) Mass density $\tilde{\rho}$, (b) force acting against gravity $|d/d\zeta(\tilde{\rho} + \tilde{b}^2/2\beta)|$ and (c) Alfvén wave pressure $\tilde{b}^2/2\beta$, plotted against gravity $\tilde{g}$ for $\beta = 10^{-3}$, $\delta = 10^{-1}$, $\tilde{k}_0 = 1.25$, $w_0 = 10^{-3}$ and increasing values of the parameter α: (i) 2, (ii) 5, (iii) 10, (iv) 50 (see also Table 4.1).

α	$\tilde{b}_0$	Figure
1.0001	3.16×10^{-4}	4.1
2	4.47×10^{-2}	4.5(i)
5	8.94×10^{-2}	4.5(ii)
10	0.134	4.5(iii)
50	0.313	4.5(iv)

Table 4.1: The value of the magnetic field perturbation at the central plane ($\tilde{b}_0$) for increasing values of the parameter α.

The importance of the gradient of wave pressure over the amplitude of the magnetic field perturbation is evident from the change induced in the profiles by increasing the parameter β, as supposed to α. Naturally, through Equation (4.38), increasing the value of β will markedly increase the magnetic field perturbation (see Table 4.2). However, Figure 4.6 shows that such an increase has very little effect on the profiles of mass density, force acting against gravity and wave pressure. This effect is apparent given that the value of the normalised Alfvén wave pressure at the central plane

$$\frac{\tilde{b}_0^2}{2\beta} = \alpha - 1$$

(from Eq. 4.38), is independent of the value of β.

The effect of varying the initial values of the derivative of the phase ($\tilde{k}_0$) and the strength of the source (w_0) are illustrated in Figures 4.7 and 4.8 respectively. Increasing the value of $\tilde{k}_0$ has split the isothermal layer into an increasing number of distinct subsheets, the mass density falling to insignificant values between the sheets (see Figure 4.7(a)(iii)). In contrast decreasing the value of $\tilde{k}_0$ has increased the dominance of the central subsheet, reducing the amount of mass in subsequent sheets and thus decreasing the amount of Alfvén wave support in the system. However, reducing the value of $\tilde{k}_0$ still further does not remove the subsheet structure entirely, the profiles remain very similar to those given in Figure 4.7(i). Raising the strength of the source is equivalent to steepening the gradient of the wave pressure at the central plane ($\zeta = 0$; $\tilde{g} = 0$). This pushes an increasing amount of mass into the first subsheet, significantly reducing the magnitude of the central sheet (that centred around $\tilde{g} = 0$). As can be seen from Figure 4.8(a)(iv) a very strong source gives the first subsheet a maximum mass density which is greater than that at the central plane.

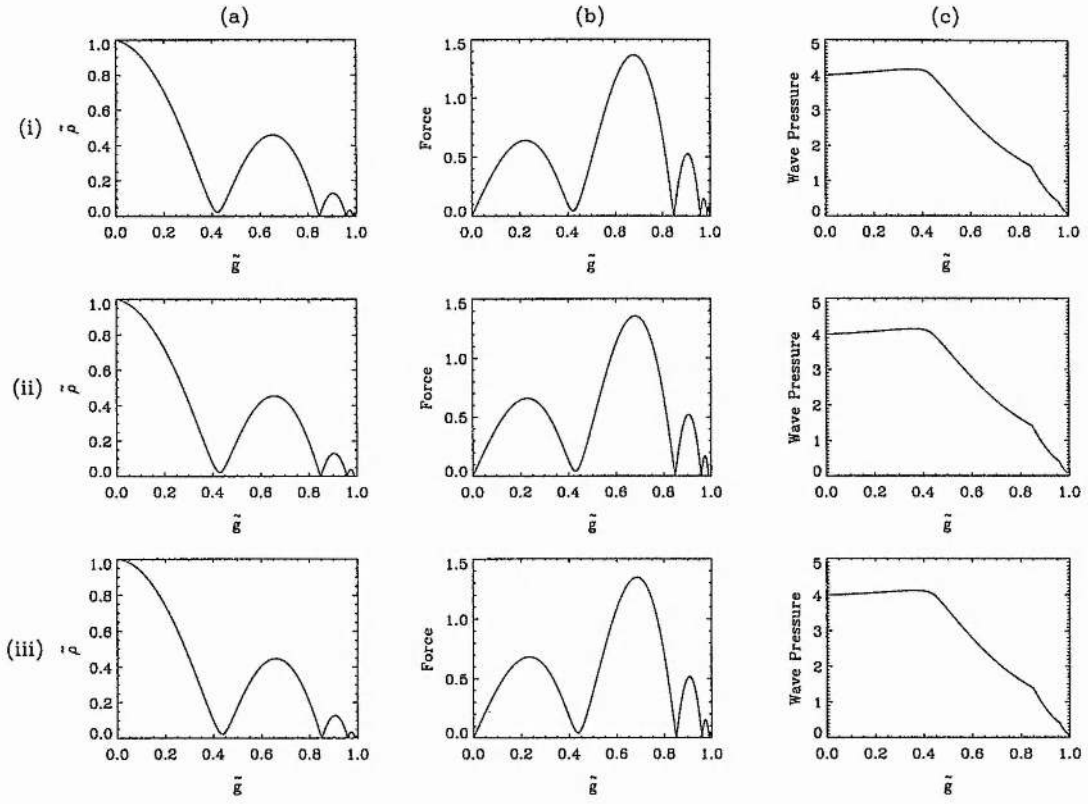

Figure 4.6: (a) Mass density $\tilde{\rho}$, (b) force acting against gravity $|d/d\zeta(\tilde{\rho} + \tilde{b}^2/2\beta)|$ and (c) Alfvén wave pressure $\tilde{b}^2/2\beta$, plotted against gravity $\tilde{g}$ for $\alpha = 5$, $\delta = 10^{-1}$, $\tilde{k}_0 = 1.25$, $w_0 = 10^{-3}$ and increasing values of the parameter β: (i) 5×10^{-4}, (ii) 10^{-3}, (iii) 5×10^{-3}, (see also Table 4.2).

β	$\tilde{b}_0$	Figure
5×10^{-4}	6.32×10^{-2}	4.6(i)
10^{-3}	8.94×10^{-2}	4.6(ii)
5×10^{-3}	0.20	4.6(iii)

Table 4.2: The value of the magnetic field perturbation at the central plane ($\tilde{b}_0$) for increasing values of the parameter β.

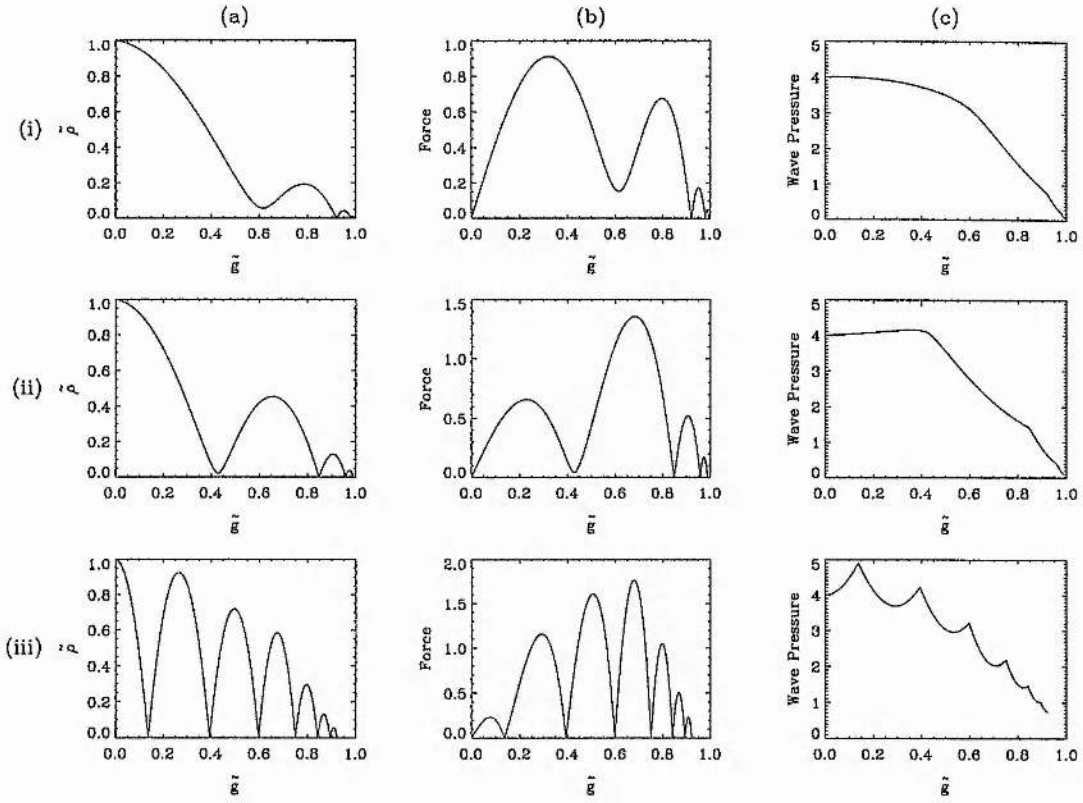

Figure 4.7: (a) Mass density $\tilde{\rho}$, (b) force acting against gravity $|d/d\zeta(\tilde{\rho} + \tilde{b}^2/2\beta)|$ and (c) Alfvén wave pressure $\tilde{b}^2/2\beta$, plotted against gravity $\tilde{g}$ for $\alpha = 5$, $\beta = 10^{-3}$, $\delta = 10^{-1}$, $w_0 = 10^{-3}$ and increasing values of the parameter $\tilde{k}_0$: (i) 0.2, (ii) 1.25, (iii) 5.0.

Approaching the WKB limit

It is important to consider how the set of equations describing this model (Eqs 4.19 – 4.22; or Eqs 4.24 – 4.27) relates back to the WKB regime described in Chapter 2. Within the WKB approximation the second-order derivative in Equation (4.19) (or Eq. 4.25) is neglected, and this limit can be recovered by setting the parameter δ to large values. This parameter is described by

$$\delta = \frac{\omega^2 H^2}{v_{A_0}^2}, \tag{4.44}$$

where ω is the frequency, H is the scale height and v_{A_0} is the Alfvén speed at the central plane ($\zeta = 0$; $\tilde{g} = 0$). Increasing the value of this parameter is equivalent to increasing the frequency of the wave, or reducing the wavelength as compared to the scale height of the cloud, i.e. returning to the WKB regime. Figure 4.9 illustrates the

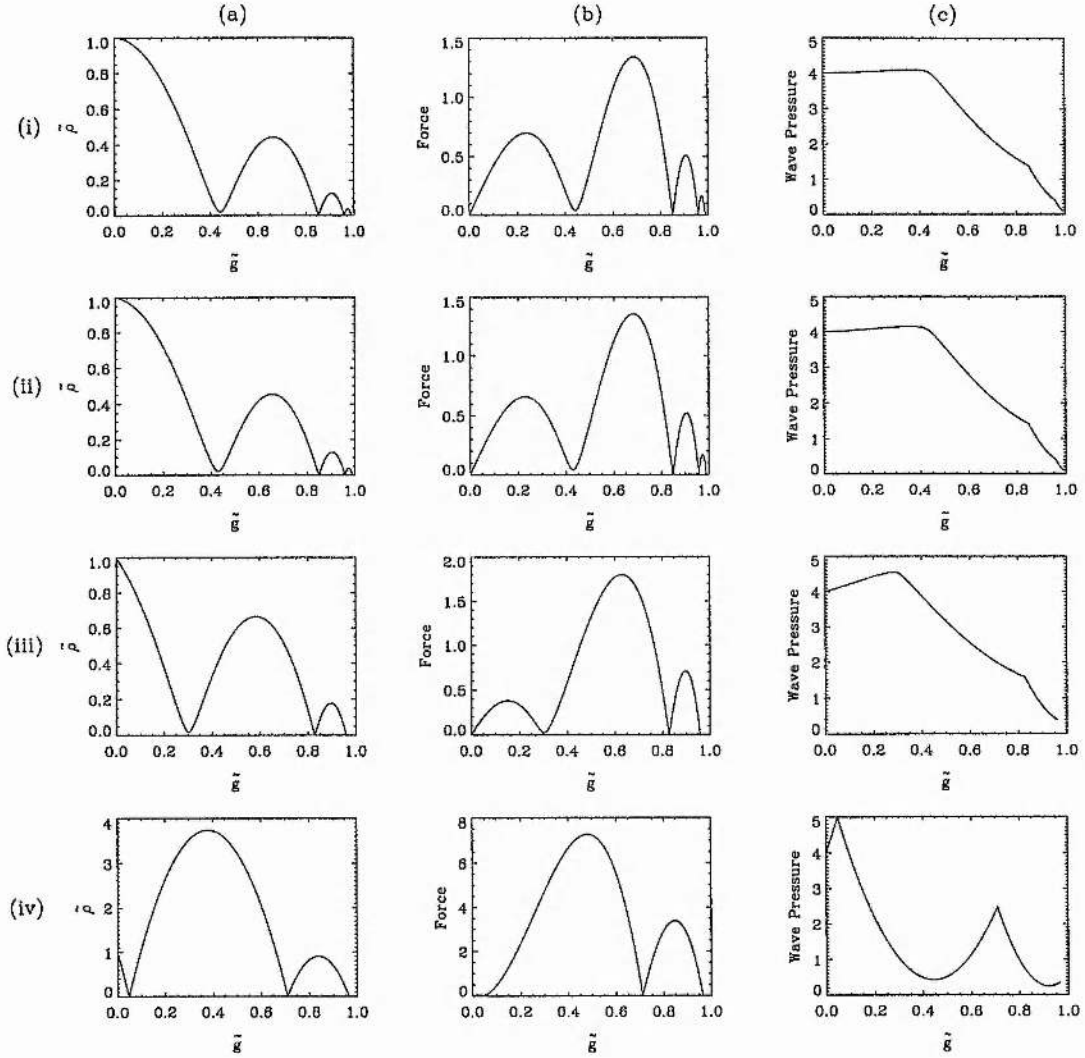

Figure 4.8: (a) Mass density $\tilde{\rho}$, (b) force acting against gravity $|d/d\zeta(\tilde{\rho} + \tilde{b}^2/2\beta)|$ and (c) Alfvén wave pressure $\tilde{b}^2/2\beta$, plotted against gravity $\tilde{g}$ for $\alpha = 5$, $\beta = 10^{-3}$, $\delta = 10^{-1}$, $\tilde{k}_0 = 1.25$ and increasing values of the parameter w_0: (i) 10^{-4}, (ii) 10^{-3}, (iii) 10^{-2}, (iv) 10^{-1}.

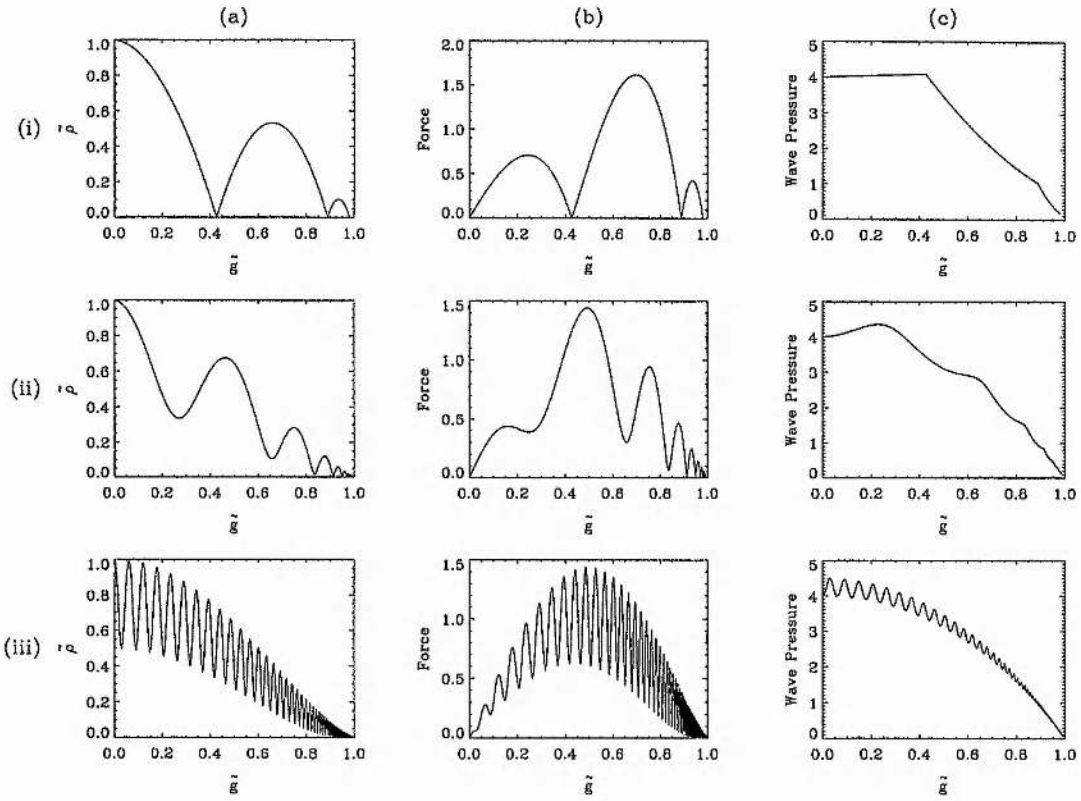

Figure 4.9: (a) Mass density $\tilde{\rho}$, (b) force acting against gravity $|d/d\zeta(\tilde{\rho} + \tilde{b}^2/2\beta)|$ and (c) Alfvén wave pressure $\tilde{b}^2/2\beta$, plotted against gravity $\tilde{g}$ for $\alpha = 5$, $\beta = 10^{-3}$, $\tilde{k}_0 = 1.25$, $w_0 = 10^{-3}$ and increasing values of the parameter δ: (i) 10^{-2}, (ii) 1, (iii) 10^2.

evolution of the mass density, force acting against gravity and wave pressure profiles as δ is increased by four orders of magnitude. Such an increase greatly improves the significance of the gradient of wave pressure as compared to the gas pressure within the mechanical equilibrium of the cloud (as described by Eq. 4.21). As a result the higher values of δ are able to support the cloud as a whole (Figure 4.9(a)(iii)) removing the presence of distinct subsheets.

The peaks in the density profiles clearly correlate with the value of δ: as the wavelength is reduced the separation of the peaks decreases. This correlation is examined further in Figure 4.10 where the logarithm of the distance (ζ) to the first density peak is plotted against the logarithm of the WKB parameter (δ). The distance to the first peak is defined to be the distance from the central plane to the maximum of the first peak in mass density. In Figure 4.10 the data points for higher values of δ (denoted

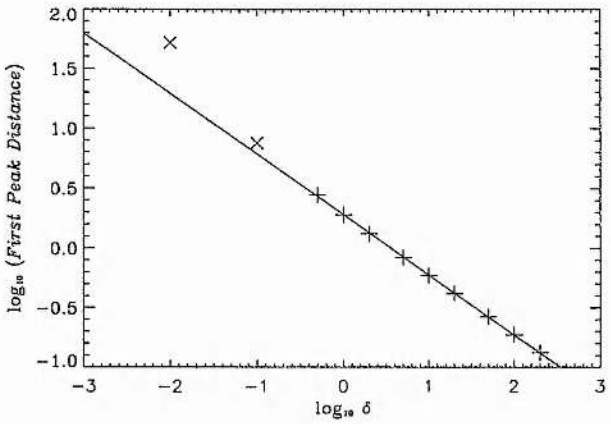

Figure 4.10: The logarithm of the distance (ζ) to the first peak in mass density plotted against the logarithm of the WKB approximation parameter (δ). The data points denoted by a + were used to determine the straight-line fit (solid line); those denoted by a × were excluded from the fit.

by +) demonstrate the linear relationship between the two quantities, the straight-line fit satisfying the equation

$$\log_{10}(\textit{First Peak Distance}) = 0.281 - 0.505 \log_{10} \delta \,. \tag{4.45}$$

Note that the data points for lower values of δ (denoted by ×) were not used in determining the fit; the mass density falls to very low values prior to the first subsheet introducing an uncertainty in the results. Equation (4.45) shows that to a very good approximation

$$\textit{First Peak Distance} \propto \delta^{-1/2} \,,$$

i.e.

$$\textit{First Peak Distance} \propto \frac{\lambda_0}{H} \,,$$

where $\lambda_0 = v_{A_0}/\omega$ is the wavelength at the central plane.

The ability for higher values of the parameter δ to support the whole cloud is again demonstrated in Figure 4.11. In this case the initial value of the derivative of the phase is set to $\tilde{k}_0 = 1$; this is a special case implying that the dispersion relation $k = \omega/v_A$ is valid at the central plane of the gas layer (see also Section 4.2.1). Within this regime increasing the value of the WKB approximation parameter (δ) not only demonstrates the ability for the waves to support the whole cloud, but also smooths the profiles, removing the peaks in mass density.

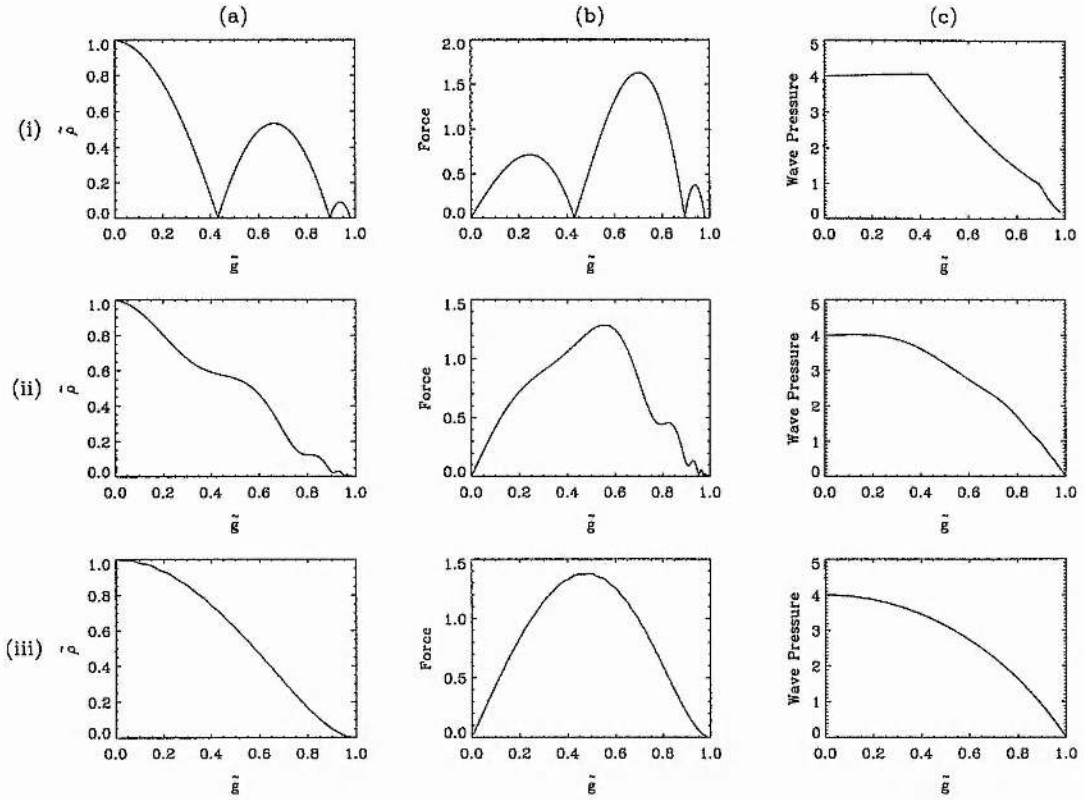

Figure 4.11: (a) Mass density $\tilde{\rho}$, (b) force acting against gravity $|d/d\zeta(\tilde{\rho}+\tilde{b}^2/2\beta)|$ and (c) Alfvén wave pressure $\tilde{b}^2/2\beta$, plotted against gravity $\tilde{g}$ for $\alpha = 5$, $\beta = 10^{-3}$, $\tilde{k}_0 = 1.0$, $w_0 = 10^{-3}$ and increasing values of the parameter δ: (i) 10^{-2}, (ii) 1, (iii) 10^2.

4.3.2 With damping

The equations describing the model — Eqs 4.19 – 4.22 in terms of the height (ζ); or Eqs 4.24 – 4.27 in terms of the gravity ($\tilde{g}$) — will now be considered in the presence of damping for values of the damping parameter $\epsilon \sim 0.1 - 0.5$ (see Section 4.2). Figure 4.12 shows how the typical profiles of mass density and wave pressure (generated from the standard values of the parameters $\alpha = 5$, $\beta = 10^{-3}$, $\delta = 10^{-1}$, $\tilde{k}_0 = 1.25$ and $w_0 = 10^{-3}$) change as the damping becomes stronger.

It can be seen that as the value of ϵ increases the subsheets farthest from the central plane ($\zeta = 0$; $\tilde{g} = 0$) diminish in size; the gradient in wave pressure is no longer sufficient to support such subsheets against the self-gravity of the layer. The fact that damping has reduced the efficiency of wave support at large distances can be clearly seen in Figure 4.13. Here the profiles of mass density, wave pressure and the

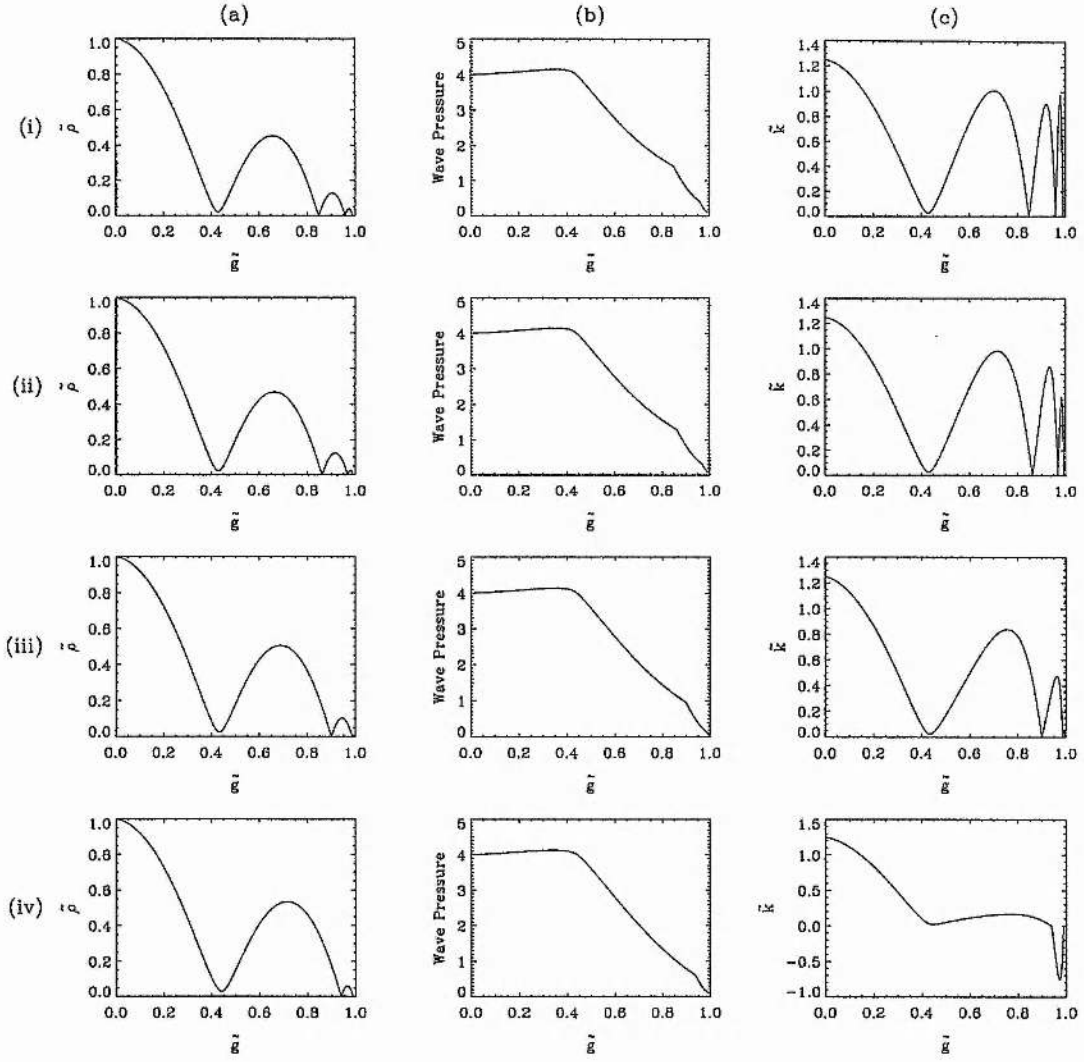

Figure 4.12: (a) Mass density $\tilde{\rho}$, (b) Alfvén wave pressure $\tilde{b}^2/2\beta$ and (c) derivative of the phase $\tilde{k}$, plotted against gravity $\tilde{g}$ for $\alpha = 5$, $\beta = 10^{-3}$, $\delta = 10^{-1}$, $\tilde{k}_0 = 1.25$, $w_0 = 10^{-3}$ and increasing values of the parameter ϵ: (i) 0, (ii) 0.05, (iii) 0.2, (iv) 0.5.

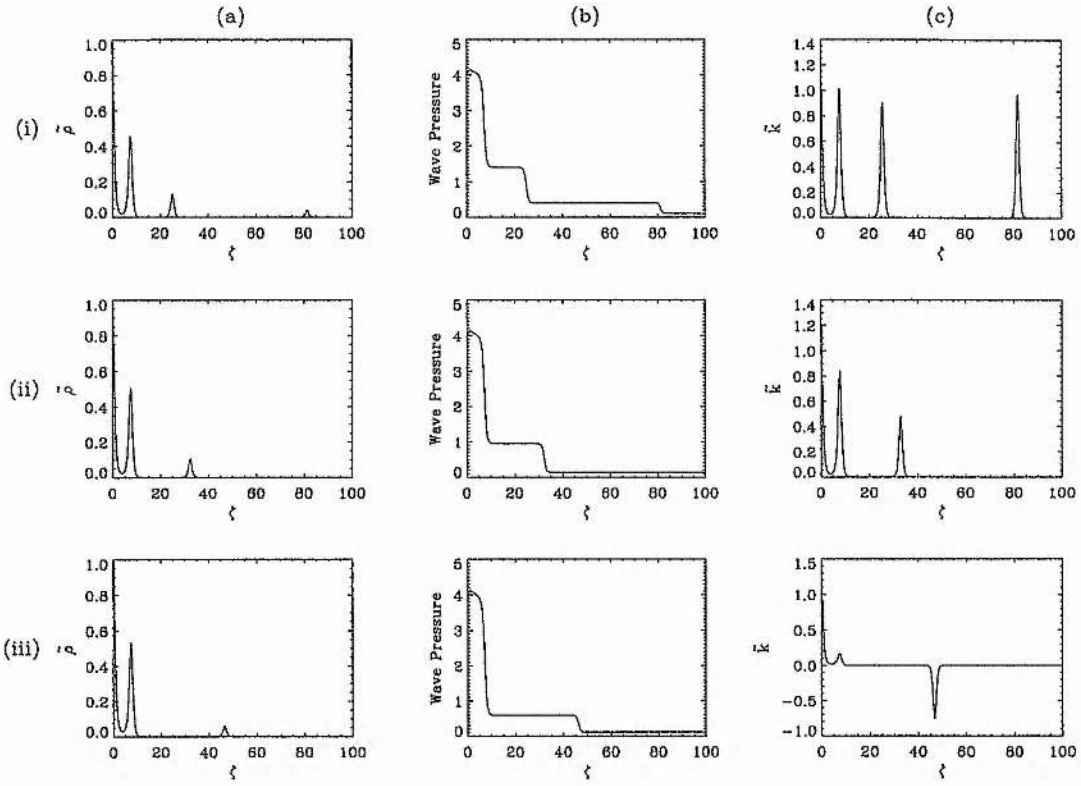

Figure 4.13: (a) Mass density $\tilde{\rho}$, (b) Alfvén wave pressure $\tilde{b}^2/2\beta$ and (c) derivative of the phase $\tilde{k}$, plotted against height ζ for $\alpha = 5$, $\beta = 10^{-3}$, $\delta = 10^{-1}$, $\tilde{k}_0 = 1.25$, $w_0 = 10^{-3}$ and increasing values of the parameter ϵ: (i) 0, (ii) 0.2, (iii) 0.5.

derivative of the phase have been plotted against height (ζ). The sequence of profiles in Figure 4.13(a) shows how the outer subsheets reduce and the inner subsheets increase in size, in accordance with the profiles of wave pressure shown in Figure 4.13(b). However, introducing the damping has had no effect on the internal structure of these subsheets which is still determined by the equilibrium between their internal gas pressure and self-gravity (see Figure 4.4). It can also be observed from Figures 4.12(c) and 4.13(c) that as the damping is increased to its strongest value the derivative of the phase ($\tilde{k}$) — which can no longer be considered in terms of the wavelength of the Alfvén waves, as it was in the WKB regime (Eq. 2.16) — becomes negative when the gravity is close to unity ($\zeta \to \infty$; $\tilde{g} \to 1$).

Allowing for the damping of the waves by ion-neutral friction has increased the amount of mass in the central subsheets. What effect will it have when there is evidence for support of the cloud as a whole, i.e. for higher values of the parameters α or δ (see

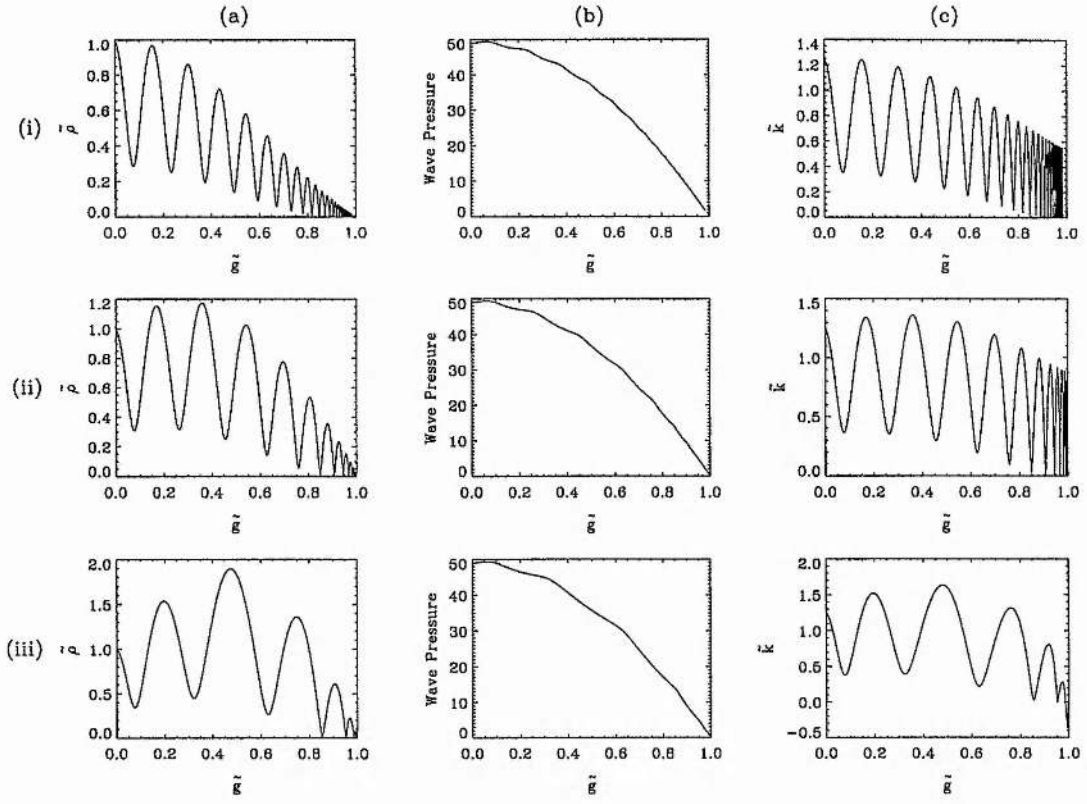

Figure 4.14: (a) Mass density $\tilde{\rho}$, (b) Alfvén wave pressure $\tilde{b}^2/2\beta$ and (c) derivative of the phase $\tilde{k}$, plotted against gravity $\tilde{g}$ for $\alpha = 50$, $\beta = 10^{-3}$, $\delta = 10^{-1}$, $\tilde{k}_0 = 1.25$, $w_0 = 10^{-3}$ and increasing values of the parameter ϵ: (i) 0, (ii) 0.2, (iii) 0.5.

Figures 4.5 and 4.9)? Figures 4.14 and 4.15 display a sequence of profiles for $\alpha = 50$ and $\delta = 10$ respectively, as the strength of the damping is increased from $\epsilon = 0$ to $\epsilon = 0.5$. Both sequences show that the total number of subsheets in the system is reduced as ϵ increases, a greater proportion of the mass being found in each. In addition there is a general increase in the mass density away from the central plane to values higher than the central density. A similar effect was observed within the WKB regime (Chapter 2, Figure 2.9). The damping has increased the gradient in wave pressure (Figures 4.14(b) and 4.15(b)) thus allowing it to support significantly larger subsheets against the self-gravity of the system.

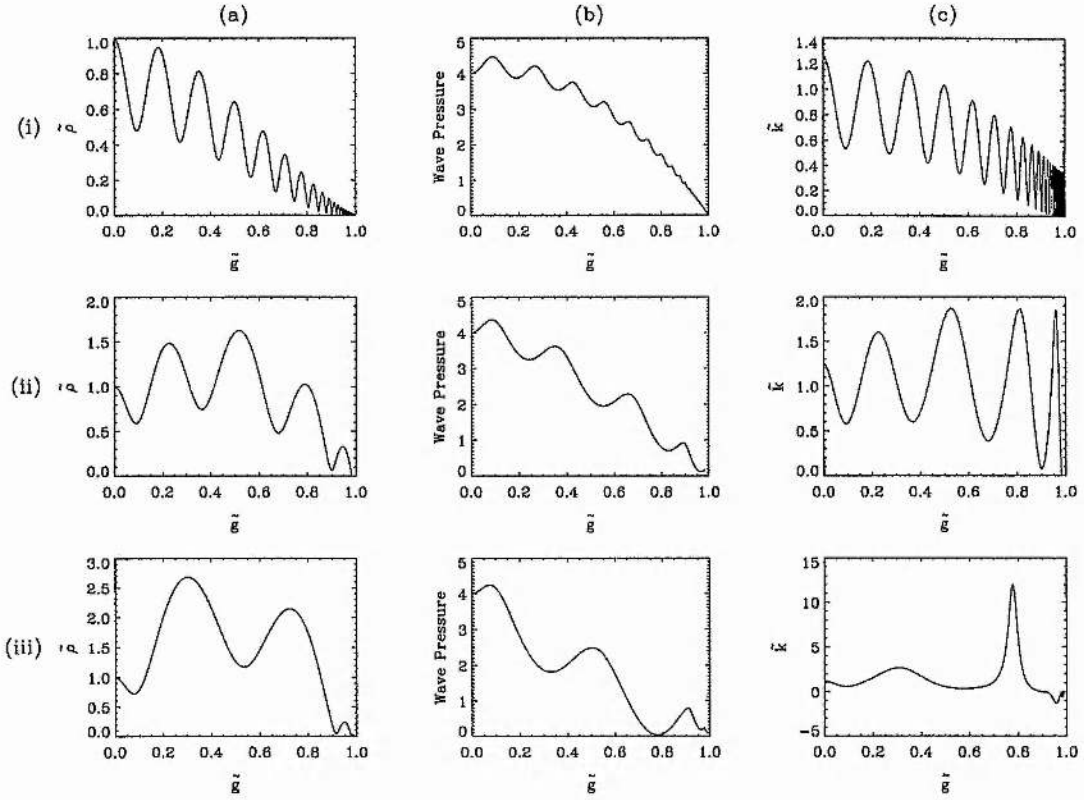

Figure 4.15: (a) Mass density $\tilde{\rho}$, (b) Alfvén wave pressure $\tilde{b}^2/2\beta$ and (c) derivative of the phase $\tilde{k}$, plotted against gravity $\tilde{g}$ for $\alpha = 5$, $\beta = 10^{-3}$, $\delta = 10$, $\tilde{k}_0 = 1.25$, $w_0 = 10^{-3}$ and increasing values of the parameter ϵ: (i) 0, (ii) 0.2, (iii) 0.5.

4.4 Introducing a source function

The results described in the previous section demonstrate how long-wavelength Alfvén waves influence the equilibrium structure of an isothermal gas slab, assuming that the waves are generated in a central source plane. This δ-function source distribution (see Eq. 4.33) will now be improved upon by introducing a density-dependent, power-law distribution of sources,

$$\mathrm{S}(\tilde{\rho}) = \Psi \tilde{\rho}^{\gamma}, \tag{4.46}$$

where the dimensionless parameters are the strength of the source Ψ and the index of the power law γ (see also Chapter 2, Section 2.4). This source distribution suggests that there will be a greater number of wave sources in regions of higher density, each source generating waves which propagate in both the positive and negative directions. The motivation for a source function of this type comes from the consideration of the

possible sources of Alfvén waves within a low-mass star-forming region (see Chapter 1, Section 1.4.1 for a fuller discussion). The waves are generated by the orbital motions of large-scale condensations of gas within the cloud and it is assumed that such condensations form in regions where the mass density is greater.

The orbital motions generating the Alfvén waves, which help to support the molecular cloud against its self-gravity, are likely to be related at different altitudes within the cloud suggesting that the waves will have a constant phase relation between them. In the WKB regime the source function acted on the equilibrium through the wave pressure term (Eqs 2.43 and 2.44), thus assuming that all of the waves were completely incoherent[1]. However, the implied coherency of long-wavelength Alfvén waves suggests that the opposite approximation would be more appropriate. Thus, assuming that the waves are completely coherent (rigourously in phase), the source function would act on the equilibrium through the amplitude of the wave perturbation ($\tilde{b}$) and hence the equations describing the model (Eqs 4.19 – 4.22) become: the wave propagation equations

$$\frac{d\tilde{b}_+}{d\zeta} = w_+\tilde{\rho} \tag{4.47}$$

$$-\frac{d\tilde{b}_-}{d\zeta} = w_-\tilde{\rho} \tag{4.48}$$

$$\frac{dw_+}{d\zeta} = \delta\left(\frac{\tilde{k}^2}{\tilde{\rho}} - 1\right)\tilde{b}_+ + \frac{\Psi}{2}\tilde{\rho}^\gamma \tag{4.49}$$

$$-\frac{dw_-}{d\zeta} = \delta\left(\frac{\tilde{k}^2}{\tilde{\rho}} - 1\right)\tilde{b}_- + \frac{\Psi}{2}\tilde{\rho}^\gamma, \tag{4.50}$$

the amplitude equation

$$\frac{d}{d\zeta}\left(\frac{(\tilde{b}_+^2 + \tilde{b}_-^2)\,\tilde{k}}{\tilde{\rho}}\right) = -\epsilon\sqrt{\delta}\,(\tilde{b}_+^2 + \tilde{b}_-^2), \tag{4.51}$$

the equilibrium equation

$$\frac{d}{d\zeta}\left(\tilde{\rho} + \frac{\tilde{b}_+^2 + \tilde{b}_-^2}{2\beta}\right) = -2\sqrt{\alpha}\,\tilde{\rho}\tilde{g} \tag{4.52}$$

and the self-gravitation equation

$$\frac{d\tilde{g}}{d\zeta} = \frac{\tilde{\rho}}{\sqrt{\alpha}}, \tag{4.53}$$

[1]If the waves are completely incoherent then the total intensity is simply the sum of the individual intensities of each of the waves. However, if the sources are coherent then the individual amplitudes of each of the waves are added, taking account of their phase differences, and squared. The resultant quantity is proportional to the total intensity.

where the quantities with a subscript + belong to the waves propagating in the positive z-direction and those with a subscript - belong to those waves propagating in the negative z-direction. Given that the waves are completely coherent there will only be one value of the phase and one value of the derivative of the phase ($\tilde{k}$) at each height (ζ), and thus there is no distinction between the value of $\tilde{k}$ for positively and negatively propagating waves.

4.4.1 Boundary conditions

The equations which describe the perturbations (Eqs 4.47 – 4.53) relate the seven dependent variables — the mass density $\tilde{\rho}$, the gravity $\tilde{g}$, the wave amplitudes $\tilde{b}_+$, $\tilde{b}_-$, the wavenumber $\tilde{k}$ and w_+, w_- — to the height ζ. As such this seventh-order system of equations requires seven independent boundary conditions.

Following the arguments given in Section 4.2.1 the amplitude equation (Eq. 4.51) can be expanded to show that

$$\left(\tilde{b}_+^2 + \tilde{b}_-^2\right)\tilde{k} \to 0 \quad \text{as} \quad \zeta \to \infty$$

and thus to conserve the total wave flux, in the absence of damping, $(\tilde{b}_+^2 + \tilde{b}_-^2) \to 0$ and hence $\tilde{b}_+$, $\tilde{b}_- \to 0$ as the wave amplitudes are real.

Introducing a continuous distribution of sources means that the gradient of the total wave amplitude is symmetrical and continuous through the origin, i.e.

$$\left.\frac{d\left(\tilde{b}_+ + \tilde{b}_-\right)}{d\zeta}\right|_{\zeta=0} = 0\,. \tag{4.54}$$

Note that this condition is consistent with there being a maximum in the total wave pressure $(\tilde{b}_+^2 + \tilde{b}_-^2)$ at the central plane and the mass density $(\tilde{\rho})$ being symmetric and continuous through $\zeta = 0$. A maximum in the total wave amplitude at the central plane implies that

$$\left.\frac{d^2\left(\tilde{b}_+ + \tilde{b}_-\right)}{d\zeta^2}\right|_{\zeta=0} < 0\,, \tag{4.55}$$

which can be written as

$$\left.\frac{d\left(w_+ - w_-\right)}{d\zeta}\right|_{\zeta=0} < 0 \tag{4.56}$$

through Equations (4.47) and (4.48) evaluated at $\zeta = 0$. This can be used to determine a condition on the value of the derivative of the phase at the central plane ($\tilde{k}_0$). Adding Equations (4.49) and (4.50) shows that

$$\delta(\tilde{k}_0^2 - 1)(\tilde{b}_{0_+} + \tilde{b}_{0_-}) + \Psi < 0\,, \tag{4.57}$$

where $\tilde{b}_{0_+}$ and $\tilde{b}_{0_-}$ are the amplitudes of the magnetic field perturbations at the central plane for waves propagating in the positive and negative z-directions respectively. In turn, this condition implies that the strength of the source $\Psi \leq 2\delta\tilde{b}_{0_+}$ as the waves are real. Note that Equation (4.57) gives a maximum value of $\tilde{k}_0 = 1$ in the absence of any source, and as the strength of the source increases to its maximum value ($\Psi \rightarrow 2\delta\tilde{b}_{0_+}$) the derivative of the phase $\tilde{k}_0 \rightarrow 0$, i.e. the phase tends towards a constant value.

The condition that the gradient of the total wave amplitude is symmetrical and continuous through the origin (Eq. 4.54) implies that the dependent variables w_+ and w_- are equal at the central plane, i.e.

$$w_{0_+} = w_{0_-} \tag{4.58}$$

(obtained by subtracting Equations (4.47) and (4.48)). Note that if $w_{0_+} = w_{0_-} = 0$ then the positively and negatively propagating waves would each have a maximum at the central plane ($\zeta = 0$).

Thus, the seven independent boundary conditions required to solve Equations (4.47) – (4.53), which describe the perturbations, are

$$\tilde{\rho}_0 = 1$$

$$\tilde{g}_0 = 0$$

$$\tilde{b}_+(\infty) = \tilde{b}_-(\infty) = 0$$

w_{0_+} , w_{0_-} are known (satisfying Eq. 4.58)

$\tilde{k}_0$ is known (satisfying Eq. 4.57).

As in the previous model for a δ-function source it is possible to translate the boundary conditions on the wave amplitudes ($\tilde{b}_+(\infty)$, $\tilde{b}_-(\infty) \rightarrow 0$ as $\zeta \rightarrow \infty$) into conditions on the value of these variables at the central plane.

In accordance with the description in Section 4.2, the absence of any explicit dependence on the independent variable ζ allows the equations (Eqs 4.47 – 4.53) to be rewritten in terms of the gravity ($\tilde{g}$). In this case the mechanical equilibrium equation (Eq. 4.52) integrates to

$$\tilde{\rho} + \frac{\tilde{b}_+^2 + \tilde{b}_-^2}{2\beta} - \frac{\tilde{b}_{0_+}^2 + \tilde{b}_{0_-}^2}{2\beta} = 1 - \alpha\tilde{g}^2 , \tag{4.59}$$

given that $\tilde{\rho} = 1$ and $\tilde{g} = 0$ at the central plane ($\zeta = 0$). At the edge of the isothermal gas layer, as $\zeta \rightarrow \infty$, $\tilde{\rho} \rightarrow 0$, $\tilde{g} \rightarrow 1$ and $\tilde{b}_+$, $\tilde{b}_- \rightarrow 0$, this expression becomes

$$\tilde{b}_{0_+}^2 + \tilde{b}_{0_-}^2 = 2\beta(\alpha - 1) . \tag{4.60}$$

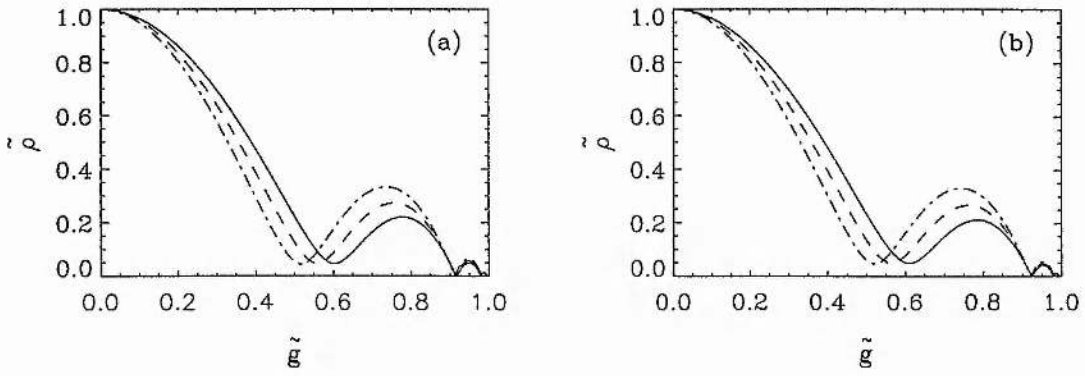

Figure 4.16: Mass density $\tilde{\rho}$ plotted against gravity $\tilde{g}$ for $\alpha = 5$, $\beta = 10^{-3}$, $\delta = 10^{-1}$, $w_{0_+} = 10^{-3}$, $\gamma = 2$, $\tilde{k}_0 = 0.45$ and increasing values of the strength of the source $\Psi = 0.0005$ (solid lines), $\Psi = 0.005$ (dashed lines) and $\Psi = 0.01$ (dot-dashed lines) for (a) $\epsilon = 0$ and (b) $\epsilon = 0.3$.

The symmetry of the model about the central plane dictates that there will be an equal number of waves propagating in each direction and hence that $\tilde{b}_{0_+}^2 = \tilde{b}_{0_-}^2$. Thus given that the amplitude of the waves is real

$$\tilde{b}_{0_+} = \tilde{b}_{0_-} = \sqrt{\beta(\alpha - 1)}\,. \tag{4.61}$$

These conditions will be used together with those listed above for the mass density $\tilde{\rho}_0$, the gravity $\tilde{g}_0$, the wavenumber $\tilde{k}_0$ and w_{0_+}, w_{0_-}, to solve the set of equations describing the distributed sources model (Eqs 4.47 – 4.53) as an initial-value problem. The numerical results are presented in the following section.

4.4.2 Results

In this section the effect of introducing a source function into the model will be examined. For typical values of the parameters $\alpha = 5$, $\beta = 10^{-3}$ and $\delta = 10^{-1}$ the boundary conditions discussed above restrict the strength of the source to $\Psi \leq 0.0126$ and the value of the derivative of the phase at the central plane ($\tilde{k}_0$) according to Equation (4.57). Together with $w_{0_+} = 10^{-3}$ and $\gamma = 2$, the effect of increasing the strength of the source for a given value of $\tilde{k}_0$ is demonstrated in the absence of damping ($\epsilon = 0$) in Figure 4.16(a) and for a typical value of the damping ($\epsilon = 0.3$) in Figure 4.16(b). In both cases the graphs of mass density ($\tilde{\rho}$) versus gravity ($\tilde{g}$) show that increasing the strength of the source actually reduces the extent of the central subsheet while enhancing the significance of the first subsheet; the profiles of the force acting against gravity

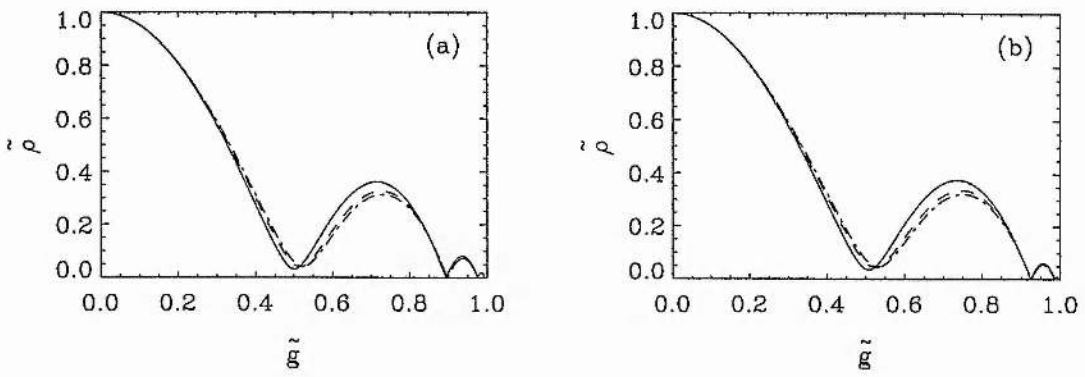

Figure 4.17: Mass density $\tilde{\rho}$ plotted against gravity $\tilde{g}$ for $\alpha = 5$, $\beta = 10^{-3}$, $\delta = 10^{-1}$, $w_{0+} = 10^{-3}$, $\Psi = 0.005$, $\tilde{k}_0 = 0.45$ and increasing values of the power-law index $\gamma = 1$ (solid lines), $\gamma = 3$ (dashed lines) and $\gamma = 5$ (dot-dashed lines) for (a) $\epsilon = 0$ and (b) $\epsilon = 0.3$.

($|d/d\zeta(\tilde{\rho} + [\tilde{b}_+^2 + \tilde{b}_-^2]/2\beta)|$), the total wave pressure ($[\tilde{b}_+^2 + \tilde{b}_-^2]/2\beta$) and the derivative of the phase ($\tilde{k}$) behave correspondingly (see Section 4.3). Conversely, if the index of the power law is increased from $\gamma = 1$ (linear relation) through to $\gamma = 5$ the central subsheet is increased while the first subsheet is diminished (see Figure 4.17). However, the effect of narrowing the source distribution is not as significant as that caused by increasing the strength of the source. Figures 4.16 and 4.17 both show that including a source function in the model has not dramatically altered the global structure of an isothermal gas layer supported by long-wavelength Alfvén waves.

However the internal structure of the subsheets is no longer simply that described by their internal gas pressure and self-gravity (Eq. 4.42). The first two subsheets of a typical mass density profile (Figure 4.16(a), dot-dashed profile) have been plotted in terms of the dimensionless height (ζ') in Figure 4.18 (dashed curves). Note that the dimensionless height (ζ') is defined such that the peak of mass density in the subsheet corresponds to $\zeta' = 0$. The profiles of the subsheets are significantly broader than the simple pressure supported profiles (Figure 4.18, solid lines) suggesting that the Alfvén wave pressure force is contributing to the support of these individual subsheets, as well as supporting the global structure of the gas layer against its self-gravity. Distributing the sources with respect to the mass density implies that every point in the cloud, including the subsheets, is a source of Alfvén waves; these waves enhancing the internal support of the individual sheets.

Figures 4.19 – 4.22 demonstrate another important consequence of distributing the sources with respect to the mass density ($\tilde{\rho}$). In Figures 4.19 and 4.20 the parameters

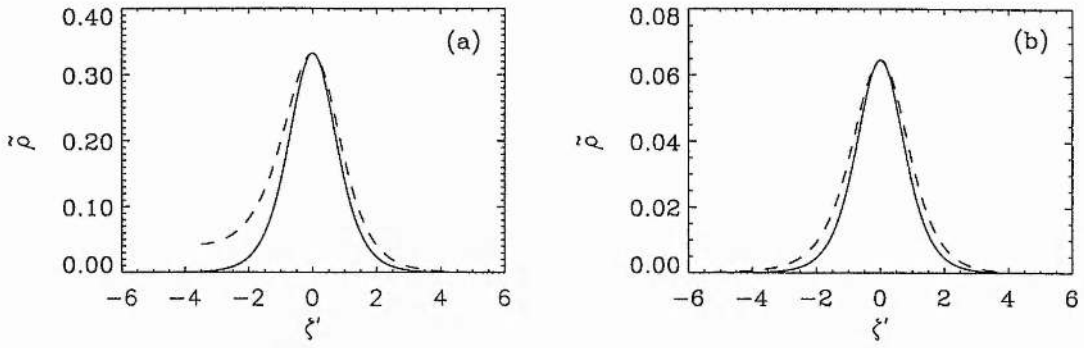

Figure 4.18: The mass density profiles of a gas pressure supported equilibrium (solid lines) compared to the mass density profiles of (a) the first subsheet and (b) the second subsheet seen in Figure 4.16(a) where the source strength is $\Psi = 0.005$ (dashed lines). The horizontal coordinate ζ' is the dimensionless height translated so that the maximum in the mass density of the subsheet is located at $\zeta' = 0$.

representing the strength of the source (Ψ) and the index of the power law (γ) are varied when the parameter $\alpha = 50$, i.e. when there is evidence for support of the whole cloud. In this case it was shown in Section 4.3.2 that for significant values of the damping there is a general increase in mass density away from the central plane to values greater than the central density. Figure 4.19(a) shows that this phenomenon can also occur in the absence of damping for small values of the initial derivative of the phase ($\tilde{k}_0$); the introduction of damping simply enhancing the increase in density. Now as the strength of the source is increased this 'bump' in mass density is dramatically reduced both in the absence of and in the presence of damping (see Figure 4.19). Indeed Figure 4.20 shows that narrowing the source distribution also reduces the bump in density caused by switching on the damping.

A similar effect can be observed in Figure 4.21 which has been plotted for a higher value of the WKB approximation parameter ($\delta = 1$)[2]. Note also the clear change in the structure of the gas layer as the strength of the source (Ψ) is increased — for the weakest source strength (Figure 4.21, solid lines) the central subsheet dominates the structure of the cloud whereas for the strongest source (Figure 4.21, dot-dashed lines) the central and first subsheets are more equivalent in size, the density not falling to

[2]For high values of the WKB approximation parameter ($\delta > 1$) combined with strong damping ($\epsilon \sim 0.5$) and low values of the derivative of the phase at the central plane ($\tilde{k}_0$) it is very difficult to obtain the equilibrium solution numerically. The combined influence of these factors makes the central subsheet vastly dominant; subsequent subsheets become comparatively insignificant physically and therefore numerically.

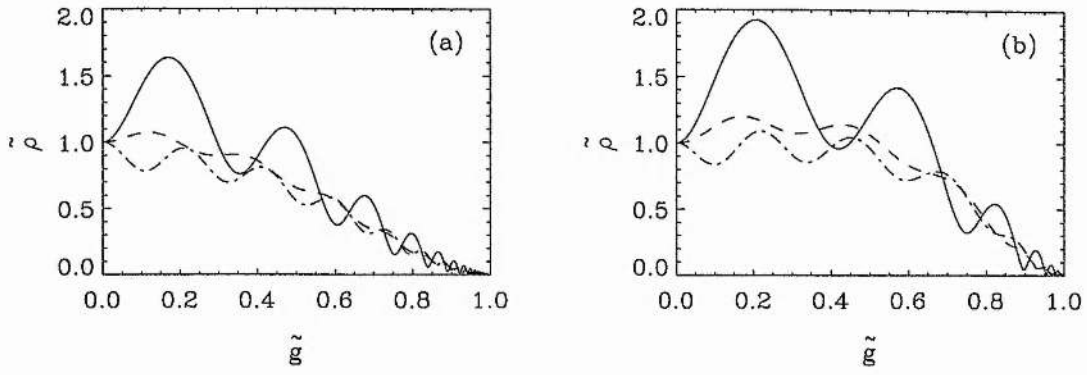

Figure 4.19: Mass density $\tilde{\rho}$ plotted against gravity $\tilde{g}$ for $\alpha = 50$, $\beta = 10^{-3}$, $\delta = 10^{-1}$, $w_{0+} = 10^{-3}$, $\gamma = 2$, $\tilde{k}_0 = 0.72$ and increasing values of the strength of the source $\Psi = 0.001$ (solid lines), $\Psi = 0.01$ (dashed lines) and $\Psi = 0.02$ (dot-dashed lines) for (a) $\epsilon = 0$ and (b) $\epsilon = 0.3$.

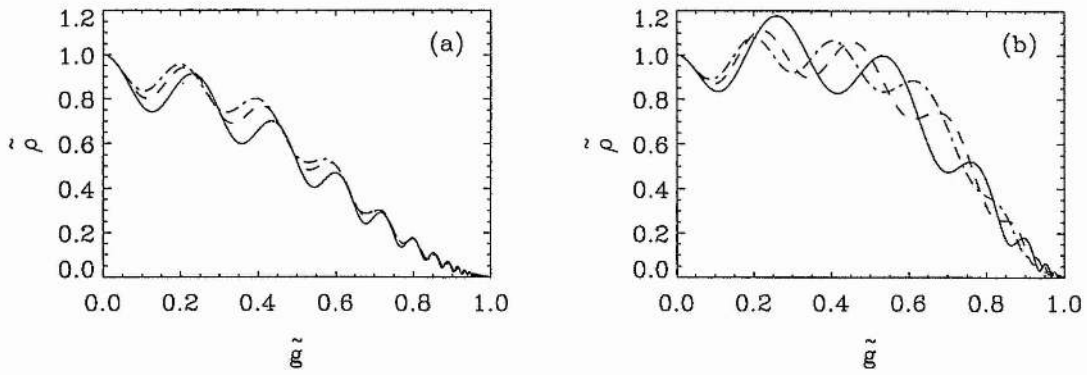

Figure 4.20: Mass density $\tilde{\rho}$ plotted against gravity $\tilde{g}$ for $\alpha = 50$, $\beta = 10^{-3}$, $\delta = 10^{-1}$, $w_{0+} = 10^{-3}$, $\Psi = 0.01$, $\tilde{k}_0 = 0.85$ and increasing values of the power-law index $\gamma = 1$ (solid lines), $\gamma = 3$ (dashed lines) and $\gamma = 5$ (dot-dashed lines) for (a) $\epsilon = 0$ and (b) $\epsilon = 0.3$.

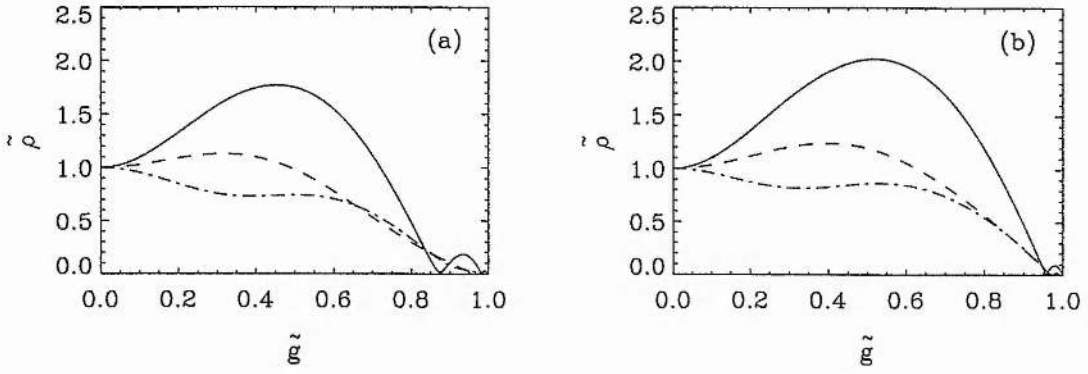

Figure 4.21: Mass density $\tilde{\rho}$ plotted against gravity $\tilde{g}$ for $\alpha = 5$, $\beta = 10^{-3}$, $\delta = 1$, $w_{0+} = 10^{-3}$, $\gamma = 2$, $\tilde{k}_0 = 0.45$ and increasing values of the strength of the source $\Psi = 0.005$ (solid lines), $\Psi = 0.05$ (dashed lines) and $\Psi = 0.1$ (dot-dashed lines) for (a) $\epsilon = 0$ and (b) $\epsilon = 0.3$.

insignificant values between the peaks. The combination of a significant value of the damping and a higher value of either the parameter α or the parameter δ does not necessarily cause a general increase in mass density away from the central plane. In Figure 4.22 narrowing the distribution of sources (increasing the value of γ) provides extra support to the central regions of the isothermal gas layer, a situation which is improved upon by the introduction of damping.

In summary, the inclusion of a source function in the model has not altered the basic global structure of the gas slab although it has provided some additional support for the individual subsheets. In addition, for reasonable values of the source parameters (Ψ and γ) it has removed any general increase in mass density away from the central plane (see also Chapter 2, Section 2.4.2).

4.5 The case for cloud support

Throughout this chapter the results have been presented in terms of the dimensionless variables. In order to ascertain the significance of these results with regard to the support of the isothermal gas layer by long-wavelength Alfvén waves, the profiles need to be considered in terms of the height (z) in parsecs. To do this the temperature (T) and the column density ($\mathcal{M}$) of the layer need to be specified to give a value for the scale-height H, where

$$H = \sqrt{\frac{c^2}{2\pi G \rho_0}},$$

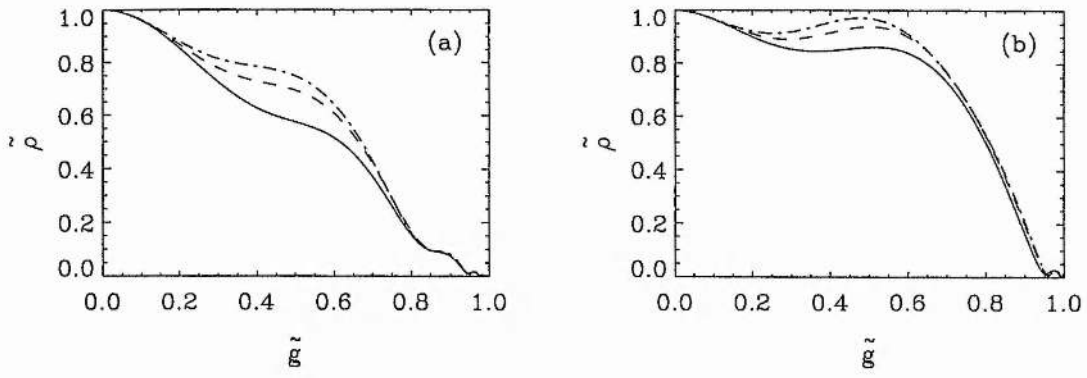

Figure 4.22: Mass density $\tilde{\rho}$ plotted against gravity $\tilde{g}$ for $\alpha = 5$, $\beta = 10^{-3}$, $\delta = 1$, $w_{0_+} = 10^{-3}$, $\Psi = 0.05$, $\tilde{k}_0 = 0.75$ and increasing values of the power-law index $\gamma = 1$ (solid lines), $\gamma = 3$ (dashed lines) and $\gamma = 5$ (dot-dashed lines) for (a) $\epsilon = 0$ and (b) $\epsilon = 0.3$.

c is the sound speed, G is the gravitational constant and ρ_0 is the central mass density. Typical values of these properties ($T = 10$ K; $\mathcal{M} = 10^{-1}$ kg m^{-2}) are combined with the standard input parameters in Figures 4.23 and 4.24 to show how the profiles of dimensionless mass density ($\tilde{\rho}$) against height (z) evolve for increasing values of the parameters α and δ respectively. With the temperature and column density specified, increasing α simply reduces the value of the mass density at the central plane, $\rho_0 = \pi G \mathcal{M}^2/(2c^2\alpha)$ (see Table 4.3), while increasing δ reduces the initial wavelength of the Alfvén waves (Eq. 4.44). In both cases the larger values of the parameters provide evidence for the support of the cloud as a whole (Figures 4.23(d) and 4.24(d)). However, increasing the value of α has substantially broadened the gas layer (by increasing the value of the scale-height) whilst increasing δ has simply altered the structure, rather than the extent of the layer.

The thickness of these density profiles is defined to be equal to twice the height at which the central mass density has fallen by a factor e, i.e. $2 \times z(\tilde{\rho} = 1/\mathrm{e})$ (as in Chapters 2 and 3). In the cases where the density falls to very low values between the subsheets the thickness of the layer is defined as the thickness of the central subsheet, for example in Figure 4.23(b); where there is evidence for more substantial support, i.e. the density does not fall to small values between the (inner) subsheets, the thickness of the layer is assumed to be given by the last subsheet which falls through $z(\tilde{\rho} = 1/\mathrm{e})$, for example Figure 4.23(c). Table 4.3 displays the thicknesses of the mass density profiles shown in Figures 4.23 and 4.24 along with their central densities (ρ_0) and scale-heights (H). These results show that increasing the parameter α has indeed increased

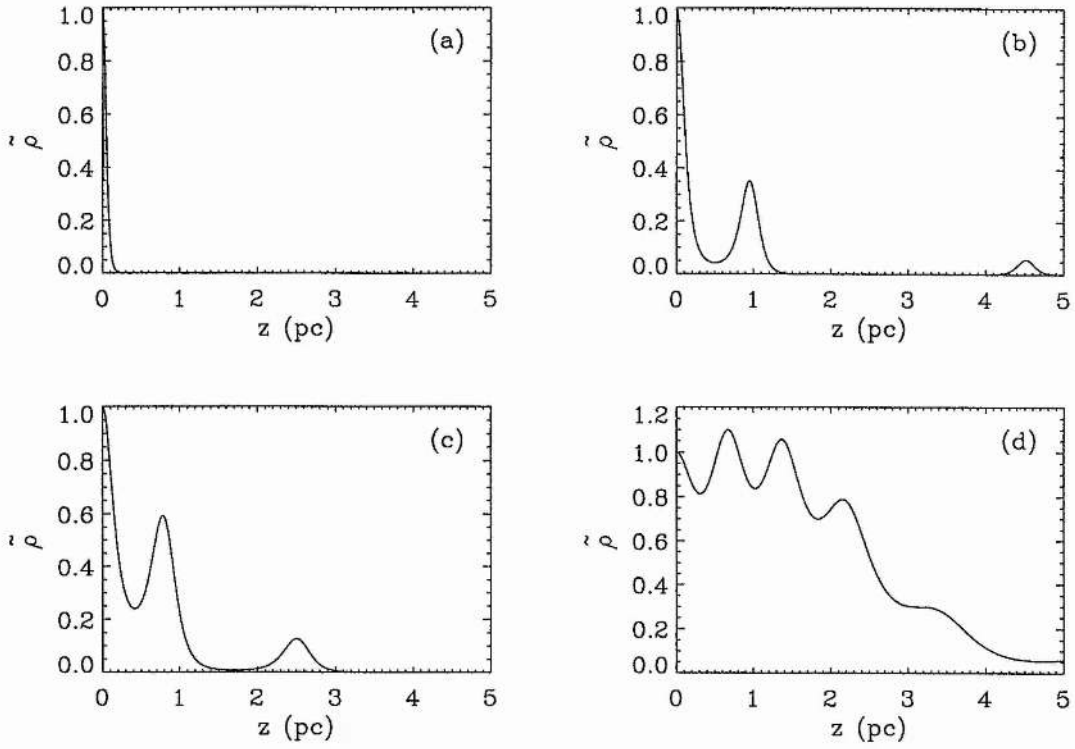

Figure 4.23: Mass density $\tilde{\rho}$ plotted against height z (pc) for $\beta = 10^{-3}$, $\delta = 10^{-1}$, $\tilde{k}_0 = 0.75$, $w_{0+} = 10^{-3}$, $\epsilon = 0.3$, $\gamma = 2$ and increasing values of the parameter α: (a) 1.0001 ($\Psi = 2.5 \times 10^{-5}$), (b) 5 ($\Psi = 0.005$), (c) 10 ($\Psi = 0.008$), (d) 50 ($\Psi = 0.019$). Note that the strength of the source Ψ is varied to ensure that $\tilde{k}_0 = 0.75$ is valid (Eq. 4.57).

the thickness of the cloud out to several parsecs which is consistent with observations (e.g. see Shu et al. 1987). In contrast increasing the value of the WKB approximation parameter δ has only slightly altered the thickness of the sheet.

Also shown in Table 4.3 are the results generated by varying the strength of the damping, through the parameter ϵ (see Figure 4.25). Although increasing the damping has altered the distribution of mass within the layer, keeping more mass in the central regions, the effect on the thickness of the slab is small. The results do show that weak values of the damping ($\epsilon \sim 0.1 - 0.2$) increase the thickness of the sheet (e.g. Figure 4.25(c)) compared to that without damping (Figure 4.25(a)), but that increasing the damping to its strongest value ($\epsilon \sim 0.5$) does actually reduce the thickness (Figure 4.25(d)). Note that if the value of the parameter α was reduced to $\alpha = 5$ the thickness of the sheet would not change with increasing damping; the damping does

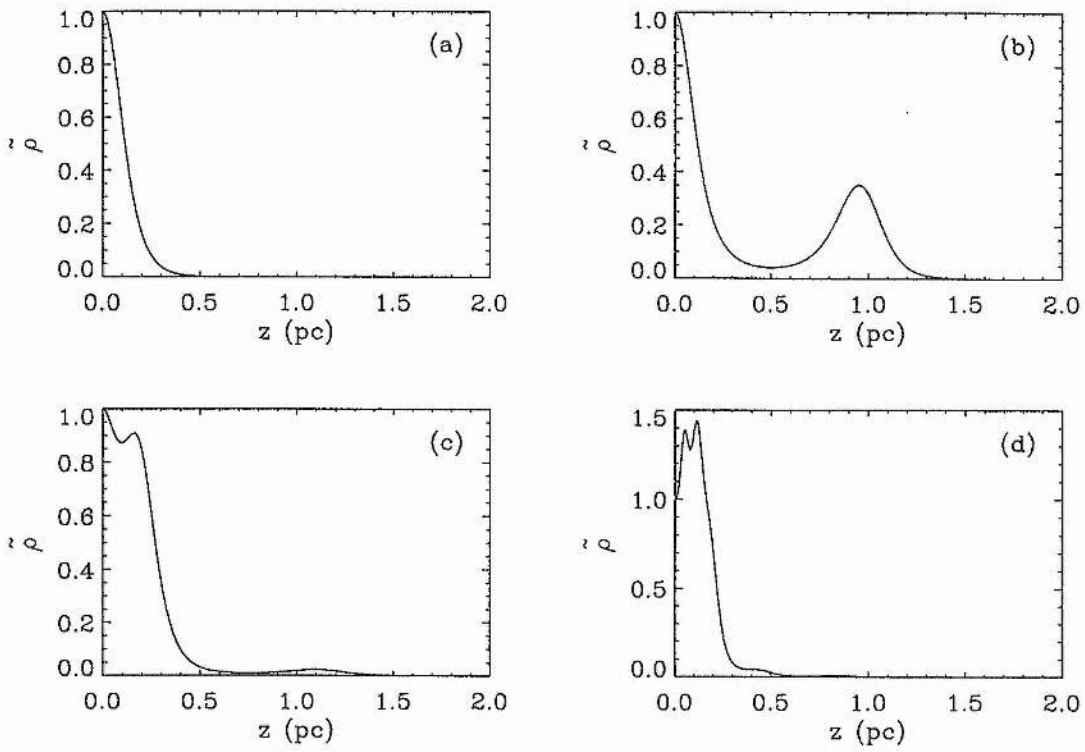

Figure 4.24: Mass density $\tilde{\rho}$ plotted against height z(pc) for $\alpha = 5$, $\beta = 10^{-3}$, $\tilde{k}_0 = 0.75$, $w_{0+} = 10^{-3}$, $\epsilon = 0.3$, $\gamma = 2$ and increasing values of the parameter δ: (a) 10^{-2} ($\Psi = 0.0005$), (b) 10^{-1} ($\Psi = 0.005$), (c) 1 ($\Psi = 0.05$), (d) 10 ($\Psi = 0.5$). Note that the strength of the source Ψ is varied to ensure that $\tilde{k}_0 = 0.75$ is valid (Eq. 4.57).

reduce the efficiency of wave support away from the central plane but does not affect the central subsheet which, for low values of α, is chosen to determine the thickness of the gas layer.

These results show that the long-wavelength Alfvén waves considered in this model do provide some support against the self-gravity of the isothermal cloud. Of the dimensionless parameters prescribed in Section 4.2, α plays the most dominant role in determining the thickness of the gas layer; higher values provide more support. The WKB parameter (δ) is important in determining the structure of the layer, and the strength and distribution of the source (Ψ and γ) and the damping (ϵ) control the general increase in density away from the central plane.

The magnetic field perturbation (b) is related to the fluid velocity (v) through the expression $b/B_0 \simeq v/v_A$, where B_0 is the background magnetic field and v_A is the Alfvén velocity. The fluid velocity is observed to be $v \sim 1 - 3\,\mathrm{km\,s^{-1}}$ and the Alfvén speed

α	δ	ϵ	ρ_0 (kg m^{-3})	H (m^{-1})	Thickness (pc)
1.0001	10^{-1}	0.3	2.92×10^{-17}	1.71×10^{15}	0.12
5			5.83×10^{-18}	3.83×10^{15}	0.30
10			2.92×10^{-18}	5.42×10^{15}	1.86
50			5.83×10^{-19}	1.21×10^{16}	5.45
5	10^{-2}	0.3	5.83×10^{-18}	3.83×10^{15}	0.27
	10^{-1}				0.30
	1				0.59
	10				0.47
50	10^{-1}	0	5.83×10^{-19}	1.21×10^{16}	5.26
		0.1			5.37
		0.3			5.45
		0.5			5.26

Table 4.3: The central mass density ρ_0, scale-height H and thickness of the layer for $\beta = 10^{-3}$, $\tilde{k}_0 = 0.75$, $w_{0+} = 10^{-3}$, $\gamma = 2$ and increasing values of the parameters α, δ and ϵ.

is determined, from observations of the magnetic field strength and number density, to be $v_A \sim 4.5\,\mathrm{km\,s^{-1}}$. These values suggest that the total magnetic field perturbation is $\tilde{b} = b/B_0 \sim 0.2 - 0.7$, the lower limit of which is given theoretically by $\alpha = 30$ and $\beta = 5 \times 10^{-4}$ for example (Eq. 4.61) (physically these figures correspond to a slight decrease in the number density from the standard value of $n_{H_2} = 10^9\,\mathrm{m^{-3}}$). As an example Figure 4.26(a) shows a density profile determined for these parameters combined with a strong ($\Psi = 0.037$), narrow ($\gamma = 4$) source and weak damping ($\epsilon = 0.15$). This profile has a thickness of 3.77 pc which is equivalent to a radius of 1.89 pc. As the fluid velocity increases towards the Alfvén value (Myers & Goodman 1988; Goodman & Heiles 1994; Mouschovias & Psaltis 1995) the total magnetic field perturbation tends to unity. Figure 4.26(b) displays the mass density profile for such a magnetic field perturbation (given by $\alpha = 80$ and $\beta = 3 \times 10^{-3}$) showing that the thickness of the slab has increased to 9.44 pc (corresponding to a radius of 4.72 pc). These two examples (Figure 4.26) display small artefacts in mass density rather than distinct subsheets and show that long-wavelength Alfvén waves can support gas layers out to radii which are consistent with observational values (Shu et al. 1987).

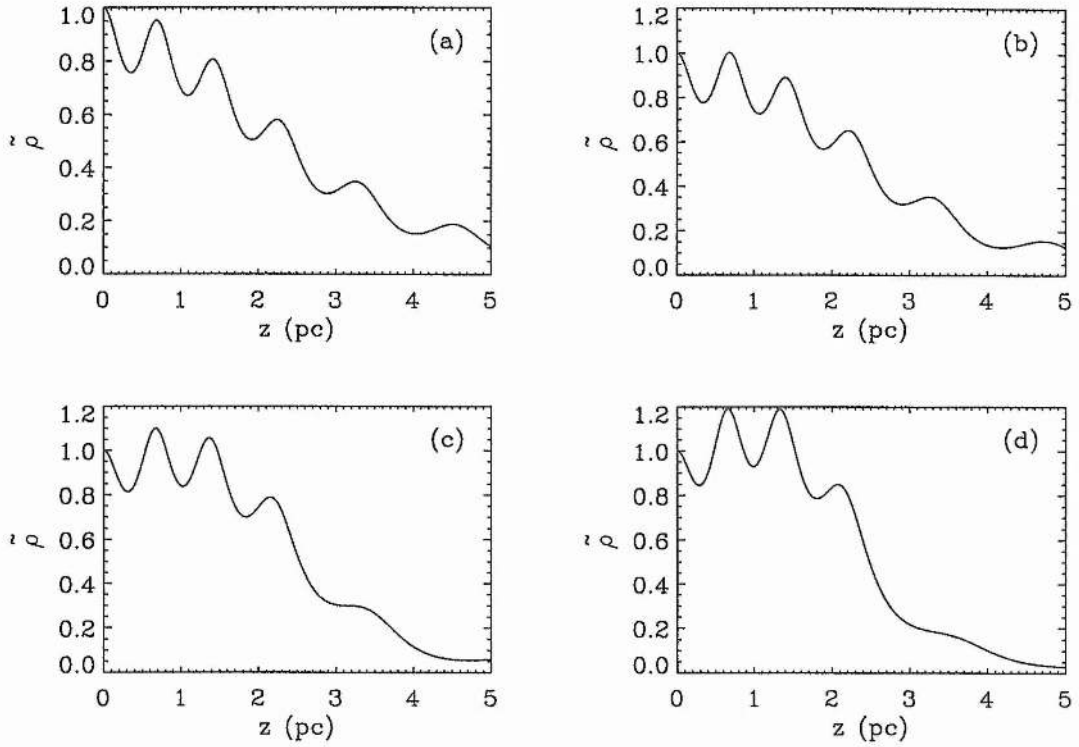

Figure 4.25: Mass density $\tilde{\rho}$ plotted against height z (pc) for $\alpha = 50$, $\beta = 10^{-3}$, $\delta = 10^{-1}$, $\tilde{k}_0 = 0.75$, $w_{0+} = 10^{-3}$, $\Psi = 0.19$, $\gamma = 2$ and increasing values of the parameter ϵ: (a) 0, (b) 0.1, (c) 0.3, (d) 0.5.

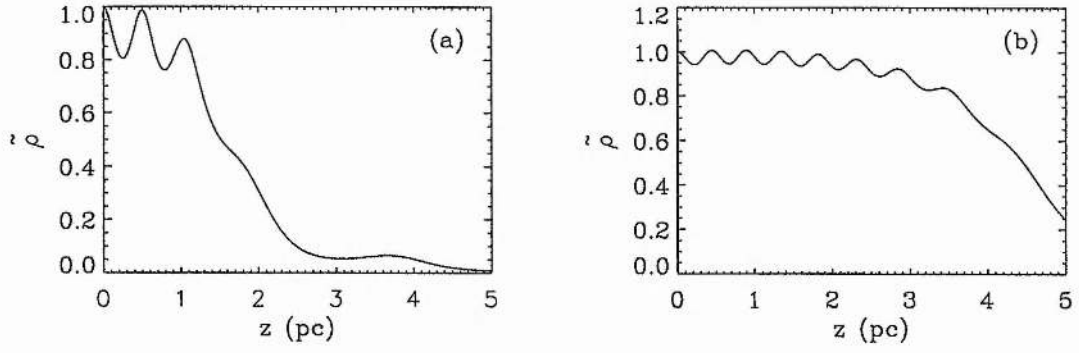

Figure 4.26: Mass density $\tilde{\rho}$ plotted against height z (pc) for $\delta = 10^{-1}$, $\tilde{k}_0 = 0.40$, $w_{0+} = 10^{-3}$, $\epsilon = 0.15$, $\gamma = 4$ and (a) $\alpha = 30$, $\beta = 5 \times 10^{-4}$ ($\Psi = 0.02$) and (b) $\alpha = 80$, $\beta = 3 \times 10^{-3}$ ($\Psi = 0.08$). Note that the strength of the source Ψ is varied to ensure that $\tilde{k}_0 = 0.40$ is valid (Eq. 4.57).

4.6 Discussion

The work in this chapter has investigated the role of long-wavelength Alfvén waves in supporting an isothermal low-mass star-forming region against its self-gravity. In its simplest form, using a δ-function source distribution in the absence of damping, this self-consistent one-dimensional model describes how the gas layer is divided into several subsheets which are held against the self-gravity of the layer by an Alfvén wave pressure force. The structure of the subsheets themselves is simply given by the equilibrium between their internal gas pressure and self-gravity. Increasing the initial value of the magnetic field perturbation and hence the Alfvén wave pressure (increasing the parameter α), or reducing the initial wavelength of the Alfvén waves (increasing the WKB approximation parameter δ) lessens the distinction between these subsheets and thus allows the waves to provide some support to the whole cloud. Indeed, in the absence of damping and without distributed sources, the distance of the first subsheet from the central, source plane is directly proportional to the initial wavelength of the Alfvén wave; the shorter the wavelength, the closer the first subsheet is to the centre of the layer.

The key factor in determining the role of the Alfvén waves and hence the structure of the gas layer is the importance of the Alfvén wave pressure within the mechanical equilibrium, specifically the magnitude of the derivative of this term. Long-wavelength, low-amplitude waves have a small Alfvén wave pressure gradient which is unable to offer support to the cloud as a whole, but which can support individual subsheets against the self-gravity of the layer. Either slightly reducing the wavelength or increasing the amplitude of the wave, or both, increases the gradient in wave pressure sufficiently for the waves to support the whole structure. Thus, if a molecular cloud is supported by low-amplitude waves which have wavelengths of the order of the size of the cloud, then a number of distinct subsheets are formed from the original slab. Simply increasing the amplitude of such waves allows the layer to remain as one structure.

The inclusion of damping in the model naturally reduces the ability for the Alfvén waves to support individual subsheets far from the central plane, and so more of the mass is found in the central regions of the cloud. However, as the damping becomes stronger there is actually a general increase in mass density away from the central plane to values higher than the central density. A similar effect was observed in Chapter 2 for strong values of the ion-neutral damping. This bump in density is made noticeably less significant by the introduction of a source function into the model. The Alfvén waves are generated within low-mass star-forming regions by the orbital motions of

large-scale condensations of gas, as discussed in Chapter 1. Such wave sources, which are likely to be related at different heights in the cloud, suggest the introduction of a completely coherent density-dependent source function within the model. The ability for all points within the gas layer to generate waves slightly enhances the support of the individual subsheets so that they are no longer simply supported by their gas pressure. A strong, narrow (high value for the index of the power law) source is the most efficient at reducing the general increase in mass density away from the central plane which can be caused by strong damping.

As in the WKB model presented in Chapter 2, the degree of support offered to the isothermal gas layer, in terms of the thickness of the layer in parsecs, is encouraging when compared to the observed values. For magnetic field perturbations which are consistent with the velocities observed in these regions, $\tilde{b} \simeq v/v_A \sim 0.2$, the thickness of the density profile is found to be of the order of a few parsecs, even in the absence of damping. Observations show that the diameters of such regions are in the range of a few to ten parsecs (Shu et al. 1987) which is in good agreement with the theoretical predictions in this chapter.

The presence of individual subsheets or artefacts (when there is support of the whole cloud) in the mass density profile raises the question of the stability of the cloud. In particular the possibility of a Rayleigh-Taylor type of instability, given that the subsheets are being supported solely by an Alfvénic pressure force.

In its entirety this self-consistent model successfully describes the support given to an isothermal gas layer by long-wavelength Alfvén waves. Although the approximations used within this model are not conducive to a direct comparison with observations, the waves are shown to offer support against the self-gravity of the layer, parallel to its ordered magnetic field. The thicknesses generated by this support are consistent with the observational values. This work, following on from that presented in Chapter 2 especially, further emphasises the importance of Alfvén waves within the mechanical equilibrium of low-mass star-forming regions.

4.6.1 A note on numerical accuracy

The equations describing the model (Equations (4.19) – (4.22) for a δ-function source, or Equations (4.47) – (4.53) for a density-dependent source) were solved as an initial-value problem using an adaptive step-size Runge-Kutta program. In the instances where the mass density fell to insignificant values between the subsheets the accuracy parameters used in the program slightly influenced the results with regard to the height (ζ) of the subsheets above the central plane. However, it is important to note that the

position of the peaks with respect to the gravity ($\tilde{g}$) remained unaffected. All of the results presented in this chapter were calculated to the same accuracy to ensure that no numerical bias was introduced.

Chapter 5

Stability analysis

Programming today is a race between software engineers striving to build bigger and better idiot-proof programs, and the Universe trying to produce bigger and better idiots. So far, the Universe is winning.

Rich Cook

Throughout the previous chapters various models have been presented in order to ascertain the significance of Alfvén waves in low-mass star-forming regions; specifically the role these magnetic waves play in supporting a molecular cloud against its self-gravity. Having established that a gas slab — which is in mechanical equilibrium between its self-gravity, the gas pressure and an Alfvén wave pressure force — can have thicknesses which are in good agreement with observational values, the question of the slab's stability must be considered: are such equilibria in fact unstable? This is the question which will begin to be addressed in this chapter. In the first instance, the stability of an infinite gas slab with a uniform magnetic field lying perpendicular to it will be considered (Nakano & Nakamura 1978; Nakano 1988). In this case the magnetic field does not influence the mechanical equilibrium of the slab, which is determined solely by the isothermal gas pressure and the self-gravity (see Chapter 1, Section 1.3). The viability of short-wavelength Alfvén wave support is clearly illustrated in Chapter 2, in particular when a distribution of wave sources is included within the model (Chapter 2, Section 2.4). The stability of such an equilibrium will be discussed in the latter half of this chapter.

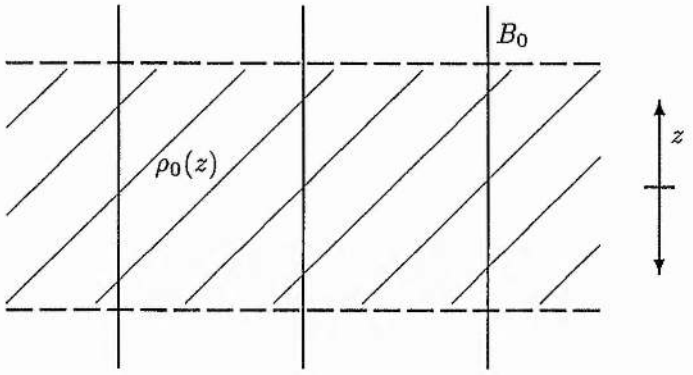

Figure 5.1: A representation of the equilibrium showing a gas slab with a constant magnetic field lying perpendicular to the sheet.

5.1 A gas-pressure-supported equilibrium

An isothermal gas slab with a constant magnetic field perpendicular to the sheet (see Figure 5.1) is supported against its self-gravity by the gas pressure. This equilibrium is described by the equation

$$\frac{\rho}{\rho_0} = \operatorname{sech}^2\left(\frac{z}{H}\right) \tag{5.1}$$

(Spitzer 1968; Eq. 1.28), where ρ is the mass density, z is the height above the central plane, $H = c^2/(\pi G \mathcal{M})$ is a scale-height, ρ_0 is the mass density at the central plane ($z = 0$), c is the sound speed, G is the gravitational constant and $\mathcal{M}$ is the column density. Such an equilibrium gives cloud thicknesses of the order of a tenth of a parsec (see Chapter 1, Section 1.3).

5.1.1 The equations

To study the stability of an isothermal gas slab as depicted in Figure 5.1 small perturbations are added to the equilibrium quantities so that the mass density, magnetic field strength, gravity and velocity are respectively described by

$$\rho = \rho_0(z) + \rho_1(\mathbf{r}, t)\,,$$

$$\mathbf{B} = B_0\,\hat{\mathbf{z}} + \mathbf{B}_1(\mathbf{r}, t)\,,$$

$$\mathbf{g} = -g_0(z)\,\hat{\mathbf{z}} + \mathbf{g}_1(\mathbf{r}, t)\,,$$

$$\mathbf{v} = \mathbf{v}_1(\mathbf{r}, t)\,,$$

where the equilibrium quantities are denoted by a subscript 0 and the perturbed quantities by a subscript 1. Substituting these expressions into the equations of magnetohydrodynamics, linearising and subtracting the equilibrium leaves the set of perturbed equations: the mass continuity equation (Eq. 1.14)

$$\frac{\partial \rho_1}{\partial t} + \nabla \cdot (\rho_0 \mathbf{v}_1) = 0\,, \tag{5.2}$$

the equation of motion (Eq. 1.15)

$$\rho_0 \frac{\partial \mathbf{v}_1}{\partial t} = -c^2 \nabla \rho_1 + (B_0 \hat{\mathbf{z}} \cdot \nabla) \frac{\mathbf{B}_1}{\mu} - \nabla \left(\frac{B_0 \hat{\mathbf{z}} \cdot \mathbf{B}_1}{\mu} \right) - \rho_1 g_0 \hat{\mathbf{z}} + \rho_0 \mathbf{g}_1\,, \tag{5.3}$$

the induction equation (Eq. 1.16)

$$\frac{\partial \mathbf{B}_1}{\partial t} = \nabla \times (\mathbf{v}_1 \times B_0 \hat{\mathbf{z}}) \tag{5.4}$$

and the self-gravitation equation (Eq. 1.17)

$$\nabla \cdot \mathbf{g}_1 = -4\pi G \rho_1\,. \tag{5.5}$$

These equations are Fourier analysed in time and space by writing the perturbed quantities in the form

$$\rho_1 = \hat{\rho}(z)\, \mathrm{e}^{i(\omega t - \mathbf{k}\cdot\mathbf{r}_\perp)} \tag{5.6}$$

for example, where $\mathbf{r}_\perp = (x, y)$, ω is the frequency and $\mathbf{k}$ is the wavenumber. As a result the perturbed equations become

$$i\omega\hat{\rho} - i\rho_0 (\mathbf{k} \cdot \hat{\mathbf{v}}_\perp) + \frac{d(\rho_0 \hat{v}_z)}{dz} = 0\,, \tag{5.7}$$

$$\begin{aligned} i\omega\rho_0 \hat{\mathbf{v}} = -c^2 \left(-i\hat{\rho} (k_x \hat{\mathbf{x}} + k_y \hat{\mathbf{y}}) + \frac{d\hat{\rho}}{dz} \hat{\mathbf{z}} \right) + \frac{B_0}{\mu} \frac{d\hat{\mathbf{B}}}{dz} \\ - \frac{B_0}{\mu} \left(-i\hat{B}_z (k_x \hat{\mathbf{x}} + k_y \hat{\mathbf{y}}) + \frac{d\hat{B}_z}{dz} \hat{\mathbf{z}} \right) - \hat{\rho} g_0 \hat{\mathbf{z}} + \rho_0 \hat{\mathbf{g}}\,, \end{aligned} \tag{5.8}$$

$$i\omega\hat{\mathbf{B}} = B_0 \left(\frac{d\hat{v}_x}{dz} \hat{\mathbf{x}} + \frac{d\hat{v}_y}{dz} \hat{\mathbf{y}} + i (\mathbf{k} \cdot \hat{\mathbf{v}}_\perp) \hat{\mathbf{z}} \right) \tag{5.9}$$

and finally

$$\frac{d\hat{g}_z}{dz} = i (\mathbf{k} \cdot \hat{\mathbf{g}}_\perp) - 4\pi G \hat{\rho}\,. \tag{5.10}$$

Equations (5.7) and (5.9) can be used to eliminate the perturbed mass density ($\hat{\rho}$) and magnetic field ($\hat{\mathbf{B}}$) respectively, from the remaining equations. The axes are chosen so

that the wavenumber lies in the x-direction $\mathbf{k} = k\hat{\mathbf{x}}$, and thus Equation (5.8) becomes in component form: the x-component

$$v_A^2 \frac{d^2\hat{v}_x}{dz^2} + \left(\omega^2 - k^2c^2 - k^2v_A^2\right)\hat{v}_x = ikc^2 \frac{1}{\rho_0}\frac{d\left(\rho_0\hat{v}_z\right)}{dz} + \omega k\hat{\phi}\,, \tag{5.11}$$

the y-component

$$v_A^2 \frac{d^2\hat{v}_y}{dz^2} + \omega^2\hat{v}_y = 0 \tag{5.12}$$

and the z-component

$$\omega^2\hat{v}_z + c^2\frac{d}{dz}\left(\frac{1}{\rho_0}\frac{d\left(\rho_0\hat{v}_z\right)}{dz}\right) = ikc^2\frac{d\hat{v}_x}{dz} + i\omega\frac{d\hat{\phi}}{dz}\,. \tag{5.13}$$

Note that the gravity (g) has been prescribed in terms of the gravitational potential $\hat{\phi}$,

$$\mathbf{g}_1 = -\nabla\phi_1$$

which implies that

$$\hat{\mathbf{g}}(z) = \left(ik\hat{\phi}(z),\ 0,\ -\frac{d\hat{\phi}}{dz}\right)\,, \tag{5.14}$$

and the equation of mechanical equilibrium (Eq. 1.26) has been used to express the equilibrium gravity in terms of the mass density, $g_0 = (-c^2/\rho_0)\,d\rho_0/dz$. Completing the set of equations is the self-gravitation equation (Eq. 5.10) which has now become

$$\frac{d^2\hat{\phi}}{dz^2} - k^2\hat{\phi} = \frac{4\pi G}{\omega}\left(\rho_0 k\hat{v}_x + i\frac{d\left(\rho_0\hat{v}_z\right)}{dz}\right)\,. \tag{5.15}$$

(This set of perturbed equations (Eqs 5.11 – 5.13 and 5.15) is in agreement with those of Nakano & Nakamura 1978.)

These equations are now written in dimensionless form, using

$$\tilde{v}_x = \frac{\hat{v}_x}{v_{A_0}} \quad , \quad \tilde{v}_y = \frac{\hat{v}_y}{v_{A_0}} \quad , \quad \tilde{v}_z = \frac{\hat{v}_z}{v_{A_0}}$$

for the perturbed velocities, where $v_{A_0} = B_0/\sqrt{\mu\rho_0(0)}$ is the equilibrium Alfvén velocity at the central plane and $\rho_0(0)$ is the equilibrium mass density at $z = 0$, plus

$$\zeta = \frac{z}{H} \quad , \quad \tilde{\rho}_0 = \frac{\rho_0}{\rho_0(0)} \quad , \quad \tilde{\phi} = \frac{\hat{\phi}}{4\pi GH^2\rho_0(0)}$$

for the height, equilibrium mass density and gravitational potential respectively, and finally

$$\tilde{k} = kH \quad , \quad \tilde{\omega} = \frac{\omega H}{v_{A_0}}$$

for the wavenumber and frequency, to leave

$$\frac{d^2\tilde{v}_x}{d\zeta^2} + \left(\tilde{\rho}_0\tilde{\omega}^2 - \beta\tilde{\rho}_0\tilde{k}^2 - \tilde{k}^2\right)\tilde{v}_x = i\beta\tilde{k}\,\frac{d\left(\tilde{\rho}_0\tilde{v}_z\right)}{d\zeta} + 2\beta\tilde{\rho}_0\tilde{\omega}\tilde{k}\tilde{\phi}\,, \tag{5.16}$$

$$\frac{d^2\tilde{v}_y}{d\zeta^2} + \tilde{\rho}_0\tilde{\omega}^2\tilde{v}_y = 0\,, \tag{5.17}$$

$$\frac{d}{d\zeta}\left(\frac{1}{\tilde{\rho}_0}\,\frac{d\left(\tilde{\rho}_0\tilde{v}_z\right)}{d\zeta}\right) + \frac{\tilde{\omega}^2}{\beta}\,\tilde{v}_z = i\tilde{k}\,\frac{d\tilde{v}_x}{d\zeta} + 2i\tilde{\omega}\,\frac{d\tilde{\phi}}{d\zeta} \tag{5.18}$$

and

$$\frac{d^2\tilde{\phi}}{d\zeta^2} - \tilde{k}^2\tilde{\phi} = \frac{\tilde{\rho}_0\tilde{k}\tilde{v}_x}{\tilde{\omega}} + \frac{i}{\tilde{\omega}}\,\frac{d\left(\tilde{\rho}_0\tilde{v}_z\right)}{d\zeta}\,, \tag{5.19}$$

where the dimensionless constant β is defined to be the ratio between the sound speed and the equilibrium Alfvén velocity at the central plane,

$$\beta = \frac{c^2}{v_{A_0}^2}\,. \tag{5.20}$$

Note that the equation describing the y-component of the velocity perturbation $\tilde{v}_y$ (Eq. 5.17) has decoupled[1], leaving a sixth-order system of equations which are to be solved to give the dispersion relation $\tilde{\omega}(\tilde{k})$ of an isothermal gas slab with a uniform magnetic field lying perpendicular to the sheet.

5.1.2 The asymptotic solution

As the magnitude of the height above the central plane (ζ) increases, the form of the equilibrium (Eq. 5.1) dictates that the equilibrium mass density (ρ_0) decreases to zero. This limit gives the asymptotic solution of the three second-order differential equations (Eqs 5.16, 5.18 and 5.19) describing the perturbations.

Firstly, Equations (5.16), (5.18) and (5.19) are written as a set of six coupled first-order equations by defining the variables

$$y_1 = \frac{\tilde{v}_x}{\tilde{\omega}} \quad , \quad y_2 = \tilde{\phi} \quad , \quad y_3 = \frac{i\tilde{v}_z}{\tilde{\omega}}$$

[1] Applying the substitution $z' = \tanh\zeta$ to Equation (5.17) leaves

$$(1 - z'^2)\,\frac{d^2\tilde{v}_y}{dz'^2} - z'\,\frac{d\tilde{v}_y}{dz'} + \tilde{\omega}^2\tilde{v}_y = 0\,,$$

a Legendre differential equation which can be solved separately (Murphy 1960) for the velocity perturbation in the y-direction ($\tilde{v}_y$) given a value for the frequency $\tilde{\omega}$. This equation will not give any additional unstable values for $\tilde{\omega}$, but will simply give solutions for $\tilde{v}_y$ which are in accordance with the dispersion relation $\tilde{\omega}(\tilde{k})$ found from Equations (5.16), (5.18) and (5.19).

$$y_4 = \frac{1}{\tilde{\omega}} \frac{d\tilde{v}_x}{d\zeta} \quad , \quad y_5 = \frac{i}{\tilde{\rho}_0 \tilde{\omega}} \frac{d(\tilde{\rho}_0 \tilde{v}_z)}{d\zeta} \quad , \quad y_6 = \frac{d\tilde{\phi}}{d\zeta}$$

so that

$$\frac{dy_1}{d\zeta} = y_4 \tag{5.21}$$

$$\frac{dy_2}{d\zeta} = y_6 \tag{5.22}$$

$$\frac{dy_3}{d\zeta} = 2\tilde{g}_0 y_3 + y_5 \tag{5.23}$$

$$\frac{dy_4}{d\zeta} = 2\beta\tilde{\rho}_0\tilde{k} y_2 - \left(\tilde{\rho}_0\tilde{\omega}^2 - \beta\tilde{\rho}_0\tilde{k}^2 - \tilde{k}^2\right) y_1 + \beta\tilde{\rho}_0\tilde{k} y_5 \tag{5.24}$$

$$\frac{dy_5}{d\zeta} = -\frac{\tilde{\omega}^2}{\beta} y_3 - \tilde{k} y_4 - 2 y_6 \tag{5.25}$$

$$\frac{dy_6}{d\zeta} = \tilde{\rho}_0\tilde{k} y_1 + \tilde{k}^2 y_2 + \tilde{\rho}_0 y_5 , \tag{5.26}$$

where $\tilde{g}_0 = g_0/g_0(\zeta \to \infty)$ is the dimensionless equilibrium gravity.

In the limit as $\zeta \to \pm\infty$ the mass density $\tilde{\rho}_0 \to 0$ and the gravity $\tilde{g}_0 \to \pm 1$ and hence the above equations become, in matrix form,

$$\begin{pmatrix} y_1' \\ y_2' \\ y_3' \\ y_4' \\ y_5' \\ y_6' \end{pmatrix} = \begin{pmatrix} 0 & 0 & 0 & 1 & 0 & 0 \\ 0 & 0 & 0 & 0 & 0 & 1 \\ 0 & 0 & \pm 2 & 0 & 1 & 0 \\ \tilde{k}^2 & 0 & 0 & 0 & 0 & 0 \\ 0 & 0 & -\tilde{\omega}^2/\beta & -\tilde{k} & 0 & -2 \\ 0 & \tilde{k}^2 & 0 & 0 & 0 & 0 \end{pmatrix} \begin{pmatrix} y_1 \\ y_2 \\ y_3 \\ y_4 \\ y_5 \\ y_6 \end{pmatrix} \tag{5.27}$$

i.e.

$$y_i' = \mathrm{M}\, y_i \qquad \text{for } i = 1, 2, \ldots, 6 \tag{5.28}$$

where a $'$ indicates the derivative with respect to ζ. The asymptotic matrix M contains constant coefficients and thus Equation (5.28) has the solution

$$y_i = \sum_i C_i \mathbf{u}_i \, e^{\Lambda_i \zeta} \qquad \text{for } i = 1, 2, \ldots, 6 \tag{5.29}$$

where C_i are the scaling coefficients, Λ_i are the eigenvalues of the matrix M,

$$+\tilde{k}, \; +\tilde{k}, \; -\tilde{k}, \; -\tilde{k}, \; +1 \pm \sqrt{1 - \tilde{\omega}^2/\beta}$$

as $\zeta \to +\infty$ and

$$+\tilde{k}, \; +\tilde{k}, \; -\tilde{k}, \; -\tilde{k}, \; -1 \pm \sqrt{1 - \tilde{\omega}^2/\beta}$$

as $\zeta \to -\infty$, and u_i are the associated eigenvectors.

5.1.3 Boundary conditions and the numerical method

The set of equations describing the perturbations (Eqs 5.21 – 5.26) are solved with the boundary conditions

$$y_i \to 0 \qquad \text{as} \qquad \zeta \to \pm\infty$$

for $i = 1, 2, \ldots, 6$. Considering the asymptotic solution these boundary conditions are satisfied by choosing the decaying eigenvalues as $\zeta \to \pm\infty$. Specifically as $\zeta \to +\infty$ the negative eigenvalues

$$-\tilde{k}, \ -\tilde{k}, \ +1 - \sqrt{1 - \tilde{\omega}^2/\beta}$$

are required, while as $\zeta \to -\infty$ the positive eigenvalues

$$+\tilde{k}, \ +\tilde{k}, \ -1 + \sqrt{1 - \tilde{\omega}^2/\beta}$$

are taken. (These are the appropriate eigenvalues given that the form taken for the perturbations (Eq. 5.6) implies that $\tilde{\omega}^2 < 0$ for the unstable regime.) Choosing the decaying eigenvalues gives the asymptotic solution as

$$\begin{pmatrix} y_1 \\ y_2 \\ y_3 \\ y_4 \\ y_5 \\ y_6 \end{pmatrix} = C_1 \begin{pmatrix} 1 \\ 0 \\ A\tilde{k}^2 \\ -\tilde{k} \\ -A\tilde{k}^2(2+\tilde{k}) \\ 0 \end{pmatrix} e^{-\tilde{k}\zeta_{max}} + C_2 \begin{pmatrix} 0 \\ 1 \\ 2A\tilde{k} \\ 0 \\ -2A\tilde{k}(2+\tilde{k}) \\ -\tilde{k} \end{pmatrix} e^{-\tilde{k}\zeta_{max}}$$

$$+ C_3 \begin{pmatrix} 0 \\ 0 \\ 1 \\ 0 \\ -\left(1 + \sqrt{1 - \tilde{\omega}^2/\beta}\right) \\ 0 \end{pmatrix} e^{\left(1 - \sqrt{1 - \tilde{\omega}^2/\beta}\right)\zeta_{max}} \qquad (5.30)$$

for $\zeta \to +\infty$ ($\zeta = \zeta_{max}$), and as

$$\begin{pmatrix} y_1 \\ y_2 \\ y_3 \\ y_4 \\ y_5 \\ y_6 \end{pmatrix} = D_1 \begin{pmatrix} 1 \\ 0 \\ -A\tilde{k}^2 \\ \tilde{k} \\ -A\tilde{k}^2(2+\tilde{k}) \\ 0 \end{pmatrix} e^{\tilde{k}\zeta_{min}} + D_2 \begin{pmatrix} 0 \\ 1 \\ -2A\tilde{k} \\ 0 \\ -2A\tilde{k}(2+\tilde{k}) \\ \tilde{k} \end{pmatrix} e^{\tilde{k}\zeta_{min}}$$

$$+ D_3 \begin{pmatrix} 0 \\ 0 \\ 1 \\ 0 \\ 1+\sqrt{1-\tilde{\omega}^2/\beta} \\ 0 \end{pmatrix} e^{\left(-1+\sqrt{1-\tilde{\omega}^2/\beta}\right)\zeta_{min}} \tag{5.31}$$

for $\zeta \to -\infty$ ($\zeta = \zeta_{min}$), where $A = 1/[\tilde{\omega}^2/\beta + \tilde{k}(2+\tilde{k})]$. Therefore there are six free parameters at the boundaries, C_1, C_2, C_3, D_1, D_2 and D_3, which correspond to the six first-order differential equations (Eqs 5.21 – 5.26). Given that this set of equations is linear, and hence multiples of solutions are solutions themselves, five of the asymptotic coefficients can be normalised with respect to the sixth (e.g. $C_3 = 1$). Thus, for each value of the wavenumber $\tilde{k}$ and the dimensionless parameter β the equations can only be solved, to give a non-trivial solution, for special values of $\tilde{\omega}^2$, giving the dispersion relation $\tilde{\omega}(\tilde{k})$ for each plasma beta (see also Fleischer 1996).

The dispersion relation is found numerically by the relaxation method (Press et al. 1992). The equations describing the perturbations (Eqs 5.21 – 5.26) are written as a set of finite difference equations, for example Equation (5.21) becomes

$$\mathrm{y}_1^{\mathrm{k}} - \mathrm{y}_1^{\mathrm{k-1}} - \frac{\Delta\zeta}{2}\left(\mathrm{y}_4^{\mathrm{k}} + \mathrm{y}_4^{\mathrm{k-1}}\right) = 0\,, \tag{5.32}$$

where $\Delta\zeta$ is the spacing between the grid points (k). The boundaries are set at a finite value $\zeta = \pm 20$, at which point the equilibrium mass density ($\tilde{\rho}_0$) has become negligible (Eq. 5.1; Nakano 1988). Eliminating the five remaining coefficients (C_1, C_2, D_1, D_2 and D_3) from the asymptotic solutions (Eqs 5.30 and 5.31) leaves a set of seven equations at the boundaries which need to be satisfied by the numerical solution of Equations (5.21) – (5.26), i.e. the problem is over-specified. By introducing the square of the frequency ($\tilde{\omega}^2$) as an additional variable, y_7 say, through the finite-difference equation

$$\mathrm{y}_7^{\mathrm{k}} - \mathrm{y}_7^{\mathrm{k-1}} = 0\,, \tag{5.33}$$

there is now a set of seven equations (Eqs 5.21 – 5.26 and 5.33) to match the seven boundary conditions. In this way the value of $\tilde{\omega}^2$ for each wavenumber $\tilde{k}$ and parameter β is obtained as part of the numerical solution.

5.1.4 Results

The dispersion curves obtained by solving the perturbed equations (Eqs 5.21 – 5.26) are shown in Figure 5.2 for different values of the dimensionless parameter β. Note

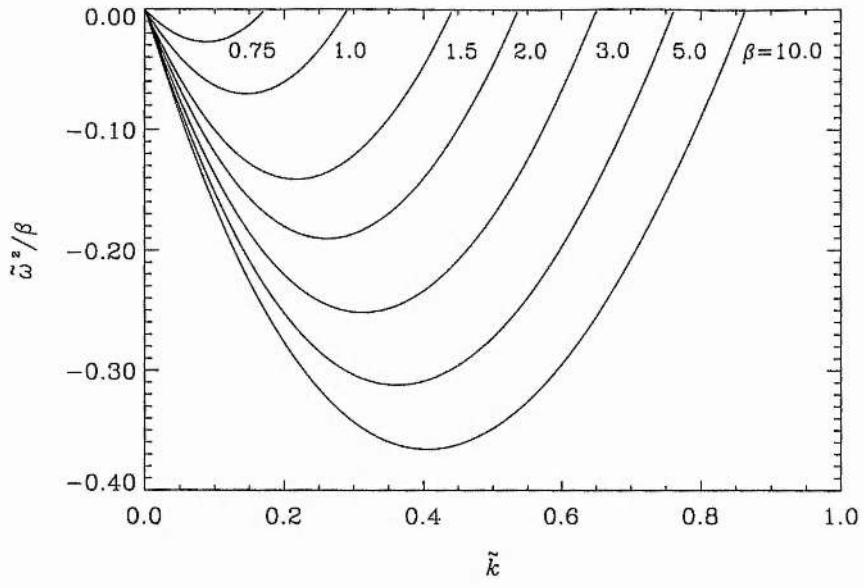

Figure 5.2: The dispersion curves for an isothermal gas slab with a constant magnetic field lying perpendicular to the sheet. The dimensionless parameter β is the ratio between the sound speed and equilibrium Alfvén velocity at the central plane ($\zeta = 0$) (see Eq. 5.20).

that the curves shown are for the minimum value of the square of the frequency ($\tilde{\omega}^2$) (the fundamental frequency) at each value of the wavenumber $\tilde{k}$. As can be seen from Equation (5.20) a value of $\beta = 1$ implies that the Alfvén and sound speeds are equal, whereas $\beta < 1$ means that the central Alfvén velocity of the equilibrium is greater than the sound speed, suggesting that the magnetic field is becoming increasingly important in the cloud dynamics. The dispersion curves show that the isothermal gas slab becomes more stable as the value of β decreases. Indeed, at a value of $\beta = 0.5$, which corresponds to the equilibrium Alfvén velocity at the central plane ($\zeta = 0$) being twice the isothermal sound speed (the magnetic pressure equalling the gas pressure), the gas sheet becomes stable for all values of the wavenumber $\tilde{k}$. Such a result shows that the magnetic field has a stabilising influence on the isothermal gas layer (see also Nakano 1988).

Figure 5.3 shows how the critical wavenumber ($\tilde{k}_c$), that for which the frequency $\tilde{\omega} = 0$, varies as the Alfvén velocity becomes significantly less important compared to the sound speed (in other words as the parameter β is increased to very large values). As can be seen both from Figure 5.2 and, in particular from Figure 5.3, the cut-off value for the critical wavenumber is equal to unity ($\tilde{k}_{cut} = 1$), i.e. if $\tilde{k} < 1$ then there can be gravitational instability depending upon the value of β. This cut-off wave number

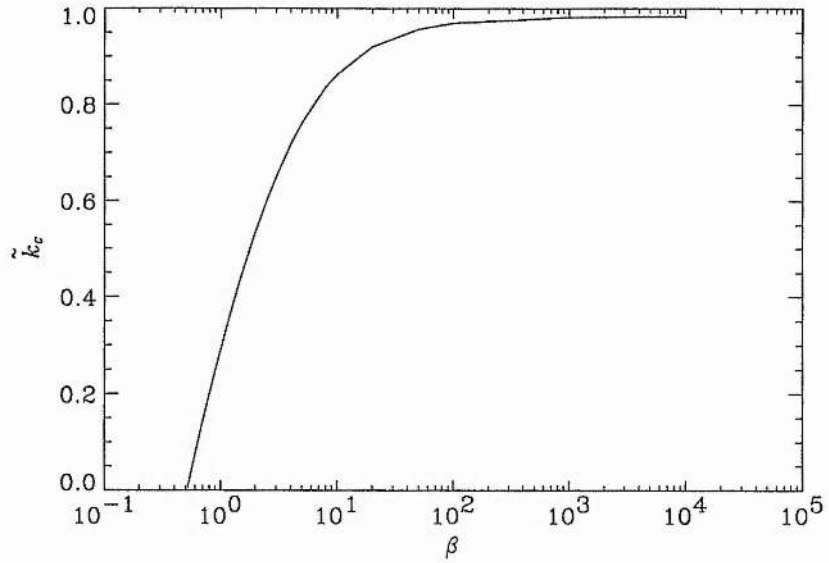

Figure 5.3: The critical wavenumber $\tilde{k}_c$, that for which the frequency $\tilde{\omega} = 0$, plotted against the dimensionless parameter β (Eq. 5.20). A cut-off value of $\tilde{k}_{cut} = 1$ is reached at very large β, as the significance of the magnetic field diminishes.

corresponds to a cut-off length of

$$L_{cut} = \frac{\pi}{k_{cut}} = \pi H \,,$$

which is the minimum length a condensation must have before it can become gravitationally unstable (see also Spitzer 1968). It is interesting to note that this length is greater than the thickness of the isothermal gas sheet, which is found to be $\simeq 2H$ (see Chapter 1, Section 1.3), and therefore precludes any instabilities from being generated by velocities which are solely in the z-direction $(v_z)^2$. Equivalently, it is not possible to have an instability if the magnetic field remains unperturbed ($\mathbf{B}_1 = 0$) as can clearly be seen from the linearised equations (Eqs 5.2 – 5.5); see Appendix B for further details.

In summary, the perturbation analysis has shown that the uniform magnetic field can stabilise the isothermal gas slab against gravitational instabilities, reaching a state of complete stability when the magnetic and gas pressures are equal ($\beta = 0.5$). Given that typical observations set the sound speed to $c \sim 0.2\,\mathrm{km\,s^{-1}}$ and the Alfvén speed to

[2]The same result was obtained for the stability of an infinite gaseous disk (without a magnetic field) by Spitzer (1968). He too found that it was not possible to generate any instabilities in the disk from motions which are only in the z-direction. This is clear given that the introduction of a uniform magnetic field, perpendicular to the sheet, does not affect the mechanical equilibrium parallel to that field (the z-direction in the notation used in this chapter).

$v_A \sim 4.5\,\mathrm{km\,s^{-1}}$ (see Chapter 1, Section 1.1), the value of the parameter β in low-mass star-forming regions is $\beta \sim 10^{-3}$, which is very encouraging for the stability of these regions.

5.2 A wave-pressure-supported equilibrium

The question of the stability of a gas slab supported by Alfvén waves will now be considered. The viability of short-wavelength Alfvén wave support is clearly illustrated in Chapters 2 and 3, while Chapter 4 considers the role of long-wavelength Alfvén waves in supporting a low-mass star-forming region.

The stability analysis of an equilibrium supported by waves proves to be even more involved than that of an equilibrium containing a uniform magnetic field (discussed in the previous section) and as a result only one class of equilibrium will be considered here. Of the equilibria examined in the preceeding chapters, the model describing short-wavelength (WKB) Alfvén wave support using a distributed wave source (Chapter 2, Section 2.4) is chosen for the stability analysis. Such an equilibrium, although assumed to be isothermal in nature, is certainly a more realistic approximation than the equilibrium generated using a δ-function source distribution for the waves (Chapter 2, Section 2.1). Indeed, a δ-function model contains a discontinuity at the central source plane which would require the inclusion of an internal boundary condition, hence complicating the numerical approach described in the previous section. The formulation of a suitable numerical method is considered to be unnecessary given the comparative ease with which a density-dependent source distribution can be introduced and the subsequent improvement in the equilibrium model.

A perturbation analysis of a system already supporting WKB waves is conceivable given that the global effect of the waves can be ascertained by averaging over the wave fluctuations (Dewar 1970). However, such an averaging is not possible in an equilibrium supported by Alfvén waves which have wavelengths similar to the length-scale of the non-uniform medium in which they propagate, and thus a perturbation analysis as carried out in this chapter would seem to be infeasible. Therefore, the following analysis will examine the stability of an isothermal gas layer which is in equilibrium between its self-gravity, the gas pressure and an Alfvén wave pressure force; this pressure force results from a density-dependent distribution of short-wavelength Alfvén wave sources.

5.2.1 The equilibrium revisited

In this section the equilibrium, which is discussed in detail in Chapter 2, will be briefly reviewed. During the analysis of the perturbed equations (in Section 5.2.3) it will become necessary to understand the behaviour of the equilibrium as the height above the central plane becomes increasingly large, i.e. as $z \rightarrow \pm\infty$. Consequently, the form of the equilibrium equations at large z will be considered in this section.

In contrast to Chapter 2 the wave energy density, previously labelled U (Chapter 2, Section 2.2.1), is now denoted by $\varepsilon = U/2$ and thus the waves propagating out from the source in the positive and negative z-directions have energy densities of ε_+ and ε_- respectively. Hence the equilibrium is described by the two wave propagation equations

$$\frac{d}{dz}\left(\frac{F}{\sqrt{\rho/\rho_0}}\right) = -\frac{\Gamma}{v_{A_0}}\varepsilon + \mathrm{S} \tag{5.34}$$

and

$$\frac{d}{dz}\left(\frac{\varepsilon}{\sqrt{\rho/\rho_0}}\right) = -\frac{\Gamma}{v_{A_0}}F, \tag{5.35}$$

plus the equilibrium equation

$$\frac{d}{dz}\left(\rho c^2 + \frac{\varepsilon}{2}\right) = -\rho g \tag{5.36}$$

and the self-gravitation equation

$$\frac{dg}{dz} = 4\pi G\rho, \tag{5.37}$$

where z is the height above the central plane, ρ is the mass density, $F = \varepsilon_+ - \varepsilon_-$ is the difference in the wave energy densities, $\varepsilon = \varepsilon_+ + \varepsilon_-$ is the total wave energy density, Γ is the ion-neutral friction damping rate (Chapter 1, Section 1.4), $v_{A_0} = B_0/\sqrt{\mu\rho_0}$ is the Alfvén velocity at the central plane, g is the gravity, c is the isothermal sound speed and G is the gravitational constant. The source function S is given by the expression

$$\mathrm{S} = \Psi\frac{\varepsilon_0}{H}\left(\frac{\rho}{\rho_0}\right)^{\gamma}, \tag{5.38}$$

in which Ψ and γ are the dimensionless source parameters, ε_0 is the total wave energy density at the central plane and $H = \sqrt{c^2/2\pi G\rho_0}$ is a scale-height.

The set of dimensionless variables is defined as

$$\zeta = \frac{z}{H} \quad , \quad \tilde{\rho} = \frac{\rho}{\rho_0} \quad , \quad \tilde{\varepsilon} = \frac{\varepsilon}{\varepsilon_0} \quad , \quad \tilde{F} = \frac{F}{\varepsilon_0} \quad , \quad \tilde{g} = \frac{g}{g_\infty}$$

where $g_\infty = g\,(z \rightarrow \infty)$. Note that the difference in the wave energy densities will be equal to zero at the central plane ($F_0 = 0$) as the symmetry of the equilibrium

means that there will be an equal number of positively and negatively propagating waves; hence $\tilde{F} = F/\varepsilon_0$. In terms of these new variables the equations describing the equilibrium (Eqs 5.34 – 5.37) become

$$\frac{d}{d\zeta}\left(\frac{\tilde{F}}{\sqrt{\tilde{\rho}}}\right) = -\Upsilon\frac{\tilde{\varepsilon}}{\sqrt{\tilde{\rho}}} + \Psi\tilde{\rho}^{\gamma}, \tag{5.39}$$

$$\frac{d}{d\zeta}\left(\frac{\tilde{\varepsilon}}{\sqrt{\tilde{\rho}}}\right) = -\Upsilon\frac{\tilde{F}}{\sqrt{\tilde{\rho}}}, \tag{5.40}$$

$$\frac{d\left(\tilde{\rho} + \lambda\tilde{\varepsilon}\right)}{d\zeta} = -2\sqrt{1+\lambda}\,\tilde{\rho}\tilde{g} \tag{5.41}$$

and

$$\frac{d\tilde{g}}{d\zeta} = \frac{1}{\sqrt{1+\lambda}}\,\tilde{\rho}, \tag{5.42}$$

where

$$\Upsilon = \frac{\kappa H}{v_{A_0}} = kH \tag{5.43}$$

is the damping parameter and

$$\lambda = \frac{\varepsilon_0}{2\rho_0 c^2} \tag{5.44}$$

(see Eq. 2.30) is the magnetisation parameter. Note that λ is identical to the magnetisation parameter defined in Chapter 2, while the damping is now a dimensionless parameter and is given by the expression

$$\Upsilon = 1.32\left(\frac{\tau}{10^5\ \mathrm{yr}}\right)^{-2}\left(\frac{B_0}{10\ \mathrm{nT}}\right)^{-1}\left(\frac{c}{0.25\ \mathrm{km\,s^{-1}}}\right)\left(\frac{n_{H_2}}{10^9\ \mathrm{m^{-3}}}\right)^{-\frac{1}{2}}. \tag{5.45}$$

By noting the minimum and maximum wave periods, which allow some Alfvén wave support of a molecular cloud (see Chapter 1, Section 1.4), the range of values for the damping is found to be $\Upsilon \sim 0.01 - 1.0$.

As the height above the central plane increases up to very large values (as $\zeta \to \pm\infty$), and hence the mass density diminishes to zero ($\tilde{\rho} \to 0$), there will be three ratios of equilibrium quantities which will be of interest when considering the asymptotic solution of the perturbation equations (see Section 5.2.3). These are the ratio between the total wave energy density and the mass density

$$R_1 = \frac{\tilde{\varepsilon}}{\tilde{\rho}}, \tag{5.46}$$

the ratio between the derivative of the mass density with respect to height and the mass density

$$R_2 = \frac{1}{\tilde{\rho}}\frac{d\tilde{\rho}}{d\zeta} \tag{5.47}$$

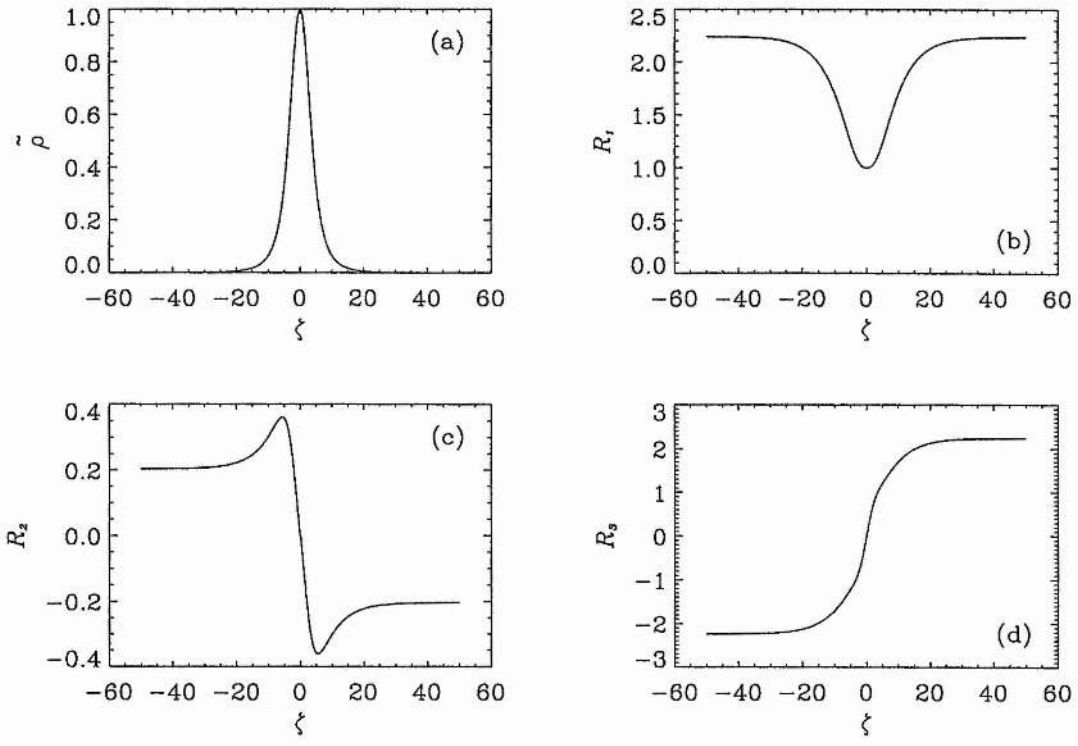

Figure 5.4: (a) The dimensionless mass density $\tilde{\rho}$, (b) the ratio $R_1 = \tilde{\varepsilon}/\tilde{\rho}$, (c) the ratio $R_2 = (1/\tilde{\rho})\, d\tilde{\rho}/d\zeta$ and (d) the ratio $R_3 = \tilde{F}/\tilde{\rho}$ plotted against the dimensionless height ζ for typical values of the magnetisation parameter $\lambda = 20$, the damping parameter $\Upsilon = 0.1$ and the power-law index of the source function $\gamma = 3$. These ratios tend towards a constant value as the height above the central plane increases to large values and, consequently, the mass density decreases to zero.

and, lastly, the ratio between the difference in the energy densities of the positively and negatively propagating waves and the mass density

$$R_3 = \frac{\tilde{F}}{\tilde{\rho}}\,. \tag{5.48}$$

The form of these three ratios is plotted in Figure 5.4 using the numerical solution of the equilibrium. As can be seen from the graphs each of the ratios reaches a constant value when the height above the central plane becomes sufficiently large.

The two wave equations (Eqs 5.39 and 5.40) can be written as

$$\frac{d}{d\zeta}\left(\frac{\tilde{F}}{\tilde{\rho}}\right) + \frac{\tilde{F}}{2\tilde{\rho}^2}\,\frac{d\tilde{\rho}}{d\zeta} = -\Upsilon\frac{\tilde{\varepsilon}}{\tilde{\rho}} + \Psi\tilde{\rho}^{\gamma-\frac{1}{2}} \tag{5.49}$$

and

$$\frac{d}{d\zeta}\left(\frac{\tilde{\varepsilon}}{\tilde{\rho}}\right)+\frac{\tilde{\varepsilon}}{2\tilde{\rho}^2}\frac{d\tilde{\rho}}{d\zeta}=-\Upsilon\frac{\tilde{F}}{\tilde{\rho}}\,, \tag{5.50}$$

which in the limit as $\zeta \rightarrow \pm\infty$ become

$$R_2R_3=-2\Upsilon R_1 \tag{5.51}$$

and

$$R_1R_2=-2\Upsilon R_3 \tag{5.52}$$

respectively. Eliminating the ratio R_2 between Equations (5.51) and (5.52) shows simply that

$$R_3=\pm R_1\,. \tag{5.53}$$

Specifically, as can be seen from Figure 5.4, $R_3=R_1$ at $\zeta\rightarrow+\infty$ whereas $R_3=-R_1$ at $\zeta\rightarrow-\infty$. When the density has fallen to sufficiently small values it is possible to infer that there will be no more wave sources. At this point any waves remaining in the system will be propagating outwards from the central plane, i.e. $\varepsilon_-\simeq 0$ at $\zeta\rightarrow+\infty$ and $\varepsilon_+\simeq 0$ at $\zeta\rightarrow-\infty$, and hence it can be deduced that $\tilde{F}=\tilde{\varepsilon}$ ($R_3=R_1$) at large heights above the central plane ($\zeta\rightarrow+\infty$) and $\tilde{F}=-\tilde{\varepsilon}$ ($R_3=-R_1$) at large heights below the central plane ($\zeta\rightarrow-\infty$) (from the definitions given below Equation (5.37)). Substituting this result back into Equation (5.51) say, gives an expression for the ratio R_2 of

$$R_2=\begin{cases}-2\Upsilon & \text{at } \zeta\rightarrow+\infty\\ +2\Upsilon & \text{at } \zeta\rightarrow-\infty\end{cases}\,. \tag{5.54}$$

The equilibrium equation (Eq. 5.41), when the height above the central plane is very large, is given by the expression

$$R_2+\lambda\left(\frac{1}{\tilde{\rho}}\frac{d\tilde{\varepsilon}}{d\zeta}\right)_{\zeta\rightarrow\pm\infty}=-2\sqrt{1+\lambda}\,\tilde{g}_\infty\,, \tag{5.55}$$

where $\tilde{g}_\infty=\pm1$ at $\zeta\rightarrow\pm\infty$. Equation (5.40) can be used to eliminate the derivative $d\varepsilon/d\zeta$ from the above equation to leave

$$R_2+2\sqrt{1+\lambda}\,\tilde{g}_\infty=-\lambda\left(\frac{R_1R_2}{2}-\Upsilon R_3\right)\,, \tag{5.56}$$

which reduces to an expression for the ratio between the total wave energy density and the mass density (R_1) in terms of the magnetisation and damping parameters, of

$$R_1=\frac{\sqrt{1+\lambda}-\Upsilon}{\Upsilon\lambda}\,. \tag{5.57}$$

The above equations and expressions describe an isothermal gas slab which is in equilibrium between its self-gravity, the gas pressure and a WKB Alfvén wave pressure force, with an emphasis on the behaviour of this equilibrium as the height above the central plane becomes very large. These results will be employed in the following sections where the question of the stability of this equilibrium will be considered.

5.2.2 The equations

For waves propagating in a non-uniform medium, which have a wavelength much shorter than the length-scale of the medium (the WKB approximation), it is possible to average over the wave fluctuations to give an equation of motion,

$$\rho \frac{\partial \mathbf{v}}{\partial t} + \rho (\mathbf{v} \cdot \nabla)\mathbf{v} = -\nabla P + (\mathbf{B} \cdot \nabla) \frac{\mathbf{B}}{\mu} - \nabla \left(\frac{B^2}{2\mu} \right) + \rho \mathbf{g} - \nabla \cdot \mathbf{P}_w , \tag{5.58}$$

that describes the motion of the system *including* the effect of the waves (Dewar 1970). Such an equation of motion describes the equilibrium state. In Equation (5.58) the effect of the waves on the medium is expressed through the wave stress tensor $\mathbf{P}_w$, which is given by

$$\mathbf{P}_w = \varepsilon_w \left[\hat{\mathbf{k}}\hat{\mathbf{k}} + \frac{1}{2} \left((1 - 2\hat{\mathbf{B}}\hat{\mathbf{B}}) v_A^2 \frac{\partial}{\partial v_A^2} + (\gamma - 1)\mathbf{1} c^2 \frac{\partial}{\partial c^2} + (\hat{\mathbf{B}}\hat{\mathbf{B}} - \hat{\mathbf{k}}\hat{\mathbf{k}}) \mu \frac{\partial}{\partial \mu} \right) \ln v_{ph}^2 \right] \tag{5.59}$$

(Dewar 1970; Jacques 1977), where $\hat{\mathbf{k}}$ and $\hat{\mathbf{B}}$ are the unit vectors in the direction of the wavenumber and the magnetic field respectively, ε_w is the wave energy density, v_A is the Alfvén velocity, c is the sound speed, $\mu = \hat{\mathbf{k}} \cdot \hat{\mathbf{B}}$, v_{ph} is the phase velocity, γ is the ratio of specific heats and $\mathbf{1}$ is the unit tensor. For Alfvén waves, whose phase velocity is given by the expression

$$v_{ph} = v_A \cos\theta$$

($\cos\theta = \hat{\mathbf{k}} \cdot \hat{\mathbf{B}}$), the wave pressure tensor simply reduces to

$$\mathbf{P}_w = \frac{\varepsilon_w}{2} \mathbf{1} . \tag{5.60}$$

The associated wave equation,

$$\frac{\partial S_w}{\partial t} + \nabla \cdot (\mathbf{v}_g S_w) = -\Gamma S_w \tag{5.61}$$

(Dewar 1970; Jacques 1977), is given in terms of the wave action density S_w which is related to the wave energy density in a static medium by

$$S_w = \frac{\varepsilon_w}{\omega}$$

(see also McKee & Zweibel 1995), where ω is the frequency of the background waves. Thus in terms of ε_w the wave equation becomes

$$\frac{\partial \varepsilon_w}{\partial t} + \nabla \cdot (\mathbf{v}_g \varepsilon_w) = -\Gamma \varepsilon_w \,, \tag{5.62}$$

where $\mathbf{v}_g$ is the group velocity and Γ is the damping rate.

The equilibrium model discussed above contains a density-dependent source function S (Eq. 5.38) which generates waves that propagate in opposite directions, i.e. in both the positive and negative z-directions. Accordingly there are two wave equations, each describing the propagation in one direction,

$$\frac{\partial \varepsilon_+}{\partial t} + \nabla \cdot (\mathbf{v}_g \varepsilon_+) = -\Gamma \varepsilon_+ + \frac{\mathrm{S}}{2} \tag{5.63}$$

for positively propagating waves and

$$\frac{\partial \varepsilon_-}{\partial t} - \nabla \cdot (\mathbf{v}_g \varepsilon_-) = -\Gamma \varepsilon_- + \frac{\mathrm{S}}{2} \tag{5.64}$$

for the negatively propagating waves, given that $\mathbf{v}_g$ is the group velocity of the positively propagating waves. In addition the wave stress tensor for Alfvén waves becomes

$$\mathbf{P}_w = \frac{\varepsilon_+ + \varepsilon_-}{2} \mathbf{1} \,. \tag{5.65}$$

Adding and subtracting these two wave equations (Eqs 5.63 and 5.64) gives

$$\frac{\partial \varepsilon}{\partial t} + \nabla \cdot (\mathbf{v}_g F) = -\Gamma \varepsilon + \mathrm{S} \tag{5.66}$$

and

$$\frac{\partial F}{\partial t} + \nabla \cdot (\mathbf{v}_g \varepsilon) = -\Gamma F \,, \tag{5.67}$$

in terms of the familiar variables $\varepsilon = \varepsilon_+ + \varepsilon_-$ for the total wave energy density and $F = \varepsilon_+ - \varepsilon_-$ for the difference in the wave energy densities.

If the equation of motion (Eq. 5.58) and the wave equations (Eqs 5.66 and 5.67) are considered within the framework of the isothermal equilibrium model — where the mass density $\rho = \rho_0(z)$, the magnetic field $\mathbf{B} = B_0 \hat{\mathbf{z}}$, the velocity $\mathbf{v} = 0$, the gravity $\mathbf{g} = -g_0(z) \hat{\mathbf{z}}$, and the wave energy densities $\varepsilon = \varepsilon_0(z)$ and $F = F_0(z)$ — they easily reduce to the equilibrium equations: the equation of motion (Eq. 5.36)

$$c^2 \frac{d\rho}{dz} + \frac{d}{dz}\left(\frac{\varepsilon}{2}\right) = -\rho g$$

and the two wave equations (see Eqs 5.34 and 5.35)

$$\frac{d}{dz}\left(\frac{B_0}{\sqrt{\mu \rho_0}} F_0\right) = -\Gamma \varepsilon_0 + \mathrm{S}$$

and

$$\frac{d}{dz}\left(\frac{B_0}{\sqrt{\mu\rho_0}}\,\varepsilon_0\right) = -\Gamma F_0\,,$$

where μ is the permeability of free space.

To study the stability of an Alfvén wave pressure supported equilibrium small perturbations are added to the equilibrium quantities, viz:

$$\rho = \rho_0(z) + \rho_1(\mathbf{r},t)\,,$$

$$\mathbf{B} = B_0\,\hat{\mathbf{z}} + \mathbf{B}_1(\mathbf{r},t)\,,$$

$$\mathbf{g} = -g_0(z)\,\hat{\mathbf{z}} + \mathbf{g}_1(\mathbf{r},t)\,,$$

$$\mathbf{v} = \mathbf{v}_1(\mathbf{r},t)\,,$$

$$\varepsilon = \varepsilon_0(z) + \varepsilon_1(\mathbf{r},t)\,,$$

$$F = F_0(z) + F_1(\mathbf{r},t)\,,$$

$$\mathbf{P}_w = \frac{\varepsilon_0(z)}{2}\,\mathbf{1} + \mathbf{P}_{w_1}(\mathbf{r},t)\,,$$

where subscripts 0 and 1 denote the equilibrium and perturbed quantities respectively. The perturbations are chosen to be Alfvénic in nature and so the perturbed wave stress tensor is simply

$$\mathbf{P}_{w_1} = \frac{\varepsilon_1(\mathbf{r},t)}{2}\,\mathbf{1}\,, \tag{5.68}$$

and the group velocity is given by the Alfvén speed

$$\mathbf{v}_g = \frac{B_0\,\hat{\mathbf{z}} + \mathbf{B}_1}{\sqrt{\mu\rho_0(1+\rho_1/\rho_0)}}\,. \tag{5.69}$$

By utilising a Taylor expansion $[(1+\rho_1/\rho_0)^{-1/2} = 1 - \rho_1/2\rho_0 + \ldots]$, subtracting the equilibrium ($\mathbf{v}_{g_0} = B_0\,\hat{\mathbf{z}}/\sqrt{\mu\rho_0}$) and linearising the above equation, the perturbed group velocity is shown to be

$$\mathbf{v}_{g_1} = \frac{\mathbf{B}_1}{\sqrt{\mu\rho_0}} - \frac{1}{2}\frac{B_0\,\hat{\mathbf{z}}}{\sqrt{\mu\rho_0}}\frac{\rho_1}{\rho_0}\,. \tag{5.70}$$

In full, the linearised, perturbed equations of magnetohydrodynamics are: the mass continuity equation (Eq. 1.14)

$$\frac{\partial\rho_1}{\partial t} + \nabla\cdot(\rho_0\mathbf{v}_1) = 0\,, \tag{5.71}$$

the equation of motion including the effect of the equilibrium waves (Eq. 5.58)

$$\rho_0\frac{\partial\mathbf{v}_1}{\partial t} = -c^2\,\nabla\rho_1 + (B_0\,\hat{\mathbf{z}}\cdot\nabla)\,\frac{\mathbf{B}_1}{\mu} - \nabla\left(\frac{B_0\,\hat{\mathbf{z}}\cdot\mathbf{B}_1}{\mu}\right) - \rho_1 g_0\,\hat{\mathbf{z}} + \rho_0\mathbf{g}_1 - \nabla\cdot\left(\frac{\varepsilon_1}{2}\,\mathbf{1}\right)\,, \tag{5.72}$$

the induction equation (Eq. 1.16)

$$\frac{\partial \mathbf{B_1}}{\partial t} = \nabla \times (\mathbf{v_1} \times B_0 \hat{\mathbf{z}}) \,, \tag{5.73}$$

the equation of self-gravitation (Eq. 1.17)

$$\nabla \cdot \mathbf{g}_1 = -4\pi G \rho_1 \,, \tag{5.74}$$

and the two wave equations (Eqs 5.66 and 5.67)

$$\frac{\partial \varepsilon_1}{\partial t} + \nabla \cdot (\mathbf{v}_{g_0} F_1) + \nabla \cdot (\mathbf{v}_{g_1} F_0) = -\Gamma_0 \varepsilon_1 + \frac{\Gamma \varepsilon_0}{2} \frac{\rho_1}{\rho_0} + s \frac{\rho_1}{\rho_0} \tag{5.75}$$

and

$$\frac{\partial F_1}{\partial t} + \nabla \cdot (\mathbf{v}_{g_0} \varepsilon_1) + \nabla \cdot (\mathbf{v}_{g_1} \varepsilon_0) = -\Gamma_0 F_1 + \frac{\Gamma F_0}{2} \frac{\rho_1}{\rho_0} \,. \tag{5.76}$$

Within the wave propagation equations the density dependent damping rate

$$\Gamma = \frac{\kappa}{\sqrt{(\rho_0 + \rho_1)/\rho_0(0)}}$$

(see Eq. 2.34) has been expanded and linearised to give

$$\Gamma = \Gamma_0 \left(1 - \frac{1}{2} \frac{\rho_1}{\rho_0}\right) \,,$$

where $\Gamma_0 = \kappa / \sqrt{\rho_0 / \rho_0(0)}$; and the source function (Eq. 5.38)

$$\mathrm{S} = \Psi \frac{\varepsilon_0(0) v_{A_0}(0)}{H} \left(\frac{\rho_0 + \rho_1}{\rho_0(0)}\right)^{\gamma}$$

has given a perturbed component of

$$\mathrm{S}_1 = \Psi \frac{\varepsilon_0(0) v_{A_0}(0)}{H} \left(\frac{\rho_0}{\rho_0(0)}\right)^{\gamma} \gamma \frac{\rho_1}{\rho_0} = \mathrm{s} \frac{\rho_1}{\rho_0} \,.$$

Fourier analysing these perturbed equations (Eqs 5.71 – 5.76) according to

$$\varepsilon_1 = \hat{\varepsilon}(z) \, \mathrm{e}^{i(\omega t - \mathbf{k} \cdot \mathbf{r}_\perp)}$$

for example, where $\mathbf{r}_\perp = (x, y)$, ω is the frequency and $\mathbf{k}$ is the wavenumber of the perturbations, leaves

$$i\omega\hat{\rho} - i\rho_0 (\mathbf{k} \cdot \hat{\mathbf{v}}_\perp) + \frac{d(\rho_0 \hat{v}_z)}{dz} = 0 \,, \tag{5.77}$$

$$i\omega\hat{\mathbf{B}} = B_0 \left(\frac{d\hat{v}_x}{dz} \hat{\mathbf{x}} + \frac{d\hat{v}_y}{dz} \hat{\mathbf{y}} + i (\mathbf{k} \cdot \hat{\mathbf{v}}_\perp) \hat{\mathbf{z}}\right) \tag{5.78}$$

and

$$\frac{d\hat{g}_z}{dz} = i (\mathbf{k} \cdot \hat{\mathbf{g}}_\perp) - 4\pi G \hat{\rho} \tag{5.79}$$

for the equations of continuity, induction and self-gravitation respectively, together with the equation of motion

$$i\omega\rho_0\hat{\mathbf{v}} = -c^2\left(-i\hat{\rho}\,(k_x\,\hat{\mathbf{x}} + k_y\,\hat{\mathbf{y}}) + \frac{d\hat{\rho}}{dz}\,\hat{\mathbf{z}}\right) + \frac{B_0}{\mu}\,\frac{d\hat{\mathbf{B}}}{dz} - \hat{\rho}g_0\,\hat{\mathbf{z}} + \rho_0\hat{\mathbf{g}}$$

$$-\frac{B_0}{\mu}\left(-i\hat{B}_z\,(k_x\,\hat{\mathbf{x}} + k_y\,\hat{\mathbf{y}}) + \frac{d\hat{B}_z}{dz}\,\hat{\mathbf{z}}\right) - \left(-i\,\frac{\hat{\varepsilon}}{2}\,(k_x\,\hat{\mathbf{x}} + k_y\,\hat{\mathbf{y}}) + \frac{1}{2}\frac{d\hat{\varepsilon}}{dz}\,\hat{\mathbf{z}}\right), \quad (5.80)$$

and the wave equations

$$i\omega\hat{\varepsilon} + \frac{d(v_{A_0}\hat{F})}{dz} - i\frac{F_0}{\sqrt{\mu\rho_0}}\left(\mathbf{k}\cdot\hat{\mathbf{B}}_\perp\right) + \frac{d}{dz}\left(\frac{F_0\hat{B}_z}{\sqrt{\mu\rho_0}}\right)$$

$$-\frac{B_0}{2}\frac{d}{dz}\left(\frac{F_0\hat{\rho}}{\rho_0\sqrt{\mu\rho_0}}\right) = -\Gamma_0\hat{\varepsilon} + \frac{\Gamma_0\varepsilon_0}{2\rho_0}\,\hat{\rho} + \mathrm{s}\,\frac{\hat{\rho}}{\rho_0}, \quad (5.81)$$

and

$$i\omega\hat{F} + \frac{d\,(v_{A_0}\hat{\varepsilon})}{dz} - i\frac{\varepsilon_0}{\sqrt{\mu\rho_0}}\left(\mathbf{k}\cdot\hat{\mathbf{B}}_\perp\right) + \frac{d}{dz}\left(\frac{\varepsilon_0\hat{B}_z}{\sqrt{\mu\rho_0}}\right)$$

$$-\frac{B_0}{2}\frac{d}{dz}\left(\frac{\varepsilon_0\hat{\rho}}{\rho_0\sqrt{\mu\rho_0}}\right) = -\Gamma_0\hat{F} + \frac{\Gamma_0 F_0}{2\rho_0}\,\hat{\rho}\,. \quad (5.82)$$

Eliminating the magnetic field $\hat{\mathbf{B}}$ (using Eq. 5.78) and choosing the axis so that the wavenumber becomes $\mathbf{k} = k\hat{\mathbf{x}}$ yields, in component form, a set of seven equations: the equation of continuity (Eq. 5.77), the x-component

$$v_{A_0}^2\frac{d^2\hat{v}_x}{dz^2} + \left(\omega^2 - k^2v_{A_0}^2\right)\hat{v}_x = \frac{c^2\omega k}{\rho_0}\,\hat{\rho} + k\omega\hat{\phi} + \frac{\omega k}{2\rho_0}\,\hat{\varepsilon}\,, \quad (5.83)$$

y-component

$$v_{A_0}^2\frac{d^2\hat{v}_y}{dz^2} + \omega^2\hat{v}_y = 0 \quad (5.84)$$

and z-component of the equation of motion

$$i\omega\rho_0\hat{v}_z = -g_0\hat{\rho} - c^2\frac{d\hat{\rho}}{dz} - \rho_0\frac{d\hat{\phi}}{dz} - \frac{1}{2}\frac{d\hat{\varepsilon}}{dz}\,, \quad (5.85)$$

where $v_{A_0}^2 = B_0^2/\mu\rho_0$ is the equilibrium Alfvén speed, the equation of self-gravitation

$$\frac{d^2\hat{\phi}}{dz^2} - k^2\hat{\phi} = 4\pi G\hat{\rho}\,, \quad (5.86)$$

where the gravity ($\hat{\mathbf{g}}$) has been written in terms of the gravitational potential $\hat{\phi}$ (see Eq. 5.14), and lastly, using the equilibrium results (Eqs 5.34 and 5.35), the two wave equations

$$\frac{d\hat{F}}{dz} - \frac{1}{2\rho_0}\frac{d\rho_0}{dz}\hat{F} = \left(\frac{\mathrm{s}}{\rho_0 v_{A_0}}\left\{1+\frac{1}{2\gamma}\right\} - \frac{F_0}{2\rho_0^2}\frac{d\rho_0}{dz}\right)\hat{\rho} + \left(\frac{\Gamma_0\varepsilon_0}{v_{A_0}} - \frac{\mathrm{s}}{\gamma v_{A_0}}\right)\frac{k}{\omega}\hat{v}_x - \left(\frac{i\omega}{v_{A_0}} + \frac{\Gamma_0}{v_{A_0}}\right)\hat{\varepsilon} + \frac{F_0}{2\rho_0}\frac{d\hat{\rho}}{dz} \tag{5.87}$$

and

$$\frac{d\hat{\varepsilon}}{dz} - \frac{1}{2\rho_0}\frac{d\rho_0}{dz}\hat{\varepsilon} = -\frac{\varepsilon_0}{2\rho_0^2}\frac{d\rho_0}{dz}\hat{\rho} + \frac{\Gamma_0 F_0}{v_{A_0}}\frac{k}{\omega}\hat{v}_x - \left(\frac{i\omega}{v_{A_0}} + \frac{\Gamma_0}{v_{A_0}}\right)\hat{F} + \frac{\varepsilon_0}{2\rho_0}\frac{d\hat{\rho}}{dz}. \tag{5.88}$$

Note that Equation (5.84), which describes the velocity perturbation in the y-direction ($\hat{v}_y$), has decoupled from the system of equations (see also Section 5.1.1). The remaining equations are written in terms of the dimensionless height ζ, perturbed velocities $\tilde{v}_x$ and $\tilde{v}_z$, gravitational potential $\tilde{\phi}$, frequency $\tilde{\omega}$ and wavenumber $\tilde{k}$ (defined in Section 5.1.1); plus the perturbed mass and wave energy densities

$$\tilde{\rho} = \frac{\hat{\rho}}{\rho_0(0)} \quad , \quad \tilde{\varepsilon} = \frac{\hat{\varepsilon}}{\varepsilon_0(0)} \quad , \quad \tilde{F} = \frac{\hat{F}}{\varepsilon_0(0)}$$

and the equilibrium quantities mass density $\tilde{\rho}_0$, wave energy densities $\tilde{\varepsilon}_0$ and $\tilde{F}_0$, and gravity $\tilde{g}_0$ (as defined in Section 5.2.1). Hence the equations become

$$\frac{d\left(\tilde{\rho}_0\tilde{v}_z\right)}{d\zeta} = i\tilde{\rho}_0\tilde{k}\tilde{v}_x - i\tilde{\omega}\tilde{\rho}\,, \tag{5.89}$$

$$\frac{d^2\tilde{v}_x}{d\zeta^2} = \beta\tilde{\omega}\tilde{k}\tilde{\rho} + \left(\tilde{k}^2 - \tilde{\omega}^2\tilde{\rho}_0\right)\tilde{v}_x + 2\beta\tilde{\omega}\tilde{k}\tilde{\rho}_0\tilde{\phi} + \beta\lambda\tilde{\omega}\tilde{k}\tilde{\varepsilon}\,, \tag{5.90}$$

$$\frac{d\tilde{\rho}}{d\zeta} + \lambda\frac{d\tilde{\varepsilon}}{d\zeta} = -2\sqrt{1+\lambda}\,\tilde{g}_0\tilde{\rho} - \frac{i\tilde{\omega}}{\beta}\tilde{\rho}_0\tilde{v}_z - 2\tilde{\rho}_0\frac{d\tilde{\phi}}{d\zeta}\,, \tag{5.91}$$

$$\frac{d^2\tilde{\phi}}{d\zeta^2} = \tilde{\rho} + \tilde{k}^2\tilde{\phi}\,, \tag{5.92}$$

$$\frac{d\tilde{F}}{d\zeta} - \frac{\tilde{F}_0}{2\tilde{\rho}_0}\frac{d\tilde{\rho}}{d\zeta} = \left(\frac{\Psi}{2}\tilde{\rho}_0^{\gamma-\frac{1}{2}}(1+2\gamma) - \frac{\tilde{F}_0}{2\tilde{\rho}_0^2}\frac{d\tilde{\rho}_0}{d\zeta}\right)\tilde{\rho} + \left(\Upsilon\tilde{\varepsilon}_0 - \Psi\tilde{\rho}_0^{\gamma+\frac{1}{2}}\right)\frac{\tilde{k}}{\tilde{\omega}}\tilde{v}_x - \left(i\sqrt{\tilde{\rho}_0}\,\tilde{\omega} + \Upsilon\right)\tilde{\varepsilon} + \frac{1}{2\tilde{\rho}_0}\frac{d\tilde{\rho}_0}{d\zeta}\tilde{F} \tag{5.93}$$

and

$$\frac{d\tilde{\varepsilon}}{d\zeta} - \frac{\tilde{\varepsilon}_0}{2\tilde{\rho}_0}\frac{d\tilde{\rho}}{d\zeta} = -\frac{\tilde{\varepsilon}_0}{2\tilde{\rho}_0^2}\frac{d\tilde{\rho}_0}{d\zeta}\tilde{\rho} + \Upsilon\tilde{F}_0\frac{\tilde{k}}{\tilde{\omega}}\tilde{v}_x + \frac{1}{2\tilde{\rho}_0}\frac{d\tilde{\rho}_0}{d\zeta}\tilde{\varepsilon} - \left(i\sqrt{\tilde{\rho}_0}\,\tilde{\omega} + \Upsilon\right)\tilde{F}\,, \tag{5.94}$$

where the dimensionless parameters are $\beta = c^2/v_{A_0}^2(0)$ (Eq. 5.20), the magnetisation parameter $\lambda = \varepsilon_0(0)/2\rho_0(0)c^2$ (Eq. 5.44), the damping parameter $\Upsilon = \kappa H/v_{A_0}(0)$ (Eq. 5.43) and the source parameters Ψ and γ (Eq. 5.38). This eighth-order system of equations, which describe the perturbations, will be examined in the remainder of this chapter in order to determine the stability of a wave pressure supported equilibrium.

5.2.3 The asymptotic solution

In accordance with the previous stability analysis (detailed in Section 5.1) it is possible to determine the asymptotic solution of the equations describing the perturbations (Eqs 5.89 – 5.94) given that the equilibrium mass density diminishes as the height above the central plane increases, i.e. $\tilde{\rho} \to 0$ as $\zeta \to \pm\infty$ (see Figure 5.4). To facilitate this the equations are written as a system of eight first-order differential equations for the variables

$$\mathrm{y}_1 = \frac{\tilde{v}_x}{\tilde{\omega}} \quad , \quad \mathrm{y}_2 = \frac{1}{\tilde{\omega}}\frac{d\tilde{v}_x}{d\zeta} \quad , \quad \mathrm{y}_3 = i\frac{\tilde{\rho}_0}{\tilde{\omega}}\,\tilde{v}_z \quad , \quad \mathrm{y}_4 = \tilde{\rho}$$

and

$$\mathrm{y}_5 = \tilde{\phi} \quad , \quad \mathrm{y}_6 = \frac{d\tilde{\phi}}{d\zeta} \quad , \quad \mathrm{y}_7 = \tilde{\varepsilon} \quad , \quad \mathrm{y}_8 = \tilde{F}$$

so that

$$\frac{d\mathrm{y}_1}{d\zeta} = \mathrm{y}_2 \tag{5.95}$$

$$\frac{d\mathrm{y}_2}{d\zeta} = \left(\tilde{k}^2 - \tilde{\rho}_0\tilde{\omega}^2\right)\mathrm{y}_1 + \beta\tilde{k}\,\mathrm{y}_4 + 2\beta\tilde{k}\tilde{\rho}_0\,\mathrm{y}_5 + \beta\lambda\tilde{k}\,\mathrm{y}_7 \tag{5.96}$$

$$\frac{d\mathrm{y}_3}{d\zeta} = \mathrm{y}_4 - \tilde{\rho}_0\tilde{k}\,\mathrm{y}_1 \tag{5.97}$$

$$\frac{d\mathrm{y}_4}{d\zeta} = \mathrm{A}\left(\mathrm{C}\,\mathrm{y}_4 - \lambda\Upsilon\tilde{F}_0\tilde{k}\,\mathrm{y}_1 - \frac{\tilde{\omega}^2}{\beta}\,\mathrm{y}_3 - 2\tilde{\rho}_0\,\mathrm{y}_6 - \frac{\lambda}{2\tilde{\rho}_0}\frac{d\tilde{\rho}_0}{d\zeta}\,\mathrm{y}_7 + \lambda\mathrm{B}\,\mathrm{y}_8\right) \tag{5.98}$$

$$\frac{d\mathrm{y}_5}{d\zeta} = \mathrm{y}_6 \tag{5.99}$$

$$\frac{d\mathrm{y}_6}{d\zeta} = \mathrm{y}_4 + \tilde{k}^2\,\mathrm{y}_5 \tag{5.100}$$

$$\frac{d\mathrm{y}_7}{d\zeta} = \mathrm{A}\left(\Upsilon\tilde{F}_0\tilde{k}\,\mathrm{y}_1 - \frac{\tilde{\omega}^2}{2\beta}\frac{\tilde{\varepsilon}_0}{\tilde{\rho}_0}\,\mathrm{y}_3 - \mathrm{D}\,\mathrm{y}_4 - \tilde{\varepsilon}_0\,\mathrm{y}_6 + \frac{1}{2\tilde{\rho}_0}\frac{d\tilde{\rho}_0}{d\zeta}\,\mathrm{y}_7 - \mathrm{B}\,\mathrm{y}_8\right) \tag{5.101}$$

$$\begin{aligned}\frac{d\mathrm{y}_8}{d\zeta} = {} & \left(\mathrm{L}\tilde{k} - \frac{\lambda\Upsilon\mathrm{A}\tilde{F}_0^2\tilde{k}}{2\tilde{\rho}_0}\right)\mathrm{y}_1 - \frac{\mathrm{A}\tilde{F}_0\tilde{\omega}^2}{2\beta\tilde{\rho}_0}\,\mathrm{y}_3 + \left(\frac{\mathrm{AC}\tilde{F}_0}{2\tilde{\rho}_0} - \mathrm{M}\right)\mathrm{y}_4 - \mathrm{A}\tilde{F}_0\,\mathrm{y}_6 \\ & - \left(\frac{\lambda\mathrm{A}\tilde{F}_0}{4\tilde{\rho}_0^2}\frac{d\tilde{\rho}_0}{d\zeta} + \mathrm{B}\right)\mathrm{y}_7 + \left(\frac{\lambda\mathrm{AB}\tilde{F}_0}{2\tilde{\rho}_0} + \frac{1}{2\tilde{\rho}_0}\frac{d\tilde{\rho}_0}{d\zeta}\right)\mathrm{y}_8\,,\end{aligned} \tag{5.102}$$

where

$$\mathrm{A} = \left(1 + \frac{\lambda\tilde{\varepsilon}}{2\tilde{\rho}_0}\right)^{-1}$$

$$\mathrm{B} = i\sqrt{\tilde{\rho}_0}\,\tilde{\omega} + \Upsilon$$

$$\mathrm{C} = \frac{\lambda\tilde{\varepsilon}_0}{2\tilde{\rho}_0^2}\frac{d\tilde{\rho}_0}{d\zeta} - 2\sqrt{1+\lambda}\,\tilde{g}_0$$

$$\mathrm{D} = \frac{\tilde{\varepsilon}_0}{2\tilde{\rho}_0^2}\frac{d\tilde{\rho}_0}{d\zeta} + \frac{\tilde{\varepsilon}_0}{\tilde{\rho}_0}\sqrt{1+\lambda}\,\tilde{g}_0$$

$$\mathrm{L} = \Upsilon\tilde{\varepsilon}_0 - \Psi\tilde{\rho}_0^{\gamma+\frac{1}{2}}$$

$$\mathrm{M} = \frac{\tilde{F}_0}{2\tilde{\rho}_0^2}\frac{d\tilde{\rho}_0}{d\zeta} - \frac{\Psi}{2}\,\tilde{\rho}_0^{\gamma-\frac{1}{2}}(1+2\gamma)\,.$$

Note that Equations (5.91), (5.93) and (5.94) have been transformed to give one differential equation for each of the dimensionless variables, mass density $\tilde{\rho}$ (y_4), total wave energy density $\tilde{\varepsilon}$ (y_7) and the difference in the wave energy densities of the positively and negatively propagating waves $\tilde{F}$ (y_8).

As the height $\zeta \to \pm\infty$ the equilibrium solution (see Chapter 2, Section 2.4.2) shows that the mass density $\tilde{\rho}_0 \to 0$, the wave energy densities $\tilde{\varepsilon}_0$, $\tilde{F}_0 \to 0$ and the gravity $\tilde{g}_0 \to \pm 1$. In this asymptotic limit Equations (5.95) – (5.102) can be written in matrix form as

$$\begin{pmatrix} y_1' \\ y_2' \\ y_3' \\ y_4' \\ y_5' \\ y_6' \\ y_7' \\ y_8' \end{pmatrix} = \begin{pmatrix} 0 & 1 & 0 & 0 & 0 & 0 & 0 & 0 \\ \tilde{k}^2 & 0 & 0 & \beta\tilde{k} & 0 & 0 & \beta\lambda\tilde{k} & 0 \\ 0 & 0 & 0 & 1 & 0 & 0 & 0 & 0 \\ 0 & 0 & -\frac{\mathrm{A}\tilde{\omega}^2}{\beta} & \mathrm{AC} & 0 & 0 & -\frac{\lambda\mathrm{A}R_2}{2} & \lambda\mathrm{AB} \\ 0 & 0 & 0 & 0 & 0 & 1 & 0 & 0 \\ 0 & 0 & 0 & 1 & \tilde{k}^2 & 0 & 0 & 0 \\ 0 & 0 & -\frac{\mathrm{A}\tilde{\omega}^2 R_1}{2\beta} & -\mathrm{AD} & 0 & 0 & \frac{\mathrm{A}R_2}{2} & -\mathrm{AB} \\ 0 & 0 & -\frac{\mathrm{A}\tilde{\omega}^2 R_3}{2\beta} & X & 0 & 0 & -Y & W \end{pmatrix} \begin{pmatrix} y_1 \\ y_2 \\ y_3 \\ y_4 \\ y_5 \\ y_6 \\ y_7 \\ y_8 \end{pmatrix} \tag{5.103}$$

where the elements in the matrix are

$$W = \frac{\lambda\mathrm{AB}R_3 + R_2}{2}$$

$$X = \frac{\mathrm{AC}R_3}{2} - \mathrm{M}$$

and

$$Y = \frac{\lambda\mathrm{A}R_2R_3}{4} + \mathrm{B}\,,$$

and the coefficients defined above have become

$$\mathrm{A} = \frac{2}{2+\lambda R_1}$$

$$\mathrm{B} = \Upsilon$$

$$\mathrm{C} = \frac{\lambda R_1 R_2}{2} - 2\sqrt{1+\lambda}\,\tilde{g}_0$$

$$\mathrm{D} = \frac{R_1R_2}{2} + R_1\sqrt{1+\lambda}\,\tilde{g}_0$$

$$\mathrm{L} = 0$$
$$\mathrm{M} = \frac{R_2 R_3}{2}.$$

The three ratios, which are defined to be $R_1 = \tilde{\varepsilon}_0/\tilde{\rho}_0$, $R_2 = (1/\tilde{\rho}_0)\, d\tilde{\rho}_0/d\zeta$ and $R_3 = \tilde{F}_0/\tilde{\rho}_0$, have been discussed in Section 5.2.1. Following the discussion in Section 5.1.2, Equation (5.103) has the solution

$$\mathrm{y}_i = \sum_i C_i \mathbf{u}_i \, \mathrm{e}^{\Lambda_i \zeta} \qquad \text{for } i = 1, 2, \ldots, 8$$

(Eq. 5.29), where C_i are the scaling coefficients, Λ_i are the eigenvalues of the square matrix and $\mathbf{u}_i$ are the corresponding eigenvectors.

The eigenvalues are determined by the usual method to be

$$+\tilde{k}, \; +\tilde{k}, \; -\tilde{k}, \; -\tilde{k}$$

and the roots of the quartic equation

$$\Lambda^4 + a_1\Lambda^3 + a_2\Lambda^2 + a_3\Lambda + a_4 = 0\,, \tag{5.104}$$

where the coefficients are

$$a_1 = -\mathrm{AC} - \frac{\mathrm{A}R_2}{2} - W$$

$$a_2 = \mathrm{A}\left(\frac{\mathrm{AC}R_2}{2} + \mathrm{C}W + \frac{WR_2}{2} - \mathrm{BY} - \frac{\lambda \mathrm{AD}R_2}{2} - \lambda \mathrm{B}X + \frac{\tilde{\omega}^2}{\beta}\right)$$

$$a_3 = \mathrm{A}^2\left(\mathrm{BC}Y - \frac{\mathrm{C}WR_2}{2} + \frac{\lambda \mathrm{D}WR_2}{2} - \lambda \mathrm{BD}Y + \left[\lambda \mathrm{B}R_3 - R_2 - \frac{\lambda R_1 R_2}{2}\right]\frac{\tilde{\omega}^2}{2\beta}\right) - \frac{\mathrm{A}W\tilde{\omega}^2}{\beta}$$

and

$$a_4 = \frac{\mathrm{A}\tilde{\omega}^2}{\beta}\left(\frac{WR_2}{2} - \mathrm{BY}\right).$$

By substituting in the expressions for A, B, etc. and using the results found in Section 5.2.1 for the ratios R_2 (Eq. 5.54) and R_3 (Eq. 5.53) the coefficients of the quartic equation reduce to

$$a_1 = \pm\frac{2\left(\lambda\Upsilon R_1 + 2\sqrt{1+\lambda} + 2\Upsilon\right)}{2 + \lambda R_1}$$

$$a_2 = \frac{2\left(4\Upsilon\sqrt{1+\lambda} + \tilde{\omega}^2/\beta\right)}{2 + \lambda R_1}$$

$$a_3 = \pm\frac{4\Upsilon\tilde{\omega}^2}{\beta\,(2 + \lambda R_1)}$$

and

$$a_4 = 0$$

at $\zeta \to \pm\infty$ respectively. Thus, as as can clearly be seen from the quartic equation (Eq. 5.104), the fifth eigenvalue is simply $\Lambda = 0$. The remaining cubic equation factorises to give

$$\frac{(\Lambda + 2\Upsilon)\left([2 + \lambda R_1]\Lambda^2 + 4\sqrt{1+\lambda}\,\Lambda + 2\tilde{\omega}^2/\beta\right)}{2 + \lambda R_1} = 0 \tag{5.105}$$

at $\zeta \to +\infty$ which implies the sixth eigenvalue is $\Lambda = -2\Upsilon$, and

$$-\frac{(2\Upsilon - \Lambda)\left([2 + \lambda R_1]\Lambda^2 - 4\sqrt{1+\lambda}\,\Lambda + 2\tilde{\omega}^2/\beta\right)}{2 + \lambda R_1} = 0 \tag{5.106}$$

at $\zeta \to -\infty$ giving the eigenvalue $\Lambda = +2\Upsilon$. The final two eigenvalues are the roots of the quadratic equation, which is given by the expression (at $\zeta \to \pm\infty$)

$$\Lambda^2 \pm \frac{4\sqrt{1+\lambda}}{2 + \lambda R_1}\Lambda + \frac{2\tilde{\omega}^2}{\beta\,(2 + \lambda R_1)} = 0\,. \tag{5.107}$$

Descartes' sign rule states that the total number of positive roots of a polynomial equation of order n,

$$a_0 x^n + a_1 x^{n-1} + \ldots + a_{n-1}x + a_n = 0\,,$$

can be determined by counting the number of sign changes in the sequence of coefficients $a_0, a_1, \ldots, a_n$. If all of the roots of the equation are real then the number of positive roots is equal to the number of sign changes; otherwise, the number of roots is an even number less than this (Bronstein & Semendjajew 1981). By examining the coefficients of the quadratic equation (Eq. 5.107), while noting that the ratio $R_1 > 0$ (Eq. 5.57 and Figure 5.4) and that the frequency $\tilde{\omega}^2 < 0$ for the unstable regime, it can be seen that there is one sign change at both $\zeta \to +\infty$ and $\zeta \to -\infty$. Thus, in either case, the solution of the quadratic will yield one positive eigenvalue (denoted by Λ_+) and one negative eigenvalue (denoted by Λ_-). (Note that, in this case, the same result can be obtained by observing that the final term in the quadratic is negative.)

In summary, the eight eigenvalues of the asymptotic matrix in Equation (5.103) are

$$+\tilde{k},\ +\tilde{k},\ -\tilde{k},\ -\tilde{k},\ 0,\ -2\Upsilon,\ \Lambda_+,\ \Lambda_-$$

at large heights above the central plane ($\zeta \to +\infty$), and

$$+\tilde{k},\ +\tilde{k},\ -\tilde{k},\ -\tilde{k},\ 0,\ +2\Upsilon,\ \Lambda_+,\ \Lambda_-$$

at large heights below the central plane ($\zeta \to -\infty$).

5.2.4 Boundary conditions and the numerical method

The boundary conditions

$$y_i \to 0 \qquad \text{as} \qquad \zeta \to \pm\infty$$

for $i = 1, 2, \ldots, 8$, are used to solve the set of equations which describe the perturbations (Eqs 5.95 – 5.102). Following the discussion given in Section 5.1.3 of this chapter, these boundary conditions are satisfied by choosing the decaying asymptotic solution (Eq. 5.29). Specifically, the negative eigenvalues ($-\tilde{k}$, $-\tilde{k}$, -2Υ and Λ_-) at $\zeta \to +\infty$ and the positive eigenvalues ($+\tilde{k}$, $+\tilde{k}$, $+2\Upsilon$ and Λ_+) at $\zeta \to -\infty$, together with their associated eigenvectors (which are detailed in Appendix C), yield a total of eight scaling coefficients which correspond to the eighth-order system of perturbation equations. By normalising seven of these coefficients with respect to the eighth, Equations (5.95) – (5.102) can be solved numerically only for particular values of $\tilde{\omega}^2$, thus giving the dispersion relation $\tilde{\omega}(\tilde{k})$ (see Section 5.1.3 for more details).

As in Section 5.1.3, the numerical technique used to solve the equations (Eqs 5.95 – 5.102) is the relaxation method (Press et al. 1992). If there are only a small number of waves supporting the equilibrium the magnetisation parameter takes a value of $\lambda \leq 1$. In this case the outer boundaries are taken at heights of $\zeta = \pm 20$. For higher values of λ the boundaries are necessarily moved outwards to values up to $\zeta = \pm 50$, to allow for the increased level of support in the equilibrium gas layer. At such heights the equilibrium mass density has certainly fallen to insignificant levels and the three equilibrium ratios have reached constant values. Once again, the square of the frequency is introduced as an additional variable, y_9 say, and thus the particular value of $\tilde{\omega}^2$ is found as part of the numerical solution (see Section 5.1.3 for details). Note that the equilibrium solution, which is required to solve the equations describing the perturbations (see Eqs 5.95 – 5.102), cannot be found analytically and so is determined using a standard numerical technique for solving ordinary differential equations.

5.2.5 Results

By solving the perturbed equations (Eqs 5.95 – 5.102), for given values of the plasma beta (β), the magnetisation parameter (λ), the damping parameter (Υ) and the source parameters (Ψ and γ), a dispersion curve is obtained and hence the stability of the equilibrium can be ascertained. However, the numerical solution of these equations proves to be very difficult and the results presented in this section are the best that could be obtained using conventional numerical techniques (Press et al. 1992). Specifically, these preliminary results were found using the relaxation method (see Section 5.2.4).

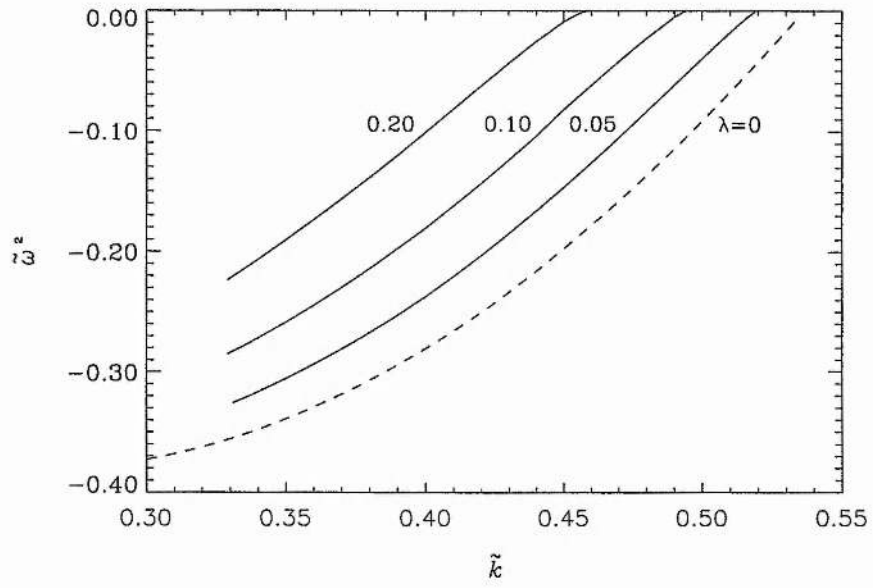

Figure 5.5: Partial dispersion curves for an isothermal gas slab which is being supported by short-wavelength Alfvén waves. The curves are plotted for increasing values of the magnetisation parameter λ (see Eq. 5.44), together with a plasma beta $\beta = 2$, damping $\Upsilon = 0.5$ and power-law index $\gamma = 3$. The dashed curve, reproduced from Figure 5.2, represents the case when there are no waves in the equilibrium.

Figure 5.5 shows some partial dispersion curves for an isothermal gas slab which is in equilibrium between the gas pressure, an Alfvén wave pressure force and its self-gravity. The curves are plotted for successive values of the magnetisation parameter (Eq. 5.44), from $\lambda = 0$ (dashed curve) to $\lambda = 0.2$, which represents a gradual increase in the number of short-wavelength Alfvén waves supporting the equilibrium. It can be observed from Figure 5.5 that the critical wavenumber (that for which $\tilde{\omega}^2 = 0$) decreases as λ is increased, and that the form of the partial dispersion curves does not appear significantly different from that obtained when there are no waves in the equilibrium ($\lambda = 0$). If this is indeed the case then these partial dispersion curves show that increasing the amount of Alfvén wave support in the equilibrium has a stabilising effect on the isothermal gas layer. The values of the parameter λ for which the results are obtained do in fact provide very little additional support to the equilibrium gas layer. Values of $\lambda = 10$ and upwards have been shown to be needed (Chapter 2, Table 2.3) in order to provide some significant support against the self-gravity. However, the curves plotted in Figure 5.5 suggest that increasing the parameter λ may actually help to stabilise the model cloud.

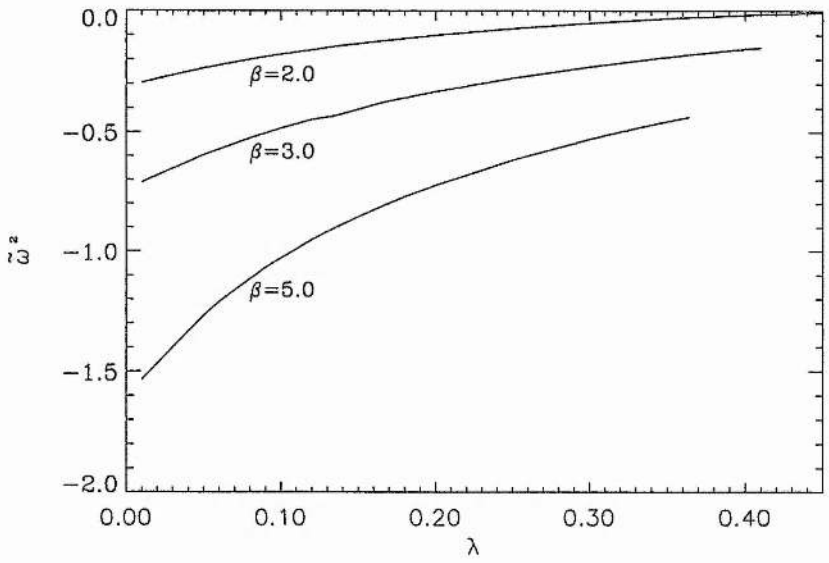

Figure 5.6: The square of the frequency ($\tilde{\omega}^2$) plotted against the magnetisation parameter λ for wavenumber $\tilde{k} = 0.4$, damping $\Upsilon = 0.5$ and power-law index $\gamma = 3$. The dimensionless parameter β is the ratio between the sound speed and the equilibrium Alfvén velocity at the central plane ($\zeta = 0$) (see Eq. 5.20).

The results plotted in Figure 5.6 show the variation of the frequency with the parameter λ for a particular wavenumber ($\tilde{k} = 0.4$), and various values of the dimensionless parameter β (Eq. 5.20). Decreasing values of β suggest that the magnetic field is becoming more important in the cloud dynamics. In the previous stability analysis (discussed in Section 5.1) it was observed that increasing the relative strength of the magnetic field had a stabilising effect on the gas layer. Such a result is again indicated by the curves in Figure 5.6. Following the evolution of these curves with increasing λ shows, as in Figure 5.5, that higher values of the magnetisation parameter significantly reduce the magnitude of the wave frequency, suggesting that increasing the number of waves in the equilibrium stabilises the model cloud. Indeed, following the $\beta = 2.0$ curve in Figure 5.6 shows that this particular case becomes stable for $\lambda \geq 0.52$ (to the accuracy of the numerics).

All of the curves shown in Figures 5.5 and 5.6 are plotted for a damping parameter of $\Upsilon = 0.5$ and source parameter $\gamma = 3$. The second source parameter Ψ is determined as part of the equilibrium solution (see Chapter 2, Section 2.4.1). The numerical results obtained suggest that a slight change in the damping appears to have very little influence on the value of the wave frequency. Note that Figures 5.5 and 5.6 both present

the minimum value of the square of the frequency ($\tilde{\omega}^2$) for a given set of parameters.

The preliminary results presented in this section give an insight into the stability of an Alfvén-wave-pressure-supported equilibrium. Whilst showing that the model can indeed become unstable, they indicate that both enhancing the significance of the equilibrium magnetic field (by decreasing the parameter β) and increasing the amount of wave support (by increasing the parameter λ) act to stabilise the cloud. This is certainly the case for the specific parameter sets depicted in both Figure 5.5 and Figure 5.6. An equilibrium is subject to a gravitational instability when the gravitational forces cause a small disturbance to grow exponentially, resulting in regions of both increasing and decreasing mass density. In regions where the mass density is increasing, gravitational condensations begin to form. As these condensations form the magnetic field lines are dragged along with the density (as the magnetic field cannot remain unperturbed — see Section 5.1.4 and Appendix B) and thus the Alfvén waves, which propagate along the field lines, are able to provide some support against the gravitational forces. If the wave support is sufficient then the condensations will not continue to grow exponentially and thus the presence of the Alfvén waves in the system can act to stabilise the cloud.

5.3 Discussion

The work presented in this chapter has considered the stability of two models which depict the equilibrium of an isothermal gas layer. The first of these models has a uniform magnetic field running perpendicular to the sheet, which is itself in equilibrium between the gas pressure and self-gravity. The key factor in determining the dispersion curves of this equilibrium is the ratio between the sound speed and the equilibrium Alfvén velocity at the central plane ($\beta = c^2/v_{A_0}^2$). As this ratio is reduced and hence the magnetic field becomes increasingly important, the stability of the cloud improves. This trend continues until the magnetic and gas pressures are equal (the Alfvén speed is twice the sound speed, $\beta = 0.5$), at which point the model gas layer is stable for all values of the wavenumber. Such a result agrees with that proposed by Nakano (1988). Observational values of the sound and Alfvén speeds, which give a typical value of $\beta = 10^{-3}$, strengthen the case for the stability of these equilibria.

Earlier chapters have been concerned with the role of Alfvén waves in low-mass star-forming regions, in particular the degree of support they can offer against self-gravity. Therefore, the second model under consideration in this chapter is that of a gas layer in equilibrium between its self-gravity, gas pressure and an Alfvén wave pressure force. The short-wavelength Alfvén waves (the WKB approximation) are generated

throughout the cloud, according to a density-dependent source function. Numerical difficulties prevented a thorough analysis of the stability of such an equilibria but the preliminary results obtained offer a useful insight into the problem. The results leave no doubt that the isothermal gas layer can become unstable. However, as in the previous analysis, the stability of the model cloud appears to improve as the magnetic field becomes more dominant in the cloud dynamics. The influence of the Alfvén waves on the stability of the slab is also suggested by the preliminary results. They show that slightly improving the wave support (increasing the value of the magnetisation parameter λ) appears to have a stabilising effect on the cloud. Although the results obtained from this analysis are limited they do provide clues to the stability which are favourable for models of an Alfvén-wave-pressure-supported equilibrium.

In general, the stability analyses conducted within this chapter show that the presence of a magnetic field within such equilibria has a stabilising effect on the model. This fact encourages continued consideration of the role of magnetic fields in low-mass star-forming regions, in particular the role these fields play in supporting such regions against their self-gravity.

Chapter 6

Conclusion

Forty-two.

Douglas Adams

6.1 A summary of the main results

The work presented throughout this thesis has considered the role of Alfvén waves in low-mass star-forming regions, in particular the ability of these waves to help support a gravitationally bound molecular cloud. Previous work has shown that a molecular cloud can be supported against its self-gravity, in the direction perpendicular to the ordered magnetic field, by the Lorentz force (e.g. Mouschovias & Spitzer 1976). It is proposed that in the direction parallel to the magnetic field a low-mass star-forming region is supported by an Alfvén wave pressure force.

In Chapter 2 a one-dimensional, self-consistent, analytical model was formulated to examine the support provided by short-wavelength Alfvén waves; those waves whose wavelength is short in comparison with the length-scale of the non-uniform medium in which they propagate, i.e. the WKB approximation. The damping of these waves was by the linear process of ion-neutral friction, as it was for each of the models presented in this thesis. As a first approximation the Alfvén waves were assumed to originate in a central, source plane. This model enabled an analytical solution of the equilibrium mass density profile to be found in the absence of damping, and clearly demonstrated that the damping of the waves was not a prerequisite for support of the cloud. Indeed, it was found that if the damping was too strong then the wave support was substantially reduced. This δ-function distribution of sources also resulted in an increase in the mass density away from the central plane, which was enhanced for larger values of the wave

amplitude and strong damping. These results agree qualitatively with those of Fatuzzo & Adams (1993) who considered the waves as a perturbation to a thermally supported equilibrium. The density enhancement was shown in the latter part of Chapter 2 to be a consequence of a δ-function source distribution. If the sources of the Alfvén waves are distributed in height according to a density-dependent source function then there is no increase in mass density away from the central plane. In addition, increasing the strength of the damping no longer imposes an upper limit on the thickness of the gas layer, rather stronger values of the damping continue to enhance the Alfvén wave pressure force and increase the extent of the layer.

Having successfully demonstrated the viability of short-wavelength Alfvén wave support, the work in Chapter 4 considered the equilibrium of a one-dimensional gas slab in the presence of long-wavelength Alfvén waves. By noting the physical properties of the Alfvén waves able to offer support to a low-mass star-forming region, as discussed in Chapter 1 (Section 1.4), it can be seen that the wavelength of these waves, being $\sim 0.1 - 1$ pc, is comparable to the typical length-scale of such a region. Thus, although the WKB approximation offered an excellent first approach to the problem, it was necessary to consider the self-consistent model in the absence of this approximation. As in Chapter 2 an equilibrium was initially constructed for a δ-function distribution of wave sources. This model showed that removing the WKB approximation introduces some sub-structure into the profiles of mass density. By analysing the parameter space the following results were obtained. Firstly, if the equilibrium contains very low-amplitude, long-wavelength Alfvén waves then the gas layer is separated into a number of distinct subsheets, which are held against the self-gravity of the layer by the jump in Alfvén wave pressure across the sheet. Each of these subsheets is itself in equilibrium between its internal gas pressure and self-gravity, the waves having no influence on their individual structure. Secondly, if the wavelength of the waves is reduced or the amplitude of the waves is increased, or both, then the model cloud can be described as displaying fine structure in its density distribution; it is no longer separated into distinct subsheets but is supported as a whole. In the absence of any damping the artefacts in density were shown to be directly proportional to the wavelength of the Alfvén wave supporting the cloud.

Other aspects of this non-WKB model correlated with those discussed in Chapter 2 for short-wavelength Alfvén wave support. The inclusion of damping, which was taken to be constant in Chapter 4, increases the amount of mass in the central subsheets and therefore increases the thickness of the layer. Specifically, it reduces the ability of long-wavelength waves to be able to support subsheets far from the central plane

and thus enhances the amount of mass in the central regions. Strong values of the damping were also found to cause a general increase in mass density away from the central plane; once again this bump in mass density was shown to be accentuated by the δ-function source distribution. It had been shown in Chapter 1 that the Alfvén waves can be generated by the orbital motions of large-scale condensations of molecular gas, and as such the source function included within the non-WKB model was chosen to be completely coherent. By allowing all points within the model to act as a source of waves the support of the individual subsheets — generated by very low-amplitude, long-wavelength Alfvén waves — was slightly enhanced.

Quantitatively the results of the models constructed in Chapters 2 and 4 show that both short-wavelength and long-wavelength Alfvén waves can provide support for a low-mass star-forming region parallel to the magnetic field. Observations of these molecular clouds show that the fluid velocities are $v \sim 1 - 3\,\mathrm{km\,s^{-1}}$ (Myers 1987; Myers & Goodman 1988) and determine the Alfvén velocity to be $v_A \sim 4.5\,\mathrm{km\,s^{-1}}$. Now the amplitude of the Alfvén wave (b) relative to the uniform magnetic field (B_0) is $b/B_0 \simeq v/v_A$ and thus can take values of $b/B_0 \sim 0.2 - 0.7$. In terms of the magnetisation parameter (λ), which is applicable to the short-wavelength model (Chapter 2), these values give $\lambda \sim 5 - 35$ which correspond to model cloud thicknesses of $\sim 1 - 4$ pc. As the fluid velocity approaches the Alfvén value the parameter $\lambda \sim 80$ and the thickness of the gas layer increases to ~ 10 pc for a typical value of the damping. For the long-wavelength model a wave amplitude of $b/B_0 \sim 0.2$ can give a cloud thickness of ~ 4 pc, while for velocities comparable to the Alfvén value ($b/B_0 \sim 1$) the thickness increases to ~ 10 pc once again. Low-mass star-forming regions are observed to have sizes of a few to ten parsecs. Thus, the equilibrium models describing short-wavelength and large-amplitude, long-wavelength support give model cloud thicknesses which are in excellent agreement with the observational values.

The support offered by large-amplitude, long-wavelength Alfvén waves is particularly encouraging when viewed together with other results determined for low-mass star-forming regions. In Chapter 1 it was demonstrated that long-wavelength Alfvén waves can provide pressure support to the whole cloud, as they allow very good coupling between the neutral and charged constituents of the molecular gas. Zweibel & Josafatsson (1983) concluded that these long-wavelength Alfvén waves, propagating parallel to the magnetic field, are the longest lived wave modes in a molecular cloud. In addition, Mouschovias & Psaltis (1995) formulated a line-width-size relation for large-amplitude, long-wavelength Alfvén waves which agrees well with the empirically determined observational result.

The other aspects of Alfvén wave support considered in the remaining chapters involve the contribution of any heating by the waves to the thermal equilibrium, and the stability of the model clouds. Chapter 3 established a simple model to describe the heating and cooling mechanisms dominant in a low-mass star-forming region: the cooling of a number of molecular species and ionized carbon, together with the heating due to cosmic rays and the Alfvén waves supporting the cloud. This temperature-dependent model showed that the heating attributed to the Alfvén wave pressure can play an important role in determining the temperature of these clouds. If the wave heating is neglected then the model clouds have an almost constant temperature of $\sim 7\,\mathrm{K}$. However, including the heating by the waves gives temperatures in the centre of the cloud of $\sim 10 - 20\,\mathrm{K}$ which increase to typically $\sim 25 - 35\,\mathrm{K}$ at the edge of the gas layer. This leads to the conclusion that a molecular cloud supported against its self-gravity by an Alfvén wave pressure, will be hotter at its outer edge than in the central regions by a factor of approximately two; in qualitative agreement with the work of McKee & Zweibel (1995). The temperature-dependent model showed that the amount of wave heating consistent with wave support does not generate cloud temperatures that strongly disagree with the observational values, which is an important consideration when investigating the role of Alfvén waves in a low-mass star-forming region.

Finally, Chapter 5 addressed the question of the stability of two one-dimensional models representing the equilibria of a low-mass star-forming region. The first of these models considered a gas slab, supported solely by the gas pressure, containing a uniform magnetic field in the direction perpendicular to the slab. The dispersion curves for this equilibrium showed that once the Alfvén speed becomes equal to twice the sound speed (the magnetic and gas pressures become equal) the model clouds are completely stable. Such a result agrees with that of Nakano (1988). In analysing the stability of an equilibrium supported by short-wavelength Alfvén waves numerical difficulties precluded a complete study of the problem, but nevertheless, the results obtained provided a useful insight into the stability. They suggest that, as for the previous equilibrium, the magnetic field has a stabilising effect on the model cloud. In addition, the partial dispersion curves obtained indicate that the Alfvén waves can also have a stabilising effect; these waves propagate along the magnetic field lines and as a result they are able to provide additional support where the condensations are forming and thus hinder the gravitational collapse.

Overall, this thesis has considered the idea of supporting molecular clouds using Alfvén waves, previously introduced by Fatuzzo & Adams (1993) and McKee & Zweibel (1995) for example, more quantitatively by constructing self-consistent models, both in

a mechanical and thermal sense, and discussing their stability. These models successfully describe a low-mass star-forming region in equilibrium between its self-gravity, gas pressure and an Alfvén wave pressure force, and estimate the amount of support both short-wavelength and long-wavelength Alfvén waves can provide. The model included a consideration of the thermal equilibrium in a molecular cloud and found that the heating generated by the waves cannot be neglected. Following on from the purely numerical work of Gammie & Ostriker (1996) the role of long-wavelength waves is considered from an analytical approach, and it is confirmed that these waves can support a cloud if the wave amplitude takes values in the range implied by the observations. This thesis has also given a first consideration to the stability of an equilibrium supported by short-wavelength Alfvén waves. In summary, this work has demonstrated the viability of an Alfvén wave pressure supporting a low-mass star-forming region. It has constructed self-consistent equilibrium models which give results for the dimensions of these clouds in good agreement with the observations, and lays the foundations for the further theoretical consideration of Alfvén waves in low-mass star-forming regions.

6.2 Further possible avenues of investigation

In this section several possible extensions to the work discussed in this thesis are briefly outlined. As an immediate extension to the stability analysis reported in Chapter 5 a more robust numerical code could be developed to solve the equations describing the perturbations and hence help construct a fuller picture of the stability of a low-mass star-forming region supported by short-wavelength Alfvén waves. It would also be interesting to study the stability of a cloud supported by long-wavelength Alfvén waves as this may introduce new features into the results found thus far.

Given the conclusion reached in Chapter 3 — that the heating attributed to the wave support can play an important role in the thermal equilibrium of molecular clouds — it would be interesting to develop a more detailed picture of the chemical processes which contribute to the heating and cooling. This would produce models that would be sophisticated enough to compare with observations, although improvements in other aspects of the models, such as the distribution of wave sources or the cloud geometry, would be equally desirable in this respect.

The most important simplification adopted in the work carried out thus far is the adoption of a one-dimensional gas slab to describe the molecular cloud. Expanding the models to two or three dimensions is important in developing a more complete picture of the support provided to a molecular cloud by the magnetic field and the waves it

supports. However, such generalisations will undoubtedly require a more numerical than analytical approach.

An additional improvement would be to treat the problem using the two-fluid magnetohydrodynamic equations for the neutrals and the plasma, which would allow a more detailed description of the coupling between the ions and neutrals (ion-neutral drag). This would demonstrate the efficiency of the ion-neutral drag as the wavelength of the Alfvén wave is varied; as well as the dissipation of the waves by the ion-neutral friction. These thoughts represent only a fraction of the many ways in which models of Alfvén wave support in a low-mass star-forming region can be further developed in the future.

Appendix A

The WKB approximation

The WKB approximation[1] (Wentzel, Kramers and Brillouin) is an asymptotic method for solving differential equations which contain a large parameter. In the specific case of a wave equation this method can be applied when the non-uniform medium is varying on a length-scale which is much greater than the wavelength of the waves propagating within the medium. Consider a wave equation of the form

$$\epsilon^2 y'' = -Q(x)\, y\,, \tag{A.1}$$

where ϵ is a small number and $'$ indicates a derivative with respect to x. Using the WKB approximation, the general solution of this equation is given by

$$y = \frac{B}{Q(x)^{1/4}} \exp\left(i\int^x \frac{\sqrt{Q(u)}}{\epsilon}\, du\right) + \frac{C}{Q(x)^{1/4}} \exp\left(-i\int^x \frac{\sqrt{Q(u)}}{\epsilon}\, du\right), \tag{A.2}$$

where B and C are the integration constants.

Proof: Take y to be of the form

$$y = \exp\left\{\pm i\left(\frac{f_0(x)}{\epsilon} + f_1(x) + \cdots\right)\right\} \tag{A.3}$$

and substitute into Equation (A.1) to give

$$(\pm i)^2\,\epsilon^2\left(\frac{f_0'(x)}{\epsilon} + f_1' + \cdots\right)^2 \pm i\epsilon^2\left(\frac{f_0''(x)}{\epsilon} + f_1'' + \cdots\right) = -Q(x) \tag{A.4}$$

which, by discarding the insignificant terms, can be written as

$$-Q(x) = -f_0'^{\,2}(x) - 2\epsilon f_0'(x) f_1'(x) \pm i\epsilon f_0''(x)\,. \tag{A.5}$$

Equating the coefficients of the linear terms

$$f_0(x) = \pm\int^x \sqrt{Q(u)}\; du\,, \tag{A.6}$$

[1] Also known as the WKBJ approximation (Wentzel, Kramers, Brillouin and Jeffreys).

and the first-order terms

$$\exp\left(\mp i f_1(x)\right) = \frac{1}{Q(x)^{1/4}}, \tag{A.7}$$

gives the solution

$$y = \frac{1}{Q(x)^{1/4}} \exp\left(\pm i \int^x \frac{\sqrt{Q(u)}}{\epsilon}\, du\right) \tag{A.8}$$

which, in a general form, is that described by Equation (A.2).

Within the solution (Eq. A.2) the term $Q^{-1/4}$ is slowly varying compared to the exponential term (given that ϵ is a small number) and thus varies on the length-scale of the medium, while the term $\sqrt{Q}/\epsilon$ varies as the wavelength of the waves propagating within the non-uniform medium.

Appendix B

No magnetic field perturbation in Equations (5.2) – (5.5)

In this appendix the stability of an isothermal gas slab, with a uniform magnetic field lying perpendicular to it, is considered in the absence of a magnetic field perturbation. In the case of a gas sheet containing a parallel magnetic field such a simplification leads to an analytic solution for the dispersion relation (Fleischer 1996; Fleischer & Schindler 1996).

If the magnetic field remains unperturbed (i.e. $\mathbf{B}_1 = 0$) the linearised differential equations (Eqs 5.2 – 5.5) are: the mass continuity equation

$$\frac{\partial \rho_1}{\partial t} + \nabla \cdot (\rho_0 \mathbf{v}_1) = 0 \,, \tag{B.1}$$

the equation of motion

$$\rho_0 \frac{\partial \mathbf{v}_1}{\partial t} = -c^2 \nabla \rho_1 - \rho_1 g_0 \hat{\mathbf{z}} + \rho_0 \mathbf{g}_1 \,, \tag{B.2}$$

the induction equation

$$0 = \nabla \times (\mathbf{v_1} \times B_0 \hat{\mathbf{z}}) \tag{B.3}$$

and the equation of self-gravitation

$$\nabla \cdot \mathbf{g}_1 = -4\pi G \rho_1 \,, \tag{B.4}$$

where the equilibrium quantities are denoted by a subscript 0 and the perturbed quantities by a subscript 1. Following the same procedure as described in Chapter 5 — Fourier analysing these equations in time and space, according to

$$\rho_1 = \hat{\rho}(z)\, \mathrm{e}^{i(\omega t - \mathbf{k}\cdot\mathbf{r}_\perp)}$$

for example, where $\mathbf{r}_\perp = (x, y)$, ω is the frequency and $\mathbf{k}$ is the wavenumber, and choosing the x-axis such that the wavenumber $\mathbf{k} = k\,\hat{\mathbf{x}}$ — the perturbed equations can

be written as

$$i\omega\hat{\rho} - i\rho_0 k\hat{v}_x + \frac{d\left(\rho_0\hat{v}_z\right)}{dz} = 0\,, \tag{B.5}$$

$$i\omega\rho_0\hat{\mathbf{v}} = -c^2\left(-ik\hat{\rho}\,\hat{\mathbf{x}} + \frac{d\hat{\rho}}{dz}\,\hat{\mathbf{z}}\right) - \hat{\rho}g_0\,\hat{\mathbf{z}} + \rho_0\hat{\mathbf{g}} \tag{B.6}$$

and

$$\frac{d\hat{v}_x}{dz}\,\hat{\mathbf{x}} + \frac{d\hat{v}_y}{dz}\,\hat{\mathbf{y}} + ik\hat{v}_x\,\hat{\mathbf{z}} = 0 \tag{B.7}$$

given that the equilibrium magnetic field $B_0 \neq 0$, plus

$$\frac{d\hat{g}_z}{dz} = ik\hat{g}_x - 4\pi G\hat{\rho}\,. \tag{B.8}$$

The z-component of the Fourier-analysed induction equation (Eq. B.7) clearly shows that

$$\hat{v}_x = 0$$

as $k \neq 0$ generally, and thus the x-component of Equation (B.6) becomes

$$0 = c^2\hat{\rho} + \rho_0\hat{\phi} \tag{B.9}$$

given that $\hat{\mathbf{g}} = (ik\hat{\phi},\, 0,\, -d\hat{\phi}/dz)$ (Eq. 5.14). In addition the y-component of the equation of motion (Eq. B.6) states that

$$\hat{v}_y = 0$$

while the z-component becomes

$$i\omega\hat{v}_z = -c^2\,\frac{d}{dz}\left(\frac{\hat{\rho}}{\rho_0}\right) - \frac{d\hat{\phi}}{dz}\,, \tag{B.10}$$

as the equilibrium gravity can be expressed in terms of the mass density through $g_0 = \left(-c^2/\rho_0\right) d\rho_0/dz$. Substituting Equation (B.9) into Equation (B.10) shows that the perturbed velocity in the z-direction is also

$$\hat{v}_z = 0$$

and hence $\hat{\rho} = 0$ (from Equation (B.5)) and finally $\hat{\phi} = 0$ (from Equation (B.9)).

These results show that in the absence of a magnetic field perturbation the velocity, mass density and gravitational potential perturbations are all also equal to zero. Thus if $\mathbf{B_1} = 0$ it is not possible to generate any gravitational instabilities within the gas sheet.

Appendix C

The detailed boundary conditions for Equations (5.95) – (5.102)

When considering the stability of an equilibrium, which is supported by a WKB Alfvén wave pressure force, the equations which describe the perturbations (Eqs 5.95 – 5.102) are solved subject to the boundary conditions

$$\mathrm{y}_i \to 0 \qquad \text{as} \qquad \zeta \to \pm\infty \tag{C.1}$$

for $i = 1, 2, \ldots, 8$, where y_i are the perturbed variables (defined in Chapter 5, Section 5.2.3) and ζ is the height above the central plane. These boundary conditions are expressed in terms of the asymptotic solution of Equations (5.95) – (5.102), which is given by

$$\mathrm{y}_i = \sum_i C_i \mathbf{u}_i \, \mathrm{e}^{\Lambda_i \zeta} \qquad \text{for } i = 1, 2, \ldots, 8$$

where C_i are the scaling coefficients, Λ_i are the decaying eigenvalues and $\mathbf{u}_i$ are the associated eigenvectors of the matrix

$$\begin{pmatrix}
0 & 1 & 0 & 0 & 0 & 0 & 0 & 0 \\
\tilde{k}^2 & 0 & 0 & \beta\tilde{k} & 0 & 0 & \beta\lambda\tilde{k} & 0 \\
0 & 0 & 0 & 1 & 0 & 0 & 0 & 0 \\
0 & 0 & -\frac{\mathrm{A}\tilde{\omega}^2}{\beta} & \mathrm{AC} & 0 & 0 & -\frac{\lambda \mathrm{A} R_2}{2} & \lambda\mathrm{AB} \\
0 & 0 & 0 & 0 & 0 & 1 & 0 & 0 \\
0 & 0 & 0 & 1 & \tilde{k}^2 & 0 & 0 & 0 \\
0 & 0 & -\frac{\mathrm{A}\tilde{\omega}^2 R_1}{2\beta} & -\mathrm{AD} & 0 & 0 & \frac{\mathrm{A}R_2}{2} & -\mathrm{AB} \\
0 & 0 & -\frac{\mathrm{A}\tilde{\omega}^2 R_3}{2\beta} & X & 0 & 0 & -Y & W
\end{pmatrix}$$

(see Eq. 5.103), where A, B, C, D, W, X and Y are defined in Chapter 5, Section 5.2.3.

As the height above the central plane increases to large positive values ($\zeta \to +\infty$) the boundary conditions (Eq. C.1) are satisfied by choosing the negative eigenvalues,

which are found to be

$$-\tilde{k},\ -\tilde{k},\ -2\Upsilon,\ \Lambda_{-}$$

where $\tilde{k}$ is the wavenumber, Υ is the damping parameter, Λ_{-} is the negative root of the quadratic equation

$$\Lambda^2 + \frac{4\sqrt{1+\lambda}}{2+\lambda R_1}\Lambda + \frac{2\tilde{\omega}^2}{\beta\,(2+\lambda R_1)} = 0\,, \tag{C.2}$$

$\tilde{\omega}$ is the wave frequency, λ is the magnetisation parameter, β is the plasma beta and R_1 is the ratio between the equilibrium quantities: total wave energy density and mass density (see Chapter 5, Section 5.2.1). Conversely, at $\zeta \to -\infty$ the chosen eigenvalues are

$$+\tilde{k},\ +\tilde{k},\ +2\Upsilon,\ \Lambda_{+}$$

where Λ_{+} is the positive root of the quadratic equation

$$\Lambda^2 - \frac{4\sqrt{1+\lambda}}{2+\lambda R_1}\Lambda + \frac{2\tilde{\omega}^2}{\beta\,(2+\lambda R_1)} = 0\,. \tag{C.3}$$

Thus the boundary conditions at $\zeta \to +\infty$ ($\zeta = \zeta_{max}$) are given by

$$\begin{pmatrix} y_1 \\ y_2 \\ y_3 \\ y_4 \\ y_5 \\ y_6 \\ y_7 \\ y_8 \end{pmatrix} = C_1 \begin{pmatrix} 1 \\ -\tilde{k} \\ 0 \\ 0 \\ 0 \\ 0 \\ 0 \\ 0 \end{pmatrix} e^{-\tilde{k}\zeta_{max}} + C_2 \begin{pmatrix} 0 \\ 0 \\ 0 \\ 0 \\ 1 \\ -\tilde{k} \\ 0 \\ 0 \end{pmatrix} e^{-\tilde{k}\zeta_{max}}$$

$$+ C_3 \begin{pmatrix} t_1 \\ -2\Upsilon t_1 \\ -2\lambda\Upsilon t_2 \\ 4\lambda\Upsilon^2 t_2 \\ 4\lambda\Upsilon^2 \\ -8\lambda\Upsilon^3 \\ -t_3 \\ -t_3 \end{pmatrix} e^{-2\Upsilon\zeta_{max}} + C_4 \begin{pmatrix} t_4 \\ \Lambda_{-} t_4 \\ 2t_5 \\ 2\Lambda_{-} t_5 \\ 2\Lambda_{-} \\ 2\Lambda_{-}^2 \\ R_1\Lambda_{-} t_5 \\ R_1\Lambda_{-} t_5 \end{pmatrix} e^{\Lambda_{-}\zeta_{max}} \tag{C.4}$$

and those at $\zeta \to -\infty$ ($\zeta = \zeta_{min}$) are

$$\begin{pmatrix} y_1 \\ y_2 \\ y_3 \\ y_4 \\ y_5 \\ y_6 \\ y_7 \\ y_8 \end{pmatrix} = D_1 \begin{pmatrix} 1 \\ \tilde{k} \\ 0 \\ 0 \\ 0 \\ 0 \\ 0 \\ 0 \end{pmatrix} e^{\tilde{k}\zeta_{min}} + D_2 \begin{pmatrix} 0 \\ 0 \\ 0 \\ 0 \\ 1 \\ \tilde{k} \\ 0 \\ 0 \end{pmatrix} e^{\tilde{k}\zeta_{min}}$$

$$+ D_3 \begin{pmatrix} t_1 \\ 2\Upsilon t_1 \\ 2\lambda\Upsilon t_2 \\ 4\lambda\Upsilon^2 t_2 \\ 4\lambda\Upsilon^2 \\ 8\lambda\Upsilon^3 \\ -t_3 \\ t_3 \end{pmatrix} e^{2\Upsilon\zeta_{min}} + D_4 \begin{pmatrix} t_4 \\ \Lambda_+ t_4 \\ 2t_5 \\ 2\Lambda_+ t_5 \\ 2\Lambda_+ \\ 2\Lambda_+^2 \\ R_1\Lambda_+ t_5 \\ -R_1\Lambda_+ t_5 \end{pmatrix} e^{\Lambda_+\zeta_{min}} \qquad \text{(C.5)}$$

where C_1, C_2, C_3, C_4, D_1, D_2, D_3 and D_4 are the eight scaling coefficients which correspond to the eight equations describing the perturbations (Eqs 5.95 – 5.102) and the terms in the eigenvectors are given by

$$t_1 = \beta\lambda\,\tilde{k}\left(4\Upsilon\sqrt{1+\lambda} - \frac{\tilde{\omega}^2}{\beta}\right),$$

$$t_2 = 4\Upsilon^2 - \tilde{k}^2,$$

$$t_3 = \left(\frac{\tilde{\omega}^2}{\beta} + 4\Upsilon\left[\Upsilon - \sqrt{1+\lambda}\right]\right) t_2,$$

$$t_4 = \beta\,\tilde{k}\,\Lambda_{\mp}\left(2 + \lambda R_1\right),$$

and

$$t_5 = \Lambda_{\mp}^2 - \tilde{k}^2.$$

References

Adams, D., In: The Hitch-Hikers Guide to the Galaxy, Pan Books Ltd

Adams, D., In: The Restaurant at the End of the Universe, Pan Books Ltd

Adler D.S., Allen R.J., Lo K.Y., 1991, ApJ 382, 475

Arons J., Max C.E., 1975, ApJ 196, L77

Begelman M.C., 1995, Cosmic-Ray Heating of the Interstellar Gas. In: Ferrara A., McKee C.F., Heiles C., Shapiro P.R. (eds) ASP Conf. Series, The Physics of the Interstellar Medium and Intergalactic Medium. San Francisco, p. 545

Black J.H., 1987, Heating and Cooling of the Interstellar Gas. In: Hollenbach D.J., Thronson H.A. (eds) Interstellar Processes. D. Reidel Publishing Company, Dordrecht, p. 731

Bonazzola S., Falgarone E., Heyvaerts J., Pérault M., Puget J.L., 1987, A&A 172, 293

Bonazzola S., Pérault M., Puget J.L., Heyvaerts J., Falgarone E., Panis J.F., 1992, J. Fluid Mech. 245, 1

Bronstein I.N., Semendjajew K.A., 1981, Taschenbuch der Mathematik, Harri Deutsch, Thun

Cesarsky C.J., Völk H.J., 1978, A&A 70, 367

Champeaux S., Gazol A., Passot T., Sulem P.-L., 1997, ApJ 486, 477

Charnley S.B., 1998, MNRAS 298, L25

Crutcher R.M., Troland T.H., Goodman A.A., Heiles C., Kazès I., Myers P.C., 1993, ApJ 407, 175

Crutcher R.M., Troland T.H., Lazareff B., Kazès I., 1996, ApJ 456, 217

de Jong T., Dalgarno A., Boland W., 1980, A&A 91, 68

Dewar R.L., 1970, Phys. Fluids 13, 2710

Dickman R.L., 1978, ApJS 37, 407

Draine B.T., Roberge W.G., Dalgarno A., 1983, ApJ 264, 485

Dyson J.E., Williams D.A., 1997, The Physics of the Interstellar Medium, IOP Publishing, Bristol

Elmegreen B.G., 1979, ApJ 232, 729

Elmegreen B.G., 1990, ApJ 361, L77

Elmegreen B.G., 1997, ApJ 480, 674
Falgarone E., Puget J.L., 1986, A&A 162, 235
Farquhar P.R.A., Millar T.J., Herbst E., 1994, MNRAS 269, 641
Fatuzzo M., Adams F.C., 1993, ApJ 412, 146
Field G.B., 1978, Conditions in Collapsing Clouds. In: Gehrels T. (ed.) Protostars and Planets. University of Arizona Press, Tucson, p. 243
Fleischer J., 1996, Ph. D. Thesis, Numerische Untersuchungen zur linearen und nichtlinearen Dynamik selbstgravitierender Plasmen, Ruhr-Universität Bochum, Bochum, Germany
Fleischer J., Schindler K., 1996, Astrophys. Lett. & Comm. 34, 237
Gammie C.F., Ostriker E.C., 1996, ApJ 466, 814
Goldsmith P.F., Langer W.D., 1978, ApJ 222, 881 (GL78)
Goodman A.A., Heiles C., 1994, ApJ 424, 208
Gredel R., Lepp S., Dalgarno A., Herbst E., 1989, ApJ 347, 289
Hartquist T.W., Rawlings J.M.C., Williams D.A., Dalgarno A., 1993, QJRAS 34, 213
Hartquist T.W., Williams D.A., 1995, The Chemically Controlled Cosmos, Cambridge University Press, Cambridge
Jacques S.A., 1977, ApJ 215, 942
Larson R.B., 1981, MNRAS 194, 809
Le Bourlot J., Pineau des Forêts G., Roueff E., Flower D.R., 1993, A&A 267, 233
Lis D.C., Goldsmith P.F., 1990, ApJ 356, 195
Martin C.E., Heyvaerts J., Priest E.R., 1997, A&A 326, 1176
McKee C.F., 1989, ApJ 345, 782
McKee C.F., Zweibel E.G., 1995, ApJ 440, 686
McKenna T., In: Bryan C.D.B., Close encounters of the fourth kind, Penguin Books
Mizuno A., Onishi T., Yonekura Y., Nagahama T., Ogawa H., Fukui Y., 1995, ApJ 445, L161
Moneti A., Pipher J.L., Helfer H.L., McMillan R.S., Perry M.L., 1984, ApJ 282, 508
Mouschovias T.C., 1991, Cosmic Magnetism and the Basic Physics of the Early Stages of Star Formation. In: Lada C.J., Kylafis N.D. (eds) NATO ASI, The Physics of Star Formation and Early Stellar Evolution. Kluwer Academic Publishers, Dordrecht, p. 61
Mouschovias T.C., 1995, Role of Magnetic Fields in the Early Stages of Star Formation. In: Ferrara A., Heiles C., McKee C.F., Shapiro P.R. (eds) ASP Conf. Series, The Physics of the Interstellar Medium and Intergalactic Medium. San Francisco, p. 184
Mouschovias T.C., Psaltis D., 1995, ApJ 444, L105

Mouschovias T.C., Spitzer L., 1976, ApJ 210, 326

Murphy G.M., 1960, Ordinary Differential Equations and their Solutions, D. Van Nostrand Company, New York

Myers P.C., 1987, Observations of Molecular Cloud Structure and Internal Motions. In: Hollenbach D.J., Thronson H.A. (eds) Interstellar Processes. D. Reidel Publishing Company, Dordrecht, p. 71

Myers P.C., 1999, Physical Conditions in nearby Molecular Clouds. In: Lada C.J., Kylafis N.D. (eds) NATO ASI, The Physics of Star Formation and Early Stellar Evolution II. Kluwer Academic Publishers, Dordrecht (in press)

Myers P.C., Benson P.J., 1983, ApJ 266, 309

Myers P.C., Goodman A.A., 1988, ApJ 326, L27

Nakano T., 1988, PASJ 40, 593

Nakano T., Nakamura T., 1978, PASJ 30, 671

Neufeld D.A., Lepp S., Melnick G.J., 1995, ApJS 100, 132

Norman C., Silk J., 1980, ApJ 238, 158

Press W.H., Teukolsky S.A., Vetterling W.T., Flannery B.P., 1992, Numerical Recipes in Fortran, Cambridge University Press, Cambridge

Priest E.R., 1982, Solar Magnetohydrodynamics, D. Reidel Publishing Company, Dordrecht

Rao R., Crutcher R.M., Plambeck R.L., Wright M.C.H., 1998, ApJ 502, L75

Robinson K.S., In: Blue Mars, HarperCollins Publishers

Scoville N.Z., 1992, Interstellar Medium, Galactic Molecular Hydrogen. In: Maran S.P. (ed.) The Astronomy and Astrophysics Encyclopaedia. Cambridge University Press, Cambridge, p. 373

Shu F.H., 1983, ApJ 273, 202

Shu F.H., Adams F.C., Lizano S., 1987, ARA&A 25, 23

Spaans M., 1996, A&A 307, 271

Spitzer L., 1968, Diffuse Matter in Space, Interscience Publishers, New York

Suchkov A., Allen R.J., Heckman T.M., 1993, ApJ 413, 542

Takahashi T., Hollenbach D.J., Silk J., 1983, ApJ 275, 145

Takano T., 1986, ApJ 303, 349

Tiné S., Lepp S., Gredel R., Dalgarno A., 1997, ApJ 481, 282

van Dishoeck E.F., Black J.H., 1986, ApJS 62, 109

Warin S., Benayoun J.J., Viala Y.P., 1996, A&A 308, 535

Watterson B., In: Calvin and Hobbes, Weirdos from another Planet, Warner Books

Yan M., Dalgarno A., 1997, ApJ 481, 296

Young J.S., Scoville N.Z., 1991, ARA&A 29, 581
Zuckerman B., Palmer P., 1974, ARA&A 12, 279
Zweibel E.G., Josafatsson K., 1983, ApJ 270, 511

The most beautiful thing we can experience is the mysterious. It is the source of all true art and science. He to whom this emotion is a stranger, who can no longer pause to wonder and stand rapt in awe, is as good as dead: his eyes are closed.

Albert Einstein